

**UNCLASSIFIED**

---

**AD 290 317**

*Reproduced  
by the*

**ARMED SERVICES TECHNICAL INFORMATION AGENCY  
ARLINGTON HALL STATION  
ARLINGTON 12, VIRGINIA**



---

**UNCLASSIFIED**

## **DISCLAIMER NOTICE**

**THIS DOCUMENT IS BEST QUALITY  
PRACTICABLE. THE COPY FURNISHED  
TO DTIC CONTAINED A SIGNIFICANT  
NUMBER OF PAGES WHICH DO NOT  
REPRODUCE LEGIBLY.**

NOTICE: When government or other drawings, specifications or other data are used for any purpose other than in connection with a definitely related government procurement operation, the U. S. Government thereby incurs no responsibility, nor any obligation whatsoever; and the fact that the Government may have formulated, furnished, or in any way supplied the said drawings, specifications, or other data is not to be regarded by implication or otherwise as in any manner licensing the holder or any other person or corporation, or conveying any rights or permission to manufacture, use or sell any patented invention that may in any way be related thereto.

**AUTHOR: ROBERT G. RICKS**



## NOTICES

When Government drawings, specifications, or other data are used for any purpose other than in connection with a definitely related Government procurement operation, the United States Government thereby incurs no responsibility nor any obligation whatsoever; and the fact that the Government may have formulated, furnished, or in any way supplied the said drawings, specifications, or other data, is not to be regarded by implication or otherwise as in any manner licensing the holder or any other person or corporation, or conveying any rights or permission to manufacture, use, or sell any patented invention that may in any way be related thereto.

Qualified requesters may obtain copies of this report from the Armed Services Technical Information Agency, (ASTIA), Arlington Hall Station, Arlington 12, Virginia.

This report has been released to the Office of Technical Services, U.S. Department of Commerce, Washington 25, D.C., for sale to the general public.

Copies of this report should not be returned to the Aeronautical Systems Division unless return is required by security considerations, contractual obligations, or notice on a specific document.

Aeronautical Systems Division, Dir/Aero-  
mechanics, Flight Dynamics Laboratory,  
Wright-Patterson Air Force Base, Ohio.  
Rpt No. ASD-TDR-62-284. A STUDY OF TANDEM  
HELICOPTER FUSELAGE VIBRATION. Final report,  
Sep 62, 285p incl illus., 12 refs.

Unclassified Report

A comprehensive research program covering  
many facets of tandem rotor helicopter  
fuselage vibration was conducted. Analytical  
portions consisted of the development of  
methods for the prediction of fuselage natural  
and forced modes; test portions of the pro-  
gram determined fuselage stiffness properties.

( over )

rotor shaft vibratory loads and in-flight  
natural frequencies, modes and vibration  
levels. The results have proven to be of  
considerable value in the design of the  
present generation of helicopters.

1. Vibration
2. Helicopters
  - I. AFSC Project 1370  
Task 137004  
Rpt No. ASD-TDR-62-284. A STUDY OF TANDEM  
HELICOPTER FUSELAGE VIBRATION. Final report,  
Sep 62, 285p incl illus., 12 refs.

- III. Vertol Division,  
The Boeing Company,  
Morton, Pe.

- IV. Robert G. Ricks

- V. R-275

- VI. Aval fr OTS

- VII. In ASTIA collection

Aeronautical Systems Division, Dir/Aero-  
mechanics, Flight Dynamics Laboratory,  
Wright-Patterson Air Force Base, Ohio.  
Rpt No. ASD-TDR-62-284. A STUDY OF TANDEM  
HELICOPTER FUSELAGE VIBRATION. Final report,  
Sep 62, 285p incl illus., 12 refs.

Unclassified Report

A comprehensive research program covering  
many facets of tandem rotor helicopter  
fuselage vibration was conducted. Analytical  
portions consisted of the development of  
methods for the prediction of fuselage natural  
and forced modes; test portions of the pro-  
gram determined fuselage stiffness properties.

( over )

rotor shaft vibratory loads and in-flight  
natural frequencies, modes and vibration  
levels. The results have proven to be of  
considerable value in the design of the  
present generation of helicopters.

1. Vibration
2. Helicopters
  - I. AFSC Project 1370  
Task 137004  
Rpt No. ASD-TDR-62-284. A STUDY OF TANDEM  
HELICOPTER FUSELAGE VIBRATION. Final report,  
Sep 62, 285p incl illus., 12 refs.

- III. Vertol Division,  
The Boeing Company,  
Morton, Pe.

- IV. Robert G. Ricks

- V. R-275

- VI. Aval fr OTS

- VII. In ASTIA collection

Aeronautical Systems Division, Dir/Aero-mechanics, Flight Dynamics Laboratory, Wright-Patterson Air Force Base, Ohio.  
Rpt No. ASD-TDB-62-284. A STUDY OF TANDEM HELICOPTER FUSELAGE VIBRATION. Final report, Sep 62, 285p incl illus., 12 refs.

Unclassified Report

A comprehensive research program covering many facets of tandem rotor helicopter fuselage vibration was conducted. Analytical portions consisted of the development of methods for the prediction of fuselage natural and forced modes; test portions of the program determined fuselage stiffness properties.

( over )

rotor shaft vibratory loads and in-flight natural frequencies, modes and vibration levels. The results have proven to be of considerable value in the design of the present generation of helicopters.

1. Vibration
2. Helicopters
  - I. AFSC Project 1370 Task 137004
  - II. Contract AF33(616)-5240
  - III. Vertol Division, The Boeing Company, Morton, Pe.
  - IV. Robert G. Ricks V. R-275
  - VI. Aval fr OTS
  - VII. In ASTIA collection

Aeronautical Systems Division, Dir/Aero-mechanics, Flight Dynamics Laboratory, Wright-Patterson Air Force Base, Ohio.  
Rpt No. ASD-TDB-62-284. A STUDY OF TANDEM HELICOPTER FUSELAGE VIBRATION. Final report, Sep 62, 285p incl illus., 12 refs.

Unclassified Report

A comprehensive research program covering many facets of tandem rotor helicopter fuselage vibration was conducted. Analytical portions consisted of the development of methods for the prediction of fuselage natural and forced modes; test portions of the program determined fuselage stiffness properties.

( over )

rotor shaft vibratory loads and in-flight natural frequencies, modes and vibration levels. The results have proven to be of considerable value in the design of the present generation of helicopters.

1. Vibration
2. Helicopters
  - I. AFSC Project 1370 Task 137004
  - II. Contract AF33(616)-5240
  - III. Vertol Division, The Boeing Company, Morton, Pe.
  - IV. Robert G. Ricks V. R-275
  - VI. Aval fr OTS
  - VII. In ASTIA collection

FOREWORD

This report was prepared by the Vertol Division of The Boeing Company, Morton, Pennsylvania under Air Force Contract AF33(616)-5240. The work was administered under the direction of Flight Dynamics Laboratory, Aeronautical Systems Division, Wright-Patterson Air Force Base, Ohio. The ASD Project Number was 1370, "Dynamic Problems in Flight Vehicles," and the Task Number was 137004, "Methods for Predicting Rotor Induced Helicopter Vibrations." Robert Cook and Channing Pao were the Project Engineers for the Laboratory. It was funded by the Department of the Army under Project No. 9R38-11-009-05 directed by John Yeates. Vertol Division's number for this report is R-275.

The studies presented began in 1957, were terminated in January 1962 and represent the effort of the Dynamics Department of the Boeing Company's Vertol Division. Although the studies were a group effort, the chief contributors were: V. Capurso, J. Dummer, R. Gabel, R. Loewy, D. Manger, D. Reed, R. Ricks, C. Shakespeare, P. Shyprykevich, D. Smyers and R. Yntema.

This report concludes the work on Contract AF33(616)-5240.

### ABSTRACT

A comprehensive research program covering many facets of tandem rotor helicopter fuselage vibration was conducted. Analytical portions consisted of the development of methods for the prediction of fuselage natural and forced modes; test portions of the program determined fuselage stiffness properties, rotor shaft vibratory loads and in-flight natural frequencies, modes and vibration levels. The results have proven to be of considerable value in the design of the present generation of helicopters.

### PUBLICATION REVIEW

This report has been reviewed and is approved.

FOR THE COMMANDER



AMBROSE B. NUTT  
Asst. Chief, Dynamics Branch  
Flight Dynamics Laboratory

TABLE OF CONTENTS

<u>Section</u>	<u>Description</u>	<u>Page</u>
I	Introduction.....	1
II	A Method for the Prediction of Natural Mode and Frequency Changes Accompanying Changes in Fuselage Mass and Stiffness.....	5
III	A Method for the Prediction of Natural Modes and Frequencies from Design Mass and Stiffness Data.....	17
IV	Load Deflection Tests on an H-21 Helicopter Fuselage to Determine Stiffness Characteristics.....	31
V	In-Flight Measurement of Steady and Oscillatory Rotor Shaft Loads.....	41
VI	In-Flight Shake Test.....	75
VII	A Method for the Prediction of Coupled Vertical- Lateral Natural and Forced Modes.....	113
VIII	A Method for the Prediction of Coupled Vertical- Lateral Modes Including Multi-Directional Damped Rotor Effective Mass.....	135
IX	Conclusions.....	167
	References.....	174

APPENDICES

A.	Derivation of the Generalized Coordinate Coupling Equations.	175
B.	Uncoupled Mode Associated Matrix Derivation and Method of Solution.....	187
C.	Coupled Mode Associated Matrix Derivation and Method of Solution.....	197
D.	Coupled, Damped Mode Associated Matrix Derivation and Method of Solution.....	245

List of Illustrations

<u>Figure</u>	<u>Page</u>
1. Program Flow Chart.....	3
<u>Generalized Coordinate Coupling Analysis</u>	
2. H-16 Weight Distribution.....	7
3. Shell Configuration Vertical Bending Stiffness Properties and Mode Shapes Used as Coupling Agent for Mass Changes.....	9
4. First Vertical Bending Mode.....	10
5. Second Vertical Bending Mode.....	11
6. Third Vertical Bending Mode.....	12
7. Shell Configuration Vertical Bending Stiffness Properties and Mode Shapes Used as Coupling Agent for Stiffness Changes.....	13
8. Comparison of Coordinate Coupling for Stiffness Changes and Matrix Vertical Bending Modes.....	15
<u>Associated Matrix Uncoupled Analysis</u>	
9. H-21 Shell Configuration Vertical Bending Modes.....	18
10. H-21 Ballasted Configuration Vertical Bending Modes.....	20
11. H-21 Shell Configuration Lateral Bending Modes.....	21
12. H-21 Ballasted Configuration Lateral Bending Modes.....	23
13. Vertical Bending, Matrix Residual Curve.....	24
14. Comparison of H-21 Vertical Bending Modes with Rigid and Flexible Engine.....	25
15. Lateral Bending, Matrix Residual Curve.....	26
16. Comparison of H-21 Lateral Bending Modes with Rigid and Flexible Engine.....	27
<u>Load-Deflection Test on the H-21</u>	
17. Overall View of a Fuselage-Half Installed in Reinforced Test Fixture.....	32
18. Method of Load Application.....	33
19. Vertical and Lateral Stiffness Characteristics.....	35
20. Torsional Stiffness Characteristics from Lateral and Vertical Deflection Measurements.....	37
21. Summary of Rotor Transmission Spring Rates.....	38
<u>In-Flight Rotor Shaft Loads</u>	
22. Rotor Shaft Calibrations.....	44
23. Flow Diagram for Converting Data to Shaft Loads.....	47
24. Sign Convention for Fixed and Rotating Hub Loads.....	48
25. Forward and Aft Rotor Directions.....	49
26. Fixed System Steady Shaft Loads.....	50

List of Illustrations

<u>Figure</u>	<u>Page</u>
27. Effect on Fixed System of Centrifugal Force Unbalance.....	51
28. Fixed System First Harmonic Loads Airspeed Sweep at 258 rpm....	52
29. Fixed System First Harmonic Loads rpm Sweep at 40 Knots.....	53
30. Fixed System First Harmonic Loads rpm Sweep at 90 Knots.....	54
31. Fixed System Second Harmonic Loads Airspeed Sweep at 258 rpm...	56
32. Fixed System Second Harmonic Loads rpm Sweep at 40 Knots.....	57
33. Fixed System Second Harmonic Loads rpm Sweep at 90 Knots.....	58
34. Fixed System Third Harmonic Loads Airspeed Sweep at 258 rpm....	60
35. Fixed System Third Harmonic Loads rpm Sweep at 40 Knots.....	61
36. Fixed System Third Harmonic Loads rpm Sweep at 90 Knots.....	62
37. Rotating System Second Harmonic Loads Airspeed Sweep at 258 rpm.....	65
38. Rotating System Second Harmonic Loads rpm Sweep at 40 & 90 Knots.....	66
39. Rotating System Fourth Harmonic Loads Airspeed Sweep at 258 rpm.....	67
40. Rotating System Fourth Harmonic Loads rpm Sweep at 40 & 90 Knots.....	68
41. Fixed System Third Harmonic Loads rpm Sweep at 90 knots, 14,685 lb.....	69
42. Correlation of Hub Loads and Vibration Measurement.....	71
<u>In-Flight Shake Test</u>	
43. In-Flight Hydraulic Shaker.....	76
44. Control Console and Shaker Installation.....	78
45. Force Available From In-Flight Shaker.....	79
46. Location of Fuselage Motion Transducers.....	80
47. Location of Engine Motion Pickups.....	81
48. Davies Airborne Magnetic Tape Recorder.....	82
49. Test Equipment Installation-Main Cabin.....	84
50. Davies Magnetic Tape Analyzer.....	85
51. Response at 258 rpm for 200 lb Lateral Force.....	86
52. Response at 258 rpm for 300 lb Vertical Force.....	87
53. Comparison of Ground Test and In-Flight Response at 258 rpm for 200 lb Lateral Force.....	90
54. Comparison of Ground Test and In-Flight Response at 258 rpm for 200 lb Vertical Force.....	91
55. Response at 240 rpm and 278 rpm for 200 lb. Lateral Force.....	95
56. Comparison of In-Flight Response at 240, 258 and 278 rpm for 200 lb Lateral Force.....	96
57. Frequency Response with Lateral Excitation.....	97
58. Response at 240 rpm and 278 rpm for 300 lb Vertical Force.....	99
59. Comparison of In-Flight Response at 240, 258 and 278 rpm for 300 lb Vertical Force.....	100
60. Frequency Response with Vertical Excitation.....	101



<u>Figure</u>	<u>In-Flight Shake Test</u>	<u>Page</u>
61.	In-Flight Forced Modes @ 8.1 and 9.2 cps.....	104
62.	In-Flight Forced Modes @ 9.1 and 9.9 cps.....	106
63.	In-Flight Forced Modes @ 10.05 and 13.2 cps.....	107
64.	In-Flight Forced Modes @ 11.1 and 13.75 cps.....	108
 <u>Coupled Vertical-Lateral Analysis</u>		
65.	H-21 Vertical-Lateral Matrix Representation.....	114
66.	Forward Fuselage Elastic Properties.....	115
67.	Forward Fuselage Simulated Deflection.....	116
68.	Aft Fuselage Elastic Properties.....	117
69.	Reference Axis Location and Weight Distribution.....	118
70.	Matrix Residual Plot.....	120
71.	First and Second Matrix Modes.....	121
72.	Third Matrix Mode.....	122
73.	Fourth Matrix Mode.....	124
74.	Fifth and Sixth Matrix Modes.....	125
75.	Seventh and Eighth Matrix Modes.....	127
76.	Ninth and Tenth Matrix Modes.....	128
77.	Eleventh and Twelfth Matrix Modes.....	129
78.	Cockpit Floor Response.....	131
 <u>Coupled, Damped Vertical-Lateral Analysis</u>		
79.	Rotor and Engine Properties.....	136
80.	In-Flight Response for 200 lb Vertical Force at Station 312.....	137
81.	In-Flight Response for 200 lb Lateral Force at Station 312.....	138
82.	Comparison of Forward and Aft Blade Calculated Response at 258 rpm for 200 lb Vertical Excitation at Station 312.....	140
83.	Forward Rotor Hub and Blade Tip Motions at 258 rpm under 200 lb Vertical Excitation at Station 312.....	142
84.	Forward Rotor Hub and Blade Tip Motions at 258 rpm under 200 lb Lateral Excitation at Station 312.....	143
85.	In-Flight Test Mode @ 8.1 cps-300 lb Vertical Force, 258 rpm Rotor Speed.....	146
86.	In-Flight Test Mode @ 9.9 cps-300 lb Vertical Force, 258 rpm Rotor Speed.....	148
87.	In-Flight Test Mode @ 10.05 cps-200 lb Lateral Force, 258 rpm Rotor Speed.....	149
88.	In-Flight Test Mode @ 11.1 cps-200 lb Lateral Force, 258 rpm Rotor Speed.....	150
89.	In-Flight Test Mode @ 13.2 cps-200 lb Lateral Force, 258 rpm Rotor Speed.....	151
90.	Comparison of In-Flight Fuselage Response at 240, 258 and 278 rpm.....	153
91.	Comparison of In-Flight Blade Tip Response at 240, 258 and 278 rpm for Fuselage Excitation.....	154
92.	Calculated Frequency Response with Vertical Excitation.....	156
93.	Calculated Frequency Response with Lateral Excitation.....	157
94.	Cockpit Floor Motion for Metal Blades.....	159
95.	Forced Response - Vertical Unit Loads.....	161
96.	Forced Response - Lateral Unit Loads.....	162
97.	Forced Response - Longitudinal Unit Loads.....	163

## SECTION 1

## INTRODUCTION

Contract AF33(616)-5240, Reference (1), is a multiple phase research program into tandem rotor helicopter dynamic characteristics. The general aim of the research is to acquire more complete knowledge of the nature of fuselage and rotor vibration and its inducing forces, and from this knowledge to develop refined methods of calculation from design data. This will permit the reliable prediction of the response of tandem rotor helicopters to rotor forcing frequencies, an important prerequisite to the minimization of helicopter vibration. The program is composed of the following phases:

- Phase I - Develop a computing machine method for accurate prediction of the changes in resonant frequencies of the helicopter, with rotors replaced by a mass, resulting from design variations and assuming a knowledge of the design data and measured resonances of the suspended helicopter.
- Phase IIa - Develop a computing machine method for accurate prediction of resonant frequencies of tandem helicopter fuselages from design data when the rotors are replaced by a mass, and establish criteria for eliminating insignificant modes.
- Phase IIb - Conduct static load deflection tests on the H-21 helicopter to obtain criteria for determining the fuselage dynamic stiffness from design data.
- Phase IIc - Extend Phase IIa to include the effects of coupling between vertical and lateral motions found to exist in the deflection tests of IIb.
- Phase III - Measure H-21 vibratory hub forces and moments in-flight at various forward speeds, rotor rpm's, and at two gross weights.
- Phase IV - Develop a method for calculating the forced response of the fuselage of tandem rotor helicopters when the rotor hub vibratory loads are known and evaluate the method by applying it to the H-21 using the hub loads measured in Phase III.
- Phase V - Conduct in-flight shake tests on the H-21 helicopter to obtain in-flight frequency response characteristics and natural frequencies and modes of the combined fuselage and rotor system.
- Phase VI - Develop a method for accurate prediction of the coupled vertical-lateral resonant frequencies and forced responses of tandem helicopter fuselages, including the effect of the rotating rotors and evaluate by comparison with in-flight shake test and flight vibration data.
- Phase VII - Conduct a study to develop a suitable method for improving the correlation between measured vibration data and pilot comments.

---

Manuscript released by Robert Ricks, March 1960, for publication as an ASD Technical Report.

The present report is a summary of the major technical phases performed under this Contract, all of which have been reported separately in more detail in References 2 to 8. Phase VII, a correlation of measured vibration data and pilot comment, has been published as ASD Report 61-66, Reference 9, and is not included herein.

Figure 1 is a flow chart of the overall research program. The two dotted blocks in the left column represent design and test information available before the program began. Initial analytical phases were Phase I which used generalized coordinate coupling to modify ground shake test vibration modes in response to changes of mass and stiffness, and Phase IIa which used an extended Associated Matrix technique, Reference 10, to predict vibration modes from design mass and stiffness data. Based on conventional procedures up to that time, the Phase IIa analysis consisted of two parts, (1) vertical, which treated motions in the vertical centerplane of the aircraft including vertical, longitudinal and pitch displacements and (2) lateral, which treated motions in the lateral planes of the aircraft including lateral, roll and yaw displacements. There was no coupling between the vertical and lateral planes.

Four test phases were conducted, Phase VII vibration and pilot comment, Phase IIb static load-deflection test to obtain fuselage stiffness properties, Phase III measurement of vibratory rotor shaft loads and Phase V an in-flight shake test. Phase IIb showed that dissymmetries between the right and left sides of an H-21 fuselage are compensated from a strength standpoint, but are not compensated from a stiffness standpoint and result in considerable structural coupling between the vertical and lateral planes. Phase III instrumented the tandem rotor shafts of the same H-21 helicopter with strain gages and obtained steady and vibratory loads and moments in all directions. Phase V equipped the same H-21 helicopter with a hydraulic shaker and vibration pickups and located in-flight natural modes.

The structural coupling revealed by Phase IIb prompted the later analytical Phases IIc and IV. This extended the Associated Matrix Method still further to handle six fully coupled degrees of freedom. It used the Phase IIb stiffness data to calculate natural modes, and the Phase III shaft loads to calculate in-flight natural modes and forced response for correlation with the in-flight shaft test results of Phase V.

The present report summarizes each of the Phases and briefly presents the method developed and the results obtained for each. The Phases are presented consecutively as follows:

<u>Section</u>	<u>Phase</u>	<u>Description</u>
II	I	A Method for the Prediction of Natural Mode and Frequency Changes Accompanying Changes in Fuselage Mass and Stiffness
III	IIa	A Method for the Prediction of Natural Modes and Frequencies from Design Mass and Stiffness Data
IV	IIb	Load Deflection Tests on an H-21 Helicopter Fuselage to Determine Stiffness Characteristics
V	III	In-Flight Measurement of Steady and Oscillatory Rotor Shaft Loads

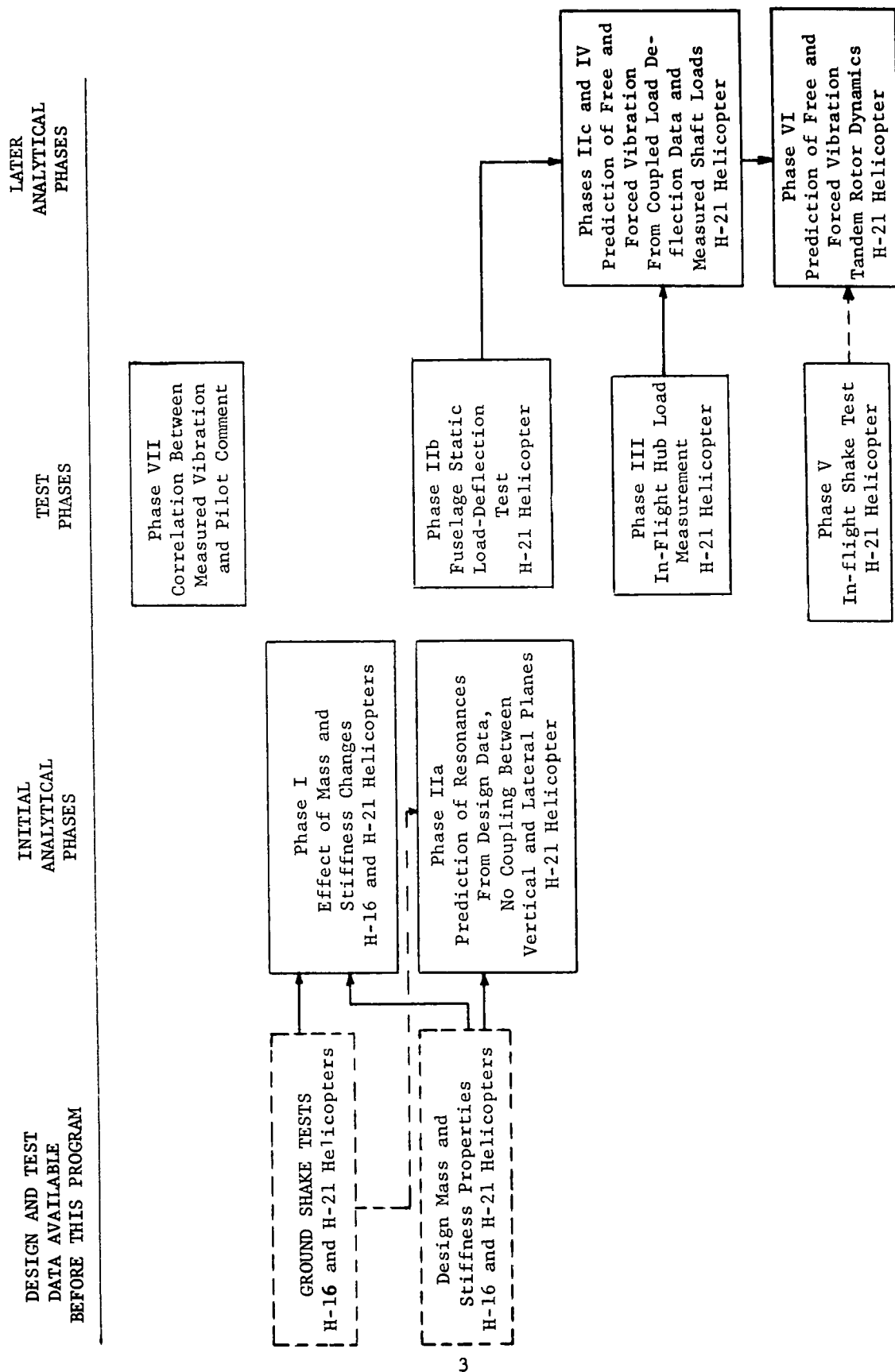


Figure 1 - Program Flow Chart

<u>Section</u>	<u>Phase</u>	<u>Description</u>
VI	V	In-Flight Shake Test
VII	IIc, IV	A Method for the Prediction of Coupled Vertical-Lateral Natural and Forced Modes
VIII	VI	A Method for the Prediction of Coupled Vertical-Lateral Modes Including Multi-Directional Damped Rotor Effective Mass

## SECTION II

### A METHOD FOR THE PREDICTION OF NATURAL MODE AND FREQUENCY CHANGES ACCOMPANYING CHANGES IN FUSELAGE MASS AND STIFFNESS

#### A. General

Evaluation of changes in aircraft natural frequency characteristics which will accompany proposed changes in mass and stiffness properties is often necessary or desirable after a prototype has been completed. Usual changes include variations in amounts or positions of useful load, the incorporation of large openings as a consequence of changes in mission, or because initial ground tests show that significant differences exist between the predicted and actual characteristics, structural changes are necessary to improve vibration characteristics.

A ground shake test to determine natural modes and frequencies of a completed aircraft is normally a part of prototype development. These experimental modes and frequencies, therefore, may be considered as known when changes are contemplated for any of the reasons mentioned previously. If these might be used as a reliable representation of the aircraft in evaluating contemplated revisions, most of the questionable stiffness predictions may be bypassed, and a simpler calculation procedure achieved.

To satisfy this need, a method was developed which is capable of using such test modes and frequencies as basic data for the prediction of new modes and frequencies resulting from changes in mass or structural stiffness. Test data were employed as modal inputs, and mass and stiffness changes as agents which couple these original modal inputs in proportionate quantities so as to produce a new set of modes and frequencies which describe the revised condition.

The particularly notable advantage of this procedure is that, in large measure, the dependence on fuselage rigidity estimates is eliminated. Use is made of natural modes and frequencies, determined by test, which should inherently be better than calculated natural modes.

#### B. Description of the Method

When a conservative dynamic system is oscillated at a natural frequency, it assumes a distinctive configuration known as a natural mode. Continuous structures are possessed of infinite numbers of natural modes, but in general applications to aircraft structures, only a limited number of the lowest of these modes are of practical significance.

The use of natural vibration modes as generalized coordinates permits the complex motion of a wing or fuselage structure to be handled simply as a superposition of a relatively small number of single degrees of freedom. If a change is made to the structure for which a set of natural modes has been obtained, the original modal orthogonality is disturbed, and in order to adequately describe the natural motions of the structure, the original modes must be coupled by terms associated with the physical changes. For example, an additional mass, moving in a previous natural mode, will disturb the original balance of inertia forces, and will induce

motion of all other modes in order to reinstate the balance necessary for oscillation about an equilibrium position. The added mass changes the dynamic system to a new one possessed of its own set of natural modes and frequencies.

The equations developed, while of general applicability, were oriented toward the tandem helicopter fuselage. Consequently, equations for two specific cases were developed; vertical bending of a fuselage involving vertical, longitudinal and pitching motions; and lateral bending-torsion involving lateral, rolling and yawing motions. This grouping is based on assumed symmetry of an aircraft structure about a vertical centerplane, which serves to uncouple the six degrees of motion into the pair of three-degree sets. Allowance was made for a wandering axis orientation within the vertical plane of symmetry, so that aircraft shapes that are not straight may be treated without limitation. In particular, the usual U-beam representation for a tandem helicopter, with a vertical pylon at each end supporting a rotor, was admissible to the analysis.

A Lagrangian approach was used to obtain the equations of motion. Equations were developed for two input modes, but were immediately extensible to a general form which can handle as many as desired. For example, if it is desired to couple six natural modes, the required terms are numerically evaluated for six equations of motion. The six equations are written in matrix form, and the Eigenvalues of the characteristic matrix are obtained. The lower of these values are good approximations to the natural frequencies of the modified structure, accounting for the effect of added mass and stiffness to the original structure. Substitution of these new natural frequencies into the characteristic matrix yields the corresponding new modal coefficients. Multiplication of the original mode shapes by these coefficients and summing, then provides a new mode shape reflecting the effect of the added masses or stiffnesses. The detailed development of the equations is shown in Reference 2 and in Appendix A.

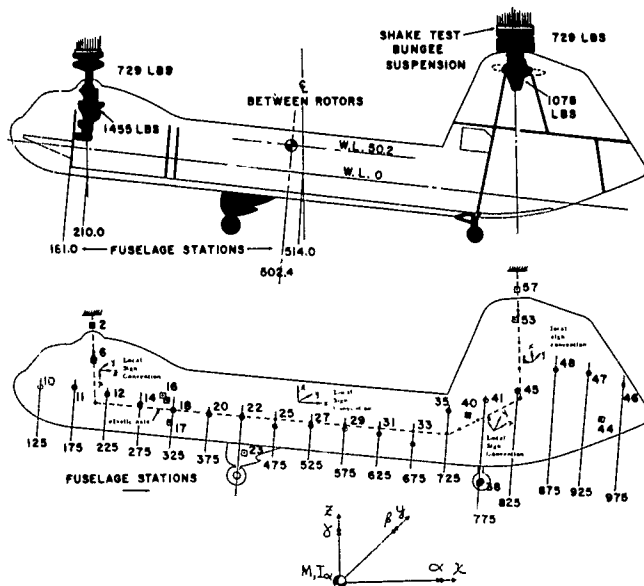
#### C. Application to the H-16 Helicopter

An extensive series of shake tests on the fuselage of the H-16 helicopter was performed in 1956 under Air Force Contract AF33(038)-6517 and reported in Reference 2. The original aim of the program was to develop a method for predicting the vibration characteristics of the then proposed H-16B helicopter.

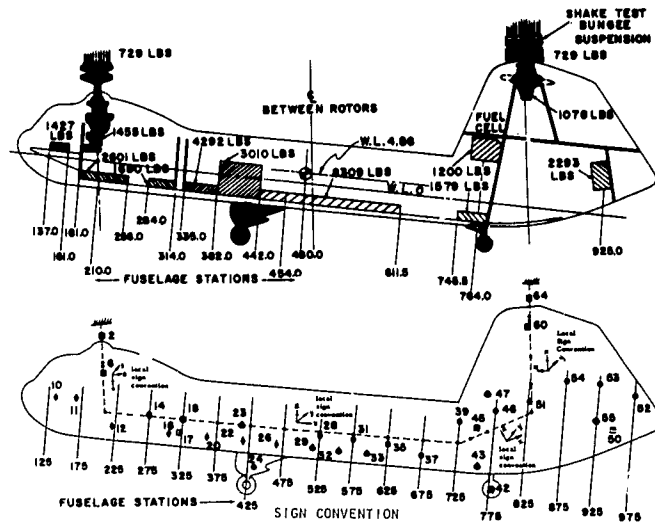
Shake tests were conducted with the fuselage supported at the two rotor shafts by long, low stiffness bungees in order to simulate a "free-free" condition as in-flight. Two configurations of the aircraft were tested, Figure 2, a basic 12,452 lb shell configuration in which all nonstructural equipment was removed, and a 45,262 lb ballasted configuration in which rigid weight was added to simulate the H-16B.

These two fuselage configurations were conveniently used to demonstrate generalized coordinate coupling. The shell was used as a basic case; its natural modes were used as generalized coordinates and, through incorporation of mass and stiffness changes, an effort was made to obtain agreement with the natural modes of the ballasted configuration.

**SHELL SHAKE TEST CONFIGURATION**  
GROSS WEIGHT = 12,452 LBS



**BALLASTED SHAKE TEST CONFIGURATION**  
GROSS WEIGHT = 45,262 LBS.



Key:

- Distributed Weight
- Concentrated Weight
- ◇ Ballast Combined with Dist. or Conc. Weight
- Ballast Weight
- Matrix Station

$$M = \frac{\# \text{ Sec}^2}{\text{In}}$$

I = Mass Moment of Inertia About Axes Through Centroid, #-Sec<sup>2</sup> In.

NO.	FUS. STA. IN.	WATER LINE IN.	MASS Lb. Sec 2/In.	I <sub>xx</sub> Lb. Sec <sup>2</sup> -In	I <sub>yy</sub> Lb. Sec <sup>2</sup> -In	I <sub>zz</sub> Lb. Sec <sup>2</sup> -In
2	193.	107	1.888	0	0	0
6	199.3	57	3.768	216.	2844	2850.
10	125.	14.3	1.171	0	0	0
11	175.	17.7	2.364	4900.	3408	7330.
12	225.	11.4	1.120	3620.	1764	2330.
14	275.	3.2	0.6711	2210.	1092	1390.
16	311.	17.0	0.2383	12.0	24	24.0
17	323.8	-17.4	0.1523	36.0	36	12.0
18	325.	0.5	0.7881	2580.	1272	1630.
20	375.	-2.8	0.6993	2270.	1104	1452.
22	425.	-2.2	1.402	4560.	2232	2920.
23	433.2	-54.0	2.431	26900.	826	27300.
25	475.	-9.0	0.7560	2360	1104	1570.
27	525.	-5.3	0.7172	2300	1104	1488.
29	575.	-4.8	0.7566	2420	1176	1572.
31	625.	-8.1	0.8474	2660.	1260	1760.
33	675.	-17.3	1.046	2980.	1224	2170.
35	725.	-33.3	1.020	3730.	2184	1980.
36	777.6	-54	0.3201	23.90	24	14.30
40	758.6	21.	0.1502	21.20	60	50.70
41	775.	42.6	1.269	1131	7272	1935.
44	947.9	38.9	0.2033	24.00	24	12.00
45	825	57.2	1.562	2760	7620	1105
46	975	79.2	0.5312	600.	144	552.
47	925	86.0	0.6975	660.	1192	2920
48	875	86.0	1.013	1140	3120	4520
53	809.6	182.5	2.790	192.0	916	935.0
57	807.0	230	1.888	0	0	0.

NO.	FUS. STA. IN.	WATER LINE IN.	MASS Lb. Sec 2/In.	I <sub>xx</sub> Lb. Sec <sup>2</sup> -In	I <sub>yy</sub> Lb. Sec <sup>2</sup> -In	I <sub>zz</sub> Lb. Sec <sup>2</sup> -In
2	193	107	1.888	0	0	0
6	199.3	57	3.768	216.	2844.	2850.
10	125.02	14.12	3.019	1519	254	1582.
11	166.22	16.08	4.212	6419	3659	8912.6
12	220.71	-19.81	7.658	10579	4465	11322.
14	275	3.20	0.6711	2210	1092	1390.
16	305.3	-22.90	4.590	2977.2	839.5	3301.4
17	313	-17.40	0.1523	36.	36.	12.
18	325	0.50	0.7881	2580	1272.	1630.
20	359.95	-23.30	11.816	11220.	3667.	12200.
22	413.40	-22.60	13.277	14445.	6657.6	15715.
23	412	0	7.798	4870	7213.	12083
24	433.2	-54	2.431	26900.	826.	27300.
26	462.8	-23.90	10.961	10213.	3476.	13693.
28	525	-5.3	0.7172	2300	1104	1488.
29	514	-25	5.451	4180	727.	4907
31	575	-4.8	0.7560	2420	1176.	1572
33	625	-8.1	0.8474	2660	1260.	1760.
35	675	-17.3	1.046	2980	1224	2170
36	725	-33.3	1.020	3730	2184	1980
40	777.6	-54.	0.3201	23.9	24	14.3
43	757	-28.	4.091	3144	165	3262.
45	758.6	+21.	0.1502	21.2	60	50.7
46	775.0	+42.6	1.269	1131	7272	1935
47	764.0	+76.0	3.109	564	564	564
50	947.9	+38.9	0.2033	24	24	12
51	825.0	57.2	1.562	2760	7620	1105
52	975	+79.2	0.5312	600.	144.	552
53	925	+86.0	0.6975	660	1192	2920
54	875	+86.0	1.013	1140	3120	4520
55	925	+53	5.940	446	446	446.
60	809.6	182.5	2.790	192.	936	935.
64	807.0	230	1.888	0	0	0

Figure 2 H-16 Weight Distribution



### Vertical Bending Modes - Mass Changes

Calculated shell modes shown in Figure 3 were used as generalized coordinates, and the mass change from 12,452 lb to 45,262 lb used as the coupling agent to calculate a ballasted set of natural modes. Natural modes for the ballasted configuration were also obtained by the matrix method for comparison. The coupling procedure was repeated several times using various combinations of the three rigid body modes with the three flexible modes. The modal results are shown in Figures 4, 5, 6, and the frequency results are summarized as follows.

<u>Description</u>	Frequency, CPS		
	<u>1st Mode</u> <u>Figure 4</u>	<u>2nd Mode</u> <u>Figure 5</u>	<u>3rd Mode</u> <u>Figure 6</u>
Shell - generalized coordinates	7.09	10.99	13.69
Ballasted matrix, a check on coupling results	5.11	8.84	10.91
6 x 6 Coupling - 3 Shell Modes with Rigid Body Vertical, Longitudinal, Pitch	5.10	9.08	10.90
5 x 5 Coupling - 3 Shell Modes with Rigid Body Vertical, Longitudinal	5.09	9.02	10.89
4 x 4 Coupling - 3 Shell Modes with Rigid Body Vertical	5.07	7.98	10.73
3 x 3 Coupling - 3 Shell Modes	4.63	7.76	10.55

It is apparent that the coupling program gives quite accurate frequency predictions when three shell flexible and three rigid body modes are used, and equally good results when only rigid body pitch is omitted. When longitudinal rigid body motion is also omitted, the second mode frequency deteriorates, and when all rigid modes are omitted, all three frequencies suffer.

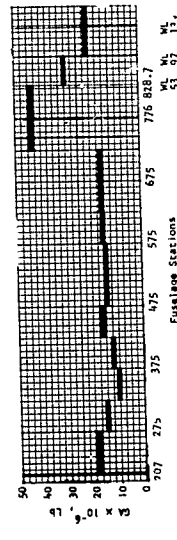
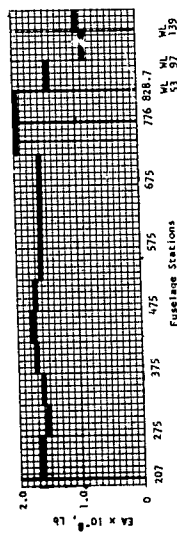
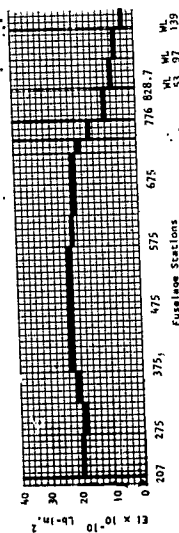
### Vertical Bending Modes - Stiffness Change

Shake test results embodying known stiffness changes were not available, so a hypothetical case having substantial changes in fuselage bending stiffness and transmission mount spring rates was utilized to form a trial case. The stiffness changes for the two cases are compared in Figure 7. A different set of shell modes was used as the generalized coordinates in investigating the stiffness change effect. These are illustrated in Figure 7 also. Frequency results were as follows.

<u>Description</u>	Frequency, CPS		
	<u>1st Mode</u>	<u>2nd Mode</u>	<u>3rd Mode</u>
Shell - generalized coordinates	8.11	14.36	17.87
Shell, after stiffness changes - matrix a check on coupling results	7.09	10.99	13.69
3 x 3 Coupling - 3 Shell Flexible Modes	7.48	13.53	17.27
6 x 6 Coupling - 6 Shell Flexible Modes	7.48	13.53	17.27

Coupling results for the first mode are fairly close to those of the matrix check case. Results for the second and third modes are very poor with respect to frequency as shown in the table above and with respect to mode shapes as shown in

Shell Configuration Stiffness Properties  
Vertical Bending Modes

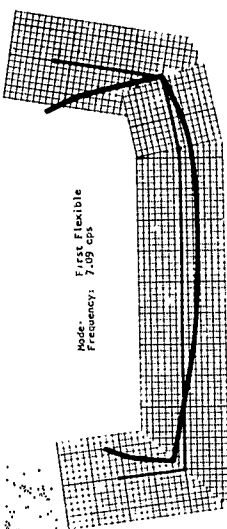


Forward Main Mounting Springs  
Pitch  $K_F = 19.1 \times 10^6$  in./rad  
Vertical  $K_F = 1.136 \times 10^6$  lb/in.  
Longitudinal  $K_F = 1.205 \times 10^6$  lb/in.

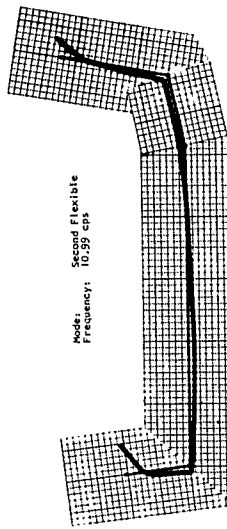
Forward Rotor Shaft  
Lower Shaft Pitch  $K = 50.6 \times 10^6$  in./lb/rad  
Upper Shaft Rigidities  
Pitch  $K_U = 0.162 \times 10^{10}$  lb/in.<sup>2</sup>  
Vertical  $K_U = 2.5 \times 10^6$  lb  
Longitudinal  $K_U = 110 \times 10^6$  lb

Aft Main Mounting Springs  
Pitch  $K_A = 88.6 \times 10^6$  in./lb/rad  
Vertical  $K_A = 1.136 \times 10^6$  lb/in.  
Longitudinal  $K_A = 12.5 \times 10^6$  lb/in.

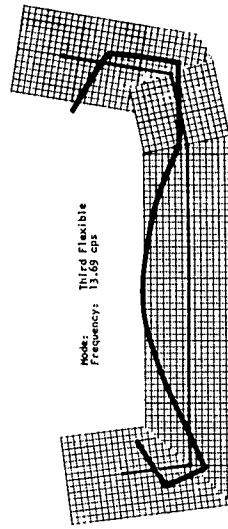
Aft Rotor Shaft  
Lower Shaft Pitch  $K = 50.6 \times 10^6$  in./lb/rad  
Upper Shaft Rigidities  
Pitch  $K_U = 0.162 \times 10^{10}$  lb/in.<sup>2</sup>  
Vertical  $K_U = 2.5 \times 10^6$  lb  
Longitudinal  $K_U = 110 \times 10^6$  lb



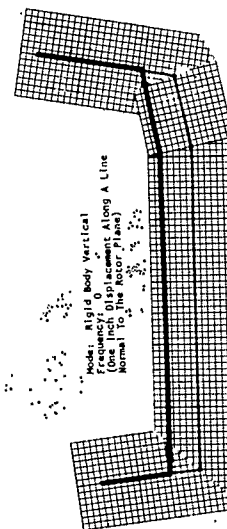
Mode- First Flexible  
Frequency: 7.09 cps



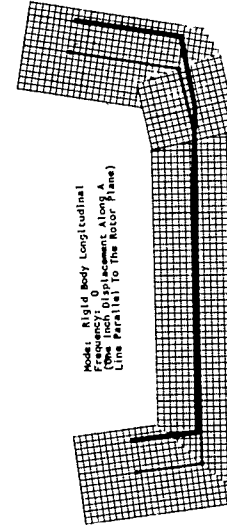
Mode- Second Flexible  
Frequency: 10.99 cps



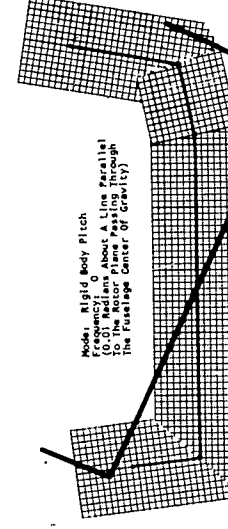
Mode- Third Flexible  
Frequency: 13.69 cps



Mode- Rigid Body Vertical  
Frequency: 0  
(One Inch Displacement Along A Line  
Normal To The Rotor Plane)



Mode- Rigid Body Longitudinal  
Frequency: 0  
(One Inch Displacement Along A  
Line Parallel To The Rotor Plane)



Mode- Rigid Body Pitch  
Frequency: 0  
(One Inch Displacement Along A Line Parallel  
To The Rotor Plane Through  
The Fuselage Center Of Gravity)

Figure 3 Shell Configuration Vertical Bending Stiffness Properties  
and Mode Shapes Used as Coupling Agent for Mass Changes

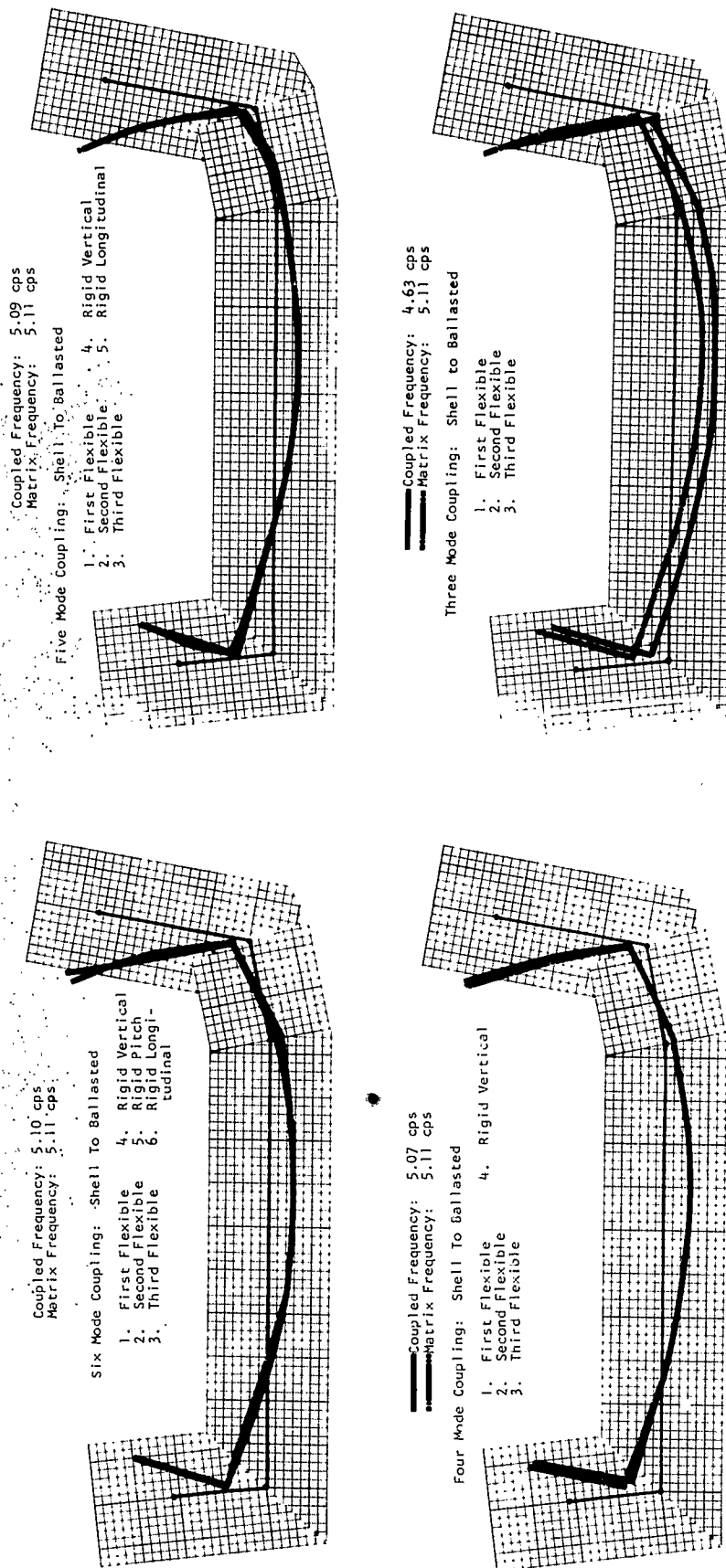


Figure 4 First Vertical Bending Mode

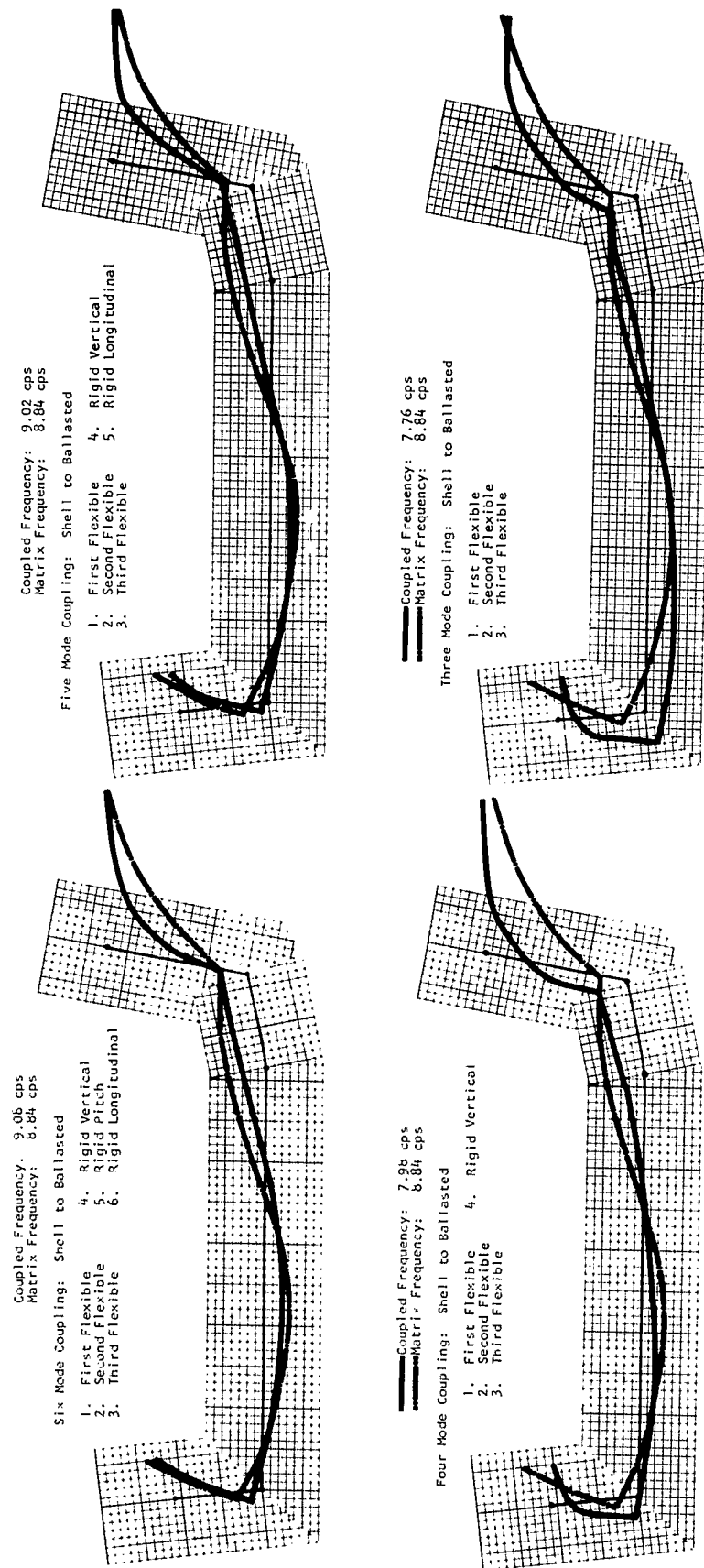


Figure 5 Second Vertical Bending Mode

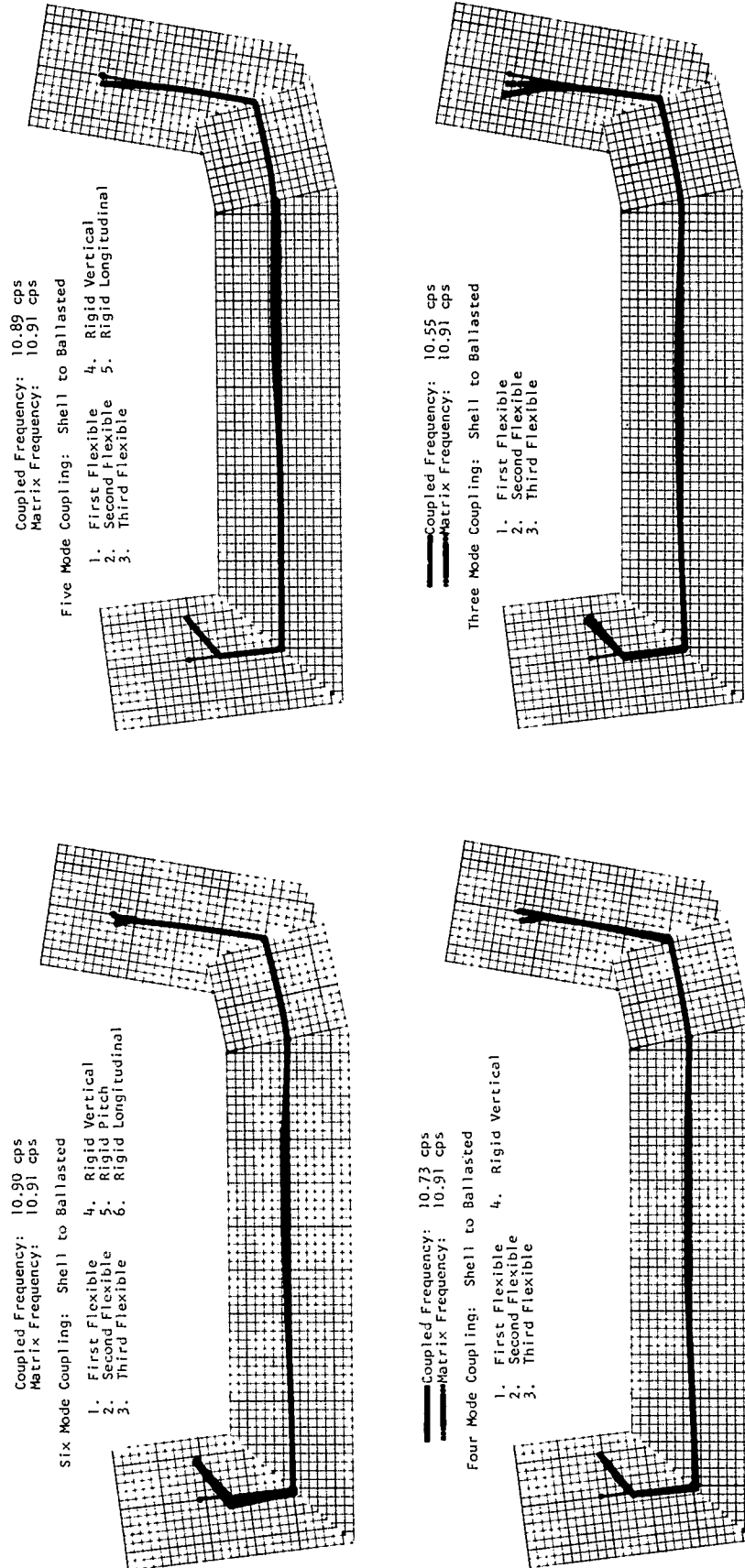


Figure 6 Third Vertical Bending Mode

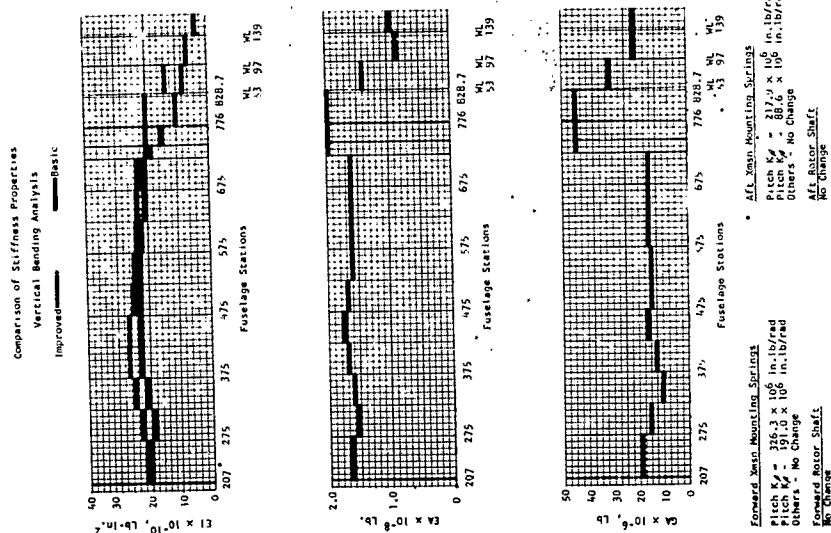
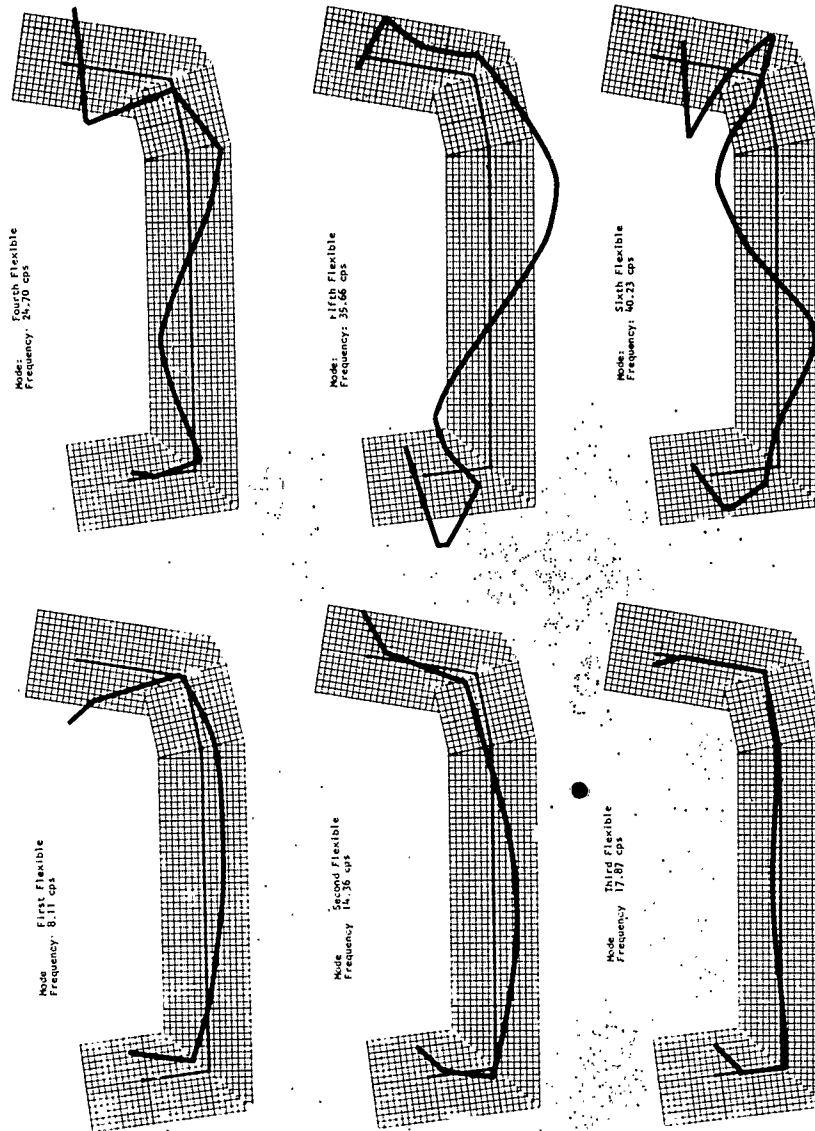


Figure 7 Shell Configuration Vertical Bending Stiffness Properties and Mode Shapes Used as Coupling Input for Stiffness Changes

Figure 8. Rigid modes are omitted since in the case of stiffness changes they make no contribution to the analysis. As shown in the tabulation above, a second calculation in which six shell flexible modes were used as generalized coordinates produced no change in the results. It is evident that the large local stiffness changes made at the transmission pitch mountings require generalized modes where such local transmission mount motions are predominant.

#### D. Discussion and Conclusions

A generalized coordinate coupling procedure was developed which permits the utilization of natural modes and frequencies, known from tests or previous calculation, as basic instruments for the prediction of changes in dynamic characteristics accompanying structural mass and stiffness alteration. An inherent advantage of this method is that data from ground shake tests, which are a part of most aircraft development cycles, and weight data, which must be known for other reasons, may be utilized directly without resorting to overall stiffness estimates which accompany the creation of a lumped mass analytic model.

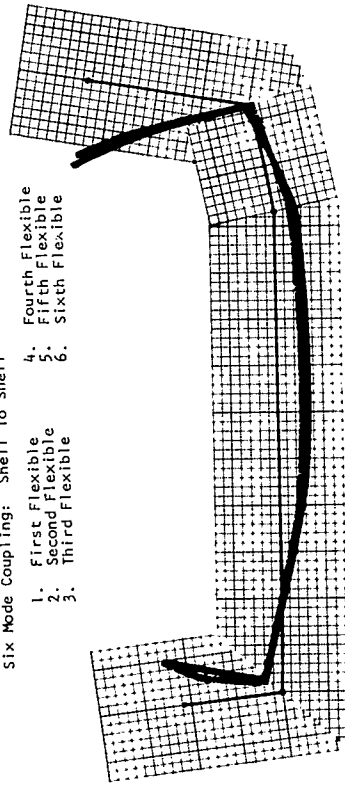
A series of applications testing the accuracy of the method are presented here briefly and in more detail in Reference 2. These applications involved mass changes, stiffness changes, and combinations of mass and stiffness changes. Vertical cases are shown herein as representative, but both vertical and lateral cases are given in the reference. For mass changes only, the coupling method closely approaches the theoretical ideal as expressed by direct associated matrix solutions of the respective before and after configurations. Coupling, using three flexible and three rigid body modes of the initial configuration, produced a final set of three flexible modes which were very nearly identical to the direct matrix solutions. If one or more rigid body modes are discarded in the coupling, accuracy diminishes, particularly for the lower frequency modes nearest the "zero" frequency rigid body modes; for higher modes it appears that they are less important. A flexible mode which contains a large proportion of a particular rigid body motion will be more adversely affected by deletion of that particular motion than will other flexible modes. It is desirable then, that in coupling mass changes to determine their influence on an original known set of natural modes, that all appropriate rigid body modes be retained. If forced by limitation of a computing program to reduce their number, then only those which do not appear significant in the original set of modes should be dropped. Because of the demonstrated importance of rigid modes, a recommended procedure in such a situation would be a repetition of the calculation using all rigids and the lower flexible modes to ascertain their importance. The use of even two nearby initial modes is often sufficient in approximating a particular single mode after a mass change, but the use of more input modes promotes rapid convergence to precise results. Accuracy of the method for both coupled vertical-longitudinal vibration and coupled lateral-torsion vibration is roughly the same.

For stiffness changes only, the coupling procedure does not function as effectively. Rigid body modes make no contribution whatever, so at least three straightforward modes which were an aid to the mass case are lost here. Further, sufficient representation of stiffness changes depends on a larger number of flexible modes as input, even though convergence on the direct solution is quite slow as these modes are added. An obvious physical illustration of this application is to picture a

First Coupled Flexible Mode  
Coupled Frequency: 7.35 cps  
Matrix Frequency: 7.61 cps

Six Mode Coupling: Shell To Shell

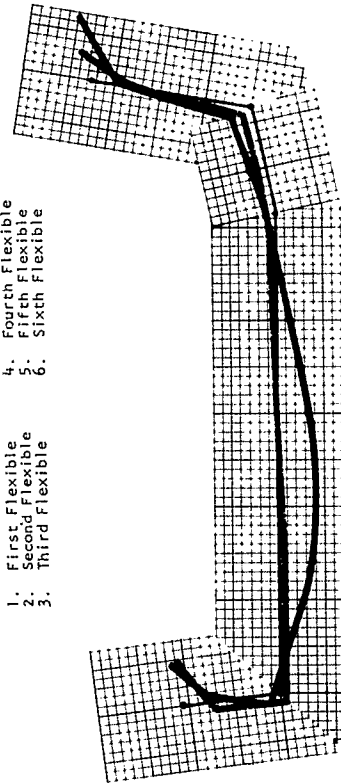
1. First Flexible
2. Second Flexible
3. Third Flexible
4. Fourth Flexible
5. Fifth Flexible
6. Sixth Flexible



Second Coupled Flexible Mode  
Coupled Frequency: 13.73 cps  
Matrix Frequency: 11.63 cps

Six Mode Coupling: Shell To Shell

1. First Flexible
2. Second Flexible
3. Third Flexible
4. Fourth Flexible
5. Fifth Flexible
6. Sixth Flexible



Third Coupled Flexible Mode  
Coupled Frequency: 17.78 cps  
Matrix Frequency: 14.58 cps

Six Mode Coupling: Shell To Shell

1. First Flexible
2. Second Flexible
3. Third Flexible
4. Fourth Flexible
5. Fifth Flexible
6. Sixth Flexible

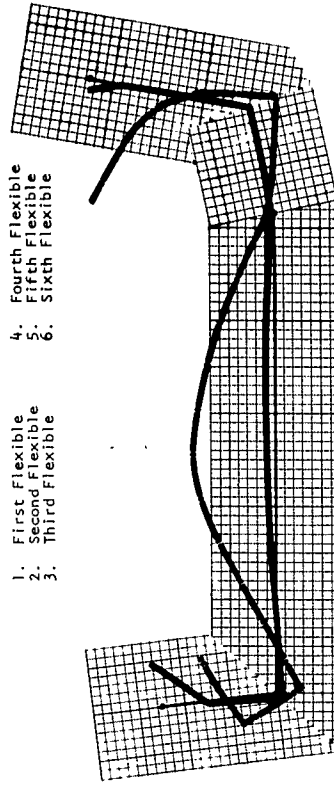


Figure 8 Comparison of Coordinate Coupling for Stiffness Changes and Matrix Vertical Bending Modes



significant change of stiffness at a local spring, such as the pitch spring representing attachment of the helicopter rotor transmission to its surrounding structure. To attain adequate modal representation of this situation it would be necessary to employ the mode in which motion at this spring predominates over all other motions of the system. Such a mode would probably exist at a rather high frequency and hence have a large modal number. In either a theoretical or test case such modes are not usually attainable and precise representation of the spring change is rendered impractical. For small changes of stiffness which would describe most structural modifications instituted for functional reasons rather than to modify vibration characteristics, the employment of a few flexible modes such as obtained in a shake test should lead to reasonable results.

### SECTION III

#### A METHOD FOR THE PREDICTION OF NATURAL MODES AND FREQUENCIES FROM DESIGN MASS AND STIFFNESS DATA

##### A. General

This portion of the program extended the Associated Matrix Technique of Reference 10 to the tandem helicopter fuselage, maintaining a division between vertical and lateral planes. Vertical, longitudinal and pitch motions were considered in one analysis, and lateral, roll and yaw motions in a separate analysis. This method was selected because of a number of operational advantages which tended to make it superior to other current procedures. Each physical beam property may be mathematically constructed by an assemblage of matrices. Because of this construction, it is quite simple to make a change of any property or sequence of properties merely by a change of numerical value or rearrangement of the matrices. Natural frequencies were obtained by (1) introduction of a trial frequency, (2) continuous multiplication of a partitioned portion of the matrix assemblage, dependent on the boundary conditions, and (3) expansion of the final collapsed matrix to a residual determinant value whose zeros are the sought naturals. No intermediate auxiliary calculations were necessary as in other current procedures. A detailed derivation of the matrices is given in Appendix B.

Successively higher natural frequencies were obtained by the same process using trial frequencies of larger magnitude. This contrasts with the influence coefficient-dynamic matrix where each successively higher natural frequency is usually obtained by an iteration process in which the latent root of each previous frequency must be removed from the dynamic matrix as an auxiliary "sweeping" matrix. In addition, with the Associated Matrices, forced response calculations can be made with the same matrix grouping.

Associated matrix natural mode calculations were conducted for the H-21 helicopter based on stiffness properties from the structural deflection test of Section IV. Two aircraft configurations were created, corresponding to those handled in an earlier shake test, a 10,983 lb gross weight shell version without engine and a 13,497 lb gross weight ballasted version with engine.

##### B. H-21 Vertical Bending Matrix Calculation

###### Shell Configuration

Figure 9 shows the results of matrix calculations for the basic shell configuration without engine compared with the test results. The basis for judgment of these modes with test results was by both mode shape agreement and natural frequency agreement. Frequency comparison shows:

<u>Mode</u>	<u>Matrix, cps</u>	<u>Mode</u>	<u>Test, cps</u>
First	10.40	First	8.9-9.1
Second	17.95	Second	12.9-13.3
Second	17.95	Third	14.9-15.4

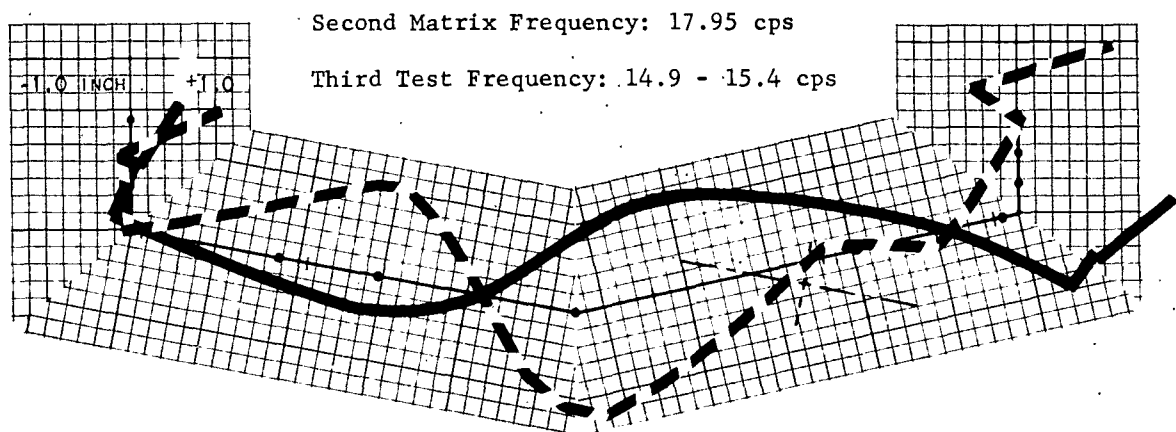
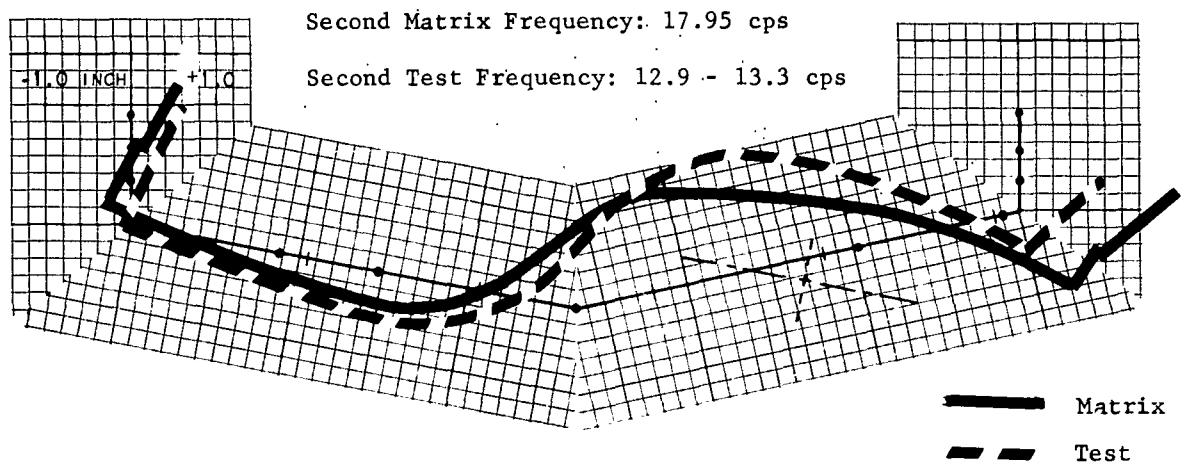
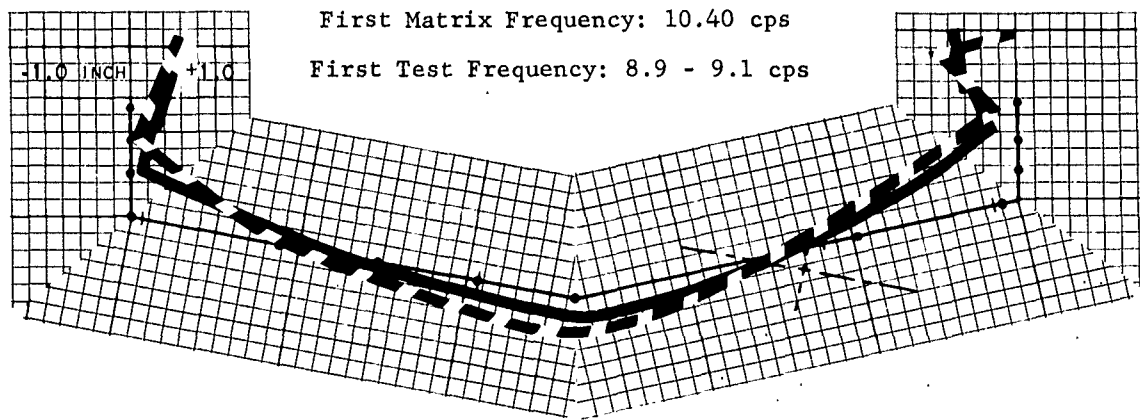


Figure 9 H-21 Shell Configuration Vertical Bending Modes

The first mode shape shows good agreement with the test shape until the aft pylon is reached, where an obvious discrepancy in rotor hub motion appears. Frequency correlation is not particularly good. The second calculated shape compared with second test indicates good shape correlation but very poor comparison in frequency. Comparing the second matrix with third test improves the frequency correlation slightly, but no correlation exists between the mode shapes.

#### Ballasted Configuration

The results of matrix calculations for the ballasted configuration with engine are compared to the H-21 shake test in which the engine was suspended on its flexible dynafocal mounts. Frequency results are compared in the following table.

<u>Mode</u>	<u>Matrix, cps</u>	<u>Mode</u>	<u>Test, cps</u>
First	8.07	First	9.2
Second	8.27	-	-
Third	12.05	-	-
Fourth	13.61	Second	13.8
Fifth	14.30	-	-
Sixth	15.10	Third	16.7

The corresponding mode shapes are compared in Figure 10. The first mode shapes are similar, both being essentially fundamental free-free beam bending. However, the frequency obtained by matrix calculation shows only fair agreement with the test value indicating possible coupling between this mode and a lateral test mode at 8.4 cps. The second and third calculated modes are predominantly vertical and pitching modes of the engine balanced by the entire fuselage. For these modes no test counterparts are available, though such may exist. The comparison of the fourth calculated mode with the second test mode shows good frequency agreement and good shape agreement for the pylons, but poor shape correlation along the fuselage. Because of this poor fuselage shape agreement, the second test mode at 13.8 cps is also compared with the fifth mode at 14.30 cps, but the shape correlation is very poor. Sixth calculated and third test show fair frequency match, and excellent shape correlation.

#### C. H-21 Lateral Bending Matrix Calculation

##### Shell Configuration

Based on calculated lateral stiffness properties matrix calculations were carried out for the shell configuration. The mode shapes are shown in Figure 11, and the natural frequencies are summarized below:

<u>Mode</u>	<u>Matrix, cps</u>	<u>Mode</u>	<u>Test, cps</u>
First	12.29	First	11.42
Second	15.59	Second	12.66
Third	21.08	Third	18.71
		Fourth	21.65
Third	21.08	Fifth	23.3

The first mode comparison is acceptable in most respects, excepting the aft pylon shape, where no reversal in slope occurs at the transmission as shown by the test data. The second calculated mode compared with the second test mode shows rather

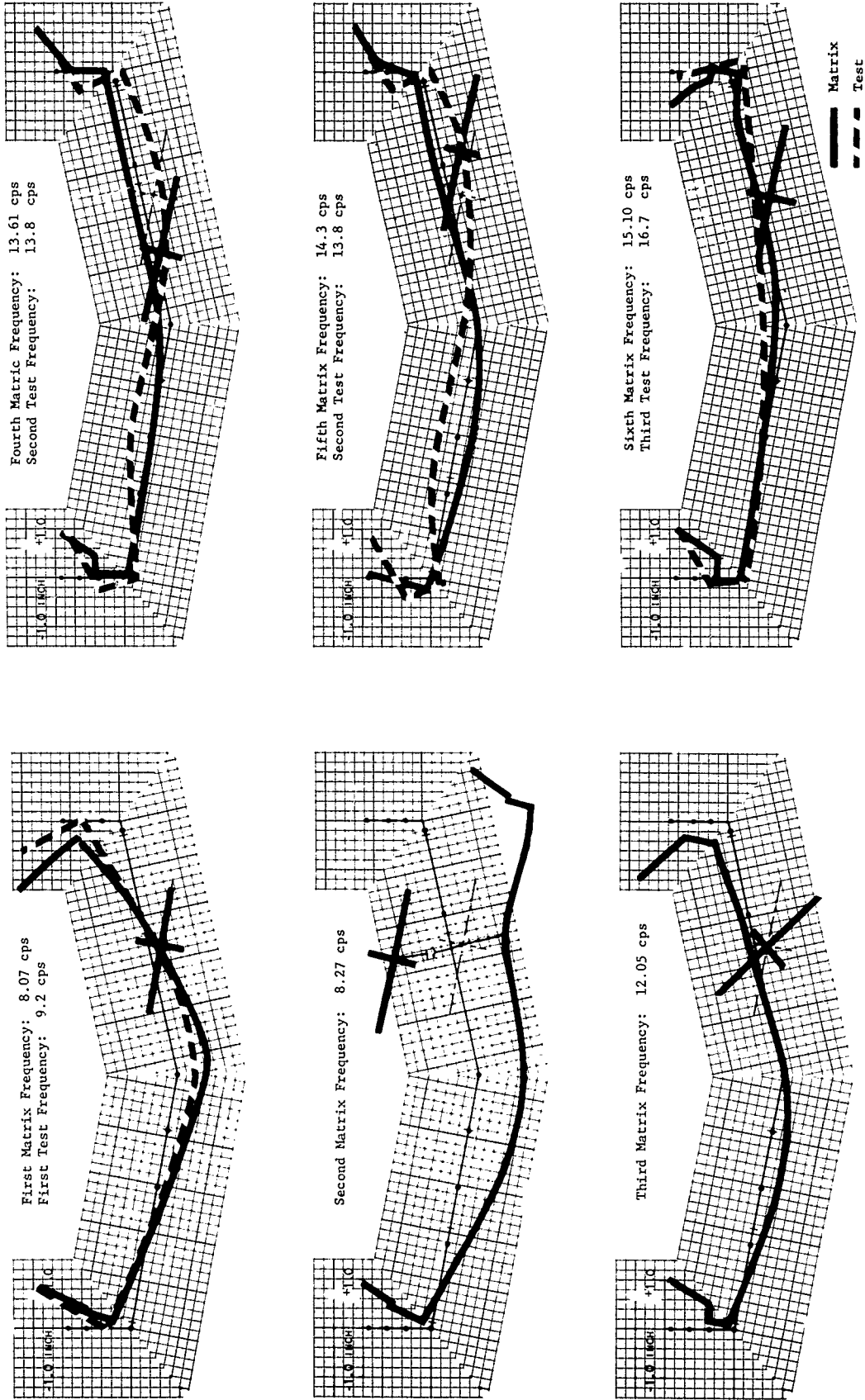
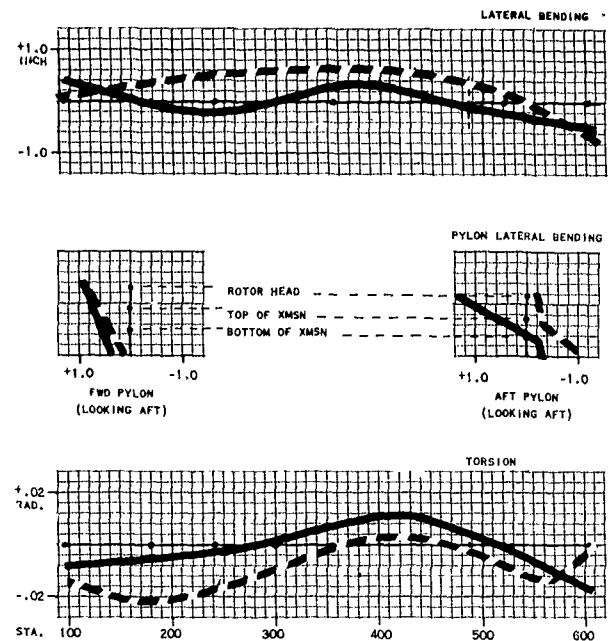
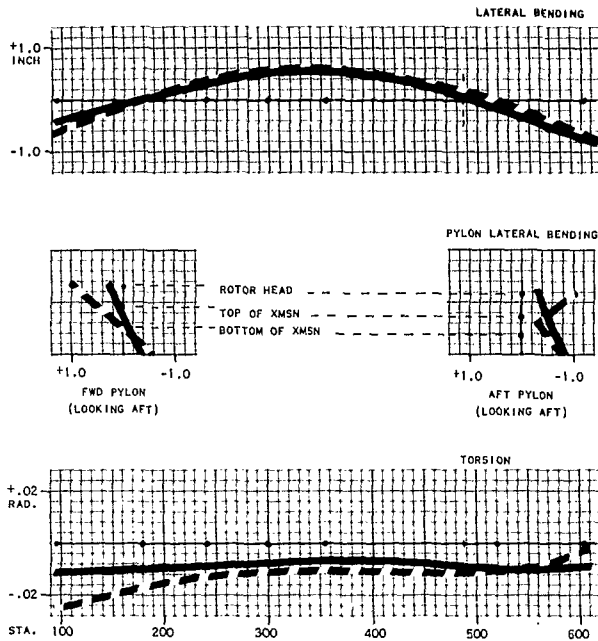


Figure 10 H-21 Ballasted Configuration Vertical Bending Modes

First Matrix Frequency: 12.29 cps  
First Test Frequency: 11.42 cps

Third Matrix Frequency: 21.08 cps  
Third Test Frequency: 18.71 cps



Second Matrix Frequency: 15.59 cps  
Second Test Frequency: 12.66 cps

Matrix  
Test

Third Matrix Frequency: 21.08 cps  
Fifth Test Frequency: 23.3 cps

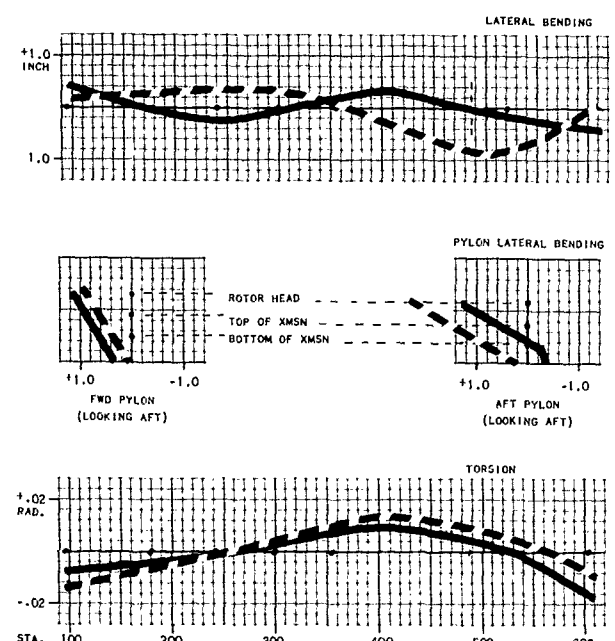
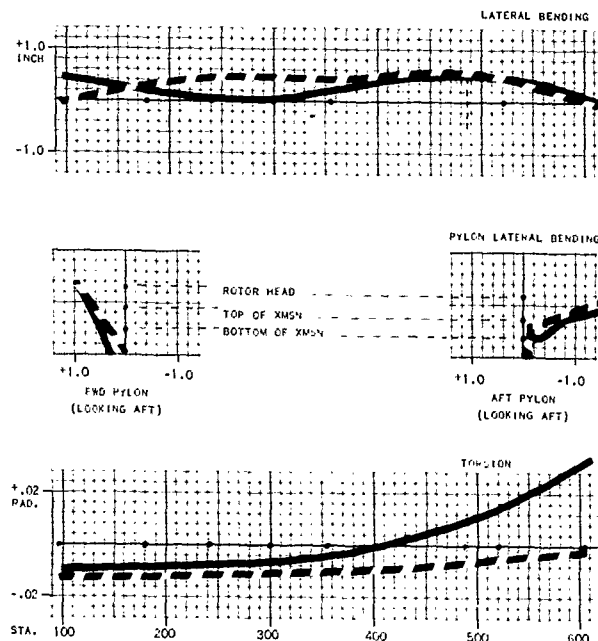


Figure 11 H-21 Shell Configuration Lateral Bending Modes

good shape agreement except for the torsion component in the aft fuselage, but the frequency comparison is poor. Third calculated and third test show good shape agreement, with a fair frequency match. Comparison of third calculated and fifth test shows moderate frequency agreement and good agreement in shape except for fuselage bending which appears out of phase.

#### Ballasted Configuration

For the ballasted configuration which includes flexible engine representation, the results of the matrix calculations are compared to the H-21 shake test results. Natural frequencies are compared below with the corresponding mode shapes shown in Figure 12.

<u>Mode</u>	<u>Matrix, cps</u>	<u>Mode</u>	<u>Test, cps</u>
First	6.81		
Second	7.15		
Third	9.80	First	8.4
Fourth	13.59	Second	11.0
		Third	13.5
Fifth	16.0		
Sixth	18.4	Fourth	18.5

First and second calculated modes are not shown as these modes are predominantly yaw and roll motions of the engines. The third matrix mode compared with the first test mode gives good shape agreement but a poor frequency match. Fourth matrix mode correlation with the second test mode is reasonable in shape except for fuselage lateral bending phasing; however, frequency comparison is poor. The fourth matrix and third test modes are quite close in frequency, but the mode shape comparison does not bear out the supposed relation. The sixth matrix, fourth test mode comparison indicates close frequency agreement, and general mode similarity except in lateral bending where the calculated mode exhibits more local shape complexities.

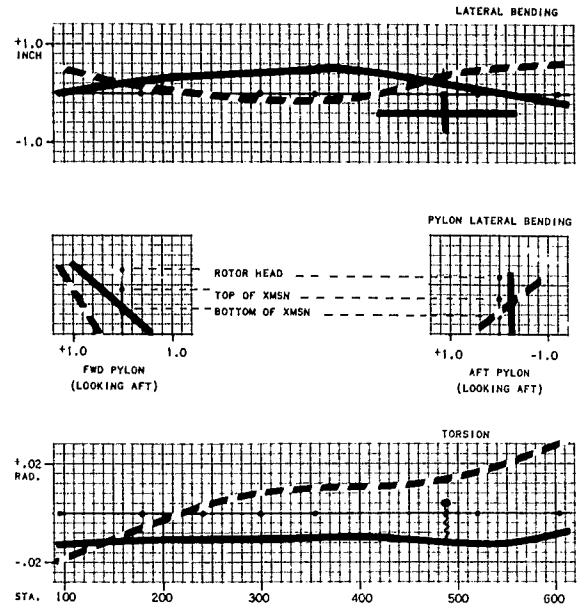
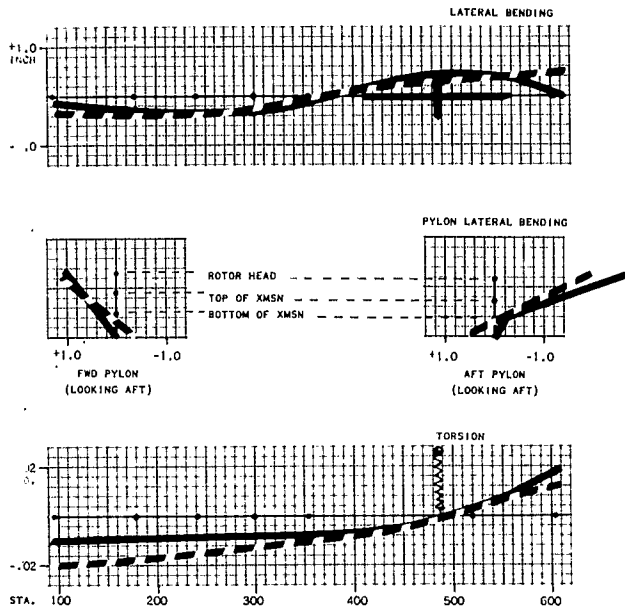
In an overall appraisal of the shake test results and matrix calculations many discrepancies exist which cannot be explained considering uncoupled vertical and lateral systems. Since structural stiffness properties were obtained from a static test under Phase IIb, Reference 4, and weight properties were obtained from a detailed weight distribution with its corresponding load and cg checks, the discrepancies must be elsewhere. The differences between matrix calculations and test results arise from the neglect of coupling between the vertical and lateral motions. Indications of coupling between these motions were evident in the deflection test, i.e. a vertical load at the forward rotor produced a measurable amount of lateral deflection and twist along the fuselage.

#### D. Effect of Flexible Engine

To evaluate the effect of the flexible engine on the lateral frequencies and modes of the H-21 with respect to a rigid engine, a matrix calculation was performed for a ballasted H-21 with rigid engine and the results compared to the matrix calculation which included the flexibility of the engine. Flexible engine mountings are introduced into the calculation by an appropriate matrix whose inputs are engine mass and inertia and calculated estimates of the suspension

Third Matrix Frequency: 9.80 cps  
First Test Frequency: 8.40 cps

Fourth Matrix Frequency: 13.59 cps  
Third Test Frequency: 13.5 cps



— Matrix  
- - - Test

Fourth Matrix Frequency: 13.59 cps  
Second Test Frequency: 11.0 cps

Sixth Matrix Frequency: 18.4 cps  
Fourth Test Frequency: 18.5 cps

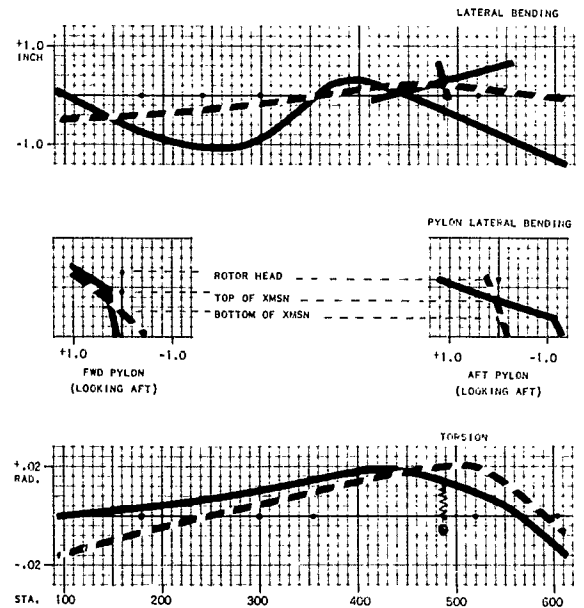
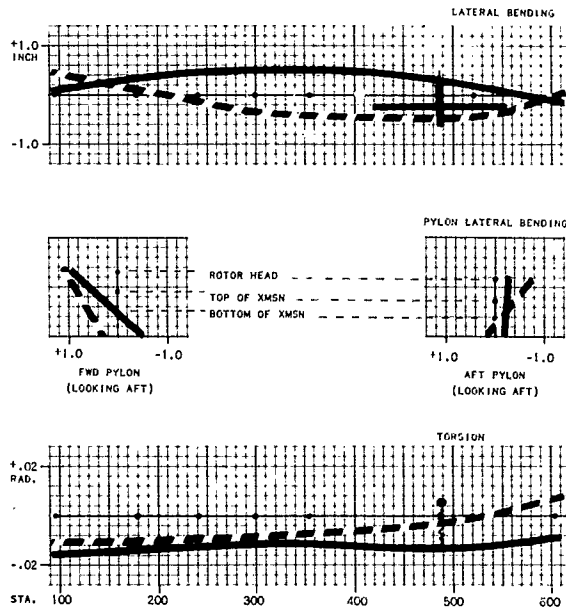


Figure 12 H-21 Ballasted Configuration Lateral Bending Modes



natural frequencies of the engine with the fuselage assumed to be a rigid back stop. The use of uncoupled frequencies is correct in an ideal dynafocal design because the dynafocals place the center of stiffness on the mass center and prevent spring coupling. However, when another elasticity, such as the steel truss ring which supports the dynafocals is included the motion of the uncoupled modes becomes less precise.

### Vertical Bending

The uncoupled natural frequencies of the engine in the vertical, longitudinal and pitch directions were calculated. These values are 7.5, 13.5 and 12.1 cps respectively and are used as input to the vertical-longitudinal fuselage matrix program. The significance of engine flexibility can be clearly demonstrated by the matrix residual curves shown below and the respective modes for the rigid and flexibly mounted engine Figure 14.

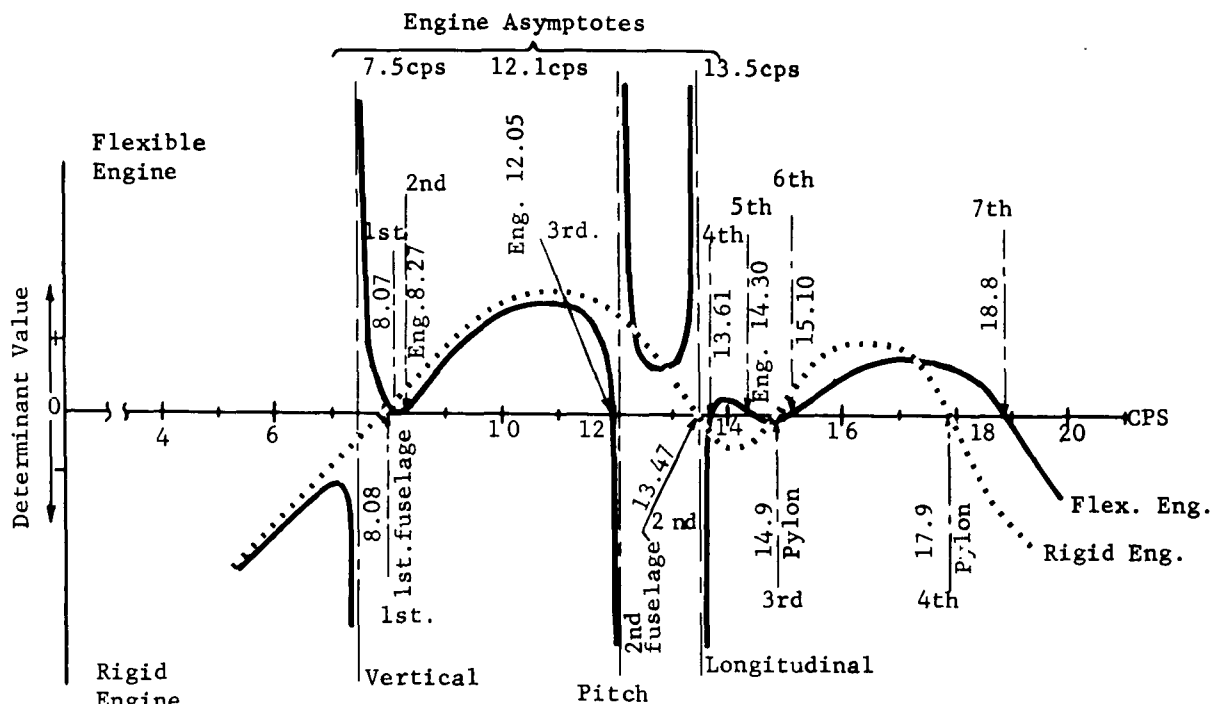


Figure 13 Vertical Bending, Matrix Residual Curve

<u>Mode</u>	<u>Ballasted - Rigid Eng.</u>	<u>Ballasted - Flex. Eng.</u>
First	8.08	8.06 cps
Second	13.47	(Eng) 8.27 cps
Third	14.9	(Eng) 12.05 cps
Fourth	17.9	13.61 cps
Fifth		(Eng) 14.30 cps
Sixth		15.10 cps
		18.8

The residual curve shows the rigid engine case to have two positive peaks and four natural frequencies in the range up to 20 cps.

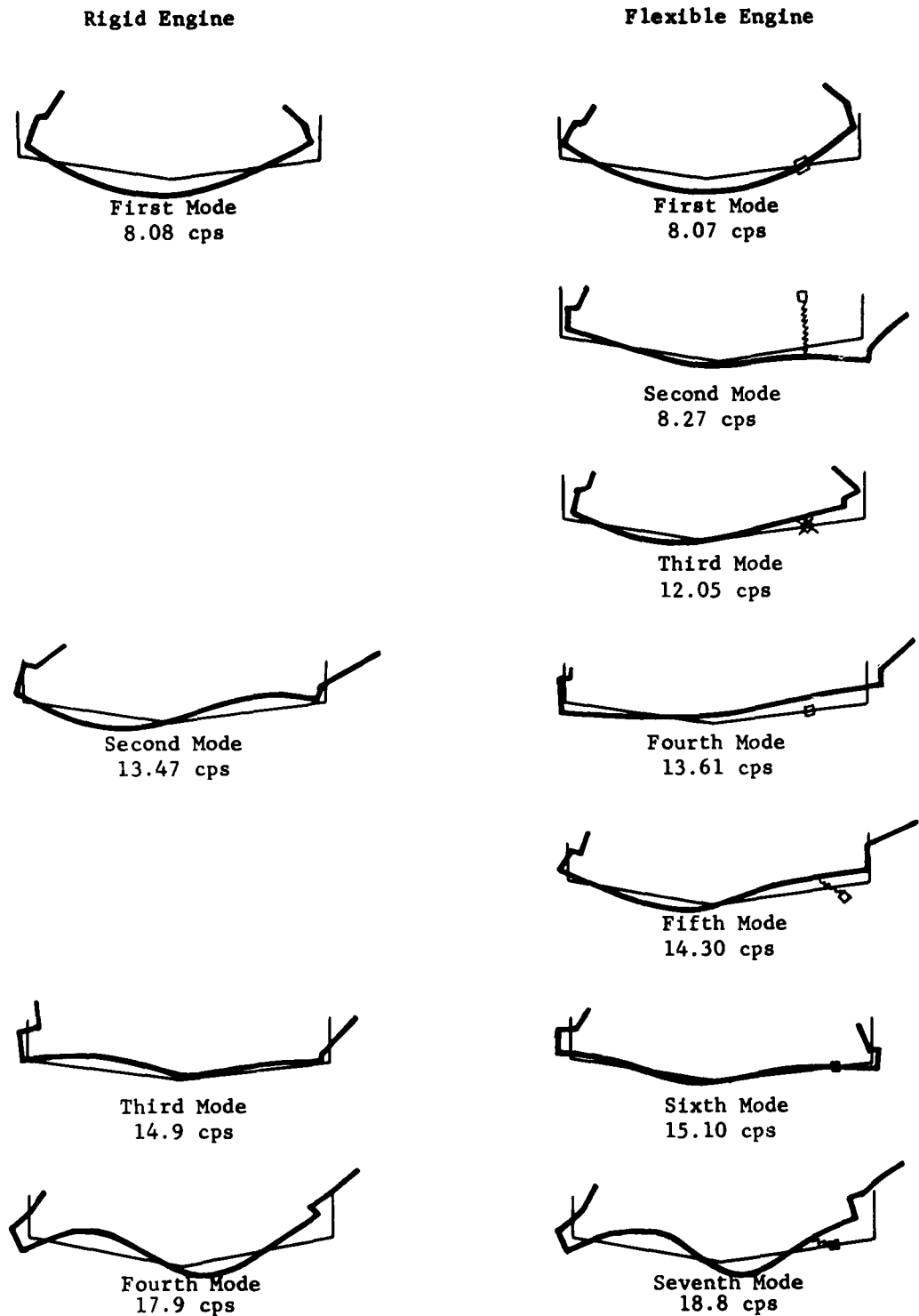


Figure 14 Comparison of H-21 Vertical Bending Modes  
with Rigid and Flexible Engine

The first mode is fundamental fuselage beam bending, the second is second fuselage beam bending and third and fourth are pylon predominant modes. The fundamental fuselage bending mode retains its shape, and changes frequency very slightly from 8.08 cps to 8.07 cps. The root now appears on the residual curve on a down-slope rather than an up-slope as was true in the rigid case. The second and third modes are new; second at 8.27 cps is engine vertical predominant and arises from the 7.5 cps engine vertical asymptote; third is engine pitch predominant and arises from the 12.05 cps engine pitch asymptote. The fourth mode at 13.61 cps is the second fuselage bending mode but, because of coupled engine motion, it is no longer as clear-cut as its rigid engine predecessor at 13.47 cps. Note again on the residual plot that the 13.61 cps fuselage natural frequency appears on an up-slope in contrast to the down-slope where it appeared at 13.47 cps with rigid engine. The fifth mode at 14.30 cps is engine longitudinal corresponding to the 13.5 cps asymptote. The engine longitudinal motion appears small only because the forward pylon longitudinal normalization has been reduced from 1.0 to 0.1 in order to plot the mode on the existing scale. The sixth mode at 15.10 cps evolves from the third mode with rigid engine; but because of an additional mode associated with engine flexibility that appears between the rigid engine second and third modes, the aft pylon undergoes a phase reversal. The seventh mode is a pylon predominant mode corresponding to the fourth with rigid engine.

#### Lateral Bending

The uncoupled engine natural frequencies were calculated in the roll, yaw and lateral directions at 6.9, 7.2 and 12.0 cps respectively. These calculations were based on measured dynafocal and support truss stiffnesses. The resulting residual curve is presented below; the mode shapes are shown in Figure 16.

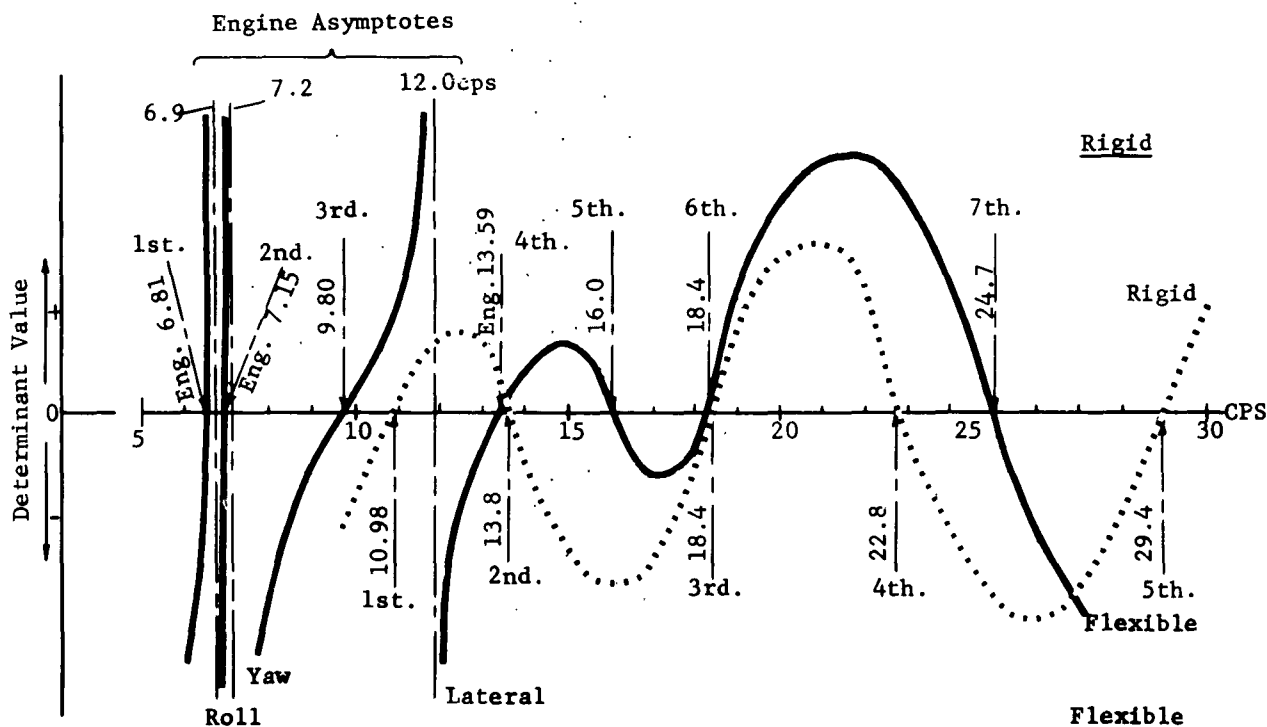


Figure 15 Lateral Bending Matrix Residual Curve

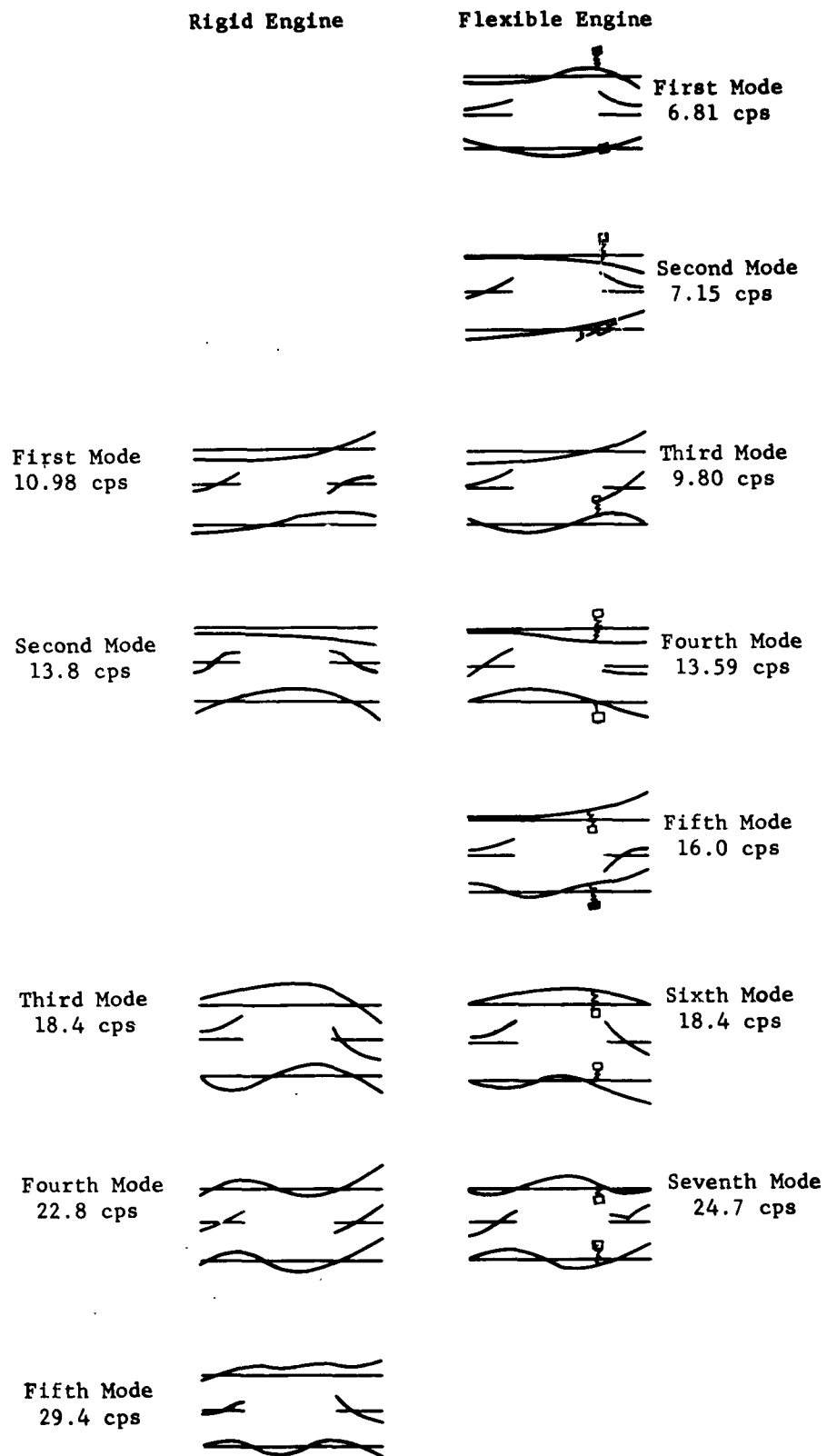


Figure 16 Comparison of H-21 Lateral Bending Modes with Rigid and Flexible Engine

<u>Mode</u>	<u>Ballasted, Rigid Eng.</u>	<u>Ballasted, Flex. Eng.</u>
First	10.98	(Eng) 6.81 cps
Second	13.8	(Eng) 7.15 cps
Third	18.4	9.80 cps
Fourth	22.8	13.59 cps
Fifth	29.4	16.0 cps
Sixth		18.4 cps
Seventh		24.7 cps

The first and second modes of the flexible engine are engine roll and engine yaw predominant respectively, and are well below the first rigid engine fuselage frequency on the residual plot. The third mode of the flexible engine case at 9.80 cps is fundamental fuselage torsion, and corresponds closely to the first rigid engine mode at 10.98 cps; coupling here has had an appreciable frequency effect, dropping a basic structural mode by a full cycle per second. On the residual curves, both 9.80 cps and 10.98 cps appear on up-slope portions, thus differing from the vertical case.

The fourth mode, flexible engine at 13.59 cps, and the second mode, rigid engine at 13.8 cps, are both fundamental fuselage lateral bending. In this instance the rigid engine case appears on a down-slope residual, the flexible engine case on an up-slope residual and engine coupling has had little influence. The fifth flexible engine mode at 16.0 cps arises from the lateral engine asymptote, so that engine lateral predominates, accompanied by large contributions from the other engine motions. The sixth mode, flexible engine, and the third mode, rigid engine, are closely related, exhibiting the second complexity of lateral bending shape (three nodes) and torsion shape (two nodes), and identical natural frequencies. Seventh mode flexible and fourth mode rigid are similar, and indicate a further degree of complexity in torsion shape (four nodes). The next mode, calculated only for the rigid case, is the fifth mode at 29.4 cps, and is the third complexity of lateral bending having four nodes. Frequencies beyond about 18 cps are not likely to be excited by the important rotor harmonics ( $3\Omega = 12.9$  cps) and are presented only for general understanding of the modal characteristics.

#### E. Conclusions

An operationally simple extended Associated Matrix method was developed which can predict vibration modes from design mass and stiffness data. Concentrated masses and inertias at any desired location, distributed stiffness properties in bending, shear or torsion, local spring properties in any direction, wandering elastic axes and engines suspended on isolators can be conveniently represented in the matrix procedure. The analyses consisted of two parts, (1) vertical, which treated motions in the vertical centerplane of the aircraft, including vertical, longitudinal and pitch displacements and (2) lateral, which treated motions in the lateral planes of the aircraft including lateral, roll and yaw displacements.

In an application to the H-21 helicopter where cutouts occupy major portions of the periphery, the separate vertical and lateral treatment was shown to

be inadequate. In such cases important coupling appeared between vertical and lateral motions, so that a fully coupled, six degree of freedom analysis was necessary.

In all configurations not including the added complexity of a flexibly mounted engine, certain patterns appeared in the fuselage modes with reasonable consistency. In vertical bending, the first mode was predominantly simple beam bending, so that the bending stiffness estimate was most important here. The second vertical bending mode consisted of anti-symmetric pylon motions along with a second bending mode of the fuselage proper. This mode was particularly dependent on the estimate of the rotor transmission attachment spring rates at both forward and aft rotor transmissions. Third and higher modes reflected all the stiffness properties and were less a function of any single property. In the lateral cases torsional stiffness predominated in the first mode, and either lateral bending or rotor transmission roll attachment in the second mode. Higher modes were dependent on a mixture of all the properties as in the vertical case. Although the addition of a flexibly mounted engine disturbed the mode pattern somewhat, it was found for those modes in which engine motion was not dominant, that the patterns described above were still applicable.

In an application to the H-16 helicopter in Reference 3 not shown in this summary report, the uncoupled analysis was reasonably representative. Here the major requirement for close modal agreement with test was in the estimation of the stiffness properties. It was found that bending and torsional stiffness of the shell structure, and rotor transmission attachment were foremost in establishing the proper natural modes and frequencies, whereas shear stiffness and tensile properties were secondary.

## SECTION IV

### LOAD DEFLECTION TESTS ON AN H-21 HELICOPTER FUSELAGE TO DETERMINE STIFFNESS CHARACTERISTICS

#### A. General

As part of an overall program to improve the prediction of dynamic response characteristics of tandem helicopter fuselages, it was considered essential to conduct load deflection tests on an existing tandem helicopter fuselage whose stiffness characteristics had been calculated and whose dynamic response characteristics were reasonably well known from shake tests. The test program was designed to yield (1) average bending, shear, and torsion stiffness characteristics for each of eight fuselage bays of selected length encompassing the complete fuselage between rotors, (2) concentrated vertical, lateral, longitudinal, pitching and rolling spring rates for the structure connecting the transmission to the fuselage and (3) spring rates for the pitch and roll springs assumed to connect the rotor shaft and the transmission at the upper bearing. A lg flight loading condition, with its accompanying skin buckling, was simulated during the test by maintaining a constant vertical load of 6,000 lb at the rotor shaft. In some cases, the loading was repeated in the absence of this steady vertical load in order to obtain data indicating the significance of skin buckling and/or other non-linearities. Maximum loads applied to the structure during the tests were limited to 95% of limit design loads to insure that yield stresses were not exceeded.

#### B. Test Procedure

Load deflection tests were performed independently first on the aft and then on the forward half of an H-21 helicopter fuselage which was disassembled at the field splice and fixed in each case to a rigid backstop at the field splice as shown in the photograph of Figure 17. Applied loads were reacted by a loading jig, and deflections were obtained relative to a measuring framework cantilevered from the rigid backstop on which the fuselage was supported. Deflections were measured with slide wire potentiometers and strain gaged cantilever beam type pickups, and recorded on a Strain Gage Graphical Plotter.

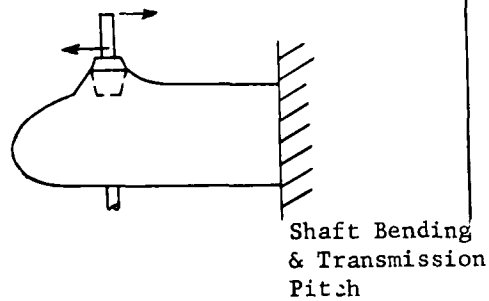
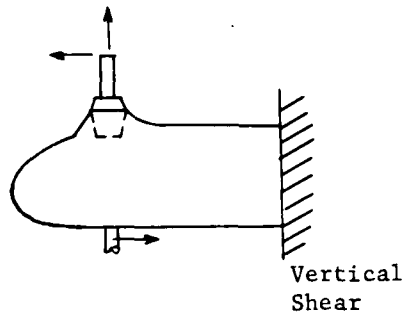
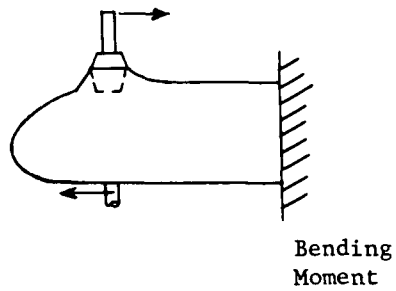
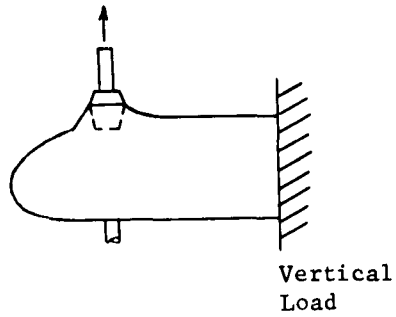
Testing on each half of the fuselage was divided into two parts which will be referred to as "vertical" and "lateral". The vertical tests included pure vertical loads, longitudinal couples to produce pure bending moments, and combinations of the two applied simultaneously with the relative magnitudes adjusted to give maximum vertical shears and minimum bending moments in each of the selected fuselage bays. Rotor shaft bending and transmission pitching were induced by a longitudinal couple applied to the rotor shaft. The lateral tests included pure lateral loads, and lateral couples to produce torsional moments. Transmission roll and rotor shaft lateral bending were obtained by a lateral couple on the rotor shaft. Deflection transducers were oriented to measure absolute vertical deflections, absolute lateral deflections, fuselage twist and the absolute and differential longitudinal deflections which define the bending slope at the end of each bay and the change in slope across the bay. The methods of loading for both the vertical and lateral tests are illustrated schematically in Figure 18.



Figure 17 Overall View of a Fuselage-Half Installed in Reinforced Test Fixture



## Vertical Tests



## Lateral Tests

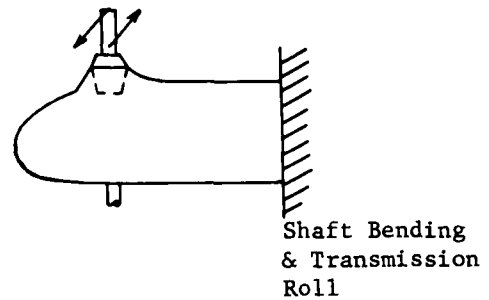
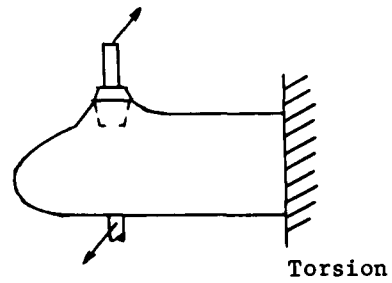
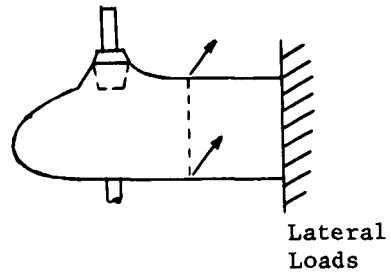


Figure 18 Method of Load Application

### C. Discussion of Results

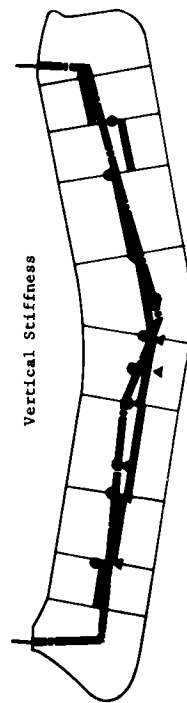
Results for each stiffness property are presented for the entire fuselage rather than for each half separately. The test stiffness values shown for each bay are the average of several values, each of which was determined from one test loading; in cases where data from one test were considered to be more accurate than from another, the average was weighted accordingly.

Vertical - Fuselage stiffness characteristics for the "vertical case" are presented in Figure 19; results are given for the vertical location of the neutral axis, the bending stiffness, and the shear stiffness. Available calculated results for neutral axis location and bending stiffness assuming alternately all skin effective, or all skin above the upper longeron ineffective, are also shown together with an assumed stiffness and neutral axis distribution (based on these calculations) which was used in previous dynamic studies of the fuselage. The calculated shear stiffness data presented were computed considering all side-skin effective.

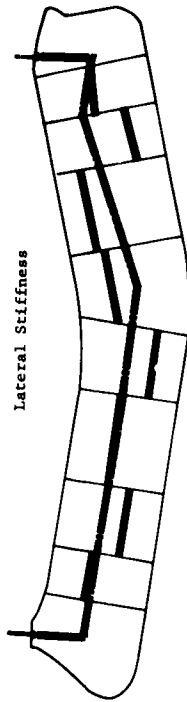
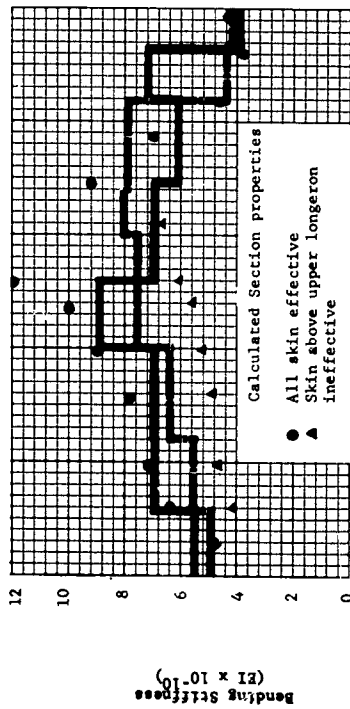
From the results it is seen that the previously assumed neutral axis is never far from the test location. Test bending stiffness results for the forward half agree best with the "all skin effective" calculations in spite of the fact that they are based on load levels which produce appreciable skin buckling. In the aft half, the test bending stiffness data are equal to or less than the calculated results assuming all skin effective, except in the region of the air exist opening. The substantial underestimation of the stiffness in this particular area is probably due to neglecting some of the doubler material added along the keel to strengthen the structure around this opening. The calculated shear stiffness properties are consistently higher except at the extreme aft end of the fuselage.

It should be noted that the test shear stiffness results in the forward half are based on vertical deflections at the fuselage plane of symmetry. Since the elastic axis was found to be laterally displaced from this location in some fuselage bays, this procedure is not strictly correct. If the shear stiffness from test had been determined for the true elastic axis position, they would have been substantially higher. The influence of shear stiffnesses of this magnitude or greater, on the lower natural modes of the subject aircraft, however, is indicated to be small by previous studies in which shear stiffness was arbitrarily varied.

Lateral - The vertical position of the shear center, determined from lateral pair loadings, and the lateral bending and transverse shear stiffness are presented in Figure 19 together with previously calculated properties assuming all skin effective. Fairly large differences in elastic axis position and in bending and shear stiffness magnitude are evident. The elastic axis is seen to be very high in the vicinity of the engine hatch doors and the next bay forward as compared to the calculated locations, while in another aft bay and two forward bays the axis is lower than calculated. Calculated lateral bending stiffness in the forward half of the fuselage, and in the engine hatch door area of the aft half, falls substantially below the values indicated by the test results, while the calculated lateral shear stiffness generally overestimates the properties arrived at by the test.



— Neutral axis location from vertical loadings  
 - - - Neutral axis location originally assumed



— Shear center location from lateral pair loadings  
 - - - Elastic axis position originally assumed

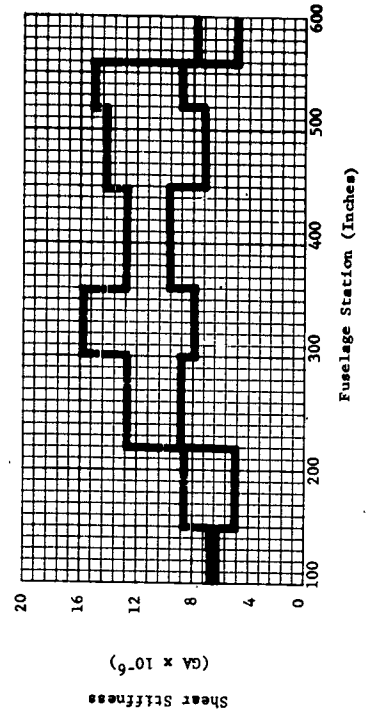
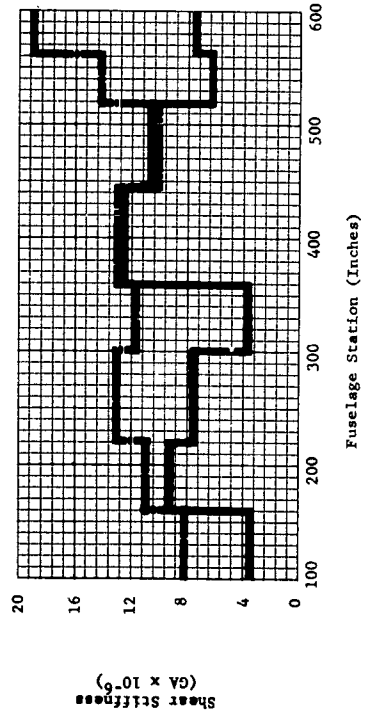
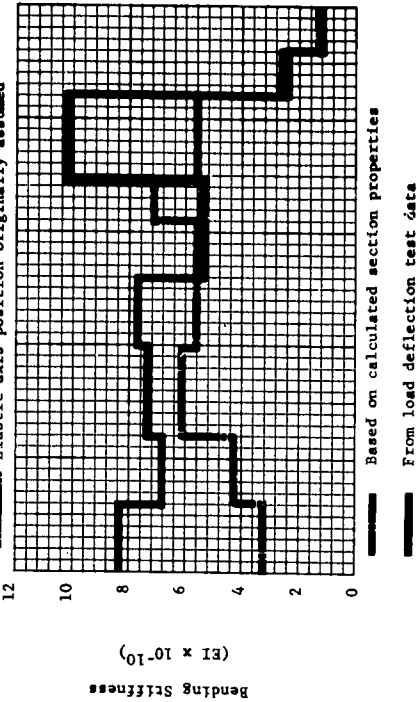


Figure 19 Vertical & Lateral Stiffness Characteristics

Torsion - The torsion stiffness and the elastic axis position as determined from torsion couple loadings are presented in Figure 20. The elastic axis position is appreciably different from the assumed location; however, it agrees quite well with the test shear center location shown in Figure 19 with the exception of the fuselage bays between stations 521.5 and 562 and stations 299.5 and 359.5. No elastic axis position is given in Figure 20 for the latter bay, since calculations indicate that it lies far outside of the fuselage cross-section.

Two sets of test torsion stiffness distributions are shown for the forward half of the fuselage in the lower part of Figure 20; both are from the same pure torque loading condition. One of these is derived from lateral deflections of the upper and lower longeron while the other is based on vertical deflections of the right and left lower longerons. If the structure had behaved as a perfect circular cylinder, according to the Saint Venant Theory, both of these results would be identical; it is clear that this is definitely not the case. Furthermore, neither result agrees very well with the calculated properties. For the aft section of the fuselage only torsional stiffness properties based on lateral deflections of the upper and lower longerons are presented - no vertical data was obtained for the aft fuselage torque loadings. The test results differ from the calculated section properties by approximately a factor of two; however, unlike the forward section, the test and calculated properties follow the same general trend indicating that the aft section responds more nearly in the theoretical manner.

Examination of the deflection data, for the torsional loading conditions, indicates that the failure of the forward section of the fuselage to behave in accordance with Saint Venant's torsional theory is due largely to racking (distortion) of the fuselage frames. Therefore, frame distortions must be considered in any analytical representation of the forward section of the fuselage. An analytical method which provides a satisfactory representation of the frame racking motions is discussed in detail in Section VII.

Rotor Transmission Spring Rates - As indicated previously several types of spring rates associated with the rotor transmissions were determined. These include the transmission support springs for longitudinal, lateral, pitch and roll motions and the assumed pitch and roll springs connecting the rotor shaft to the transmission at the upper bearing. Results for these characteristics from the tests and by previous calculations are compared in Figure 21. In most cases the test values represent the average of several test runs. The error in the spring rates is estimated to be less than plus or minus 15%.

The precise agreement between the test and calculated spring rates for the clock springs connecting the shaft and transmission,  $K_{S_3}$ , indicates the significant flexibility to be in the shaft segment within the transmission rather than in the supporting bearings, since the calculated value was obtained ignoring bearing flexibility. For the aft transmission the calculated lateral, longitudinal, roll and pitch spring rates are in reasonable agreement with the test results considering the complexity of the fail safe structure. Calculated results for the forward transmission, however, are generally in poor agreement with the test data except for the pitching spring rate which is in fair agreement with the test value. It is of interest to note that the center of rotation of each transmission in pitch and roll is nearly coincident as indicated by the similarity of distances of the spring locations below the top of the shafts.

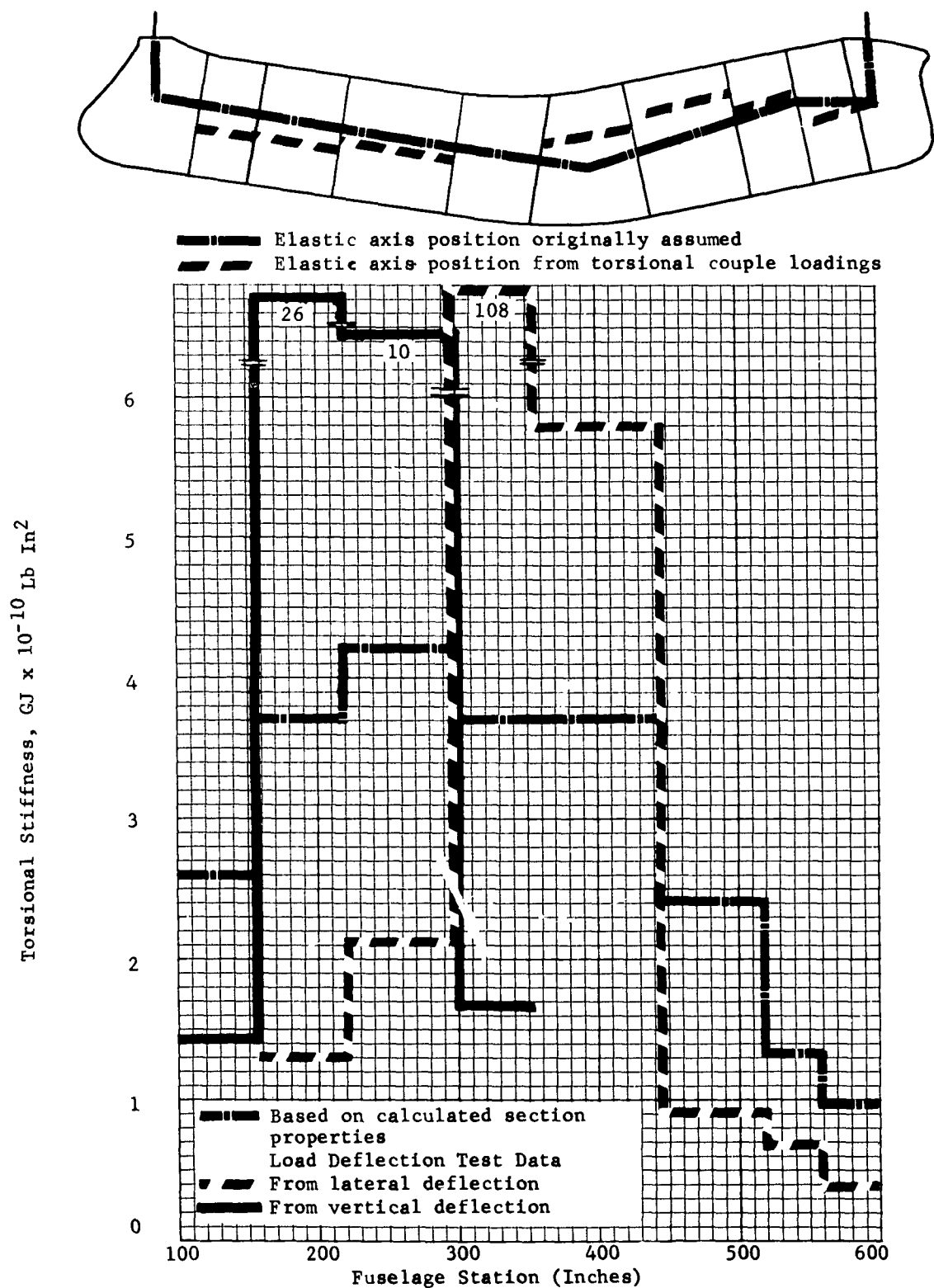


Figure 20 Torsional Stiffness Characteristics From Lateral and Vertical Deflection Measurements

Location	Direction	Spring*	Loc. Below Top of Shaft Inches	Spring Rate		Dimensions
				Test x 10 <sup>6</sup>	Calculated x 10 <sup>6</sup>	
Forward	Roll	$K_{s\alpha}$	Upper Bearing	25	25	In-Lb./Rad.
	Roll	$K_{t\alpha}$	32.4"	70	35	In-Lb./Rad.
	Lateral	$K_{ty}$	32.4"	0.35	0.13	Lb./In.
	Pitch	$K_{s\beta}$	Upper Bearing	25	25	In-Lb./Rad.
	Pitch	$K_{t\beta}$	32.2"	40	33.3	In-Lb./Rad.
	Longitud- inal	$K_{tx}$	32.2"	0.023	0.127	Lb./In.
Aft	Roll	$K_{s\alpha}$	Upper Bearing	25	25	In-Lb./Rad.
	Roll	$K_{t\alpha}$	46.2"	30	33.0	In-Lb./Rad.
	Lateral	$K_{ty}$	46.2"	0.13	0.178	Lb./In.
	Pitch	$K_{s\beta}$	Upper Bearing	25	25	In-Lb./Rad.
	Pitch	$K_{t\beta}$	44"	38	33.0	In-Lb./Rad.
	Longitud- inal	$K_{tx}$	44"	0.139	0.161	Lb./In.

- \*  $K_s$  - Shaft root spring relative to transmission
- $K_t$  - Transmission springs relative to fuselage proper
- $\alpha$  - Roll motion
- $\beta$  - Pitching motion
- y - Lateral deflection
- x - Longitudinal deflection

Figure 21 Summary of Rotor Transmission Spring Rates

#### D. Conclusions

Stiffness properties were determined for the H-21 tandem helicopter including, fuselage vertical and lateral bending and transverse shear; fuselage torsion; transmission vertical, lateral, and longitudinal, pitch and roll spring restraints relative to the fuselage; and rotor shaft pitch and roll spring restraint relative to the transmission.

1. Substantial coupling was found between vertical bending and torsion due to the large asymmetrically located cabin doors. Such coupling has always heretofore been neglected in dynamic calculations for tandem helicopter fuselages.
2. Torsional deformation of the cabin structure involves appreciable racking (distortion) of the fuselage frames and thus is not definable by the simple Saint Venant torsion theory as was heretofore assumed.
3. Vertical bending and shear stiffness characteristics of the forward half, and to a lesser extent the aft half, are nonlinear, i.e., they vary appreciably with vertical load level.
4. Cross sectional distortion of many of the fuselage frames for loads at the rotor shafts is substantial.
5. Calculated values, with notable exceptions, were judged to be reasonably accurate for purposes of preliminary dynamic analysis of the fuselage. The exceptions were the torsional stiffness characteristics including the location of the elastic axis and the lateral bending stiffness in the engine hatch and forward cabin areas.

## SECTION V

### IN-FLIGHT MEASUREMENT OF STEADY AND OSCILLATORY ROTOR SHAFT LOADS

#### A. General

The shaft load program was initiated to provide a reliable set of hub loads throughout the normal airspeed and rotor speed range, and at two helicopter gross weights for use in evaluating the accuracy of the prediction methods derived in the other phases.

It was the purpose of this program to (1) develop an accurate and reliable shaft load measuring system, (2) to record and analyze in-flight hub forces and moments from an H-21 helicopter, and (3) to correlate these loads with vibratory motions measured at the cockpit floor. The first step was the development of a rotor shaft load measuring system with sufficient sensitivity and accuracy to provide reliable results. From results of an earlier pioneering effort aimed at measurement of vibratory hub loads on a tandem helicopter, this was known to be a critical area. Apart from the present contract, Vertol funded the development of an advanced instrumentation system for the H-21 rotor shafts. When the present program began, this shaft instrumentation was used.

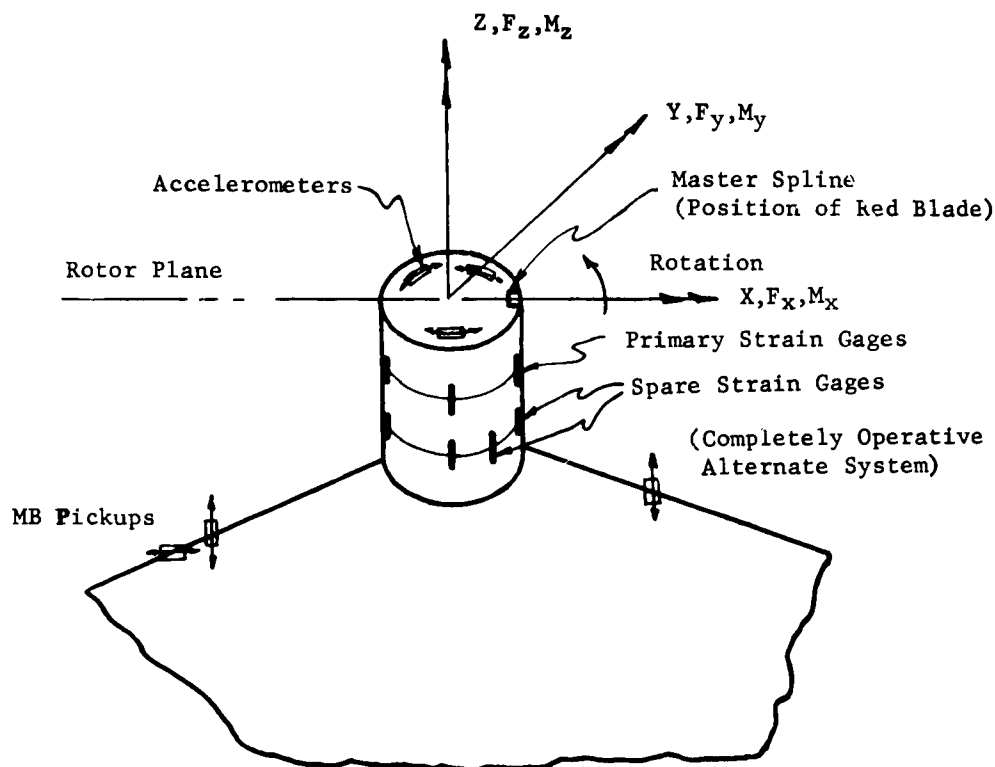
Strain gage bridges located at several shaft levels and at two azimuth positions were used. These permitted the measurement of rotor lift, shaft torsion, transverse shear in two mutually perpendicular directions, and shaft bending moments in the same two directions. Static load calibration of all the instrumentation was conducted, and means for accounting for load interaction developed.

Recorded measurements for the program were compiled during two flights, C-96X120 at a takeoff gross weight of 14,685 lb, cg 29 inches forward of the center line between rotors, and C-96X121 at a takeoff gross weight of 13,500 lb and a cg location 19.0 in. fwd. At the normal gross weight of 13,500 lb test runs were made which included an airspeed sweep at normal rotor speed, and five increment rpm sweeps at 40 and 90 knots; at the overload gross weight of 14,685 lb, test runs were made which included three airspeed points, 80, 90, and 100 knots, and a three increment sweep at 90 knots. Harmonic analyses of the vibration data were performed to obtain the first three harmonics of rotor speed; for the rotating system hub loads, harmonic analyses were performed to obtain the first four harmonics of rotor speed. The first three harmonics of fixed system loads were obtained by a direct transformation from the rotating coordinate axis system to a coordinate axis system fixed in the helicopter. As a final analytic step, recorded motions of the rotor hubs together with effective analytic rotor inertia expressions were used to determine the portion of measured hub loads and moments due to rotor inertia and damping, thus permitting the determination of the aerodynamic exciting forces.

#### B. Instrumentation

The H-21 helicopter, S/N 55-4141, used in this program was equipped with instrumentation to measure the following loads and motions:





Forward and aft transmission and rotor shafts:

1.  $F_x$ , Shear in the rotor plane in the direction of the master spline.
2.  $F_y$ , Shear in the rotor plane in a direction normal to the master spline.
3.  $M_x$ , Moment in the rotor plane, about the rotating X axis.
4.  $M_y$ , Moment in the rotor plane, about the rotating Y axis.
5.  $F_z$ , Lift force in the shaft vertical direction.
6.  $M_z$ , Torque about the shaft axis.
7. Transmission case fixed system motion, referred to longitudinal and lateral motion on the shaft at the rotor hub, MB measurements.
8. Rotor hub motion, oscillation in the rotating x and y axis system, measured by accelerometers on the rotating hub.
9. Blade pitch link loads, 3 links on forward rotor, 1 link on aft rotor.

#### Fuselage:

10. Cockpit floor motion, vertical, lateral and longitudinal, MB measurements.
11. Forward rotor shaft tilt.

The requirements of this measurement program were such that success was dependent on maintaining a high degree of accuracy. Prior to commencing work on this program, a realistic goal was established specifying the required accuracy essential for each load measurement as previously noted. Check points were established within this program to determine if the measurement system was satisfactory from both an accuracy and a reliability standpoint. Chronologically this procedure together with the check points, consisted of the following items:

1. Static load calibration (including interaction)
2. Sensitivity check prior to the rotor test stand runs
3. Rotor test stand runs
4. Sensitivity check after rotor test stand runs
5. Installation in the helicopter
6. Preflight sensitivity check, each flight
7. Program flights
8. Post-flight sensitivity check, each flight
9. Static load calibration after flight program

#### Static Load Calibration

Each transmission was installed in a specially constructed fixture, and known loads were applied individually at the rotor hub level in all directions. Figure 22 illustrates the manner of load application. The response of all gages to each load was recorded regardless of the direction of the load in order to obtain interaction as well as primary load calibration factors. Both the primary strain gages, and the spare gage alternate system were calibrated in this manner.

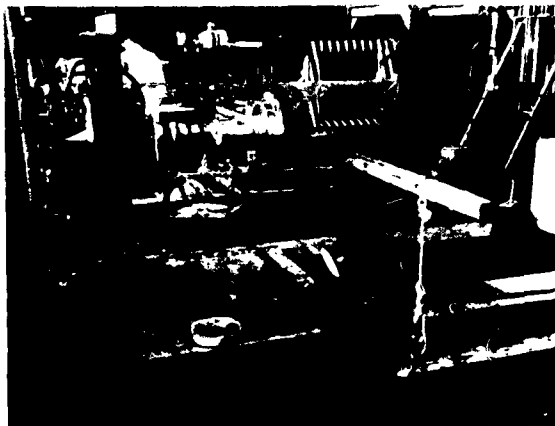
The results of the primary load calibration are tabulated on page 45, along with an estimate of the load-through-record accuracy based on an assumed oscillograph trace reading error of  $\pm 0.02$  inches. This data was based on a number of repeated static loadings and readings.



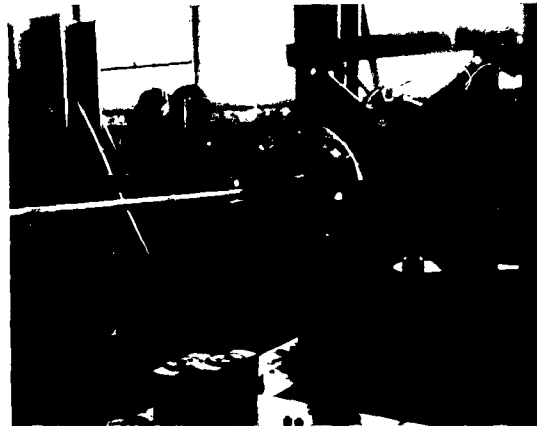
Torque Loading  
External Weight Couple Load System



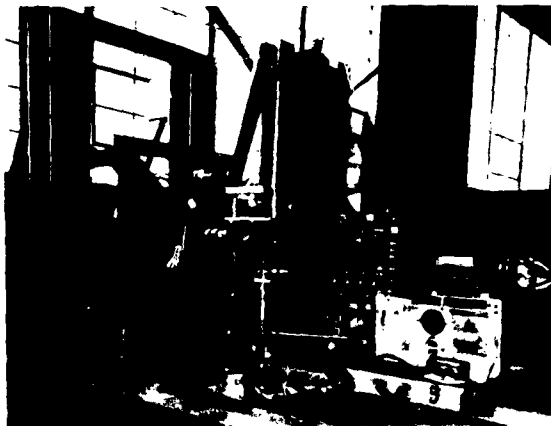
Lift Loading  
Hydraulic Jack



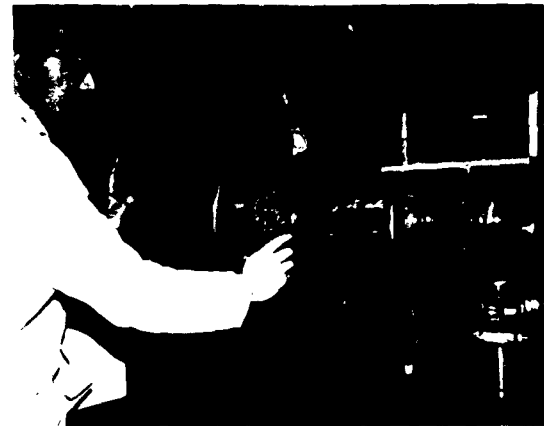
Torque Loading  
Closed Loop Cable Load System



Lift Loading  
Lift Load at Rotor Shaft



Shear Loading  
Hydraulic Jack Load System and Load Cell



Shear Loading  
Inclinometer Check

Figure 22 Rotor Shaft Calibrations

# ACCURACY ESTIMATE

<u>Item</u>	<u>Trace Calibration Factor</u>	<u>Estimated Reading Accuracy @ <math>\pm 0.02"</math></u>	<u>Estimated Overall Accuracy</u>	<u>Typical Load Value</u>	<u>% Accuracy</u>
F <sub>x</sub>	1,000 lb/in.	$\pm$ 20 lb	$\pm$ 36 lb	1,000 lb	4
F <sub>y</sub>	1,115 lb/in.	$\pm$ 22 lb	$\pm$ 36 lb	1,000 lb	4
F <sub>z</sub> Steady	6,050 lb/in.	$\pm$ 120 lb	$\pm$ 360 lb	7,000 lb	5
F <sub>z</sub> Alt.	721 lb/in.	$\pm$ 20 lb	$\pm$ 30 lb	500 lb	6
M <sub>x</sub>	22,050 $\frac{\text{in. lb}}{\text{in.}}$	$\pm$ 440 in.lb	$\pm$ 500 in.lb	5,000 in.lb	10
M <sub>y</sub>	19,290 $\frac{\text{in. lb}}{\text{in.}}$	$\pm$ 400 in.lb	$\pm$ 450 in.lb	5,000 in.lb	9
M <sub>z</sub> Steady	92,500 $\frac{\text{in. lb}}{\text{in.}}$	$\pm$ 1,860 in.lb	$\pm$ 2,400 in.lb	100,000 in.lb	3
M <sub>z</sub> Alt.	14,710 $\frac{\text{in. lb}}{\text{in.}}$	$\pm$ 300 in.lb	350 in.lb	5,000 in.lb	7

### C. Data Processing, Oscillograph Records to Rotor Hub Loads

The general procedure used to obtain the fixed system rotor loads from the recorded oscillograph data will be followed in chronological order. Strain gage bridges on the forward and aft rotor shafts measure axial shaft load and torque; and shear and bending moments in two directions. A square matrix of numerical coefficients, derived from calibration data, is then applied to the data to account for interaction, i.e., apparent response of a load measuring device to loads it should not theoretically respond to. The corrected loads in the rotating shaft are next transferred into equivalent loads in the fixed coordinate system of the fuselage. Accelerometers at the top of the shaft give the longitudinal and lateral shaft motions, and MB pickups on the transmission define vertical shaft oscillatory motions as well as linear and angular motions of the transmission; which, with a knowledge of shaft stiffness permit determination of hub pitch and roll motions. These hub motions are used, together with calculated effective rotor mass magnitudes, to determine the inertia forces generated by the rotor due to motions imposed by fuselage vibration. These inertia loads are then subtracted from the measured shaft loads to obtain the rotor exciting loads which are termed "aerodynamic rotor loads", although it is recognized that some of them may result from blade dynamics as well.

Figure 23 presents a flow diagram which illustrates the steps necessary to convert the data to final shaft loads. The initial step in processing the oscillograph data, after it had been reviewed for general acceptability, was the selection of a typical rotor cycle for each flight condition. Subsequently, this cycle of all load and motion traces was subdivided into 24 equal time increments and ordinates from a zero position read at each point using the Benson Lehner Data Reader. The resulting data was then harmonically analyzed, and programmed on a digital computer to obtain the steady loads and the important harmonics. Following the harmonic analyses, each steady term of the series was adjusted to correct for the difference between the base line from which all the ordinates were measured and the zero load position obtained during the preflight calibration.

Continuing to the right on the flow diagram, the harmonic components are converted to shaft loads by applying the amplitude and phase calibration constants obtained from the load calibration tests and adjusted for preflight and post-flight sensitivity checks. Following these corrections, the measured data is regrouped into steady and alternating terms in Items 1-4, alternating terms only in Items 5 and 6, and steady coefficients in Items 7 and 8. As shown in the chart, the final correction is the application of the load interaction matrices.

### D. Discussion of Results

The results of the hub load measurement program are presented in the form of plots of the recorded data. Both measured shaft loads and adjusted loads termed "aerodynamic" loads are given. The sketch on page 48 shows the position of the measured loads in the fixed and rotating systems, together with the sign convention.

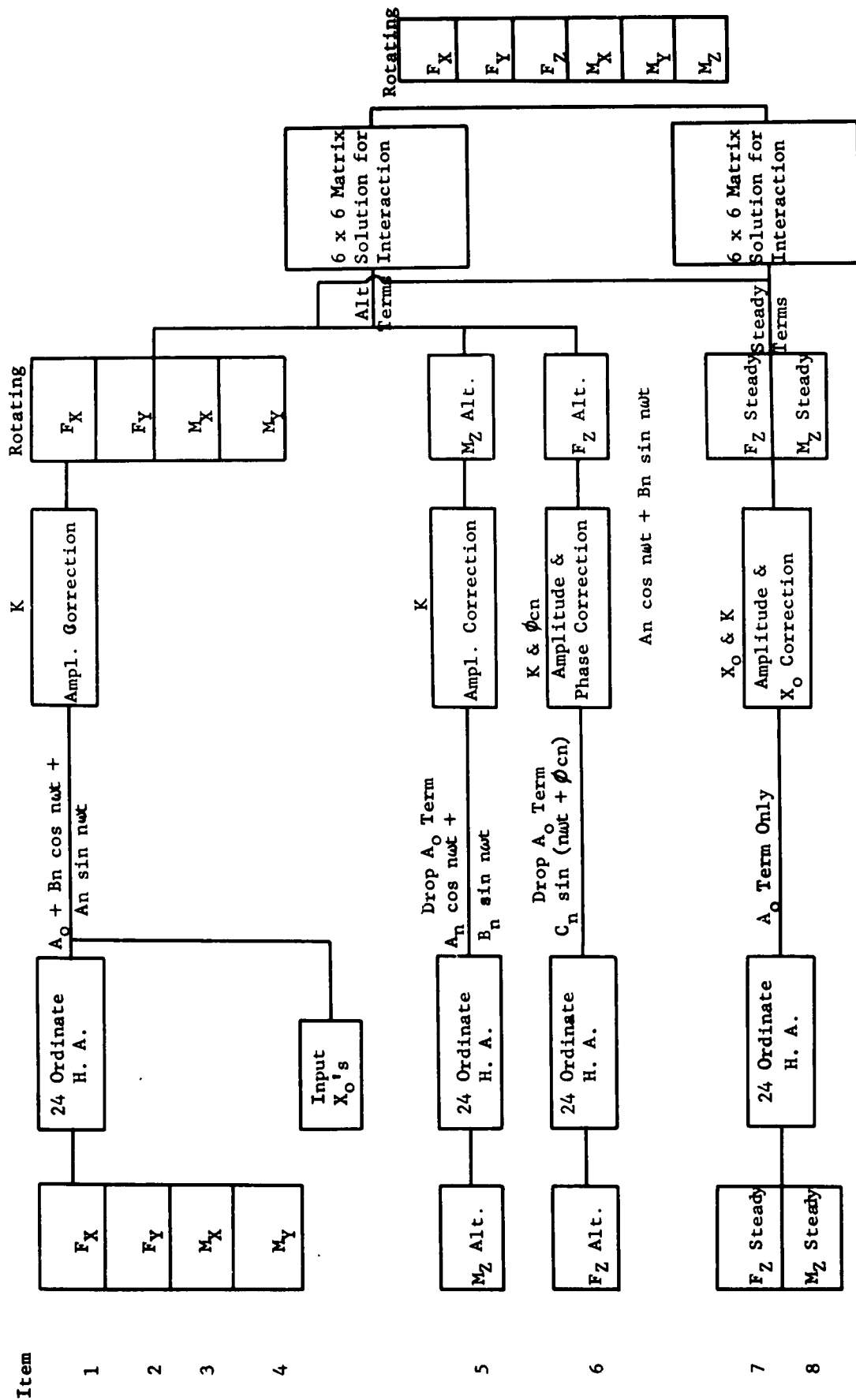


Figure 23 Flow Diagram for Converting Data to Shaft Loads

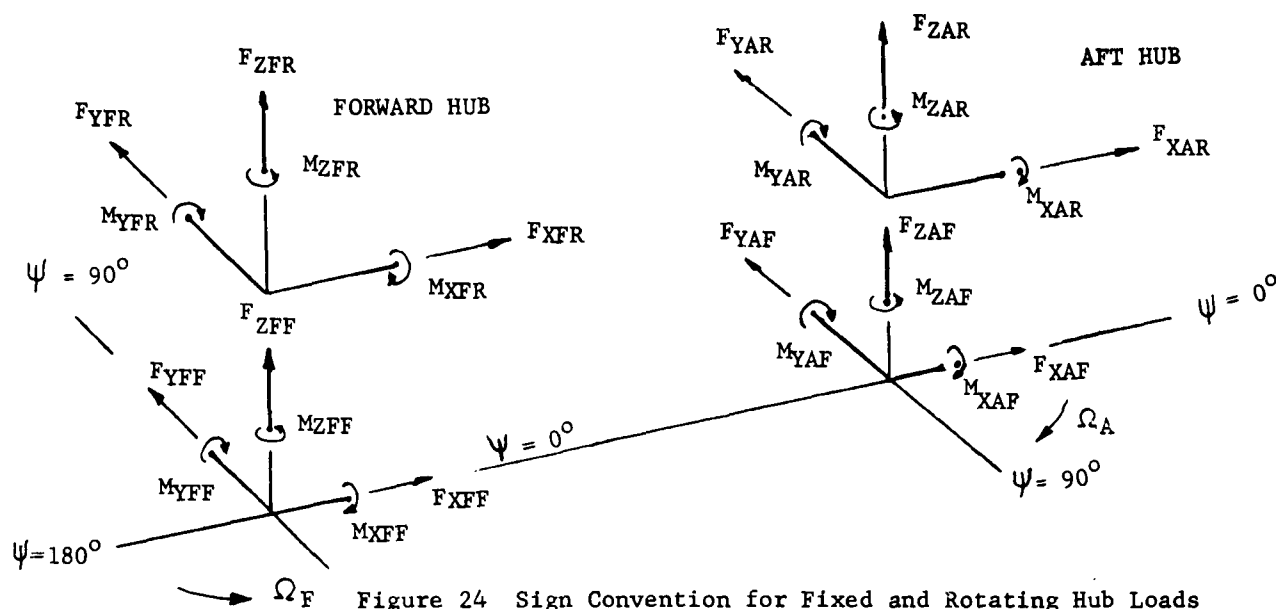


Figure 24 Sign Convention for Fixed and Rotating Hub Loads

Load plots are given containing the steady, first, second and third harmonic fixed system results, and second and fourth harmonic rotating results. Each harmonic load set contains six directional loads and moments as sine and cosine components and their resultants. The sine and cosine time reference is when the red blade is in its trail position.

Shaft loads appear on the left, aerodynamic loads on the right. Each of these is subdivided into sine and cosine components, and resultant. All six directional loads are given; longitudinal force  $F_x$ , lateral force  $F_y$ , vertical force  $F_z$ , roll moment  $M_x$ , pitch moment  $M_y$ , and yaw moment (torque)  $M_z$ . Among the harmonics, the load scales are the same,  $\pm 2,000$  lb for the forces, and  $\pm 10,000$  inch lb for the moments. The steady load scales differ in order to accommodate the larger load magnitudes. For the normal 13,500 lb gross weight flights, sets of plots are given for (1) an airspeed sweep at normal 258 rpm, (2) a rotor speed sweep at 40 knots airspeed, and (3) a rotor speed sweep at 90 knots airspeed.

Fixed System Steady Loads - Figure 26 presents the fixed system loads, an airspeed sweep and two rpm sweeps respectively. Note that the vertical forces  $F_z$  of the forward and aft rotors add to form the gross weight of 13,500 lb, within the limits of the experimental accuracy.

The H-21 forward and aft rotor shafts are parallel, but are rigged to produce a dihedral effect which promotes better speed stability. A side effect of this feature is that in order to maintain a hover attitude, the combination of longitudinal cyclic and differential collective pitch control must provide a greater aft longitudinal force at the forward rotor than the aft rotor. This is shown by a 500 lb aft force at the forward rotor, and a 200 lb forward force at the aft rotor in hover. As speed increases, the forward force at the aft rotor decreases, and above 80 knots reverses direction. The aft longitudinal force at the forward rotor increases with airspeed. The same trend with speed is shown in the  $M_y$  pitching moment records, also indicating a close relation to the speed stability.

The torque trace  $M_z$  shows that the aft rotor uses about 160,000 inch-lbs., and the forward rotor about 60,000 inch-lb in forward flight. The rotor directions are as sketched below.

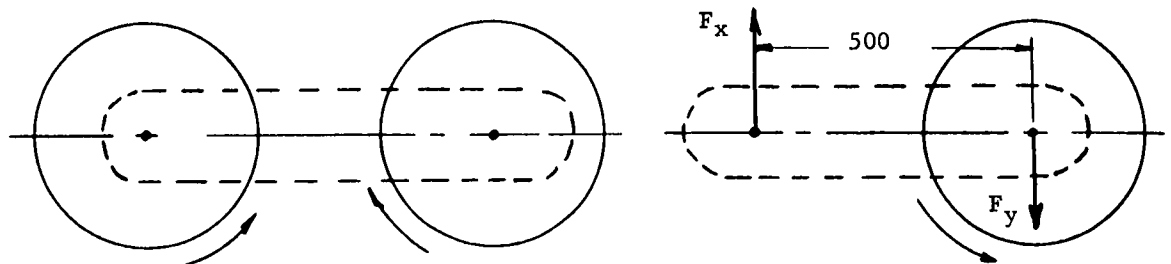


Figure 25 Forward and Aft Rotor Directions

Forward Rotor	Aft Rotor	Differential Torque
Counterclockwise	Clockwise	$160,000 - 60,000 = 100,000$ in.lb
		acting on aircraft

The torque differential of 100,000 in. lb due to the larger aft rotor torque acts counterclockwise on the aircraft, and must be balanced by approximately equal and opposite lateral loads at both rotors. The necessary load magnitude is

$$F_y = \frac{100,000 \text{ in. lb}}{500 \text{ inches}} = 200 \text{ lb}$$

In Figure 26 it is seen that these loads do occur in the measured  $F_y$  traces, averaging about 200 lb to the right at the forward rotor and to the left at the aft rotor. Roll moment  $M_x$  is also related to this effect since the forward rotor roll moment is roll right, and the aft rotor moment is roll left. In hover, the rotor torques becomes nearly equal.

The RPM sweeps in Figure 26 do not generally show any significant trend. However, a small variation with rotor speed appears for longitudinal force  $F_x$ , with the related  $M_y$  pitching moment showing a moderate downtrend with increasing rotor speed. Also, some torque reduction occurs at 90 knots for both rotors when the rotor speed is increased.



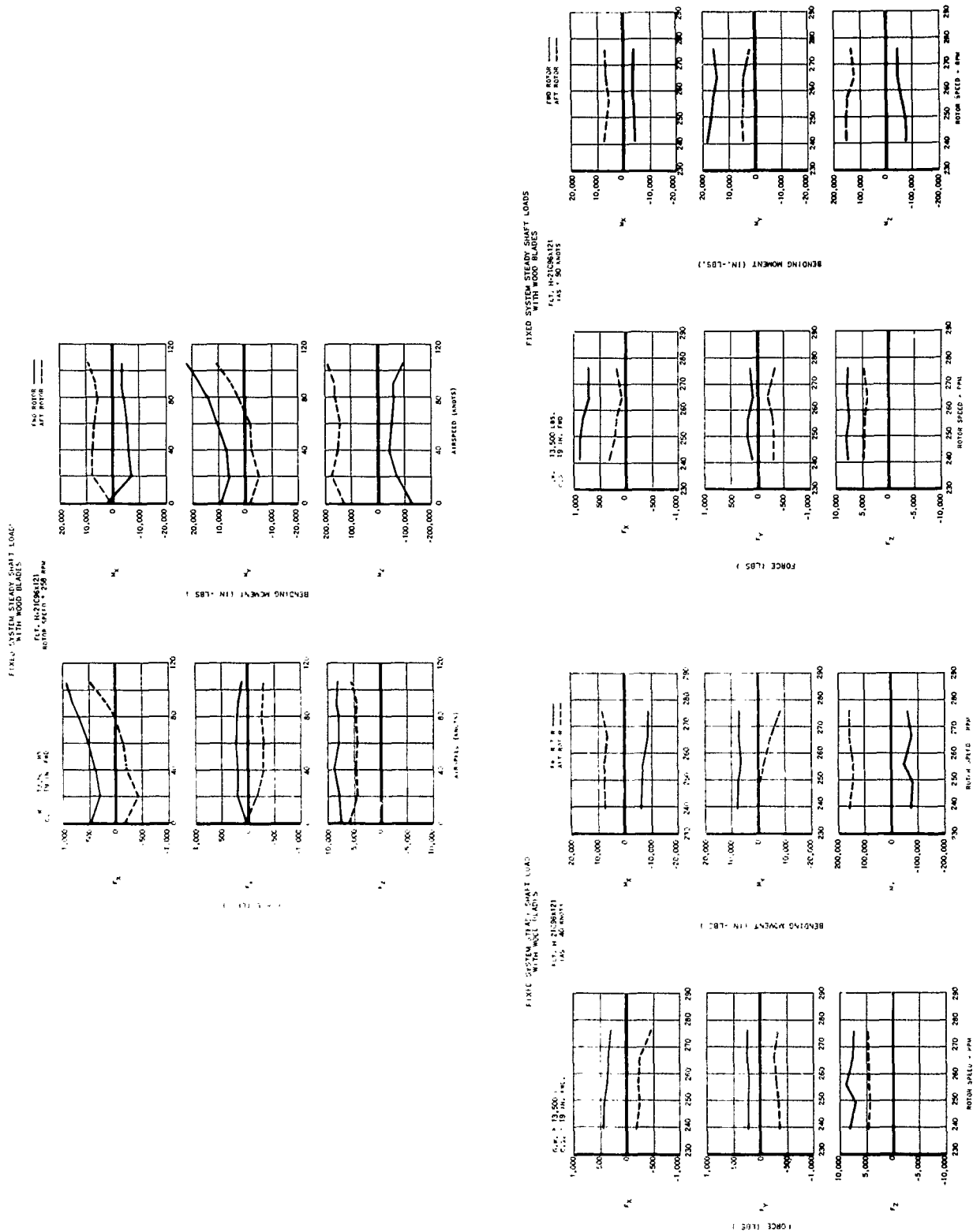


Figure 26 Fixed System Steady Shaft Loads

### First Harmonic Fixed System Loads

The first harmonic fixed system in-plane loads result from steady and second harmonic rotating loads; vertical first harmonic fixed system and rotating system loads are the same. For example, consider the effect on the fixed system of a rotating centrifugal force produced by simple mechanical unbalance.

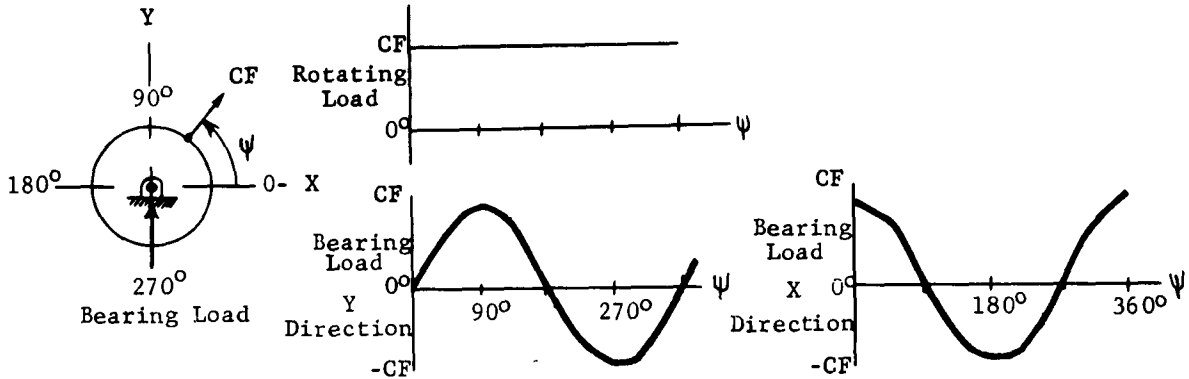


Figure 27 Effect on Fixed System of Centrifugal Force Unbalance

The rotating C.F. plotted vs azimuth  $\psi$  in the rotating system is a constant. The fixed system bearing load in the y direction is a first harmonic sine function, since at  $0^\circ$  and  $180^\circ$  azimuth, the C.F. is perpendicular to y, and at  $90^\circ$  and  $270^\circ$  the C.F. reaches full value in the y direction. Similarly in the x direction, the bearing load is a first harmonic cosine function. In a like manner it can be shown that second harmonic rotating loads are felt as both first harmonic and third harmonic loads in the fixed system.

Figures 28,29,30 present the first harmonic fixed system loads; sine, cosine and resultant loads are shown in each case. These plots and all subsequent harmonic load plots are arranged with the shaft loads on the left and the aerodynamic loads on the right. The first figure gives first harmonic fixed system loads for an airspeed sweep at the normal rotor speed of 258 rpm. In general, the force plots indicate no strong trend with airspeed, however, force peaks in  $F_x$ ,  $F_y$  and  $M_y$  at the aft rotor appear in transition and hover, where vibration is normally highest. It is to be noted that for both the aerodynamic and shaft loads, the resultant curves of the in-plane loads,  $F_x$  and  $F_y$ , are very nearly identical. This similarity between the resultants evolves from the similarity of the component loads as follows:

FWD ROTOR	AFT ROTOR
$F_x \begin{pmatrix} \text{sine} \\ \text{component} \end{pmatrix} = -F_y \begin{pmatrix} \text{cosine} \\ \text{component} \end{pmatrix}$	$F_x \begin{pmatrix} \text{sine} \\ \text{component} \end{pmatrix} = F_y \begin{pmatrix} \text{cosine} \\ \text{component} \end{pmatrix}$
$F_x \begin{pmatrix} \text{cosine} \\ \text{component} \end{pmatrix} = F_y \begin{pmatrix} \text{sine} \\ \text{component} \end{pmatrix}$	$F_x \begin{pmatrix} \text{cosine} \\ \text{component} \end{pmatrix} = -F_y \begin{pmatrix} \text{sine} \\ \text{component} \end{pmatrix}$

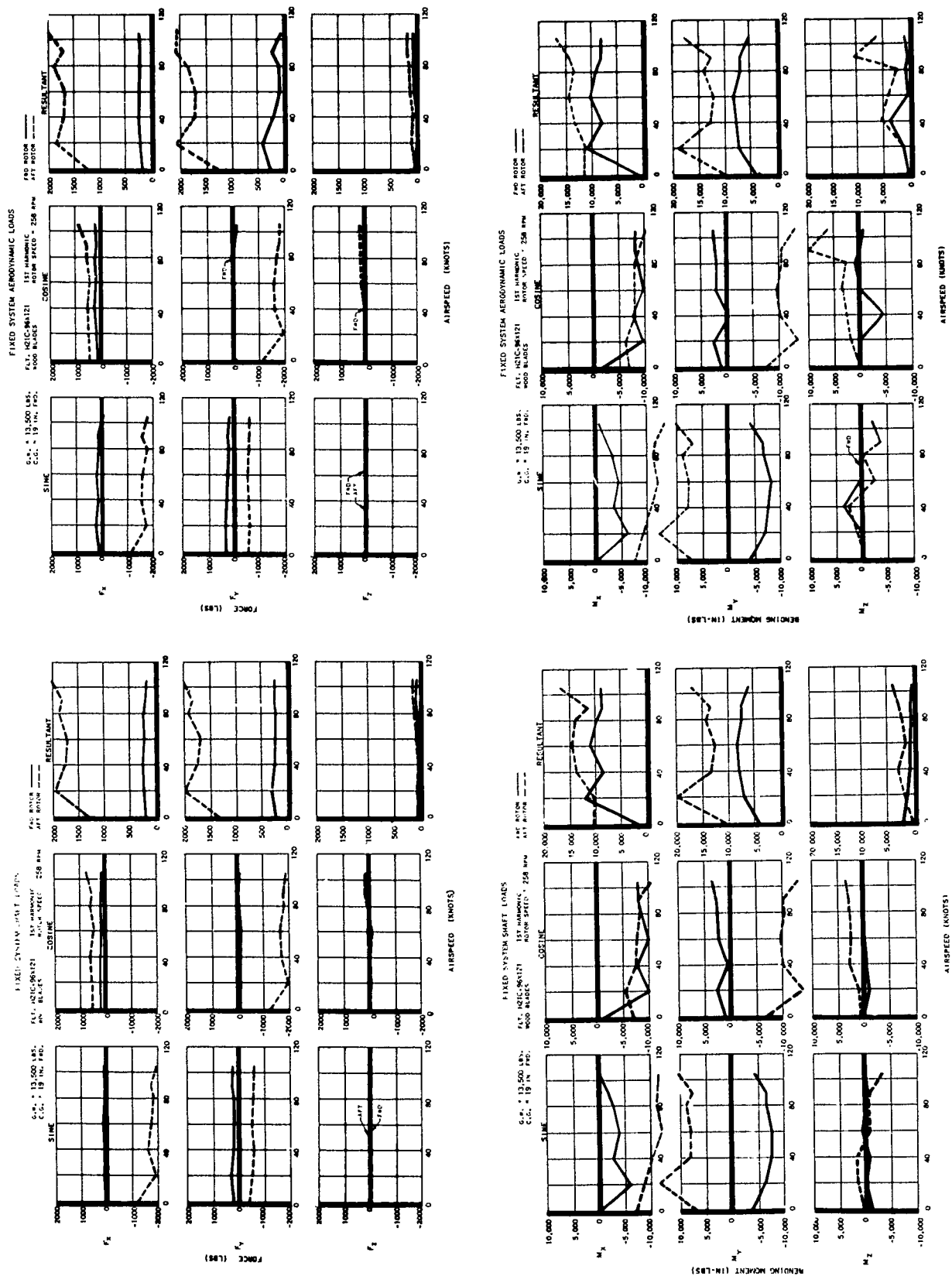


Figure 28 Fixed System First Harmonic Loads  
Airspeed Sweep at 258 rpm

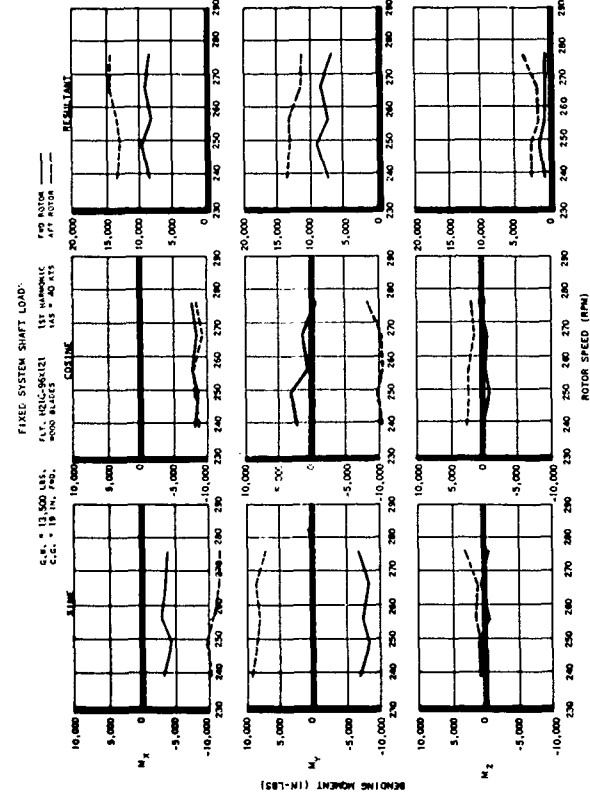
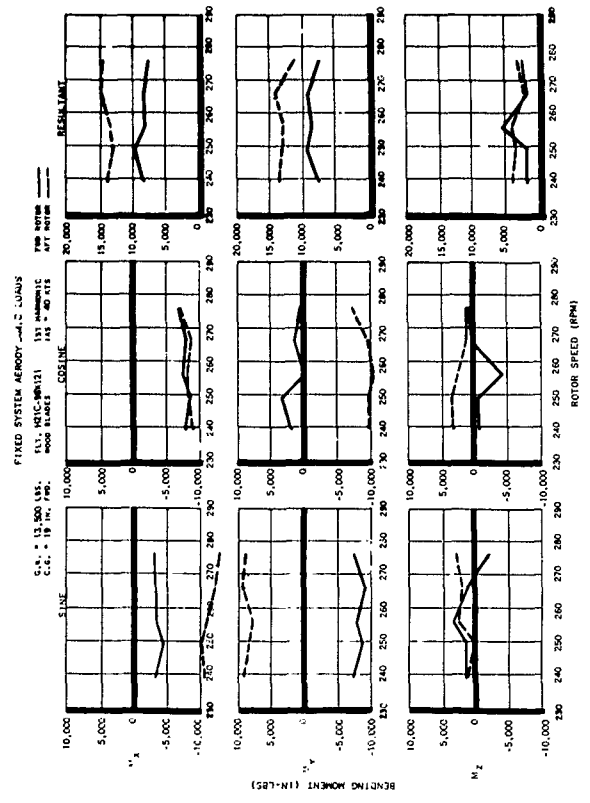
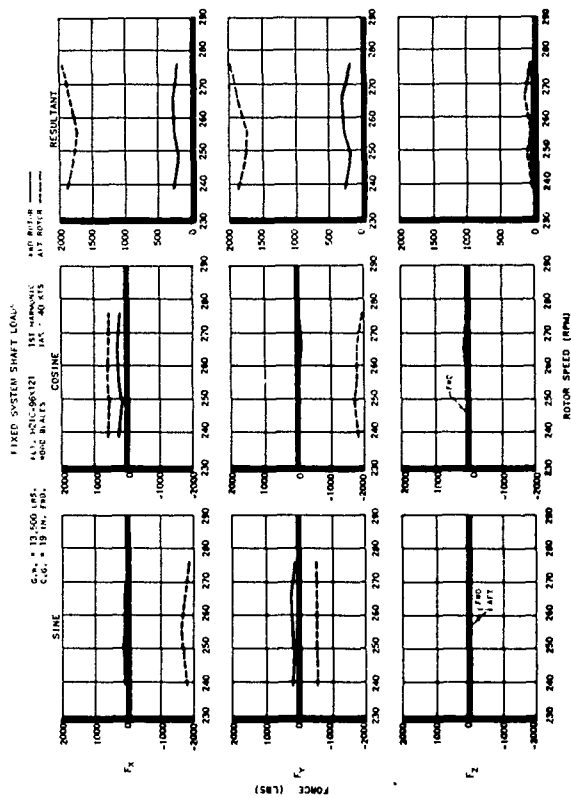
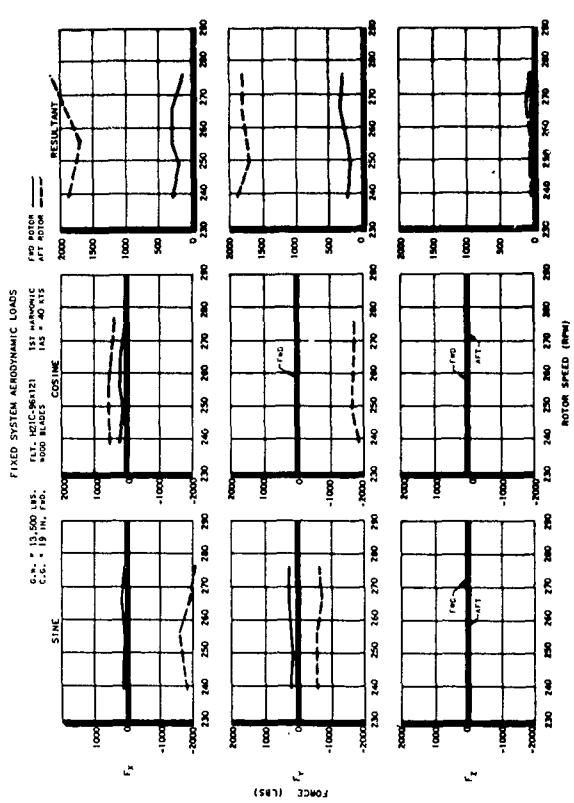


Figure 29 Fixed System First Harmonic Loads  
rpm Sweep at 40 Knots

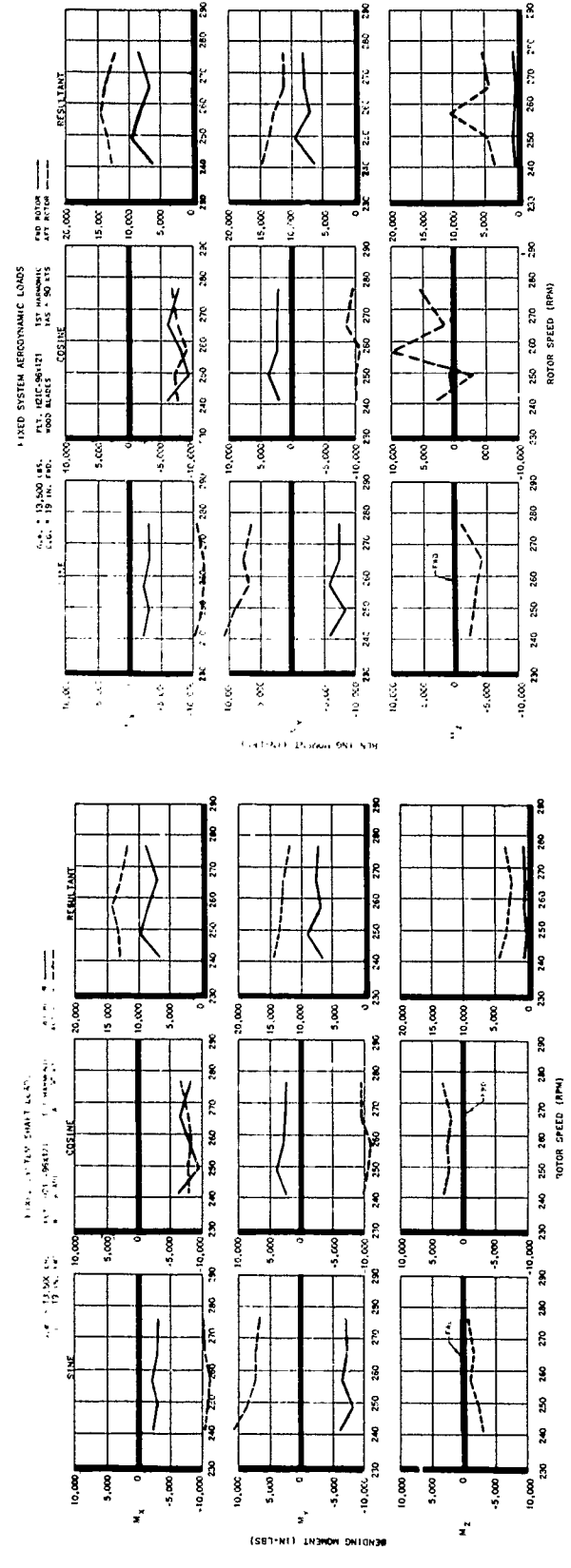
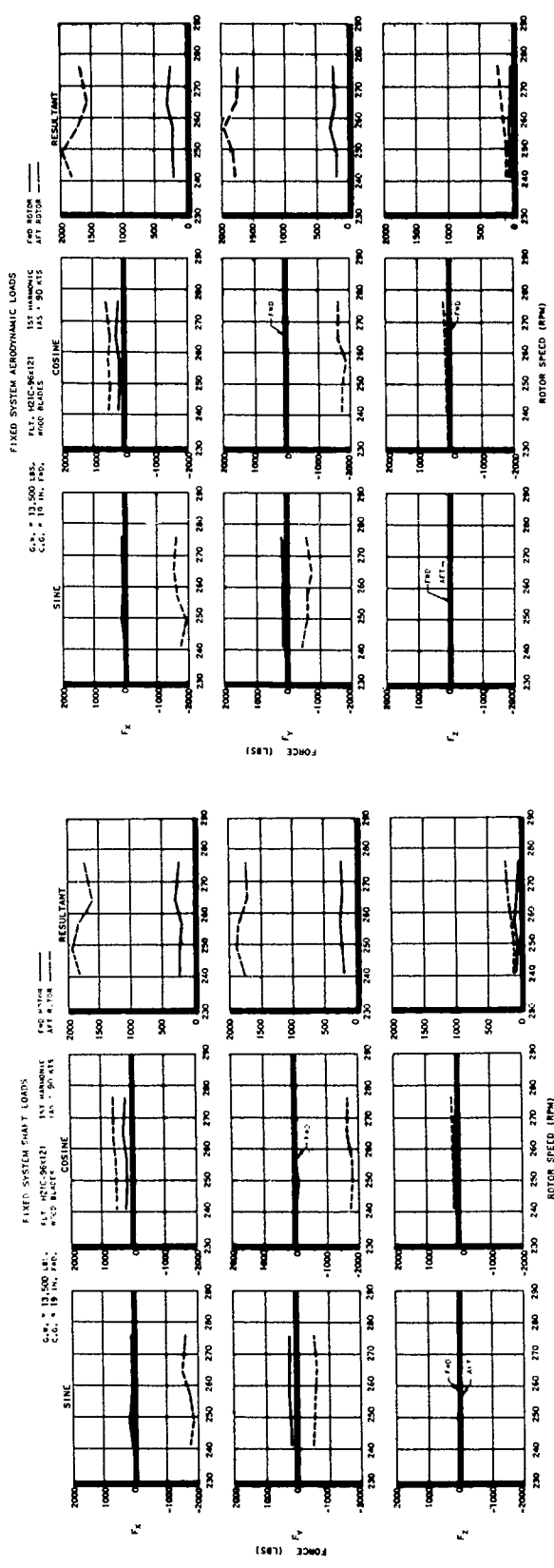


Figure 30 Fixed System First Harmonic Loads  
rpm Sweep at 90 Knots

## Second Harmonic Fixed System Loads

Fixed system second harmonic loads are presented as follows:

<u>Item</u>	<u>Figure</u>
Airspeed Sweep	31
40 Knot rpm Sweep	32
90 Knot rpm Sweep	33

The second harmonic loads average the following load magnitudes:

	<u>Fwd Rotor</u>	<u>Aft Rotor</u>
$F_x$	80 lb	80 lb
$F_y$	80 lb	50 lb
$F_z$	70 lb	80 lb

These load levels, while small with respect to the other harmonics presented here can nevertheless produce significant vibration levels if a fuselage natural mode is near  $2\Omega$ .

During an airspeed sweep at normal rpm, the in-plane resultant force and moment curves indicate a slight increase with speed at the forward rotor, while at the aft rotor the loads remain nearly constant except for a peak moment value at 20 knots. In-plane resultant moment curves for  $M_x$  and  $M_y$  are nearly identical following the previously established pattern. In addition, it is noted that the resultant curves of the shaft in-plane moments are approximately equal to the aerodynamic moments. In this airspeed sweep, the aft torque curves show an initial increase with speed from 0 to 20 knots but no clear cut trend above this speed.

Figure 32 presents the loads measured during an rpm sweep at 40 knots. Force levels are again small, while in-plane moment curves for each rotor show a reasonable order of magnitude agreement between  $M_x$  and  $M_y$ .  $M_x$  aerodynamic loads at 256 rpm show a peak near 4,000 in.-lb. This variation which exists at 256 rpm is a result of the rotor inertia correction which normally produces a load variation near 10%. Inclusion of the rotor inertia effect has little effect on  $M_z$  torque.

The 90 knot rpm sweep similarly shows very small force levels, and moment levels which do not display any definite speed trend. Forward rotor  $M_x$  and  $M_y$  moments at 90 knots are near 5,000 in.-lb, slightly higher than the 4,000 in.-lb moments at the 40 knot rpm sweep.

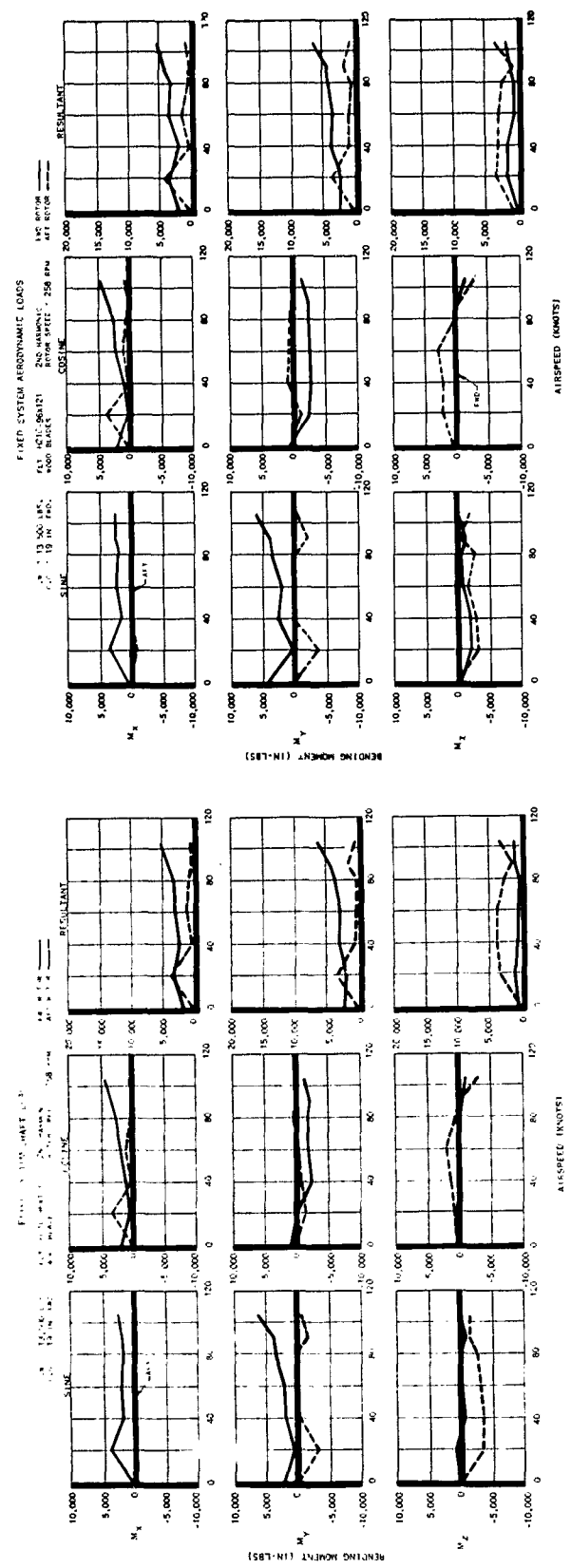
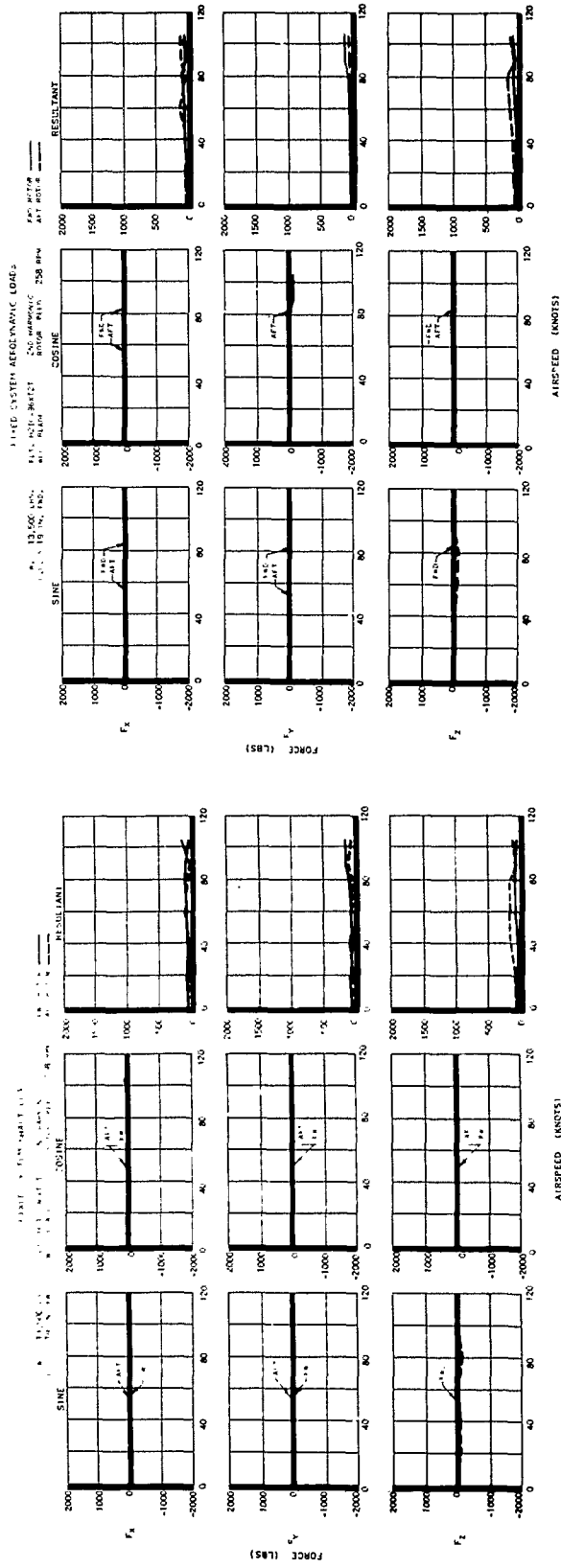


Figure 31 Fixed System Second Harmonic Loads  
Airspeed Sweep at 258 rpm

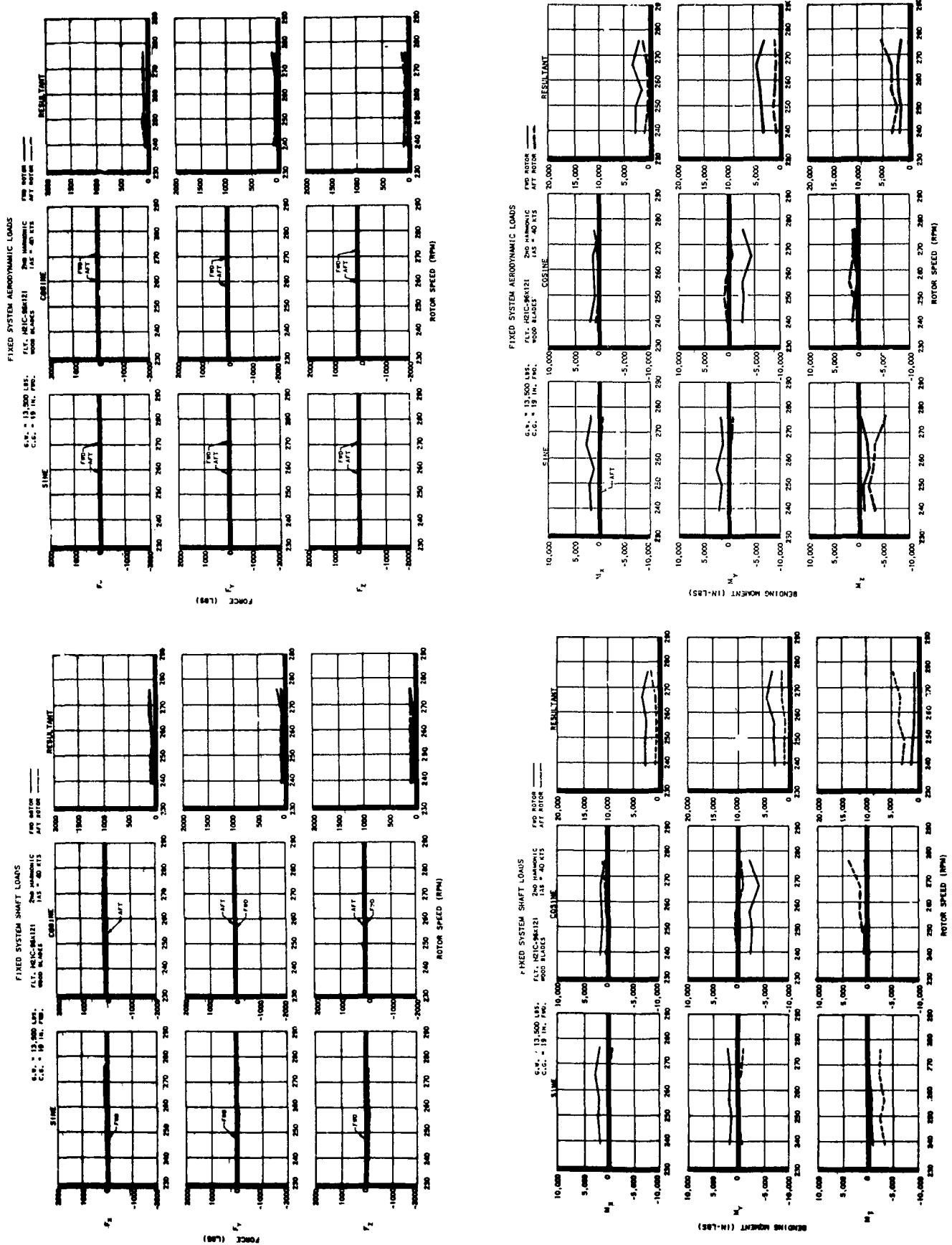


Figure 32 Fixed System Second Harmonic Loads  
rpm Sweep at 40 Knots



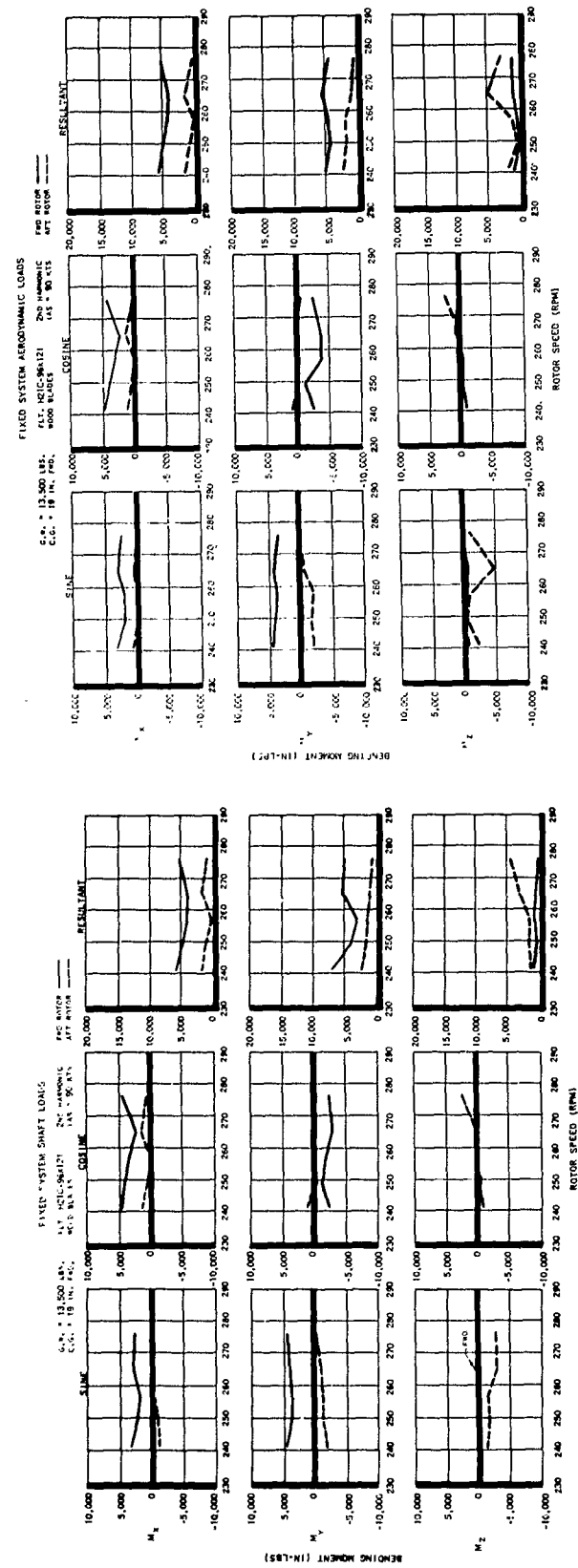
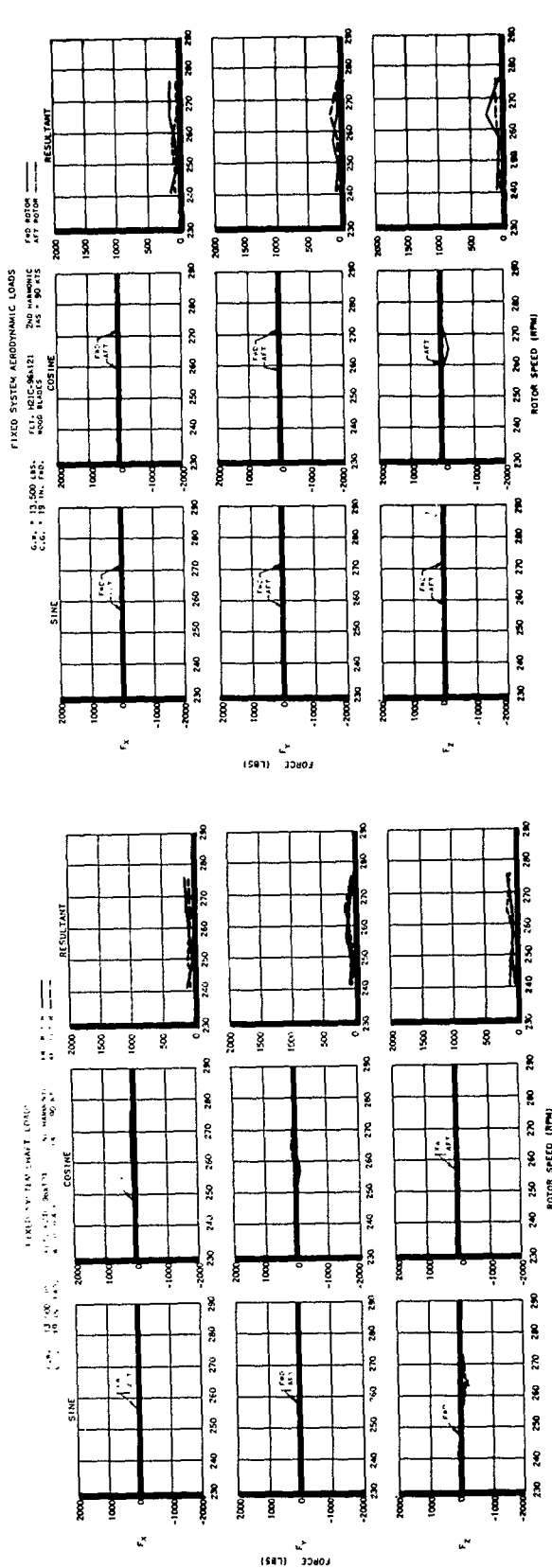


Figure 33 Fixed System Second Harmonic Loads  
 rpm Sweep at 90 Knots

### Third Harmonic Fixed System Loads

With a three bladed helicopter, third harmonic vibration levels are usually the dominant portion of the vibration environment. This section presents third harmonic fixed system loads measured on the H-21, along with second and fourth harmonic rotating shaft loads from which the third harmonic in-plane loads derive.

Figures 34 through 40 give the third harmonic fixed system loads and the related second and fourth harmonic rotating loads. In particular,

<u>Harmonic</u>	<u>Figure No.</u>		
	<u>Airspeed</u> <u>Sweep</u>	<u>40 Knot</u> <u>RPM Sweep</u>	<u>90 Knot</u> <u>RPM Sweep</u>
3 $\Omega$ Fixed System	34	35	36
2 $\Omega$ Rotating System	37	38	38
4 $\Omega$ Rotating System	39	40	40

The 3  $\Omega$  airspeed sweeps show that shaft load resultant magnitudes average,

<u>Rotor</u>	<u>F<sub>x</sub> lb</u> <u>Longitudinal</u>	<u>F<sub>y</sub> lb</u> <u>Lateral</u>	<u>F<sub>z</sub> lb</u> <u>Vertical</u>
Forward	800	250	200
Aft	1300	500	400

The longitudinal loads are easily the largest, and the aft rotor loads are larger than those at the forward rotor. This is particularly marked at 60 knots where the aft load is almost three times the forward load. No clear general trend with airspeed is evident in Figure 34, but the resultant longitudinal forward rotor load variation is typical of measured airspeed vibration data for the H-21 which is normally low in hover, high at 20 knots transition from hover to forward speed, low near 60 knots cruise speed, and finally exhibits a steep increase with forward speed to the 105 knot maximum speed reached in these tests. Both the sine and cosine components are low in hover but increase to large negative values at 20 knots; the cosine stays nearly constant with further airspeed increases, while the sine drops to a near zero magnitude from 60 to 80 knots and then rapidly increases to a large positive value at 105 knots. The vertical forces surprisingly peak at 60 knots on the aft rotor, however the forward rotor vertical has a minimum in this speed region and shows a rapid, fairly steep rise to 105 knots. "Aerodynamic loads" in Figure 34 are obtained by separating fuselage induced rotor inertia loads from the total measured shaft loads. Longitudinal load,  $F_x$ , is most affected by the inertia adjustment, with the aerodynamic resultants being higher than the shaft loads. The aft rotor longitudinal load is raised by this adjustment from 1300 lb average to nearly 2000 lb. Slight changes occur in the trends with airspeed for the other loads but the magnitudes are little affected.

The rotor speed sweeps at 40 knots and 90 knots indicate an extremely rapid load buildup with rpm for longitudinal load at both rotors and for vertical load at the aft rotor. The sine component is largely responsible for this trend at 40 knots, while both the sine and cosine contribute at 90 knots. Aft rotor longitudinal load was nearly twice as large as the corresponding forward rotor load. Forward rotor vertical load is less sensitive to rotor speed, and in fact shows a slight downward trend with speed.

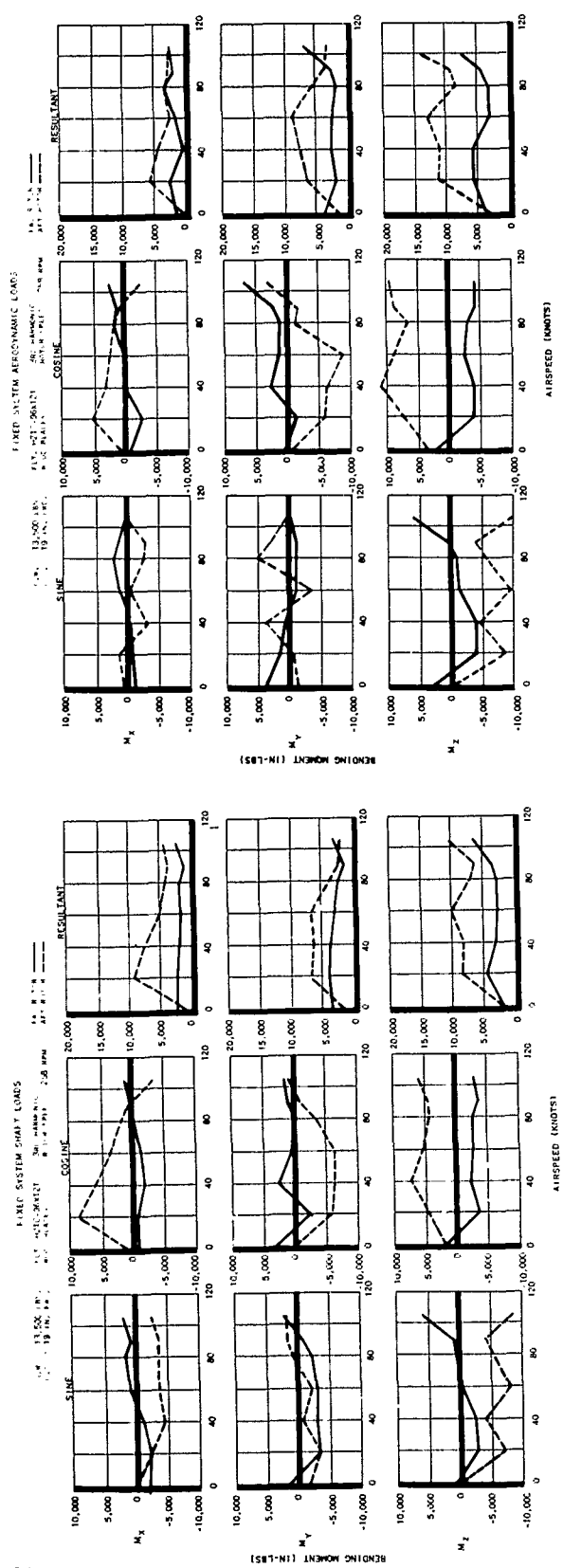
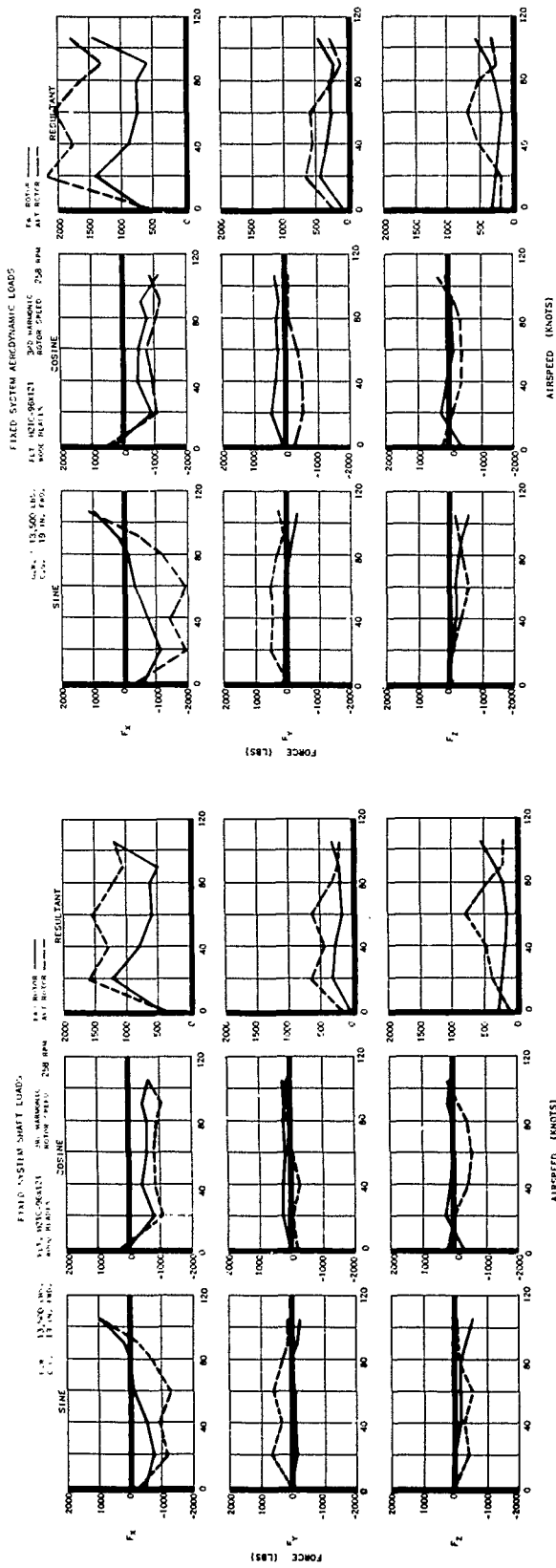


Figure 34 Fixed System Third Harmonic Loads  
 Airspeed Sweep at 258 rpm

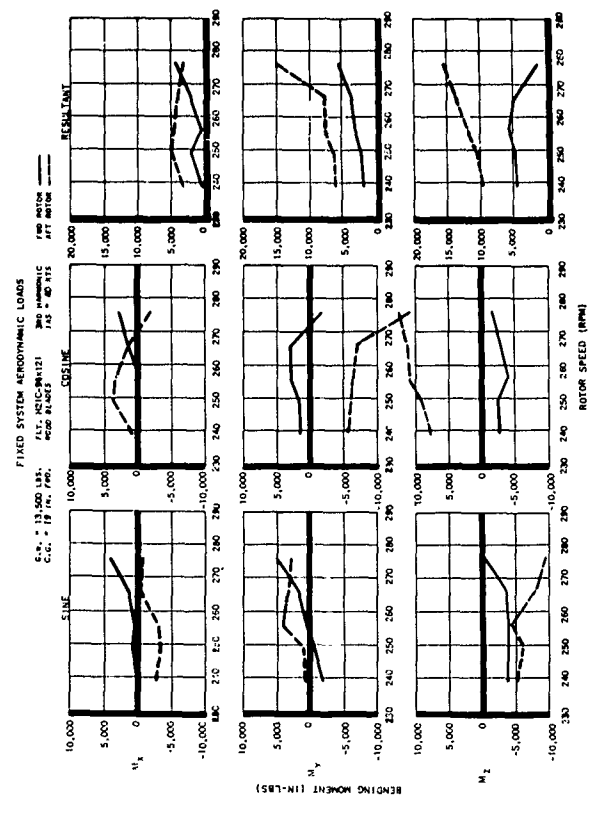
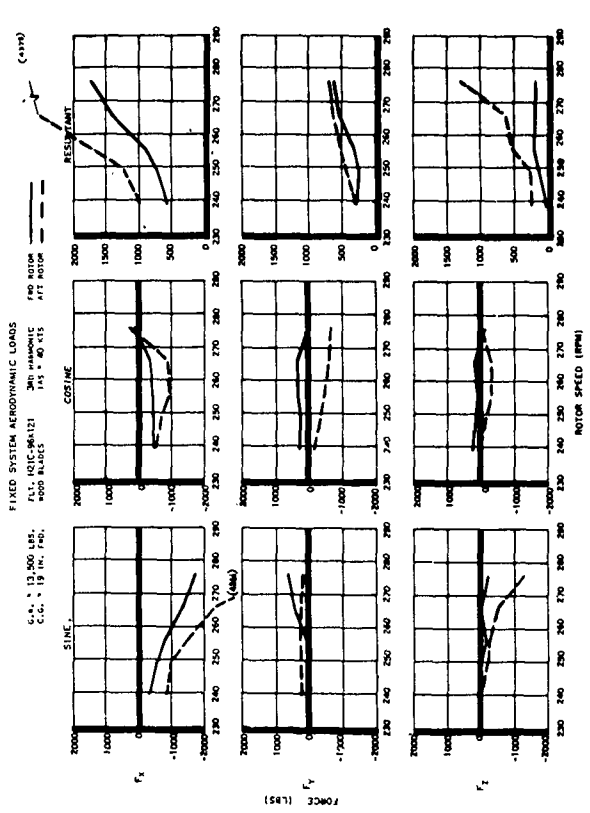


Figure 35 Fixed System Third Harmonic Loads  
 rpm Sweep at 40 Knots

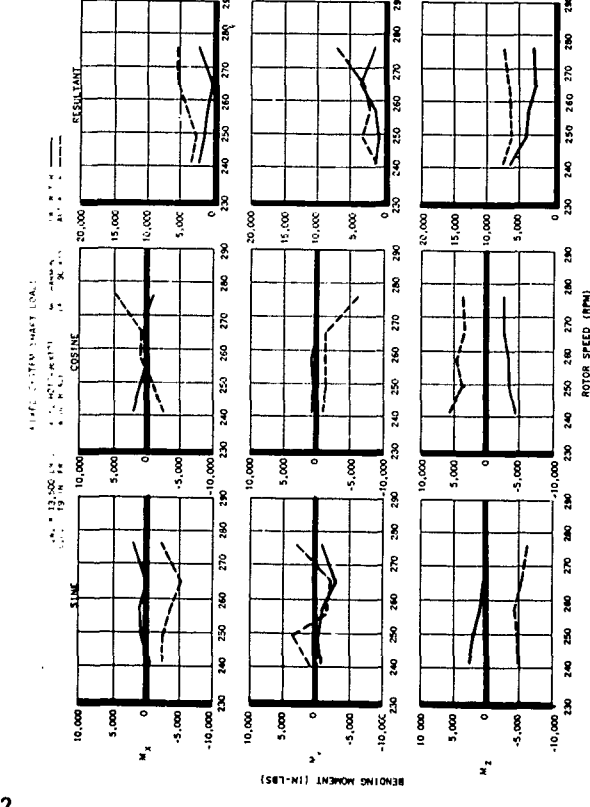
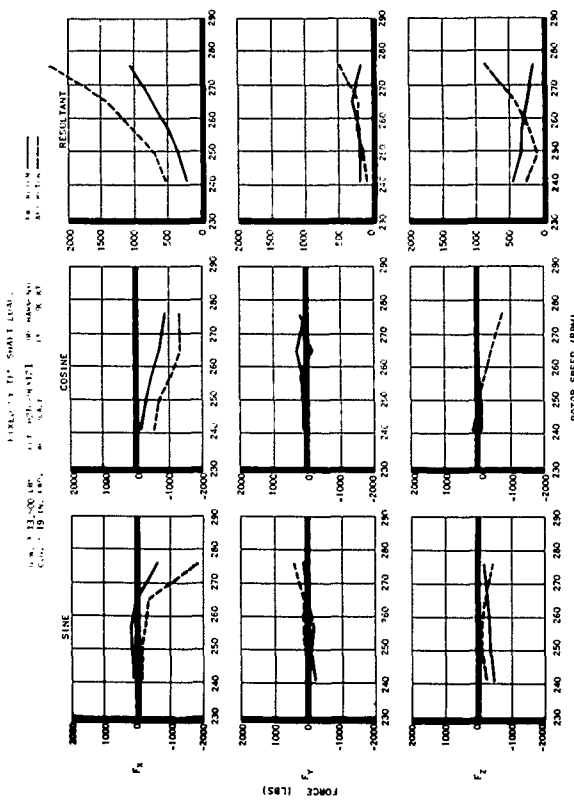
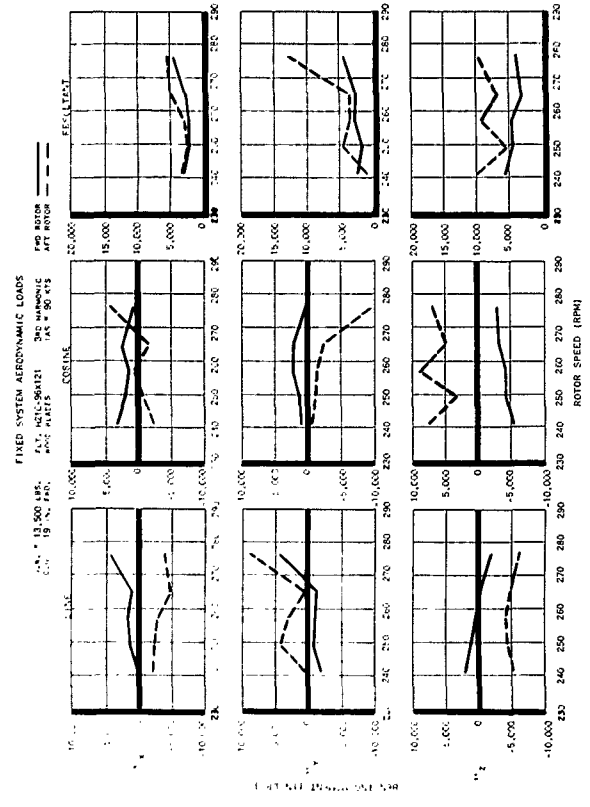
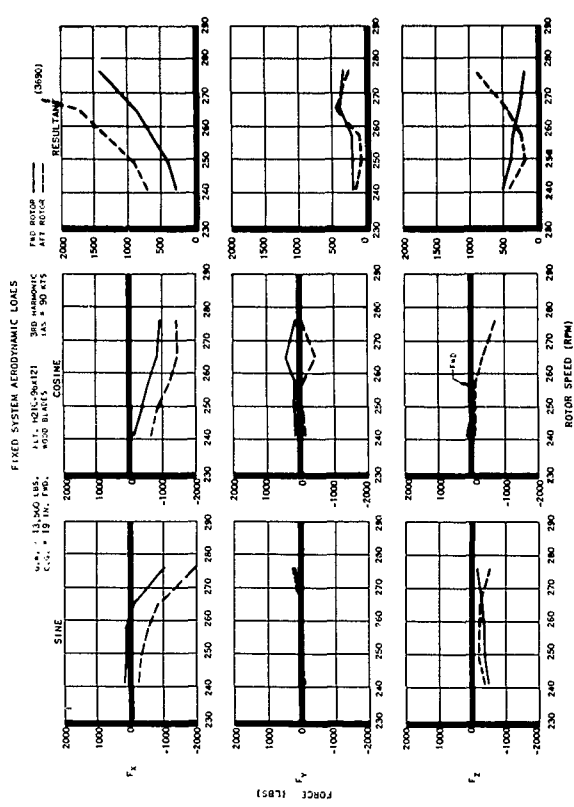


Figure 36 Fixed System Third Harmonic Loads  
rpm Sweep at 90 Knots

Third harmonic vertical loads arise from direct addition of third harmonic blade root vertical shears. Third harmonic in-plane loads come from second and fourth harmonic blade root horizontal shears. The blade root loads combine in the rotating system to form the shaft loads which were measured by the strain gages. These rotating  $F_x$  and  $F_y$  loads are then combined as follows to form third harmonic fixed system loads.

$$F_{x3} = 1/2 (F_{x2c} + F_{y2s} + F_{x4c} - F_{y4s}) \cos 3\Omega t \\ + 1/2 (-F_{y2c} + F_{x2s} + F_{y4c} + F_{x4s}) \sin 3\Omega t$$

$$F_{y3} = 1/2 (F_{y2c} - F_{x2s} + F_{y4c} + F_{x4s}) \cos 3\Omega t \\ + 1/2 (F_{x2c} + F_{y2s} - F_{x4c} + F_{y4s}) \sin 3\Omega t$$

$F_{x3}$ ,  $F_{y3}$  = third harmonic fixed system longitudinal and lateral loads.

$F_{x2s}$ ,  $F_{x2c}$       second and fourth harmonic rotating sine and cosine  
= in-plane loads acting in the direction of the  
 $F_{x4s}$ ,  $F_{x4c}$       master spline

where

$F_{y2s}$ ,  $F_{y2c}$       second and fourth harmonic rotating sine and cosine  
= in-plane loads acting 90° from the direction of the  
 $F_{y4s}$ ,  $F_{y4c}$       master spline

Figures 37 through 40 present the rotating second and fourth harmonic in-plane loads. The second harmonic resultant loads show a tendency toward the high hover, low cruise characteristic in the forward rotor, but not in the aft rotor. The fourth harmonic airspeed sweep produces relatively constant resultants with, in most cases, a tendency to increase sharply at high forward speeds. Numerical combination of these loads into the fixed system third harmonic loads may be illustrated for the forward rotor at 20 knots.

#### Longitudinal Fixed System Load

$$F_{x3} = 1/2((-510) + (-438) + (-340) - (338)) \cos 3\Omega t \\ + 1/2 (-(515) + (-497) + (-234) + (-232)) \sin 3\Omega t \\ F_{x3} = -814 \cos 3\Omega t - 739 \sin 3\Omega t$$

#### Lateral Fixed System Load

$$F_{y3} = 1/2 ((515) - (-497) + (-234) + (-232)) \cos 3\Omega t \\ + 1/2 ((-510) + (-438) - (-340) + (338)) \sin 3\Omega t \\ F_{y3} = 273 \cos 3\Omega t - 135 \sin 3\Omega t$$

These third harmonic resulting combinations can be checked against the values plotted in Figure 34. It is of interest to note certain similarities among the second harmonic airspeed sweep curves in Figure 37. The  $F_x$  sine curve of the forward rotor is the negative of the  $F_y$  cosine curve; the  $F_y$  sine curve is the same as the  $F_x$  cosine curve of the forward rotor. The aft rotor shows similar characteristics, however the pattern differs in sign relation because of the opposite direction of shaft rotation. The fourth harmonic airspeed sweep illustrates its own pattern. The  $F_x$  sine curve is the negative of the  $F_x$  cosine curve.

$$\begin{array}{llll} F_{y2c} = 515 & F_{x2c} = -510 & F_{x4c} = -340 & F_{y4c} = -234 \\ F_{x2s} = 497 & F_{y2s} = -438 & F_{y4s} = 338 & F_{x4s} = -232 \end{array}$$

In this instance, three comparisons are quite close, while the fourth -510 to -438 is not too close due possibly to an unfavorable combination of measurement errors. Not all of the numbers are quite this close, however, the pattern is apparent.

$$\begin{array}{ll} F_{x2s} = -F_{y2c} & F_{x4s} = F_{y4c} \\ F_{y2s} = F_{x2c} & F_{y4s} = -F_{x4c} \end{array}$$

In the numerical example above, the second and fourth harmonic rotating loads are additive in forming the longitudinal fixed system third harmonic load, subtractive in forming the lateral fixed system harmonic load, hence longitudinal loads are in almost all instances larger than lateral loads. Further, the second harmonic loads are generally larger than the fourth harmonic loads.

The same similarity patterns between longitudinal and lateral second and fourth harmonic loads are also evident in the rpm sweeps. As a consequence of the pattern, both  $F_x$  and  $F_y$  rotating resultants for any individual airspeed or rpm sweep are nearly identical within the accuracy of the data. At low rpm the second harmonic is generally larger than the fourth harmonic, but as rpm is increased the difference tends to be masked by the extremely rapid load buildup.

While not as clear as the patterns discussed previously, there is also an apparent relation between second harmonic rotating in-plane loads and third harmonic vertical loads. Consider the 40 knot rpm sweep in Figure 38. The second harmonic rotating load set  $F_x$  sine or its equivalent  $F_y$  cosine, bear a resemblance to third harmonic  $F_z$  sine; similarly  $F_{y2s}$  and its equivalent  $F_{x2c}$  resemble  $F_{z3c}$ . Limited third harmonic comparison data at 14,685 lb gross weight is shown in Figure 41, an rpm sweep at 90 knots.

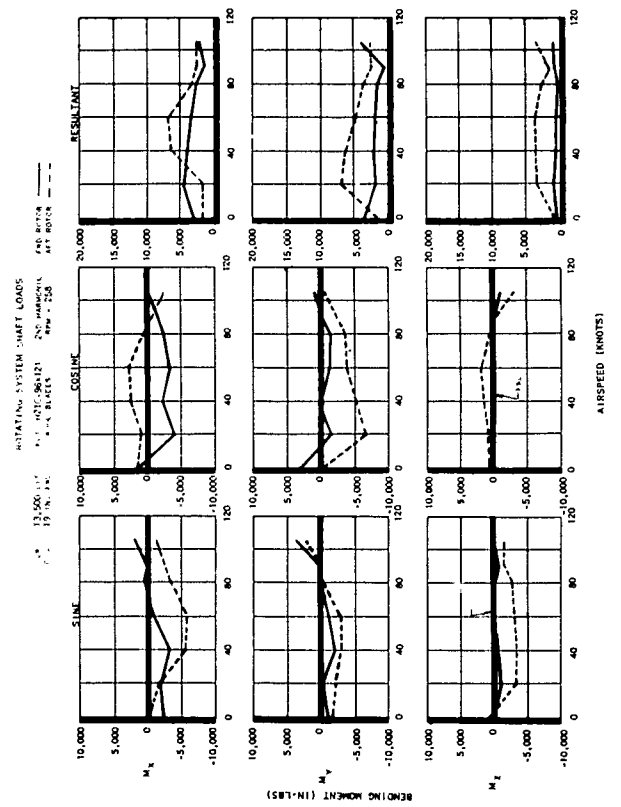
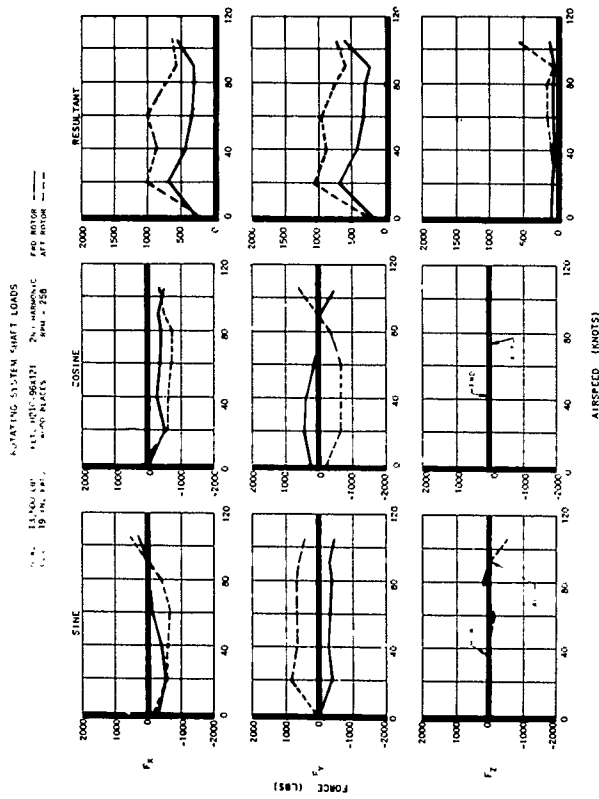


Figure 37 Rotating System Second Harmonic Loads  
Airspeed Sweep at 258 rpm



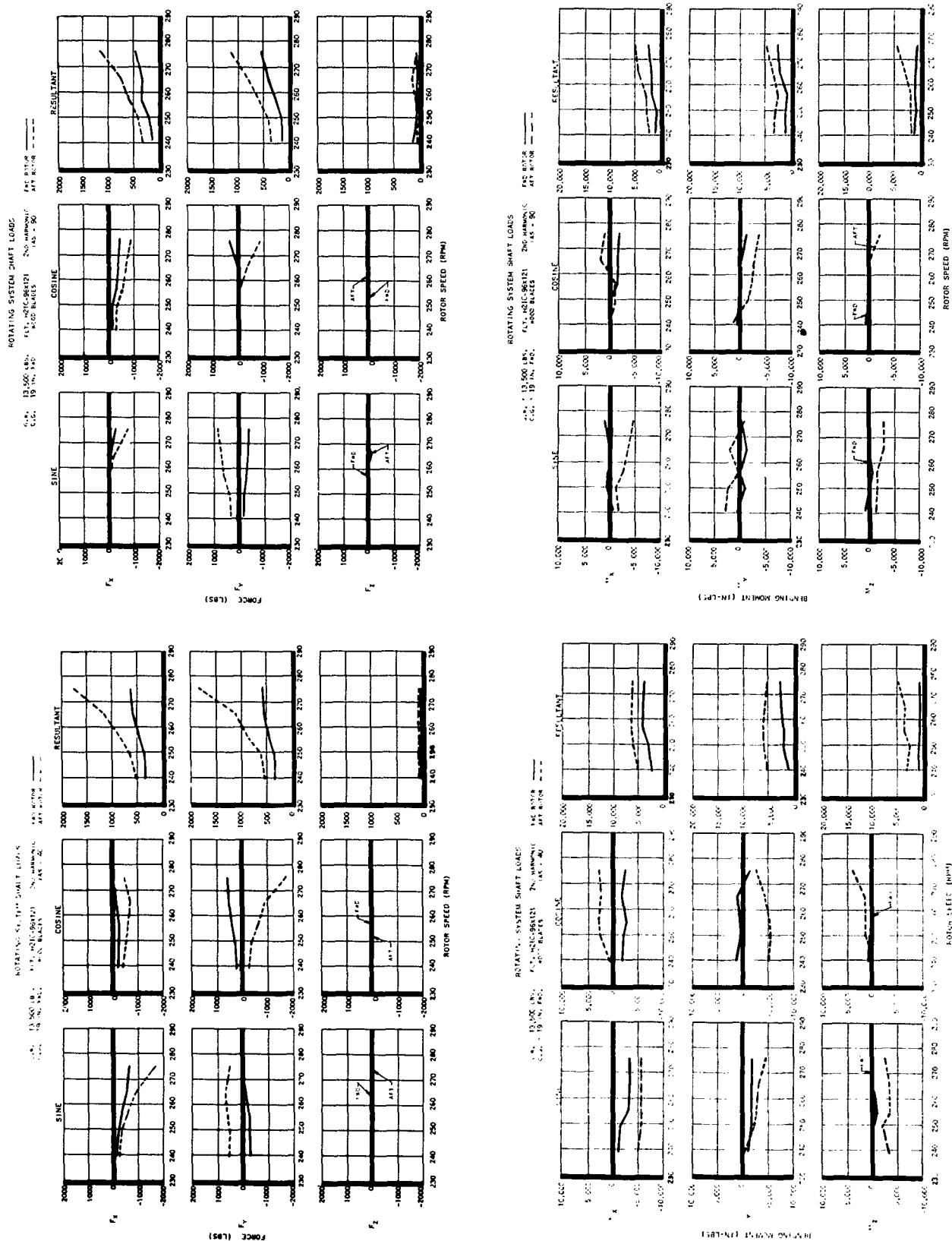


Figure 38 Rotating System Second Harmonic Loads  
rpm Sweep at 40 and 90 Knots

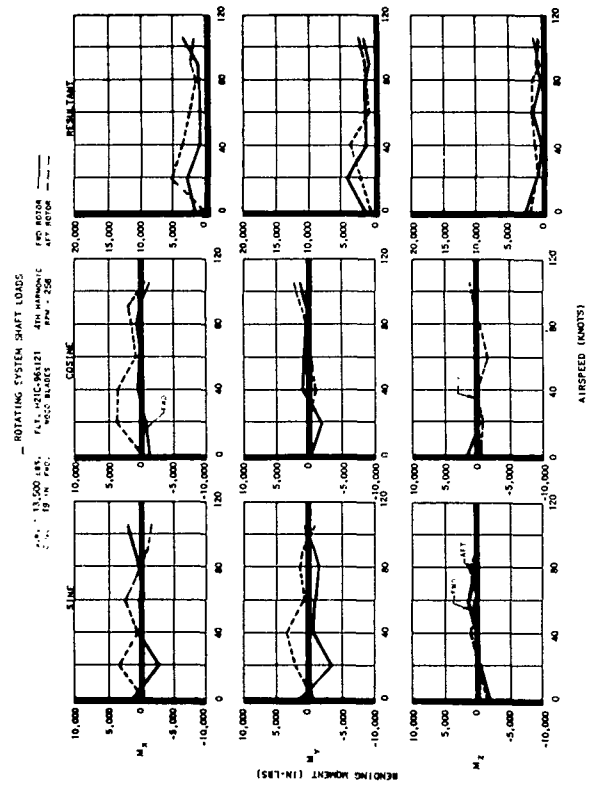
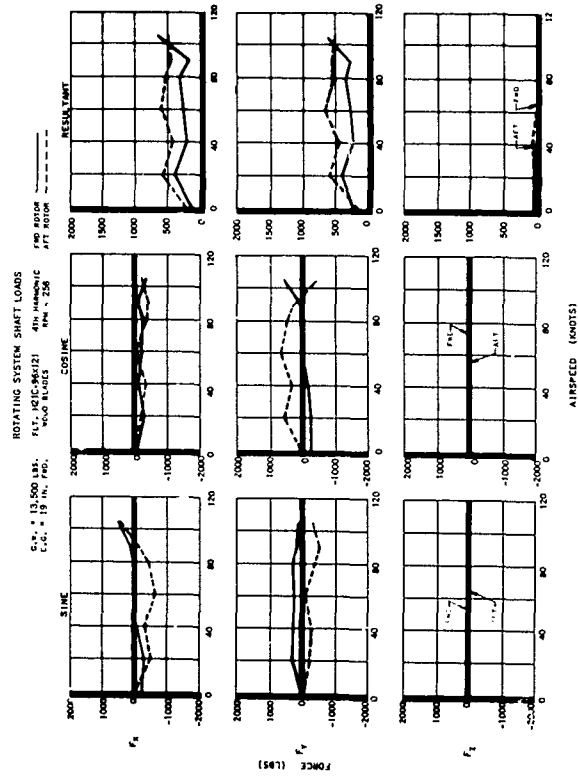
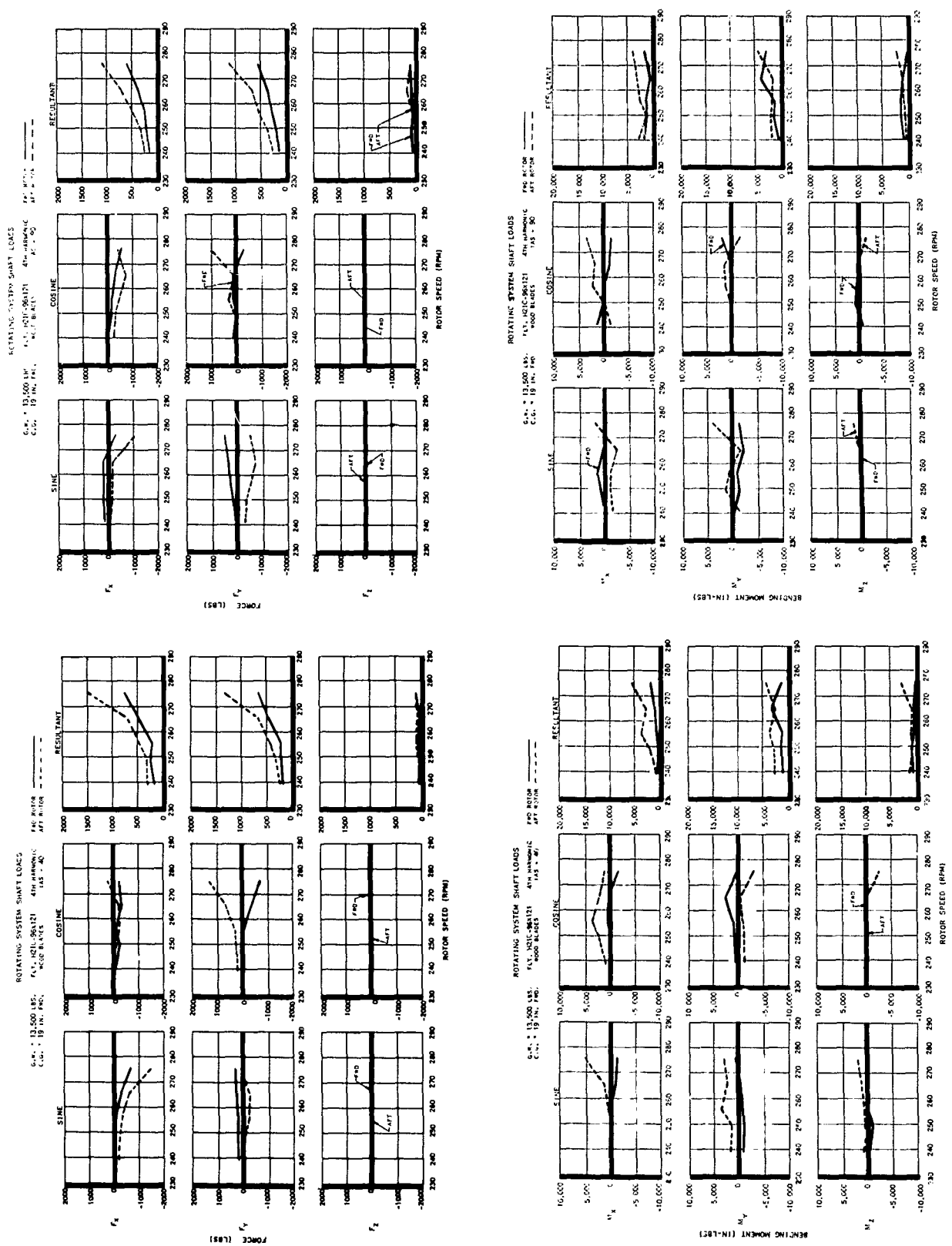


Figure 39 Rotating System Fourth Harmonic Loads  
 Airspeed Sweep at 258 rpm



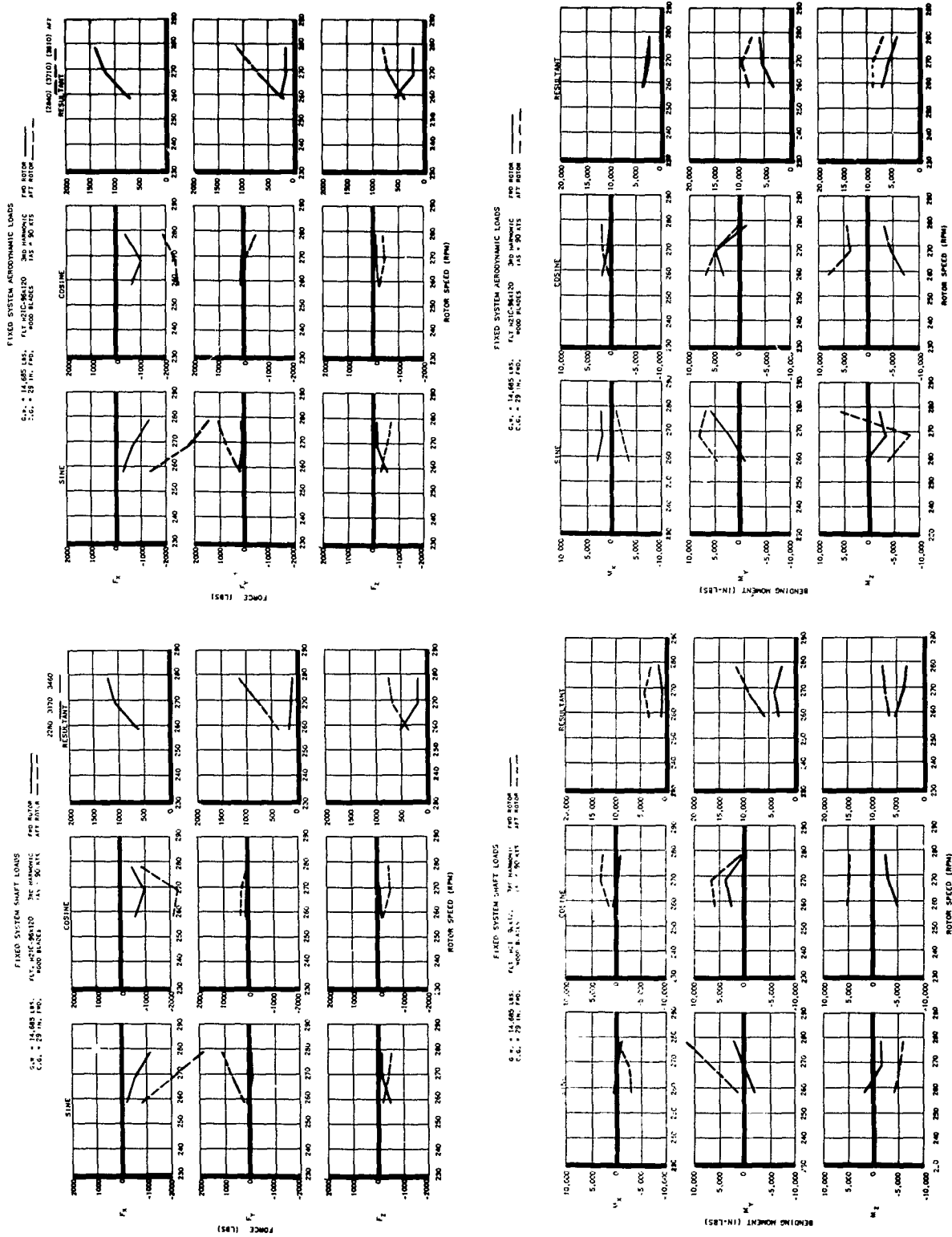


Figure 41 Fixed System Third Harmonic Loads rpm Sweep at 90 Knots, 14,685 lb

#### E. Correlation of Hub Loads and Vibration Measurement

Accelerometers at the rotor hubs and velocity pickups in the fuselage provided data which was reduced to forward and aft rotor motions and cockpit floor motion. This motion data was recorded in order to study the fuselage motion coincident with the measured loads so as to gain further insight into the forced response characteristics of the fuselage. As mentioned previously, with a three bladed rotor, third harmonic vibration levels are generally the dominant portion of the vibration environment, so that a comparison of forces and motions in this harmonic is made.

Figure 42 presents the third harmonic load-motion plots. The figure is divided into three sections which are (1) airspeed sweep at normal rpm, (2) rpm sweep at 40 knots, and (3) rpm sweep at 90 knots. Columns divide each section into vertical, lateral and longitudinal directions; rows divide the section into resultant loads, cockpit floor motions and rotor hub motions.

First consider the airspeed sweep load-vibration comparison. The load row shows that vertical and lateral loads average 500 lb, and that the longitudinal loads are close to 1000 lb. Longitudinal and lateral load show similar trend patterns with airspeed, low in hover, an increase to transition, and then a drop towards 80 knots and finally a rise near 105 knots. The vertical load trend differs; the forward rotor load is high at hover and high speed, low at intermediate speeds; aft rotor load is just the opposite, peaking at 60 knots. Longitudinal vibration levels generally follow the longitudinal force trend, lateral vibration follows the lateral forces, including a peak at 60 knots corresponding to the aft lateral load. Vertical motion is very high at hover and drops with airspeed. This vertical data, while corresponding exactly in time to the measured forces, is not typical of H-21 vertical airspeed trends which generally look much like the longitudinal motion data. Examination of the record from which this particular run came shows that there was difficulty in stabilizing the run, that is, magnitude differences in both load and motion occur within the run, and the point read happened to be one of the larger levels. Rotor hub motions in both the vertical and longitudinal directions follow the longitudinal load trend, and lateral hub motion follows the lateral load.

The 40 and 90 knot rpm sweeps indicate an increase of all aft rotor loads with rpm. At the forward rotor, longitudinal load increases with rpm while vertical load decreases; lateral has no clear trend. The motion data is characterized by rather large changes in magnitude with rotor speed. Looking first at the rotor hub motions, in-plane lateral and longitudinal amplitudes at both rotors increase with rpm and generally follow their respective load trends. Vertical hub motions do not follow any single load precisely, but are apparently closest to being just the reverse of the vertical load trends.

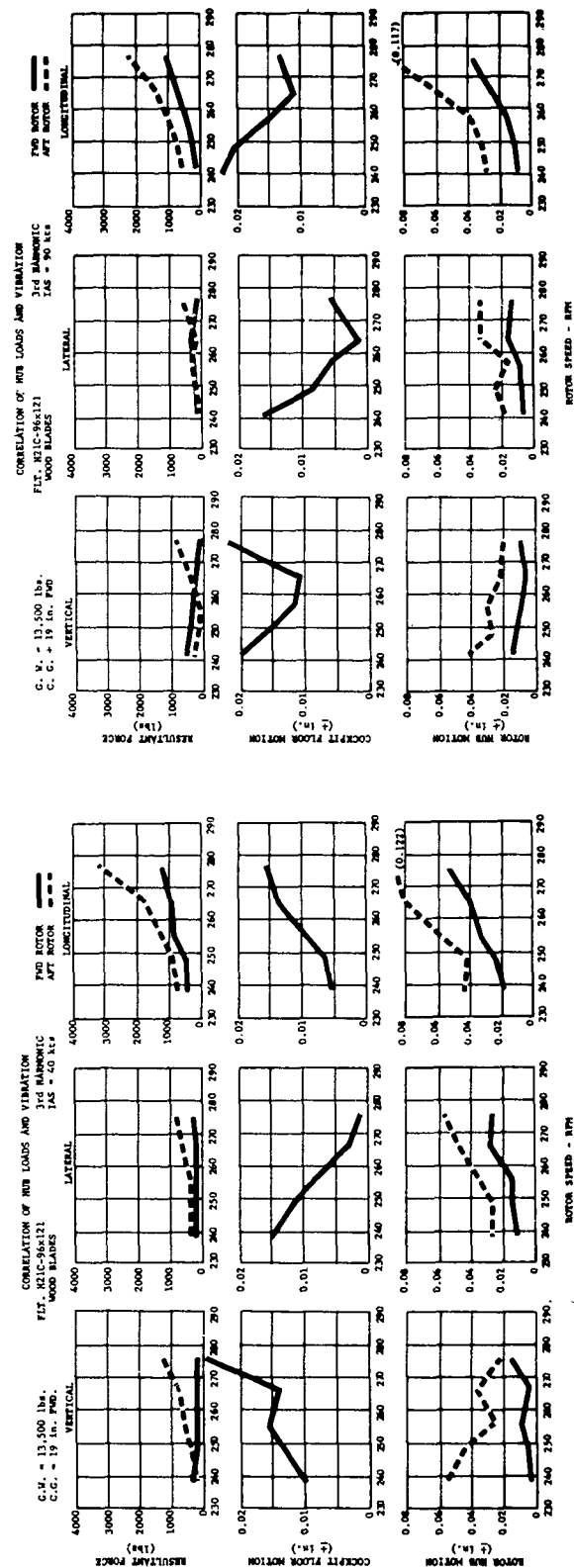
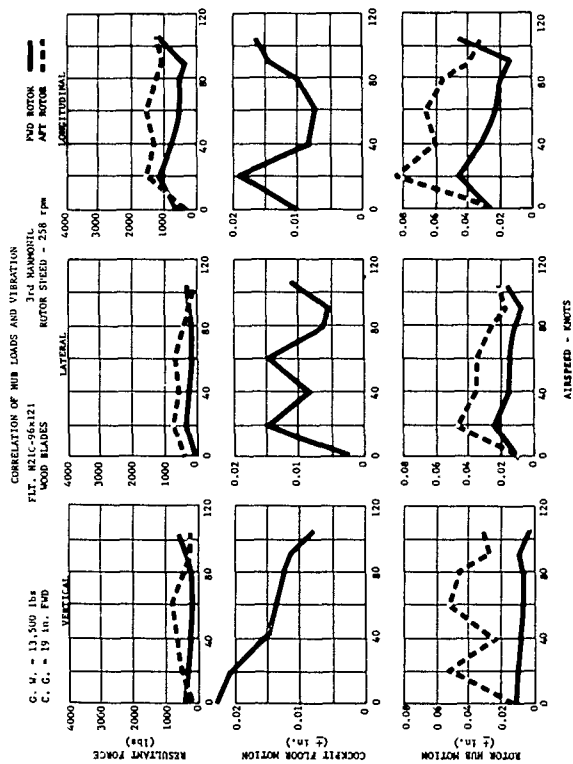


Figure 42 Correlation of Hub Loads and Vibration Measurement

## F. Conclusions

An extensive rotor hub load measurement program has been conducted, giving for the first time a complete picture of all the steady and oscillatory loads acting in the rotor shafts of a tandem helicopter. Shaft strain gage instrumentation was developed, calibrated and flown which had average accuracies of 6% for steady load and 4% for oscillatory load. Cockpit floor motions and shaft motions were measured concurrently to permit correlation of load and vibration data. The helicopter was flown at 13,500 lb gross weight through an airspeed sweep and two rotor sweeps, and at 14,685 lb for a lesser number of points. The data was processed to provide the steady and first four harmonics of rotating loads, and the steady and first three harmonics of fixed coordinate system loads on the fuselage.

The steady loads checked against known data, that is, the total lift at both rotors checked closely against takeoff gross weight, and the torque total agreed with known power requirements. Forward and aft rotor torques were equal in hover, but in forward flight, the aft rotor averaged 2.5 times the forward and the torque differential was shown to be reacted by a measured lateral couple at the two rotors.

First harmonic fixed system results indicated that in-plane loads were of appreciable magnitude but vertical loads were always small. Aft rotor in-plane loads were much larger than the forward, averaging 1,700 lb forward, 250 lb forward, 250 lb aft. At a given rotor, the lateral and longitudinal loads were nearly identical. The first harmonic loads did not show any consistent trend with either airspeed or rotor speed change, but did in a few instances show a load rise from hover to transition. Adjustment for blade inertia loads induced by hub motions made little difference, except in the yaw direction where increases as large as four times occurred.

Second harmonic fixed system loads were generally quite small with loads averaging 100 lb and moments 2500 in. lb. There was a slight load uptrend with airspeed, but little consistent trend with rotor speed. The inertia adjustment made little change to the load levels. These load levels, while small with respect to other harmonics presented here, can nevertheless produce significant vibration levels if a fuselage natural mode is near  $2\Omega$ .

With a three bladed helicopter, third harmonic vibration levels are usually the dominant portion of the vibration environment, so that the third harmonic loads measured here are particularly important. Longitudinal shaft loads were the largest, averaging 800 lb at the forward rotor and 1300 lb at the aft; lateral loads averaged 250 and 500 lb forward and aft respectively; vertical loads averaged 200 and 400 lb forward and aft respectively. Both roll and pitch moments averaged 2500 in. lb at the forward rotor and 5000 in. lb at the aft rotor. The inertia adjustment due to rotor hub motion caused increases as large as 50% in the longitudinal loads, but had little effect on the other directions.

In-plane loads exhibited a trend with airspeed, low in hover, high at 20 knots transition, low at 80 knots cruise, and then a rise toward the top speed at 105 knots. Vertical loads differed; the forward rotor was high at hover and 105 knots, low at 60 knots; the aft rotor was low at hover and 105 knots, and peaks at 60 knots. Rotor speed sweeps at 40 and 90 knots indicated an extremely rapid load buildup with rpm for longitudinal load at both rotors and vertical load at the aft rotor. Lateral loads and the moments were not strongly affected by rpm.

Third harmonic vertical loads arise from direct addition of the vertical components of third harmonic blade root normal flap shears. Third harmonic in-plane loads come from second and fourth harmonic blade root lag shears and from horizontal components of second and fourth harmonic blade root normal flap shears. The measured second and fourth harmonic resultant rotating loads were the same in the longitudinal and lateral directions; in the rotating system these directions refer to the master hub spline azimuth and its perpendicular. The equality of these rotating longitudinal and lateral loads is a proof that the causative blade root shears are harmonically repetitive at each of the three blades. Second harmonic rotating loads averaged 500 lb at the forward rotor; 900 lb at the aft rotor. They displayed a tendency toward the high hover, low cruise, force levels which are characteristic of the fixed third harmonic airspeed sweep, and showed a definite increase with rotor speed. Fourth harmonic rotating loads averaged 250 lb at the forward rotor and 500 lb at the aft rotor. There were moderate changes with airspeed, but large increases with rotor speed. In converting to the fixed third harmonic system, second and fourth add to produce large longitudinal loads and subtract to produce small lateral loads.

An effort at correlation of cockpit floor vibration and rotor loads was made. Longitudinal and lateral vibration levels generally followed the longitudinal and lateral force trends with airspeed, low in hover, an increase to transition, a drop towards 80 knots cruise and an increase at 105 knots. Vertical vibration for the airspeed run recorded was high at hover and dropped with airspeed, so that it did not correlate consistently with any single force.



## SECTION VI

### IN-FLIGHT SHAKE TEST

#### A. General

While shake testing of helicopters has been conducted in the past, these tests with very few exceptions have been restricted to ground tests in which the helicopter is suspended from the rotor heads (or rotor head in the case of single rotor machines) on a soft suspension system with the rotor blades replaced by static weights. This type of testing has provided information regarding the basic natural modes of the helicopter fuselage; however, it can be demonstrated analytically that coupling between the fuselage and the rotating rotor blades produces a completely new set of coupled blade-fuselage modes. The primary purpose of the present program was to obtain natural frequencies and modes which reflected the effects of the rotor system dynamics in order to evaluate the analytical methods used in determining the coupled blade-fuselage modes. An earlier test of a similar type was conducted by NASA on an HUP helicopter and reported in Reference 11.

Due to the presence of rotor induced vibration of the helicopter, two major problems are confronted in conducting an in-flight shake test. First, a controlled source of excitation must be provided which is capable of producing a fuselage response detectable above the background vibration, and secondly, a recording and analysis system is required which can readily reduce the recorded wave form of the fuselage response into its component parts.

In-flight shake tests on H-21C-96, U. S. Army S/N 55-4141, were conducted using a specially designed hydraulic inertia shaker which, at frequencies above 5 cps, was capable of producing an exciting force in excess of 200 pounds. Fuselage and rotor blade responses were obtained from suitable transducers, recorded on magnetic tape, and harmonically analyzed on a Davies Magnetic Tape Analyzer.

#### B. In-Flight Hydraulic Shaker

In order to meet the requirements for a compact lightweight airborne shaker system, a large hydraulic inertia shaker was developed specifically for the present program. While hydraulic shakers as a class are known to have somewhat inferior wave form characteristics, this disadvantage is far outweighed by the advantages of a high force output and a ready source of power in the helicopter.

Essentially the Vertol in-flight shaker, shown in the photograph of Figure 43 consists of a servo-controlled double-acting cylinder with a 100 pound piston which is driven through a sinusoidal displacement relative to the case. Piston displacement from the mid-stroke position is sensed by a linear potentiometer and compared with a sinusoidal driving voltage supplied by a signal generator. The resulting error signal, when amplified, is used to drive a hydraulic servo-valve, which in turn produces a sinusoidal motion of the piston. Since the piston motion relative to the case is sinusoidal, the reaction force at the mounting point of the cylinder must also be sinusoidal.

The amplitude of the piston motion and hence the shaker output force is controlled by varying the amplitude of the driving voltage supplied by the signal generator. Amplitude of the piston motion is monitored for this purpose with a second potentiometer and a precision peak to peak voltmeter.

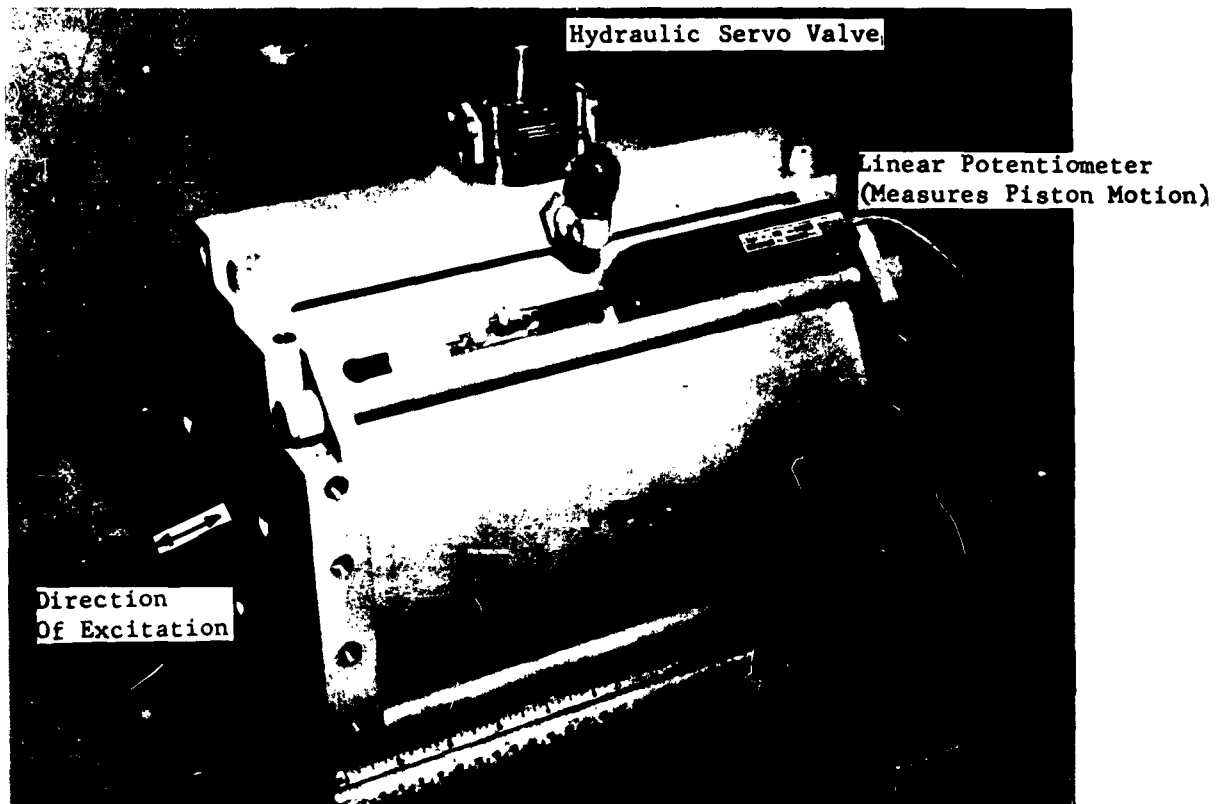


Figure 43 In-Flight Hydraulic Shaker

Photographs of the control console and shaker installation in the helicopter are presented in Figure 44. As shown in the photograph of the shaker installation, the shaker is equipped with a swivel-based trunnion mount to facilitate changes in the shaker orientation.

As stated previously, the in-flight shaker is hydraulically operated; hence, it was necessary to provide a regulated high pressure fluid source in the aircraft installation. Due to the high demand and the cyclic nature of the load, the H-21 rescue hoist system was modified to provide power for the shaker rather than drawing from the helicopter's main hydraulic system. The H-21 hoist system as originally designed uses a fixed displacement axial piston pump driven off the forward rotor transmission. Pump discharge flow is normally bypassed directly to the return system through the hoist control valve which regulates flow to the hoist motor by throttling the bypass flow. Since a fixed displacement pump is not suitable for use with the shaker, the hoist system was modified by fitting an adapter on the drive pad of the forward transmission which permitted installation of a New York Air Brake 67WA200 pressure compensated variable displacement pump in place of the existing pump, and by connecting the shaker in place of the hoist. The New York Air Brake pump had a capacity of 3.87 gpm at normal rotor speed and was equipped with a modified pressure compensator to reduce the full cutoff pressure from 3,000 to 1,500 psi.

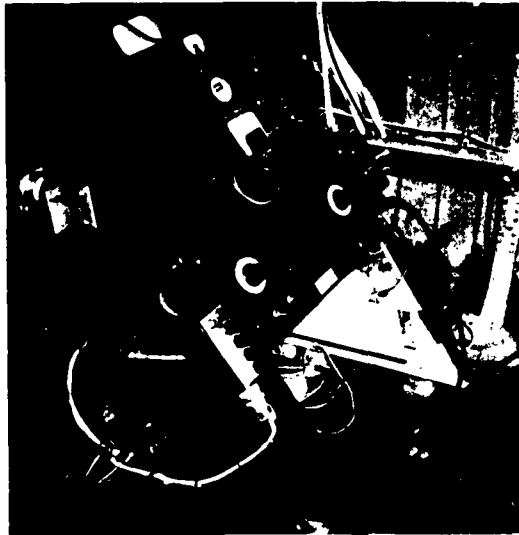
The available force output of the shaker as a function of frequency is controlled by several factors. The upper curve of Figure 45 represents the theoretical maximum force output of the shaker as determined by the piston mass and maximum piston stroke. In practice, however, the force available is governed by such practical considerations as pressure and flow characteristics of the hydraulic power source and the advisability of using only a portion of the full piston stroke to prevent bottoming of the piston during a transient. Based on the above considerations, the practical limit on shaker force for the aircraft installation is approximately as indicated by the lower curve of Figure 45

#### C. Instrumentation, Recording, and Analysis

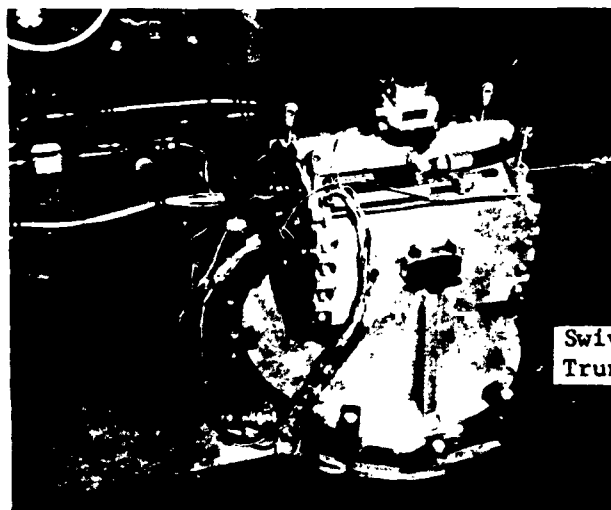
Fuselage vibratory motions were measured with a total of 35 MB Type 124 velocity transducers in conjunction with CEC Type 1-112C linear-integrate amplifiers. Since displacement rather than velocity is the more conventional form for presenting vibration data, all amplifiers were used in the integrating mode. The locations of the fuselage and engine transducers are presented in Figures 46 and 47 respectively. Polarity of the transducers was arranged to provide the sign convention shown. Transducer locations were chosen to provide the best possible definition of the modal shapes without using an excessive number of pickups.

#### Recording System

All in-flight test data was recorded on magnetic tape using a Davies Airborne Tape Recording System Model 585J. Simultaneous oscillograph records were also obtained for editing purposes and as a back-up recording system. A photograph of the airborne tape system is shown in Figure 48. Clockwise from the left are the power supply, an F.M. recording oscillator package, the tape transport, a second F.M. recording oscillator package, a remote control box, a junction box, and the calibration oscillator. The system provides a total of thirteen frequency



Control Console



Swivel Based  
Trunnion Mount

Shaker Installation

Figure 44 Control Console and Shaker Installation

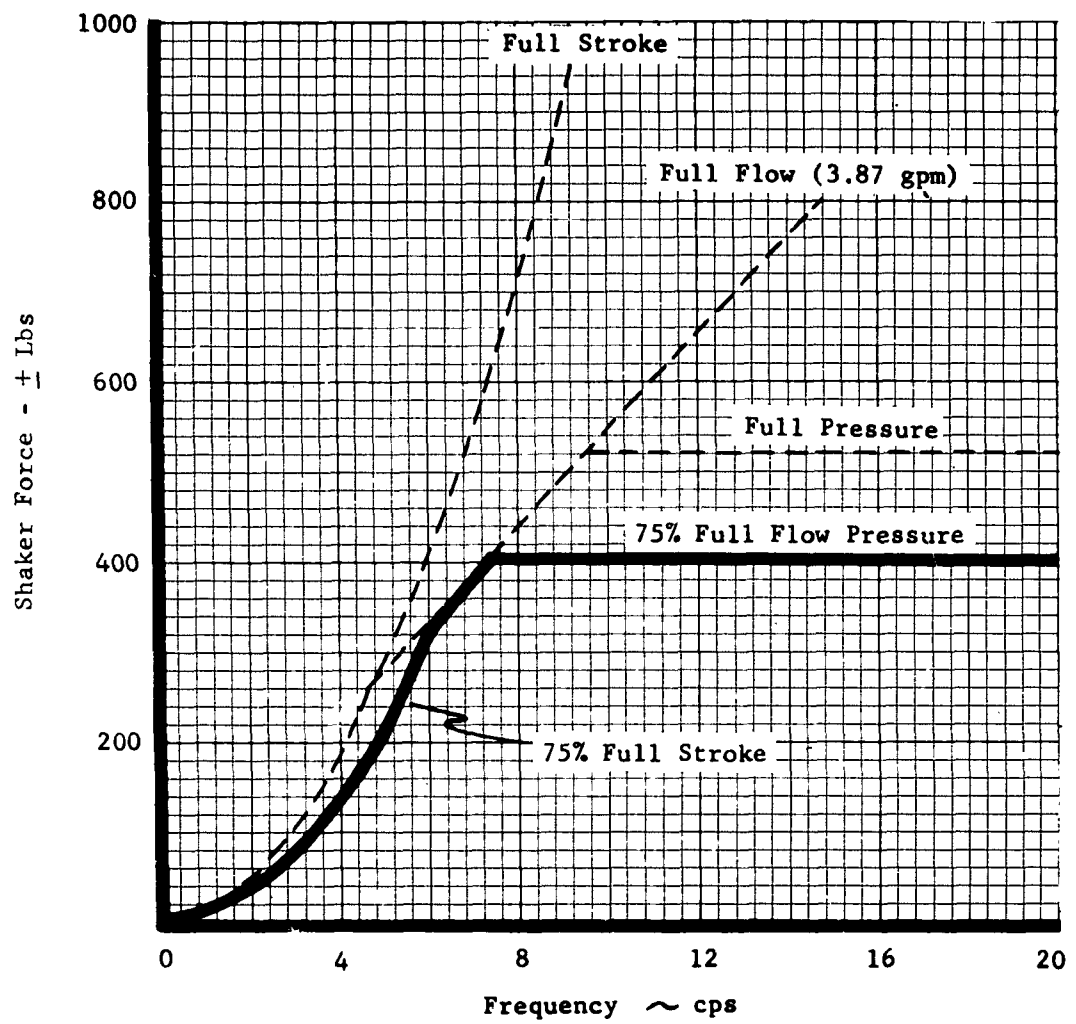
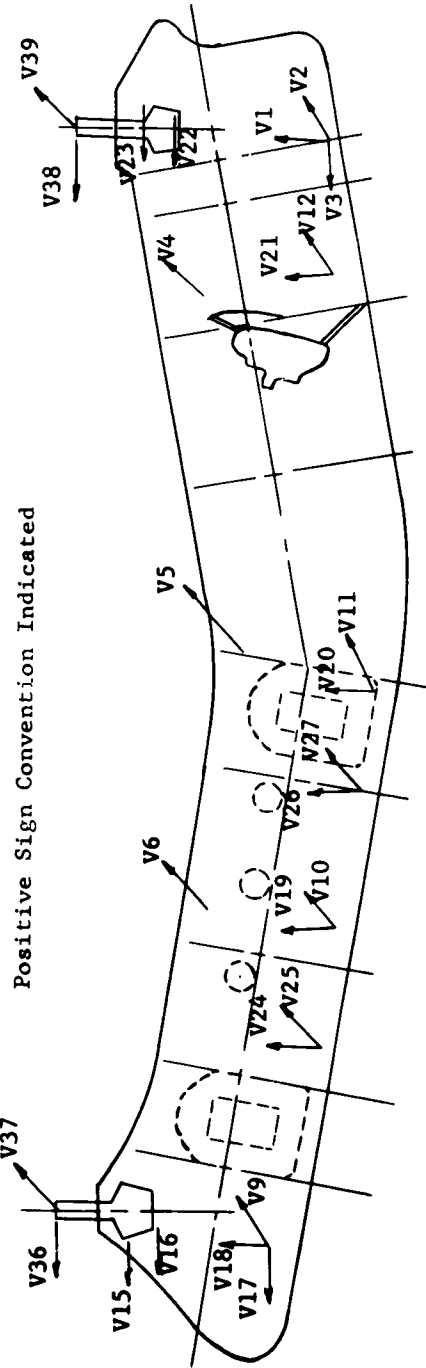
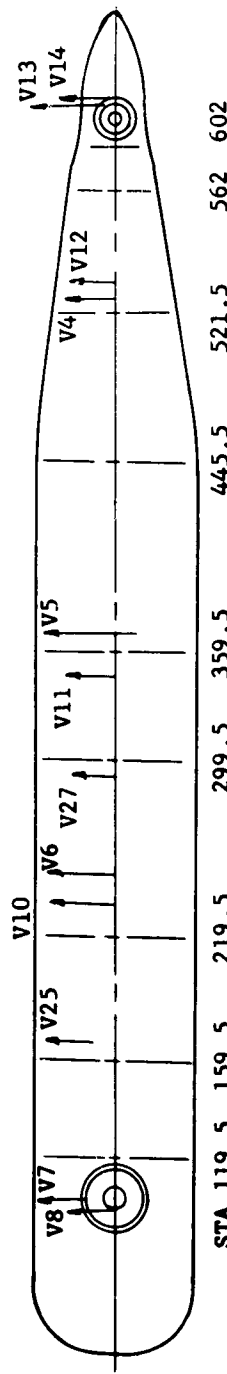


Figure 45 Force Available From In-flight Shaker

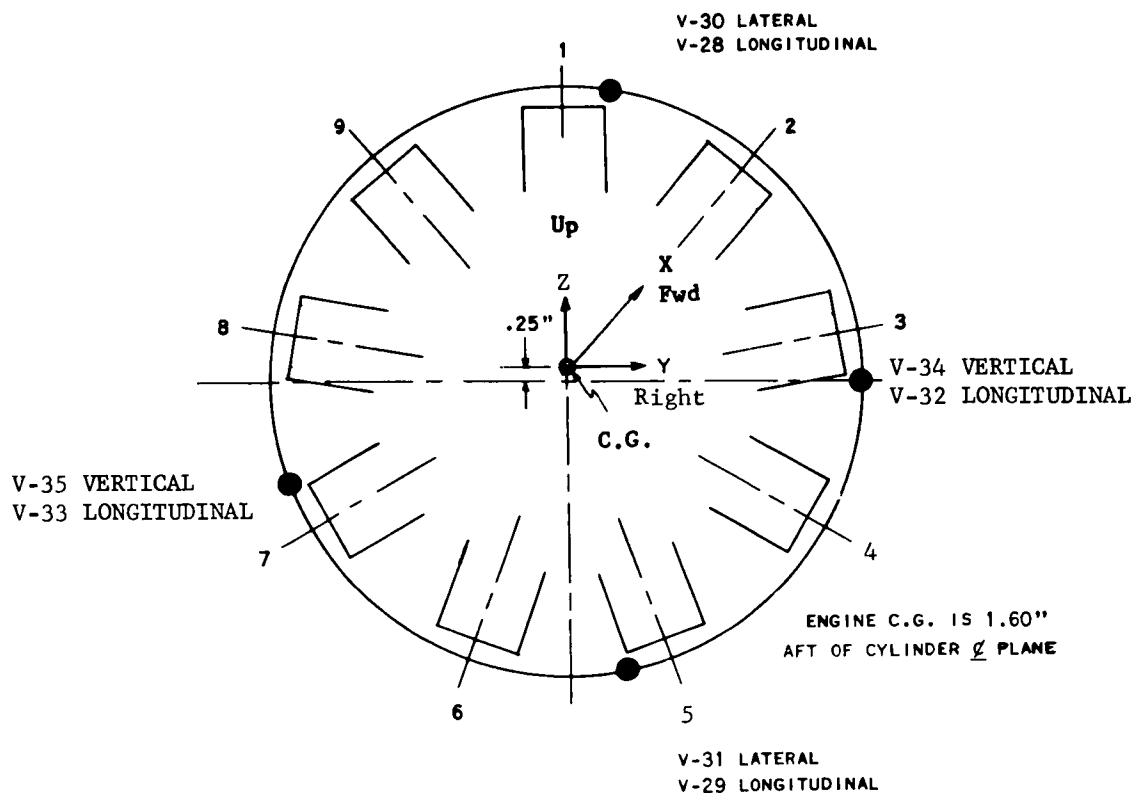


Positive Sign Convention Indicated

PICKUP	STA.	W.L.	B.L.	PICKUP	STA.	W.L.	B.L.	PICKUP	STA.	W.L.	B.L.	DIR.
V-1	602	-50.5	-1	V-12	527	-42	0	V-22	BOTTOM OF AFT XMSN.			LONG.
V-2	602	-52.5	0.5	V-13	BOTTOM OF AFT. XMSN.			V-23	TOP OF AFT. XMSN.			LONG.
V-3	602	-52.5	-1	V-14	TOP OF AFT. XMSN.			V-24	179	-33	12	VERT.
V-4	531	21	-2	V-15	TOP OF FWD. XMSN.			V-25	179	-33	12	LAT.
V-5	359	44	4	V-16	BOTTOM OF FWD. XMSN.			V-26	299	-33	0	VERT.
V-6	241	41	0	V-17	COCKPIT FLOOR			V-27	299	-33	0	LAT.
V-7	TOP OF FWD. XMSN.			V-18	COCKPIT FLOOR			V-36	* FWD. ROTOR HEAD			LONG.
V-8	BOTTOM OF FWD. XMSN.			V-19	239	-33	0	V-37	* FWD. ROTOR HEAD			LAT.
V-9	COCKPIT FLOOR			V-20	354	-33	0	V-38	* AFT ROTOR HEAD			LONG.
V-10	239	-33	0	V-21	527	-42	0	V-39	* AFT ROTOR HEAD			LAT.
V-11	354	-33	0									

\* Pickups for Ground Test Only

Figure 46 Location of Fuselage Motion Transducers



Pickup Locations From C.G., Inches

	v-28	v-29	v-30	v-31	v-32	v-33	v-34	v-35
X	-1.2	-1.2	-1.0	-1.9	-1.2	1.6	-2.2	-1.2
Y	5.8	6.2	7.4	8.7	26.6	-26.8	27.2	-26.2
Z	25.3	-25.6	24.9	-27.1	-1.3	-9.7	-2.7	-7.8

Figure 47 Location of Engine Motion Pickups

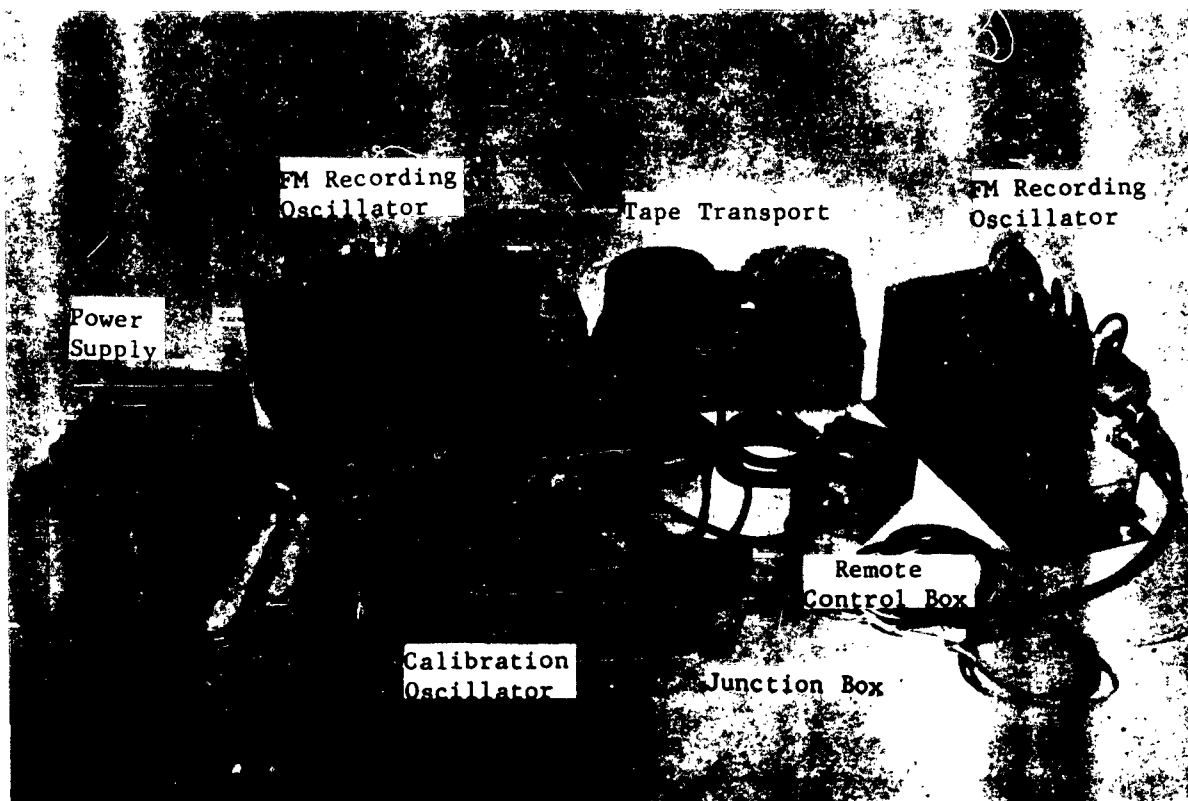


Figure 48 Davies Airborne Magnetic Tape Recorder



modulated data channels which have a flat response from 0 to 60 cps. Recording is by the pulse saturation method. In addition to the data channels, two channels are provided for voice identification and speed compensation respectively. Photographs showing the aircraft installation of the airborne recording equipment, transducer amplifiers, and associated equipment are presented in Figure 49

#### Analysis System

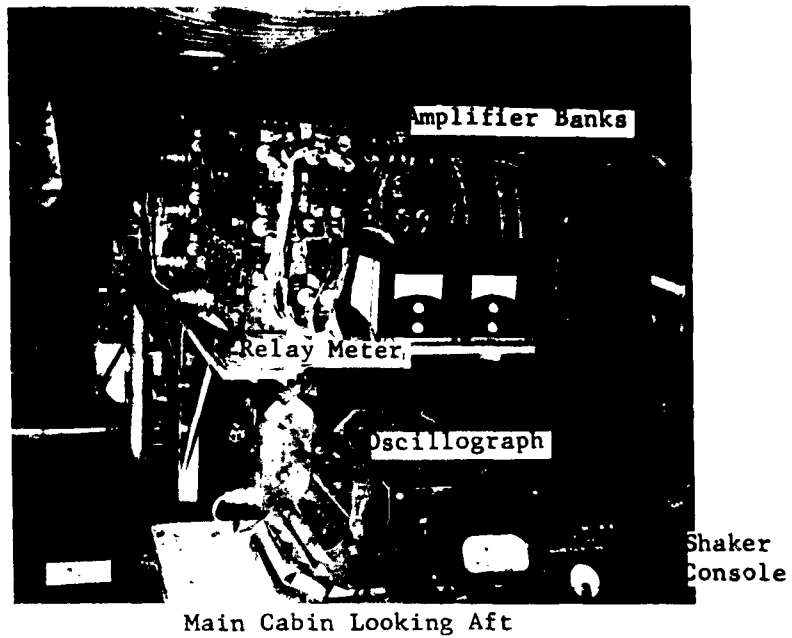
Magnetic tape data from the flight test program was harmonically analyzed on the Davies Magnetic Tape Analyzer. The analyzer system, Figure 50, consists of three major elements: a direct recording unit on which the original tape may be copied two channels at a time, a two-channel, 3-speed playback unit which reproduces the data signal as originally recorded, and a two-channel wave analyzer with recording units which produce a plot of amplitude versus frequency for components of a complex wave form. The wave analyzer utilizes the heterodyne principle in which the multiple frequency incoming signal is mixed with a variable frequency local oscillator to produce a series of beat frequencies which are then passed through a fixed frequency filter tuned to 3,000 cps. Since the beat frequencies generated contain all of the information in the original signal, the amplitude of each of the component frequencies is determined by slowly varying the frequency of the local oscillator so that each of the component frequencies in turn produces a 3,000 cps beat frequency. The filtered signal is rectified and the average RMS value of the filtered signal displayed on the recorder. Selectivity of the analyzer, i.e., ability to discriminate between signals of two different frequencies, is controlled by the bandwidth of the fixed frequency filter and the choice of tape speed. Increasing the tape speed of the playback raises the component frequencies of the input signal and the resulting beat frequencies are farther apart; thus, the ability of the fixed frequency filter to distinguish between two adjacent frequencies is improved. Frequency response of the complete analyzer system is practically independent of the playback speed and flat within  $\pm 5\%$  for real time frequencies from approximately 4 to 60 cps.

Frequency response at selected locations was obtained by reproducing the original flight data on approximately 50-inch loops at the original recording speed of 6 ips. The loops were then played back through the analyzer at the maximum tape speed of 60 ips. Inasmuch as a single known frequency was of interest on any particular record, it was only necessary to analyze a small portion of the frequency spectrum. To aid in identification of the shaker response and detect any response due to rotor or other excitation, each record was scanned over a portion of the spectrum which included the shaker frequency and the nearest rotor harmonic. In order to obtain the best accuracy possible, the shaker frequency was determined from oscillograph records of the shaker piston displacement, while the piston displacement, which was not quite sinusoidal, was obtained from an analysis of the magnetic tape records.

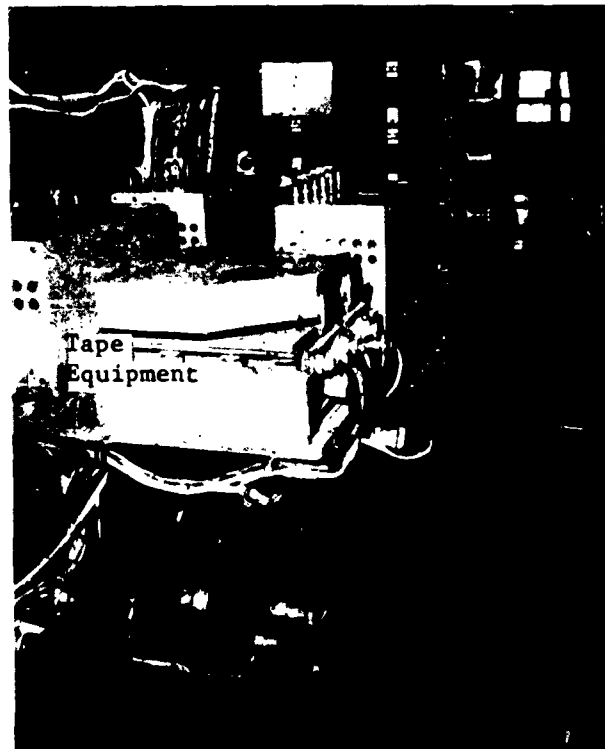
#### D. Results

##### Forced Response Under Vertical and Lateral Excitation

In-flight Frequency Response, Normal Rotor Speed - In-flight response at normal rotor speed is presented in Figures 51 and 52 for lateral and vertical excitation respectively. Response curves present double amplitude motion in inches



Main Cabin Looking Aft



Main Cabin Looking Forward

Figure 49 Test Equipment Installation - Main Cabin

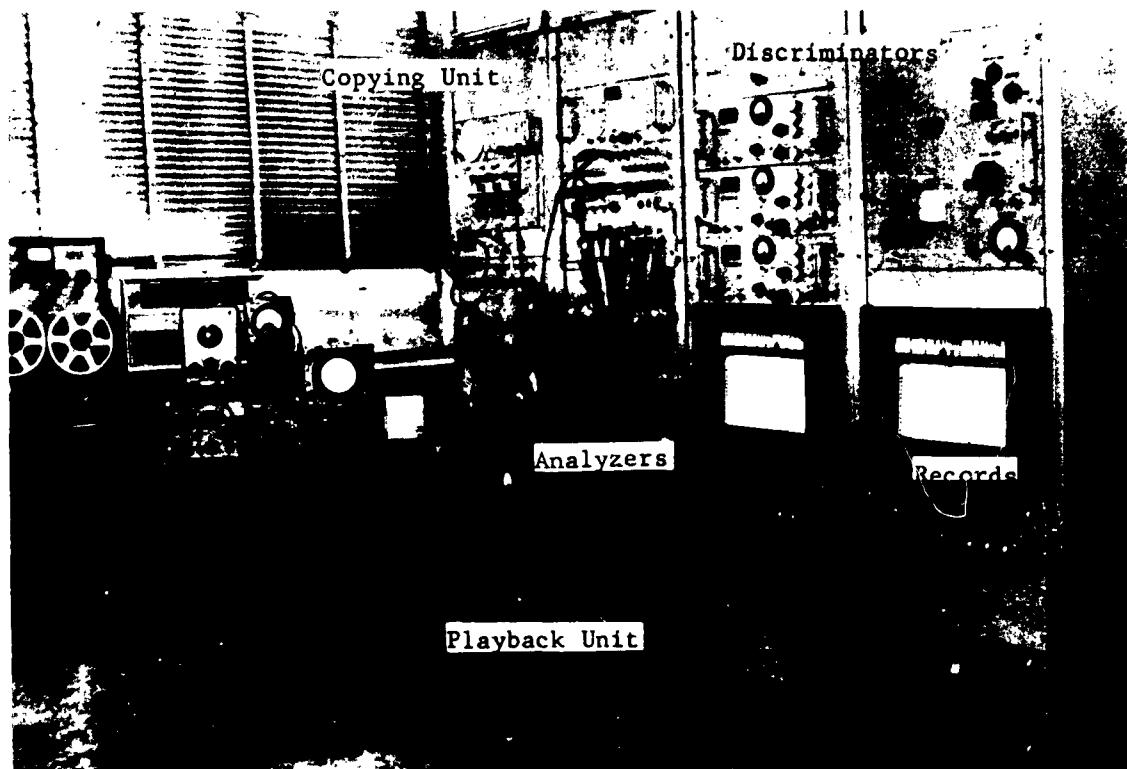


Figure 50 Davies Magnetic Tape Analyzer

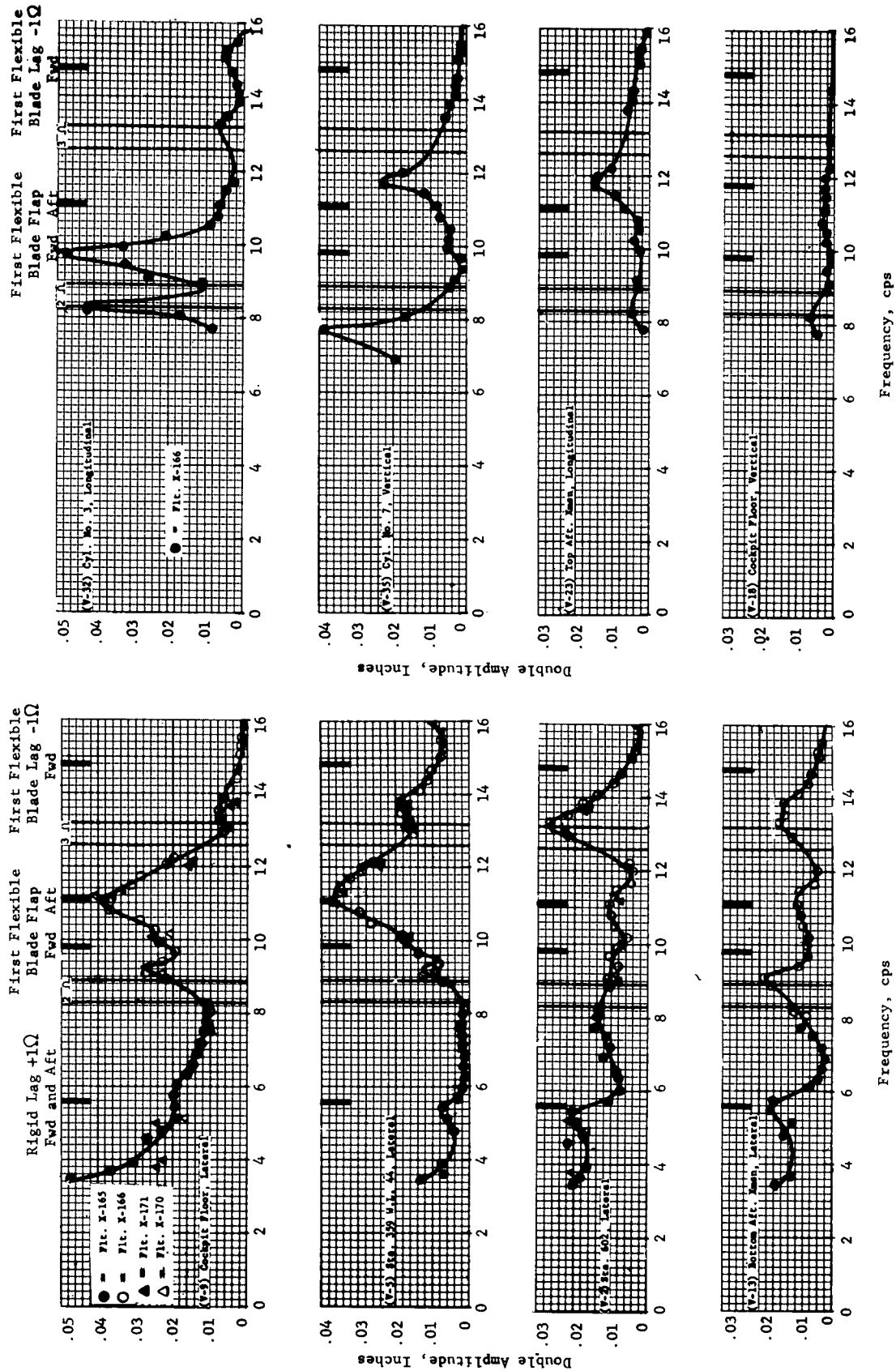


Figure 51 Response at 258 rpm for 200 lb Lateral Force

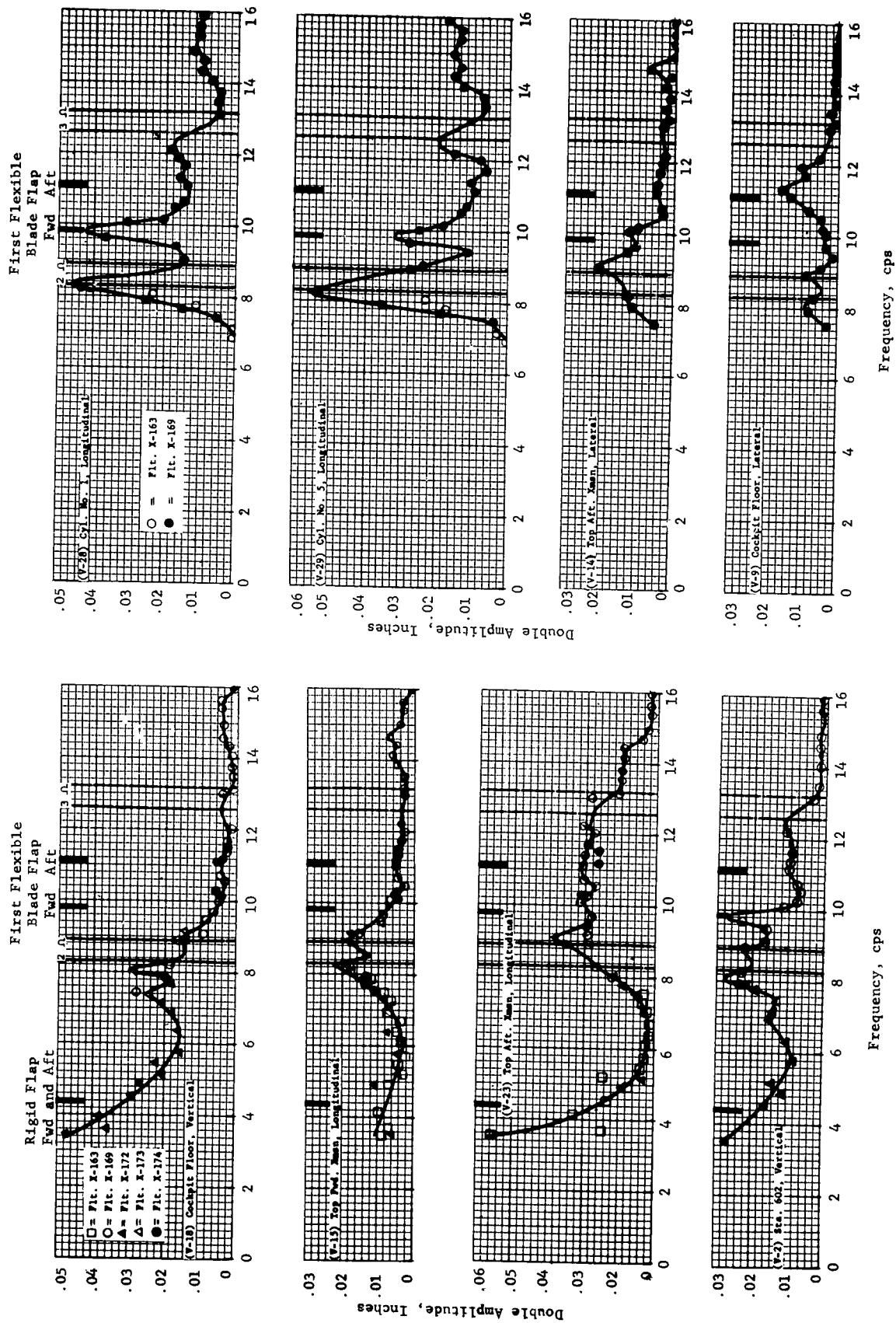


Figure 52 Response at 258 rpm for 300 lb Vertical Force

as ordinate against shaker frequency in cps as abscissa for the pickup locations noted on each curve. The response curves include motions at four critical stations in the direction of excitation, two stations normal to the direction of excitation and two engine pickup stations. Measured data points are shown on the response curves using a different symbol for each flight.

As shown on the curves, the  $2\Omega$  and  $3\Omega$  rotor orders are banded by vertical lines to enclose the frequency region for which flight response data could not be accurately measured. Several data points are within these rotor order bands and appear to be reasonable, but generally the response within the bands was not separable. In the regions between rotor orders the response curves were accurately defined from the data points shown; near the rotor orders with no available data the trends were interpolated from the response data at 240 and 278 rpm.

Comparison of Normal Rotor Speed Data with Ground Tests - Prior to the in-flight shake test, the same fuselage was ground shake tested using the same hydraulic shaker installation. Comparison plots, Figures 53 and 54, permit an evaluation of the effect of multi-directional rotor coupling, blade natural frequencies both chord and flap, and rotor damping. To prepare the comparison, measured in-flight response from vertical excitation was proportioned downward linearly from the 300 lb shaker force level used in flight to the 200 lb level used in the ground test.

As an aid in the interpretation of the test results, it is useful to consider the calculated natural frequencies of the rotor blades. The H-21 has a fully articulated rotor system with all metal, 22 ft., 18 in. chord blades. A 20 lb weight restrained by a strap in the hinge is located at 50% span in each forward rotor blade as a natural frequency control device. The aft blades do not contain these weights. In the flap direction there is a characteristic rigid body natural frequency close to rotor speed,  $1\Omega$ , a fundamental bending mode near  $2.5\Omega$ , and a second bending mode near  $5\Omega$ .



Rigid Body Flap  
Fwd.  $1.02\Omega$   
Aft  $1.02\Omega$

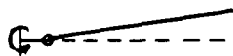


Fundamental Bending  
Fwd.  $2.28\Omega$   
Aft  $2.59\Omega$



Second Bending  
Fwd.  $4.8\Omega$   
Aft  $4.93\Omega$

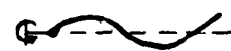
In the lag direction, the blade modes are:



Rigid Body Lag  
Fwd.  $0.30\Omega$   
Aft  $0.30\Omega$



Fundamental Bending  
Fwd.  $5.3\Omega$   
Aft  $5.3\Omega$



Second Bending  
Fwd.  $13.65\Omega$   
Aft  $13.65\Omega$

These rotating natural modes couple to the fuselage in the fixed system of the fuselage body. Flapwise blade frequencies are felt in the fixed system directly at the same frequency, but chordwise blade frequencies are felt in the fixed system at frequencies  $1\Omega$  above the  $1\Omega$  below that in the rotating system. Blade frequencies vary with rotor speed, so that it is necessary to calculate them over the range of normal operation.

The following table summarizes the blade frequencies that are pertinent to a review of the in-flight shake test results:

Fixed System Rotor Blade Frequencies, cps

<u>Rotor</u>	<u>Rotor Speed</u>	<u>Rigid Flap</u>	<u>Fundamental Flap Bending</u>	<u>Rigid Lag + Rotor Speed</u>	<u>Fundamental Lag Bending - Rotor Speed</u>
Fwd	240	4.1	9.2	5.2	14.8
	258	4.4	9.8	5.6	14.8
	278	4.7	10.4	6.0	14.8
Aft	240	4.1	10.4	5.2	17.5
	258	4.4	11.1	5.6	17.5
	278	4.7	11.8	6.0	17.5

For further background the uncoupled ground shake test results for the engine are,

<u>Direction</u>	<u>Frequency, cps</u>
Roll	7.43
Longitudinal - Pitch	8.40
Yaw	9.67
Lateral - Yaw	12.12
Vertical	12.14
Longitudinal	15.44

Figures 53 and 54 contain a comparison of ground and flight data for lateral and vertical shaker excitation respectively. Data is given at the forward transmission, cockpit floor, cabin ceiling at Sta. 359, the engine, aft keel at Sta. 602 and the aft transmission. A review of these comparisons can be summarized as a group of major and minor peak responses as follows:

Vertical Shaker (Figure 54)

Lateral Shaker (Figure 53)

<u>Pickup</u>	<u>In-flight, cps</u>	<u>Ground, cps</u>	<u>Pickup</u>	<u>In-flight, cps</u>	<u>Ground, cps</u>
Forward		4.5			
Xmsn	8.5 *	8.2 *			
Long.	11.1	11.8			
Page 91	12.5	13.1			
	14.7				

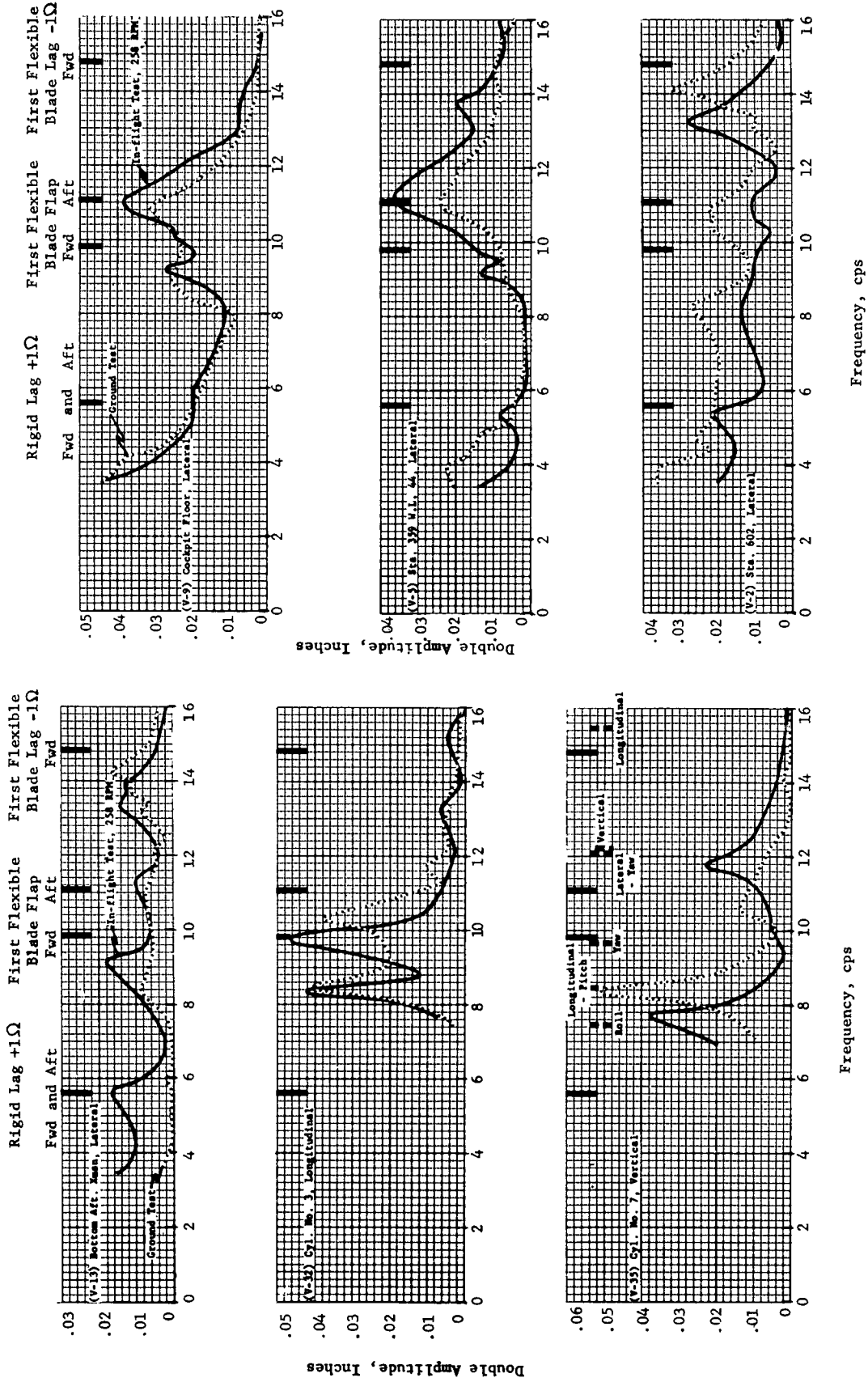


Figure 53 Comparison of Ground Test and In-flight Response at 258 rpm for 200 lb Lateral Force



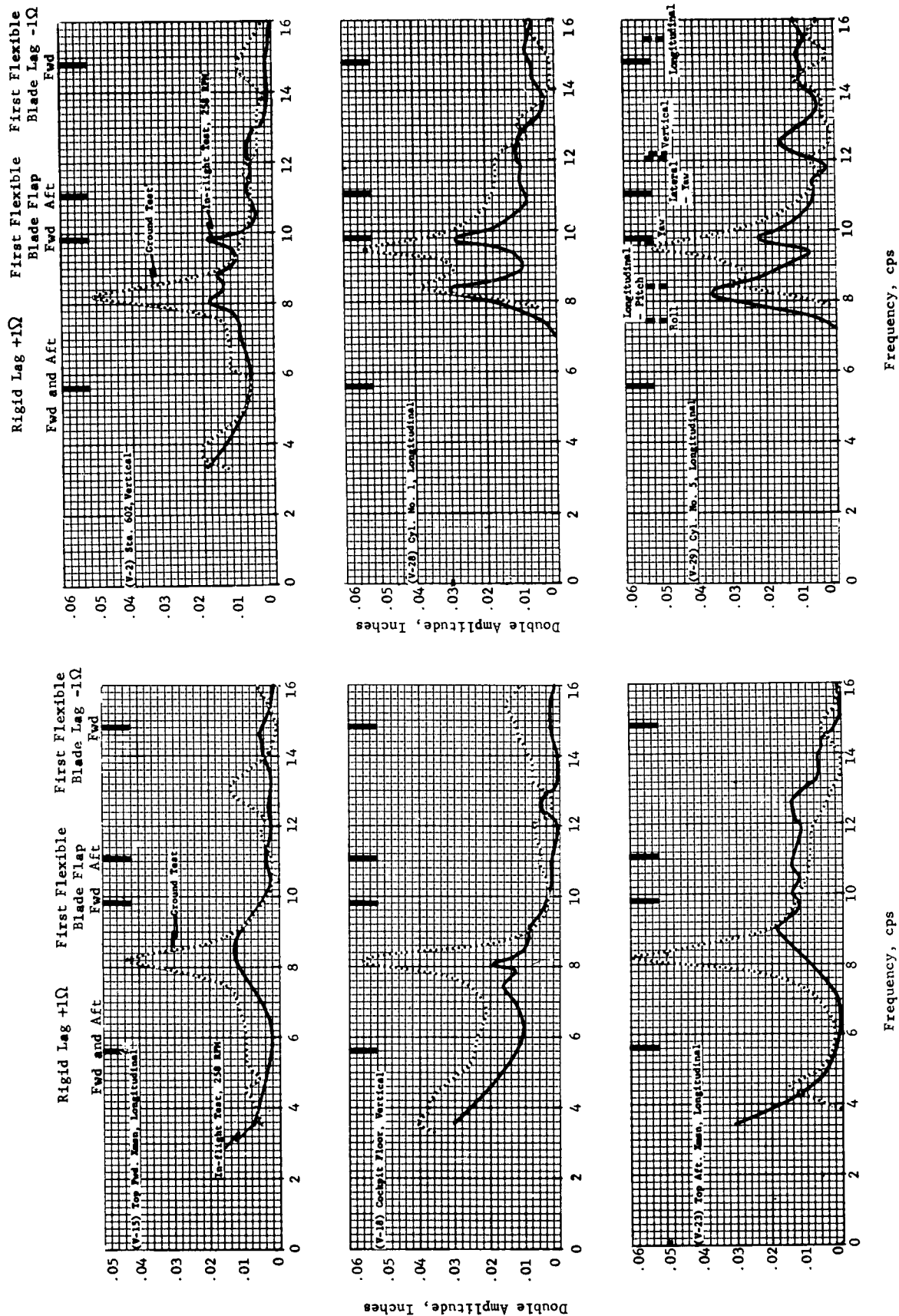


Figure 54 Comparison of Ground Test and In-flight Response at 258 rpm for 200 lb Vertical Force

Vertical Shaker			Lateral Shaker		
Pickup	In-flight cps	Ground cps	Pickup	In-flight cps	Ground cps
Cockpit	7.4 *		Cockpit	5.8	
Floor	8.1 *	8.1 *	Floor	9.2 *	8.9 *
Vertical	9.1		Lateral	10.05	
Page 91	12.7 *	12.1	Page 90	11.1 *	10.9 *
	15.3	15.5		13.5	
			Ceiling	5.4 *	4.0
			Sta. 359	9.2 *	8.9
			Lateral	11.2 *	11.1 *
			Page 90	13.7	14.7
Cylinder 1	8.3 *	8.4 *	Cylinder 3	8.3 *	8.4 *
Long.	9.8 *	9.5 *	Long.	9.8 *	10.3 *
Page 91	11.4	11.8	Page 90		11.8
	12.5	13.1		13.3	12.8
	14.4				13.7
	15.2	16.0		15.3	
Cylinder 5	8.3 *	8.5 *	Cylinder 7	7.7 *	8.4 *
Long.	9.8 *	9.5 *	Vertical	10.1	10.6 *
Page 91	11.4	12.1	Page 90	11.8 *	14.1
	12.5	13.2			
	14.4	14.3			
	15.0	15.6			
	16.0				
Keel		6.2	Keel	5.4	4.7
Sta. 602	8.1	8.2	Sta. 602	8.1	8.3
Vertical	8.8		Lateral		
Page 91	9.8		Page 90		10.4 *
	11.2	11.8		11.1	10.9 *
	12.5			13.2 *	12.1
					13.1
		14.7			14.2 *
Aft		4.5 *	Aft	5.6 *	
Xmsn	9.0 *	8.2 *	Xmsn	9.2 *	8.4 *
Long.	10.1		Lateral		
Page 91	10.8		Page 90	11.1	10.9
	12.7				12.1
				13.3	
	13.7			13.8	13.8
		14.7 *			14.2 *

\* Clear peak area or sharp peak

With lateral excitation the first noticeable in-flight peak appears near 5.8 cps at the cockpit near 5.4 cps at Sta. 602 and at the aft transmission. These correspond to the fixed system rigid lag frequency (Rigid Lag -  $1\Omega$ ) at 5.6 cps. There is, of course, no corresponding ground test peak. The lack of response at this frequency with vertical excitation (Figure 54) is reasonable, indicating that the lag modes of the rotor are not easily excited by vertical excitation. The next higher frequency appears at engine Cyl. 7, at 7.7 cps, and at 7.4 cps at the cockpit floor. This frequency is related to uncoupled engine roll.

The general peak area in the tabulated vertical shaker data above, from 8.1 to 8.4 cps in-flight, is the fundamental vertical beam bending mode and is virtually at the same frequency as the ground shake test result shown in Figure 54. However, the general impression made by all these curves is that in-flight response of the fuselage is suppressed in amplitude relative to the ground data. The lateral shaker data shows this vertical beam mode only in the aft fuselage where Sta. 602 peaks at 8.1 cps. The amplitude of the flight data is generally half that of the ground data in this frequency region. Engine Cylinder 3 also peaks at 8.3 cps for the lateral shaker, as do Cylinders 1 and 5 for the vertical shaker. These responses are also related to the uncoupled engine longitudinal pitch mode at 8.4 cps.

A major peak of the vertical data is present at 8.8 to 9.1 cps and is evident at the cockpit floor, the aft transmission and at Sta. 602. This is also seen as a major lateral peak at 9.2 cps at the cockpit floor, Sta. 359, and at the aft transmission, Page 90. The nearest ground test peak is less sharply defined but is in evidence at 8.9 cps at the cockpit floor with lateral excitation. No response near this frequency is apparent during the ground test with vertical excitation. The next important peak occurs from 9.8 to 10.1 cps. It is strong at Sta. 602, Page 90, and is a severe spike on most of the engine pickups. Note that the fundamental flap bending mode of the forward blades is at 9.8 cps, that an uncoupled engine yaw mode is at 9.67 cps, and that coupled ground test modes are near 10.4 cps.

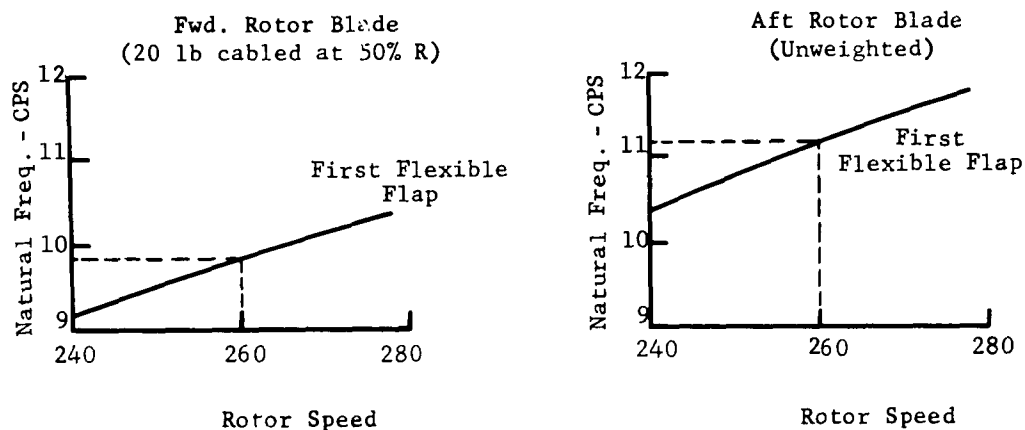
The next important lateral peak is one of the largest and is generally at 11.1 cps, Page 90. It corresponds closely with a large ground test peak which is a strong lateral-torsion mode of the fuselage. There is also a calculated fundamental flap bending mode of the aft blades at 11.1 cps, and it is likely that these modes are interrelated. In Figure 51, Page 86, at Sta. 359 and 602 there is some evidence from the data points that there are actually two peaks near 11 cps, but this is not assured because the differences lie within the accuracy of the measuring system. Cylinder 7 in the lateral data exhibits a strong peak at 11.8 cps in-flight, differing from the ground test result at 10.8 cps.

At 12.5 to 12.7 cps the next vertical peak occurs. It is a slight frequency increase over the 11.8 to 12.1 cps ground test data peaks, which contain considerable forward pylon longitudinal motion. In this same frequency region with excitation at 13.2 cps, a large peak appears at Sta. 602, Page 90 and at the aft transmission, Page 90. This response can be compared on the basis of similar magnitude with a ground test mode at 14.1 cps indicating considerable in-flight difference.

Page 90, Sta. 359 shows another in-flight peak at 13.75 cps which may be related to the small ground test peak at 13.1 cps, such as appears at Sta. 602, Page 90. A high peak is present in the range from 14.4 to 15.2 cps which is most apparent at the forward transmission, Page 91, and engine pickups, Page 91, in the vertical shaker data. These are close to the uncoupled engine longitudinal mode at 15.44 cps and the forward blade lag -  $1\Omega$  mode at 14.8 cps.

Effect of Rotor Speed with Lateral Excitation - Frequency response curves for lateral excitation at rotor speeds of 240 and 278 rpm are illustrated first in Figure 55 to present the measured data points. These curves are then combined with those for normal rotor speed to provide a comparison of response from lateral excitation at 240, 258 and 278 in Figure 56. Response data presented in the comparison consists of cockpit floor lateral, Sta. 359 lateral and Sta. 602 lateral.

Blade frequency spectrums for the forward and aft rotor are presented below for reference in the following discussion.



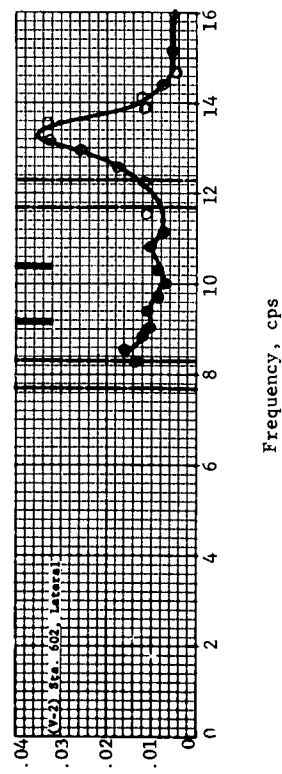
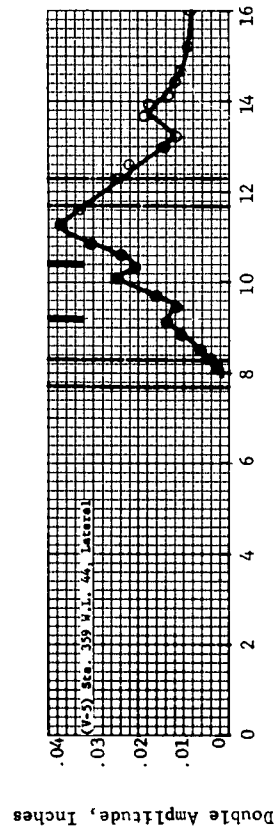
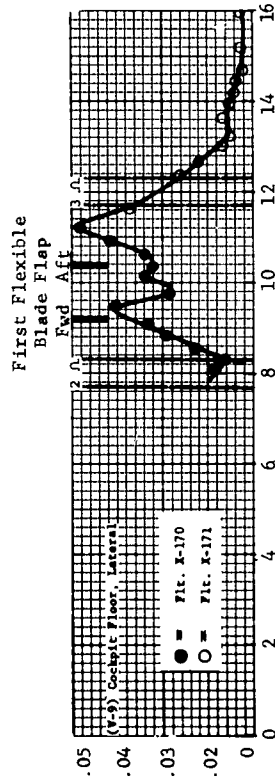
These spectrums illustrate the relation between the first flexible flap frequency and the operating rotor speed. As an example, the forward flap frequency at 260 rpm is obtained by projecting the rotor speed vertically to the diagonal line representing the mode and then reading the natural frequency as 9.8 cps on the ordinate frequency axis.

Since the in-flight response depends on the coupled rotor-fuselage system, the response peaks are plotted in Figure 57 on a spectrum containing the blade frequencies, the ground test data as horizontal bands because they are not related to rotor speed, and the in-flight response peaks as the data points "X".

Uncoupled frequencies corresponding to the fuselage modes from the ground shake test and blade fundamental flap bending modes from stationary test extrapolated to rotor speed are shown on the plot by solid lines. Using these uncoupled frequencies for comparison, the in-flight peak response frequencies are shown as data points and connected between rpm's using dashed lines.

At 240 rpm, the fuselage mode at 9.2 cps, 0.3 cps higher than the 8.4 to 8.9 cps ground test mode, and the forward blade flap mode combine within the limits of the data increment to form the peak response measured during the in-flight

240 rpm



278 rpm

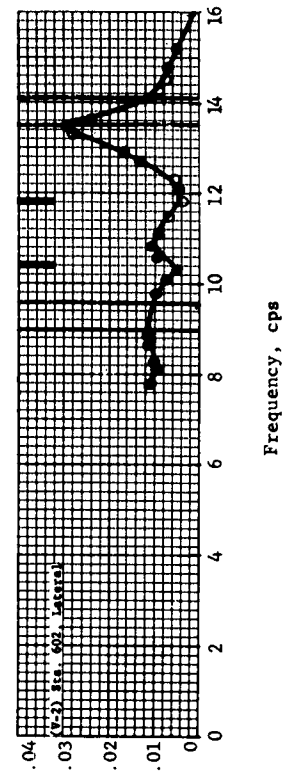
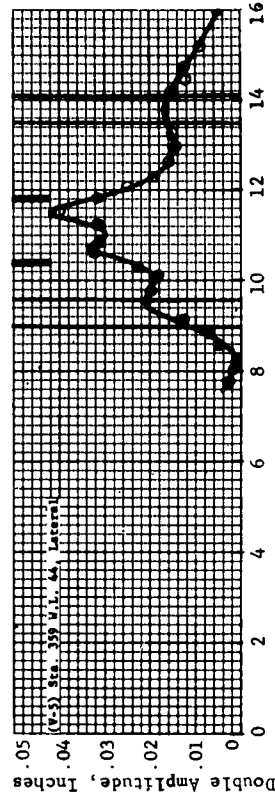
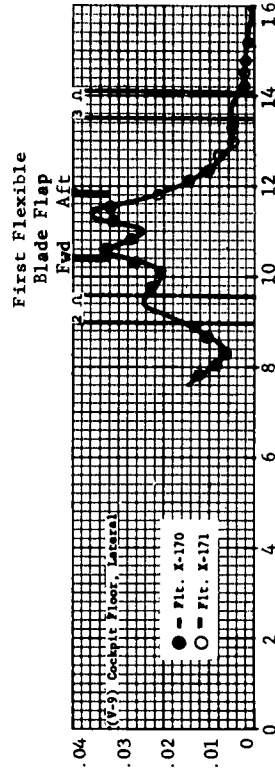


Figure 55 Response at 240 rpm and 278 rpm for 200 lb. Lateral Force

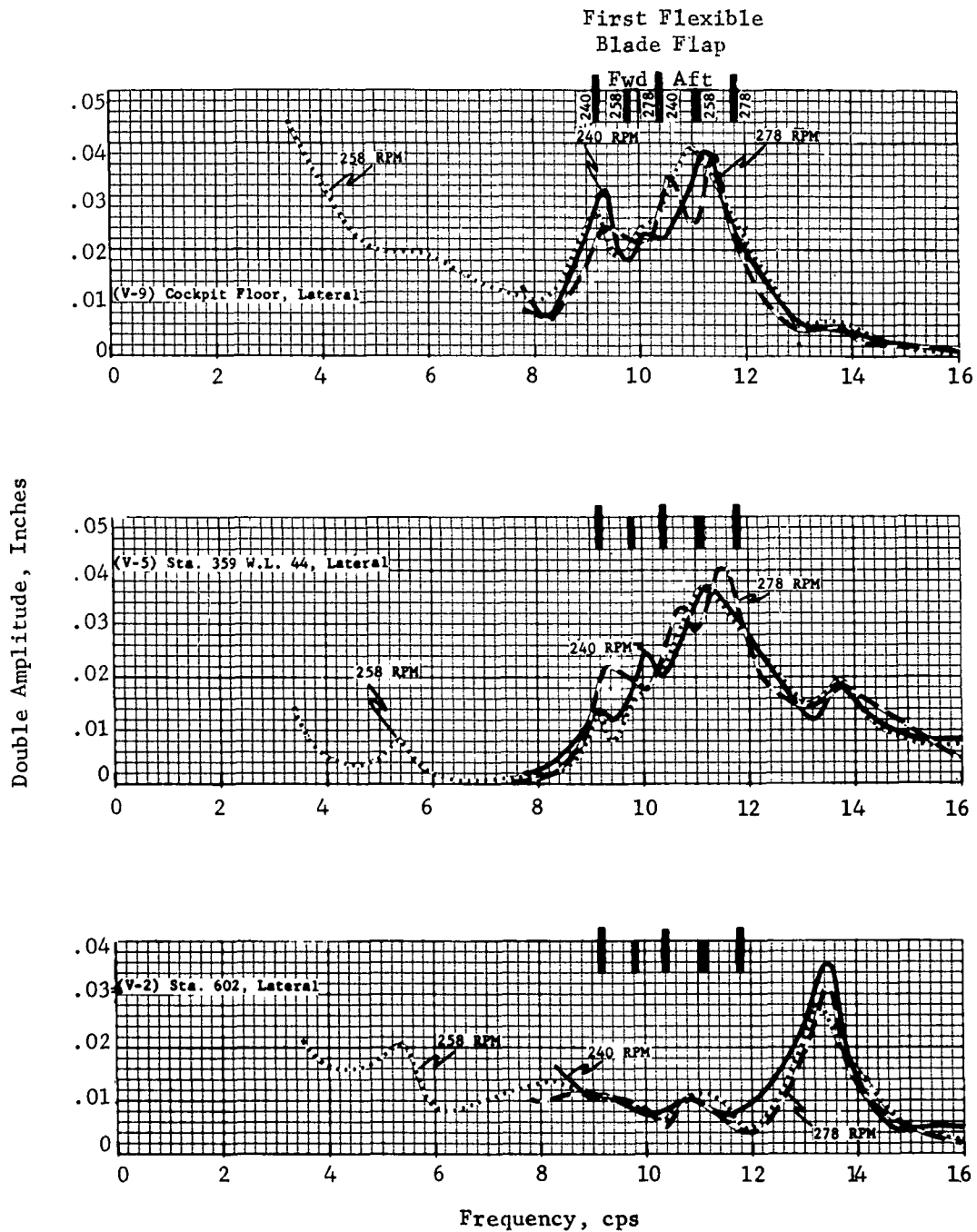


Figure 56 Comparison of In-flight Response at 240, 258 and 278 rpm for 200 lb. Lateral Force

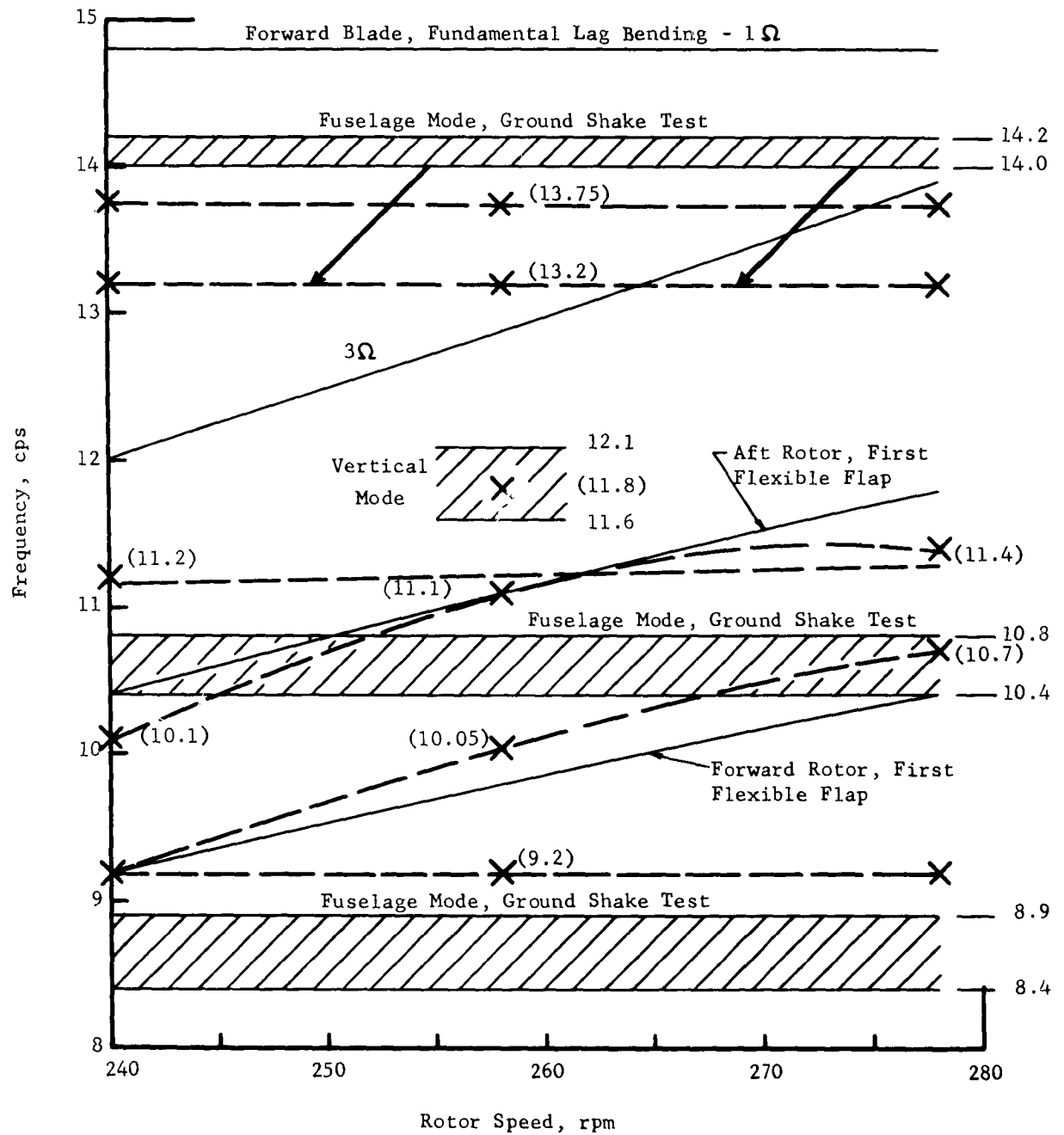


Figure 57 Frequency Response with Lateral Excitation

test. In-flight peak responses appear at 10.1 and 11.2 cps corresponding to the aft blade flap mode and the ground test frequency 10.4 - 10.8 cps.

At 258 rpm, the flight data peak at 9.2 cps repeats and is not affected by the rotor speed, affirming its relation to the ground test fuselage mode. A response peak at 10.05 cps represents the forward blade flap frequency. Aft blade flap response appears at 11.1 cps combined with the fuselage response corresponding to the 10.4 to 10.8 cps ground test mode.

The next data point at 11.8 cps from Cylinder 7 vertical, Page 90, has a corresponding lateral ground test point at 11.8 cps. However, this 11.8 cps does not appear to be a predominant lateral mode, but is a coupled response from the vertical mode.

At 278 rpm, the 9.2 cps peak appears once again near the ground test data. A flight data point at 10.7 cps corresponds to the forward blade flap frequency. The next point 11.4 cps appears as a combination of the ground test mode 10.4 to 10.8 cps, and aft blade fundamental bending. Significant deviation from the aft blade line is apparent.

Above the blade flap frequency lines, two modes appear at 13.2 and 13.75 cps. From the mode shape, which is illustrated later, the 13.2 cps data point is related to the 14.1 cps ground test mode. The in-flight peak at 13.75 cps may result from the forward blade (fundamental lag bending -  $1\Omega$ ) frequency line. Blade lag frequencies vary with rotor speed as does flap, but the variation is much flatter so that over the range shown the lag frequency is close to a straight line.

Effect of Rotor Speed with Vertical Excitation - Frequency response curves for vertical excitation at rotor speeds of 240 and 278 are illustrated first in Figure 58 to present the measured data points. These curves are then combined with those for normal rotor speed to provide a comparison of response at 240, 258 and 278 rpm in Figure 59. Response data in the comparison consists of cockpit floor vertical and forward and aft transmission longitudinals.

These response curves, compared with those from lateral excitation, indicate somewhat less response in the region of blade flap bending frequencies and relatively obscure peaks. Inasmuch as the vertical force was 100 lb greater than lateral, and in addition the fuselage modes are clearly defined, it is evident that blade responses are more easily excited by a lateral force. This may be because vertical excitation must excite the whole helicopter mass in order to transmit vertical excitation to the blades, while lateral excitation at the cabin floor can roll the fuselage about its cg and excite the blades in differential vertical motion on right and left sides of the rotor.

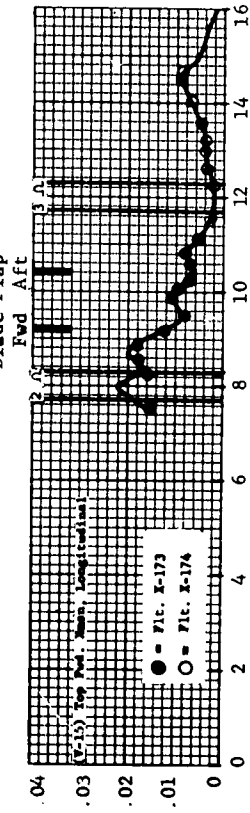
As with response to lateral excitation, the response peaks are presented on a frequency spectrum in Figure 60 to evaluate the combining of blade flap and ground test fuselage frequencies.

At 240 rpm the flight data points are at 8.1 cps in the 8.1 to 8.5 ground test band, and at 8.9 cps just below the 9.0 to 9.5 cps ground test band. Test points at 9.8 cps and 10.8 cps correspond to forward and aft blade fundamental flap bending natural frequency lines. Response peaks appear in the  $3\Omega$  region at 12.6 and 14.0 cps above the corresponding ground test modes of 11.6 to 12.1 cps and 12.8 to 13.1 cps. The next in-flight data point at 14.5 cps appears at the center of the 14.2 to 14.7 cps ground test band.



240 rpm

First Flexible  
Blade Flap



278 rpm

First Flexible  
Blade Flap

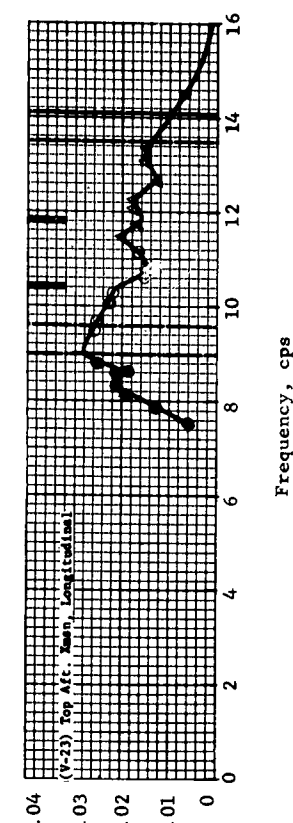
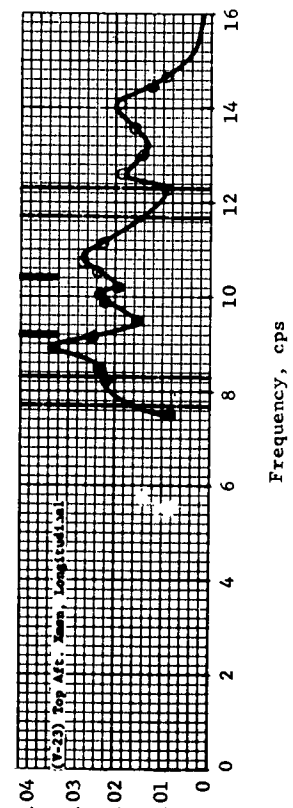
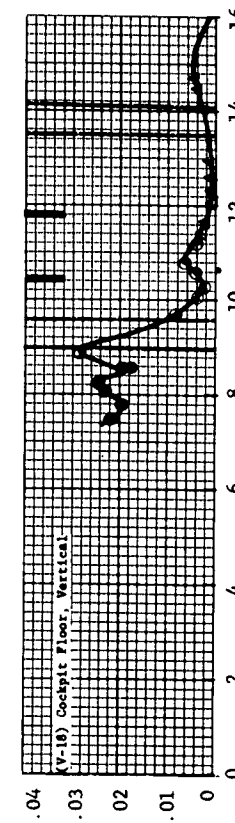
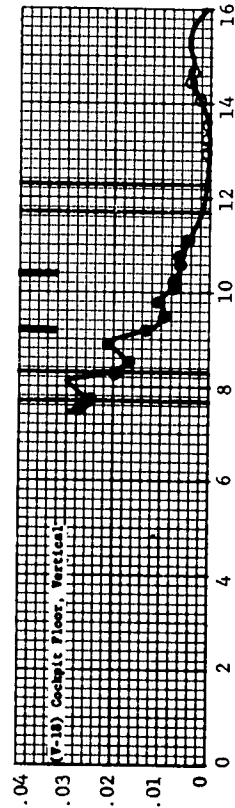
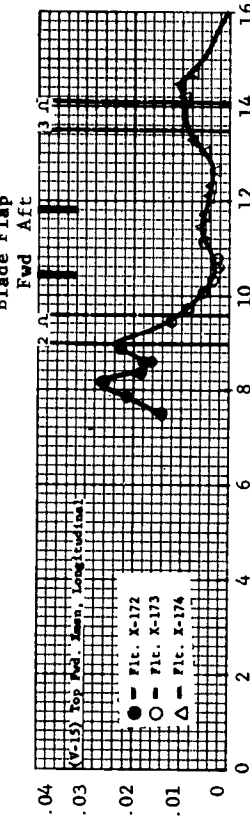


Figure 58 Response at 240 rpm and 278 rpm for 300 lb. Vertical Force

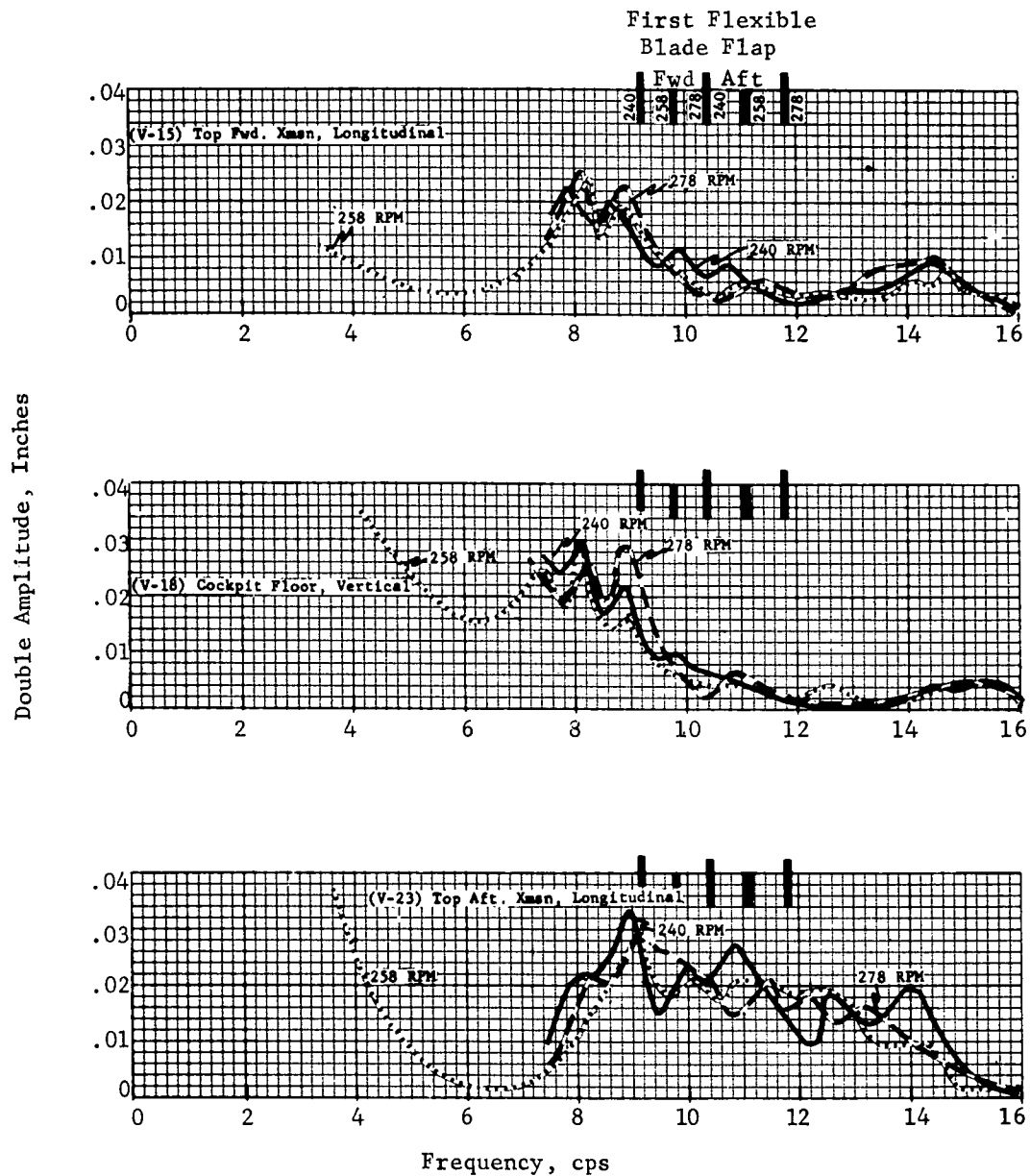


Figure 59 Comparison of In-Flight Response at 240, 258 and 278 rpm for 300 Lb Vertical Force

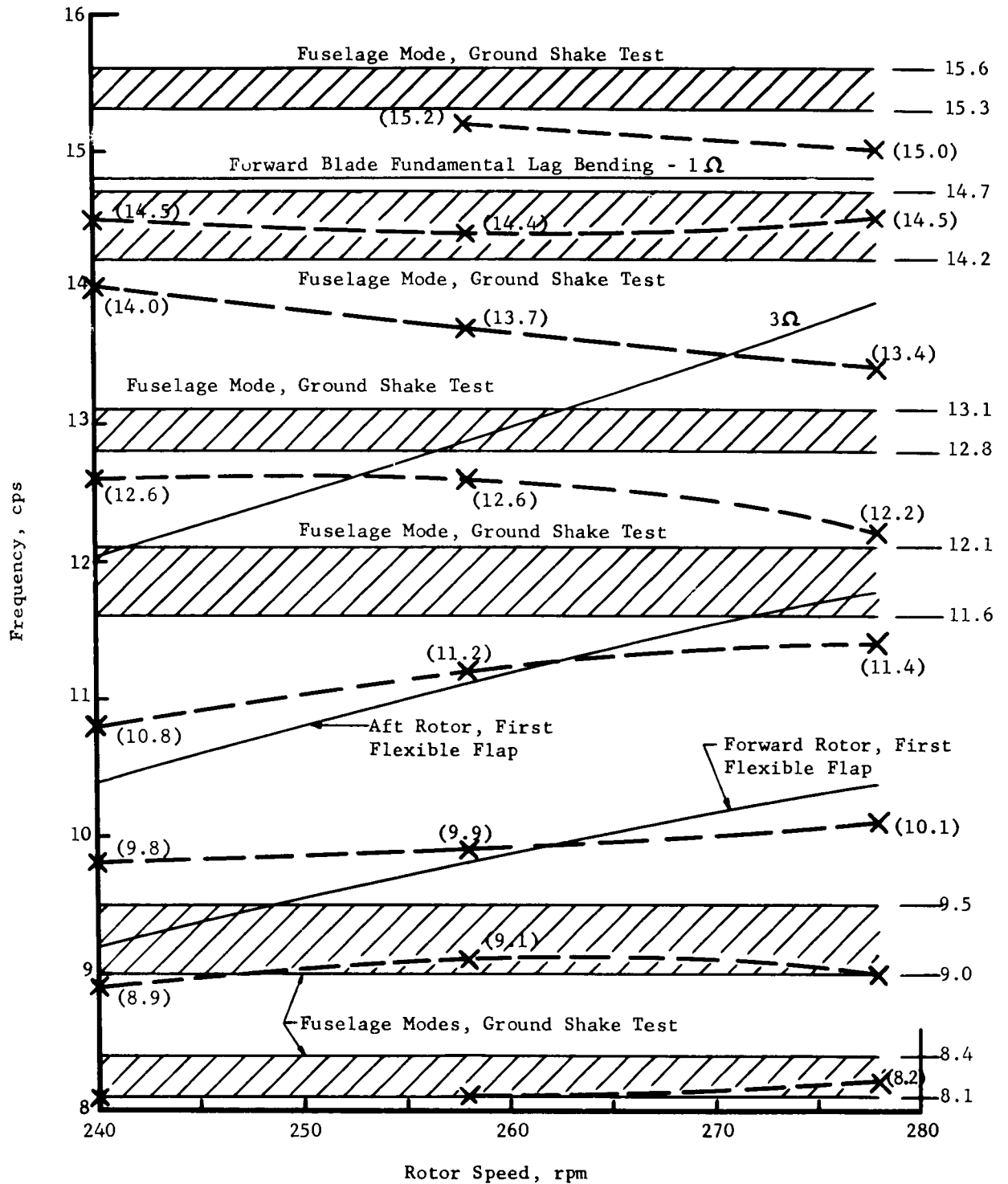


Figure 60 Frequency Response with Vertical Excitation

At 258 rpm fundamental fuselage vertical bending remains at 8.1 cps and second vertical bending at 9.1 cps. Response peaks which average 9.9 and 11.2 cps correspond to the calculated blade flap natural frequencies. Response curves again peak at 12.6 cps above the 11.6 to 12.1 ground test band. Peak response at 13.7 represents a 0.3 cps reduction from the corresponding response at 240 rpm. Again, a response peak appears at 14.4 cps close to the center of the 14.2 to 14.7 cps ground test band. Showing a correlation with (fundamental lag -  $1\Omega$ ) blade frequency and the 15.3 to 15.6 cps band, the next peak in-flight appears at 15.2 cps.

At 278 rpm, fuselage bending is again at 8.2 and 9.0 cps. Blade related responses are at 10.1 and 11.4 cps. Response at 12.2 cps shows a significant reduction probably related to the aft blade flap bending line. Continuing the previous rpm trend, the 13.4 cps peak represents a nearly linear variation with rpm. Similar response peaks appear at 14.3 and 15.0 cps.

It is interesting to note that most measured rotor shaft loads increase with rpm in Section V. This may be related to the 14.0, 13.7, 13.4 cps mode line approaching the  $3\Omega$  resonance line in Figure 60.

#### Forced Modes with Vertical and Lateral Excitation

Using the frequencies of peak response from the previous figures, the comparable in-flight and ground results are shown below:

<u>Excitation</u>	<u>In-flight Response Frequency, cps</u>	<u>Ground Response Frequency, cps</u>
Vertical	8.1	8.1 - 8.4
Lateral	9.2	8.4 - 8.9
Vertical	9.1	9.0 - 9.5
Vertical	9.9	} Blades Removed
Lateral	10.05	
Lateral	11.1	10.4 - 10.8
Vertical	12.6	11.6 - 12.1
	Mode Data Not Available	
Vertical	13.7	12.8 - 13.1
	Mode Data Not Available	
Lateral	13.2	14.0 - 14.2
Lateral	13.75	13.2
		Mode Data Not Available
Vertical	14.5	14.2 - 14.7
	} Mode Data Not Available	
Vertical	15.2	15.3 - 15.6

For the most significant in-flight responses from above, the forced modes are defined from measured data and presented in Figures 61 to 64. The forced modes are shown below compared to the corresponding ground shake test results.

<u>In-flight, cps</u>		<u>Ground Test, cps</u>	<u>Figure</u>
8.1	Vertical	8.1 - 8.4	61
9.2	Lat. - Tors.	8.4 - 8.9	61
9.1	Coupled V-L	9.0 - 9.5	62
9.9	} Blade Modes	} Blade Removed	62
10.05			63
11.1	Lateral	10.4 - 10.8	64
13.2	Lat. - Tors.	14.0 - 14.2	63
13.75	Lat. - Tors.	13.2	64

In-flight modal response plots present the measured data as the sine and cosine time components of the response. Heretofore, as in the ground test, the response modes were defined from the instantaneous response of the system without regard to damping effect on the mode shape. As the modal presentation differs between ground and in-flight, the shape comparison is not absolute, but only provides an indication of relative shape. Since in-flight the wave forms were phased to instantaneous zero shaker force, the sine component indicates the in or out of phase response, the undamped response, and the cosine component represents the 90 degree phase, in or out of phase with velocity. In the ground test, the instantaneous modes are normalized to maximum response of the forward rotor. Assuming the structural damping of the fuselage as being small, the ground test modes correspond to the in-flight sine component.

#### In-flight Forced Mode at 8.1 cps - Figure 61

In-flight the fundamental vertical bending mode is at 8.1 cps showing excellent frequency correlation with the ground test mode at 8.1 - 8.4 cps. The in-flight sine mode, compared with the instantaneous ground mode, shows good agreement in shape for vertical motion along the fuselage and engine motions in both the pitch and yaw directions. Aft pylon motions, longitudinal and lateral, show a relative decrease in flight; forward pylon lateral motion increases. In the cosine mode, fuselage vertical motion decreases; pitch and yaw of the engine respond with pitching amplitude decreasing. However, pylon motion changes appear most significant with larger forward pylon lateral and aft pylon longitudinal motions in the cosine response. Since rotor and engine motion predominate, it appears that the flight response is influenced by damping of the rotors and the engine.

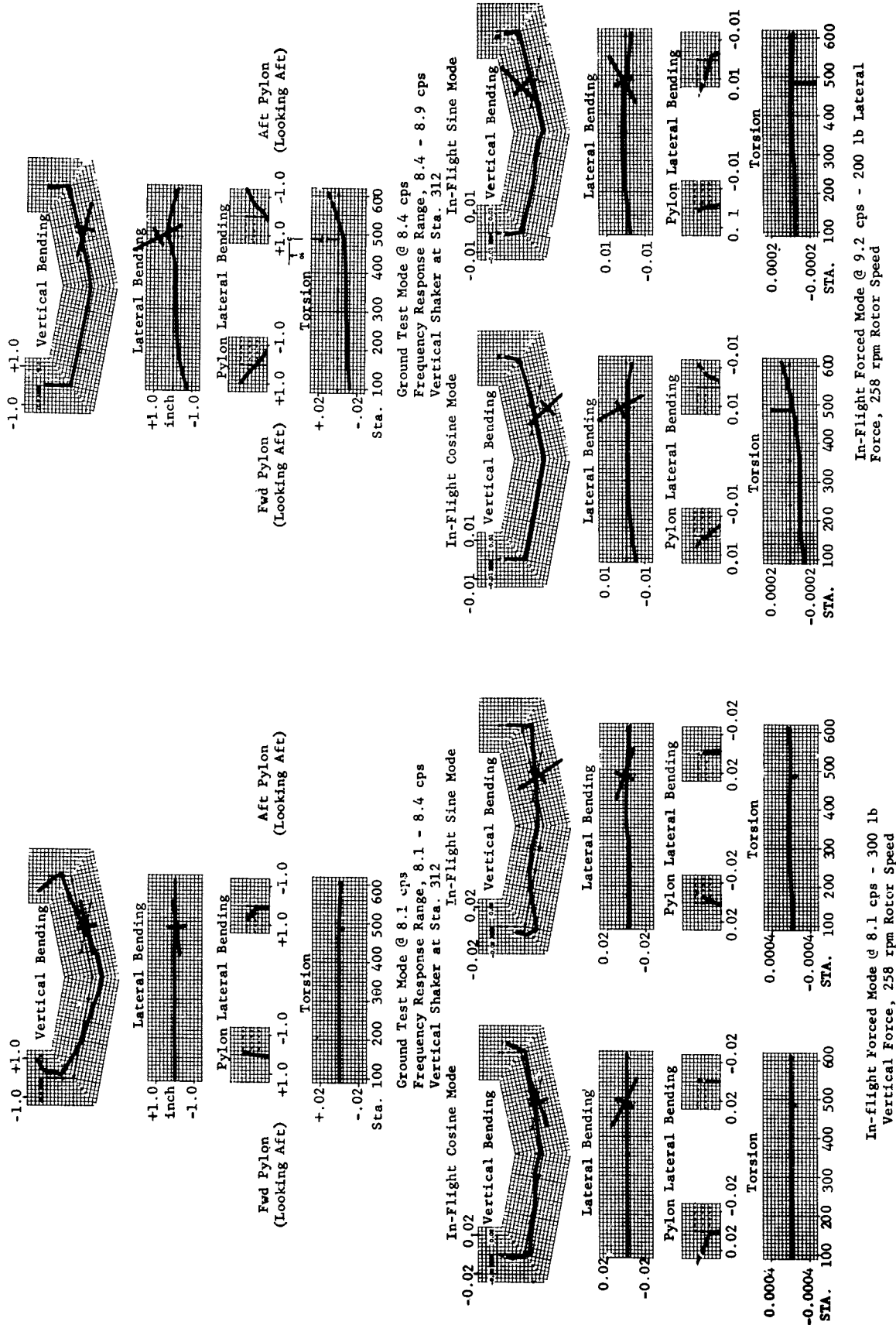


Figure 61 In-Flight Forced Modes @ 8.1 and 9.2 cps

#### In-flight Forced Mode at 9.2 cps - Figure 61

The in-flight test mode at 9.2 cps appears as a lateral-torsion mode of the fuselage coupled strongly to engine motion. In the ground test, the comparable modal response was between 8.4 and 8.9 cps showing the in-flight rotor coupling increases the peak response mode by 0.2 cps considering the upper limit of the band. Unlike the fundamental vertical mode, the cosine mode shows very good agreement in shape. Fuselage response includes first torsion out of phase with the engine, and first fuselage lateral bending with in-phase engine motion and out-of-phase yaw motion. No significant coupling is noted with vertical-longitudinal motion of the fuselage, but the engine responds with vertical-pitch motion. Sine response for the mode appears similar overall, but the relative phases are unlike the ground test mode. For lateral bending to the right as shown, the engine motions are shifted  $180^\circ$  in phase, forward pylon motion continues to the right, but the aft pylon direction reverses.

#### In-flight Forced Mode at 9.1 cps - Figure 62

Corresponding to a response peak with vertical excitation, the in-flight forced mode at 9.1 cps is a highly coupled vertical-lateral mode with relatively large engine motions. Comparable ground response between 9.0 and 9.5 cps for vertical excitation shows excellent frequency comparison, but the modal shape shows only limited similarity. Both the ground test mode and cosine mode component in-flight respond in the fundamental vertical bending mode, but the pylons show a longitudinal reversal. Lateral motions of the aft pylon are comparable, with both bending to the right. Pitch response of the engine appears on the ground; in flight the only engine response is lateral. The sine response indicates a vertical fuselage motion, without pylon reversals. Except for a phase reversal between the engine and fuselage, lateral-torsion compares well with the ground test mode between 8.4 - 8.9 illustrated in Figure 61.

#### In-flight Forced Mode at 9.9 cps - Figure 62

Appearing only in flight, the peak response at 9.9 cps corresponds to the forward blade fundamental flap bending frequency with vertical excitation. The cosine mode continues with fundamental vertical bending, but this mode is highly coupled with engine motion in all directions. Fuselage lateral-torsion motion appears similar to that shown for the in-flight cosine mode at 9.1 cps, except that the lateral pylon motion is reversed. In all directions except longitudinal and roll, engine motion continues to be relatively large in the sine mode. Vertical motion of the fuselage decreases, but longitudinal motion of the aft pylon increases with a reversal in direction; lateral motion at the aft pylon decreases to nearly zero.

#### In-flight Forced Mode at 10.05 cps - Figure 63

The in-flight response related to the forward blade fundamental flap bending frequency is at 10.05 cps. Rotor hub motions provide a partial explanation for the response shift between vertical and lateral excitation. As illustrated in Figure 62 for vertical excitation, the rotor hubs move in a vertical direction exciting in-phase flapping of the blade; with lateral excitation no vertical response occurs at the rotors, only pitching and rolling which excite out-of-phase blade response. Since the out-of-phase response excitation from the fuselage varies with azimuth position a response would be expected.

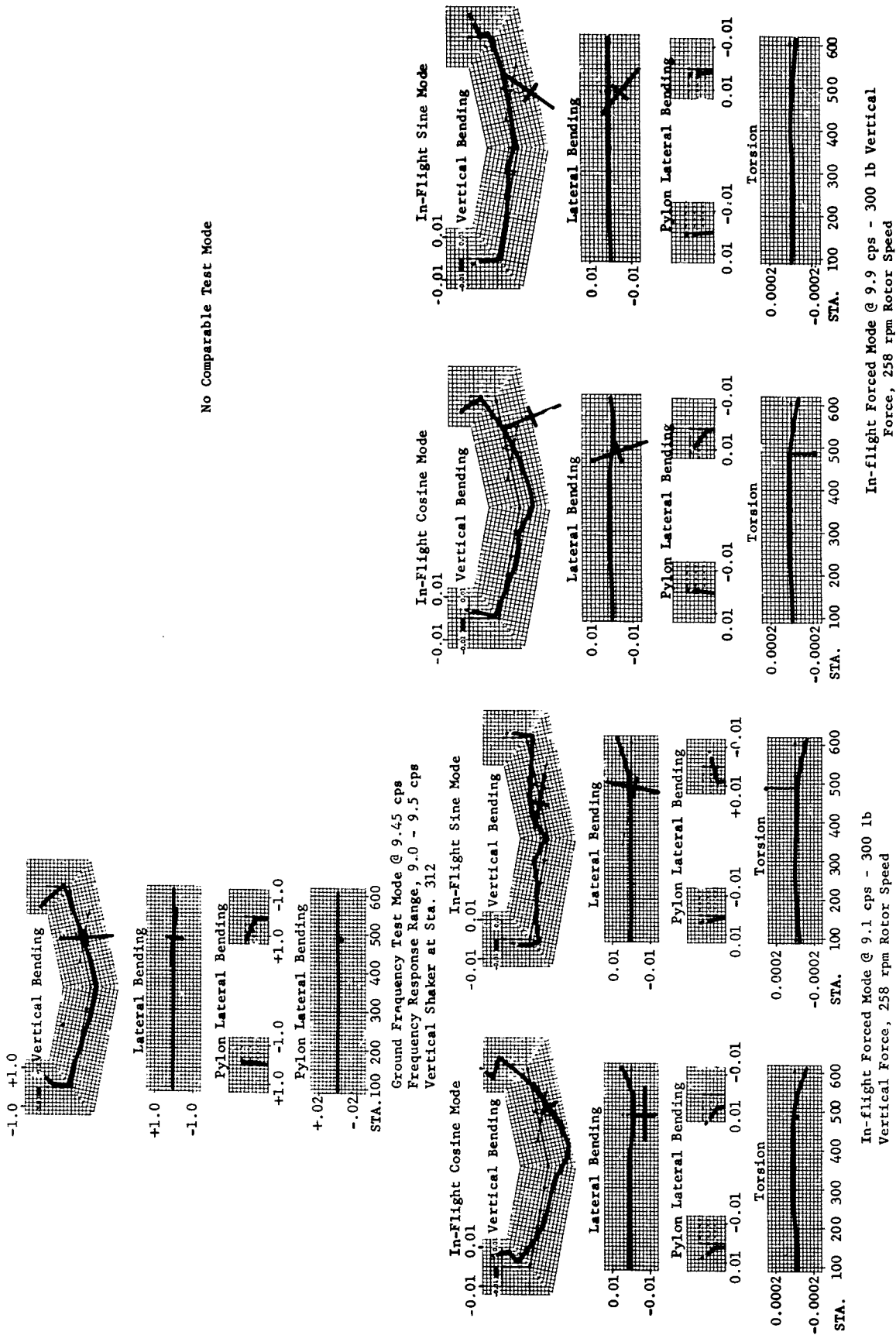


Figure 62 In-Flight Forced Modes @ 9.1 and 9.9 cps



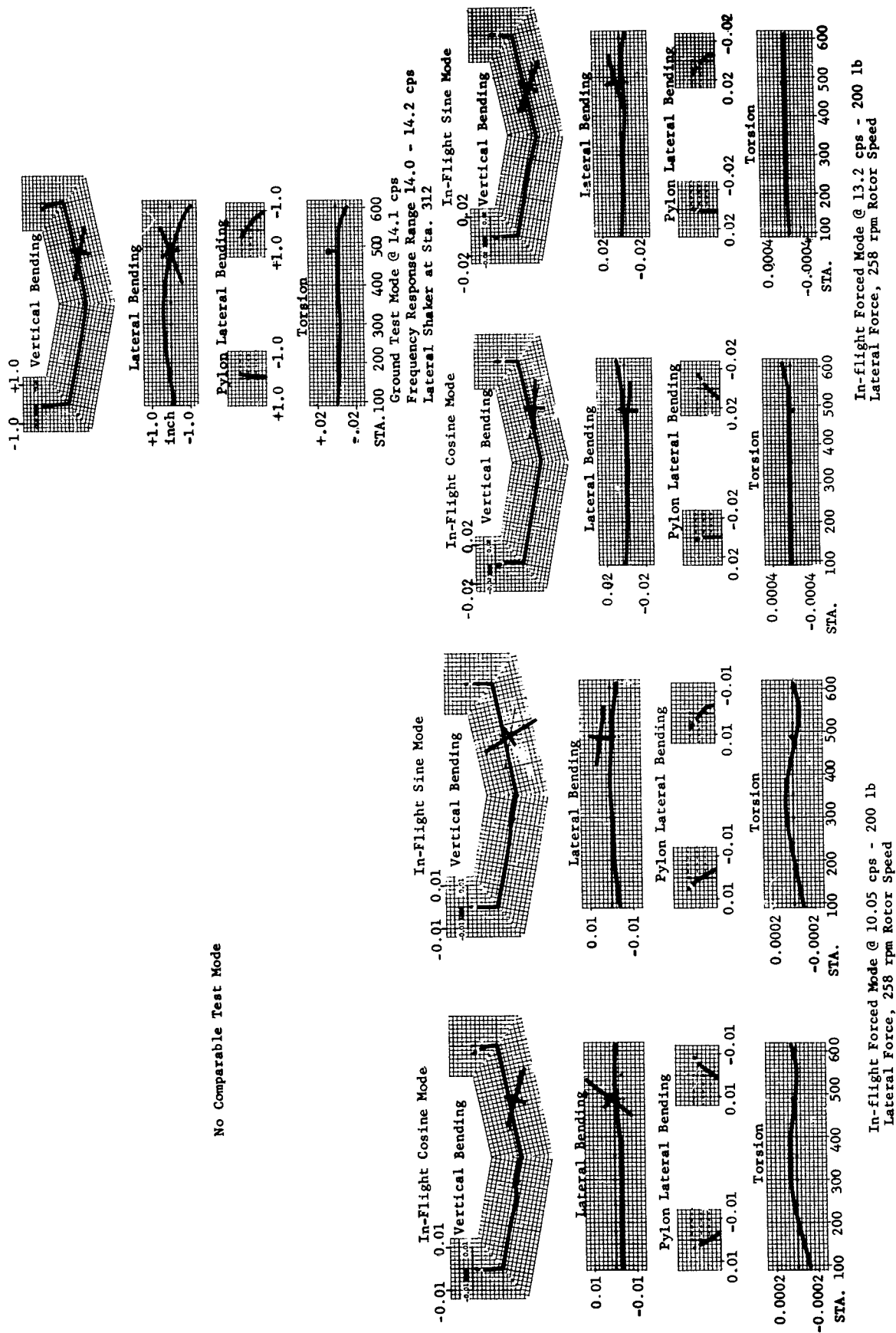


Figure 63 In-flight Forced Modes @ 10.05 and 13.2 cps

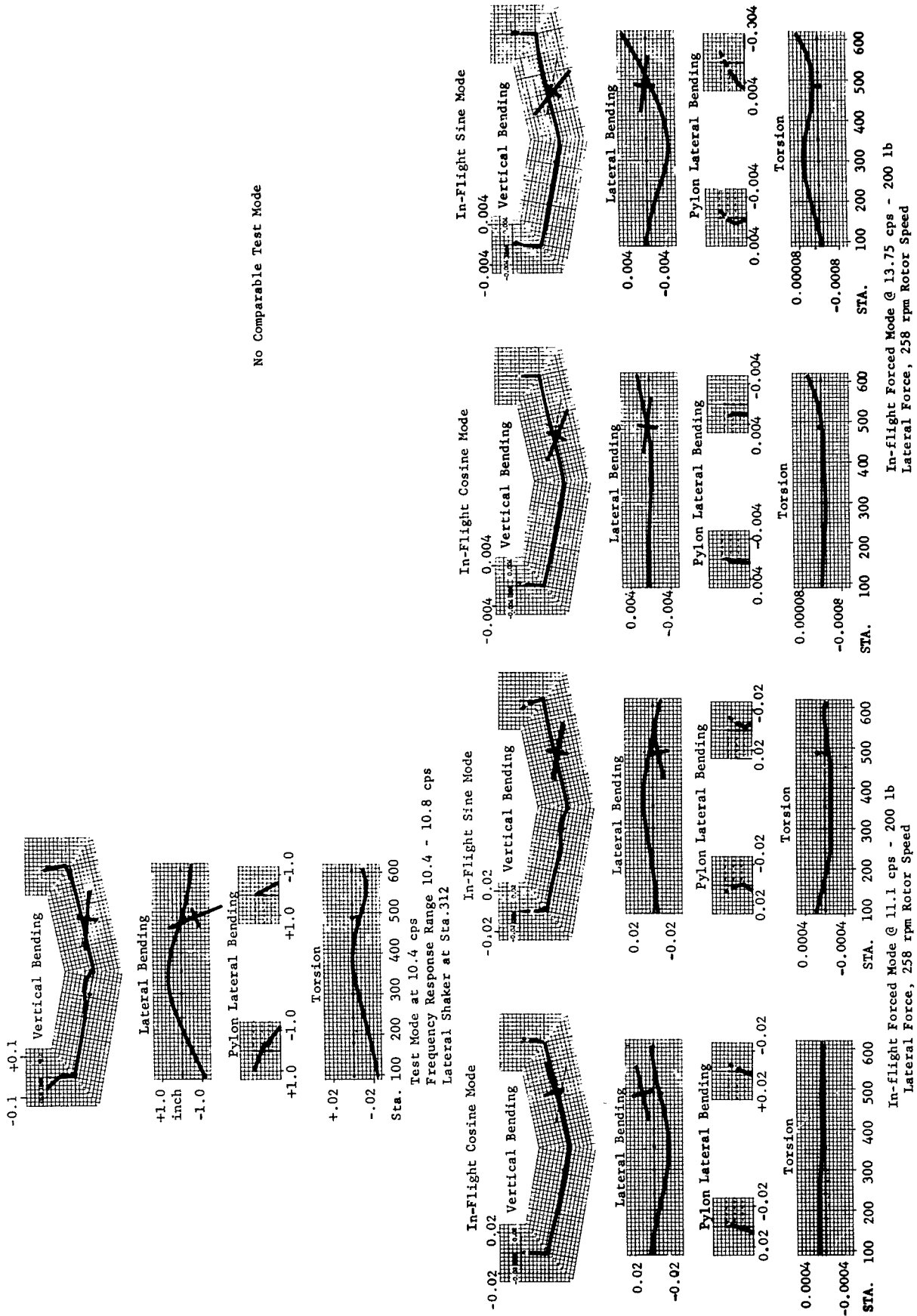


Figure 64 In-flight Forced Modes @ 11.1 and 13.75 cps

Fuselage vertical-longitudinal motion is nonexistent in the response except for a localized shaker motion and a relatively small longitudinal motion of the aft pylon in the cosine mode. Engine motions appear in the yaw direction in the cosine shape; pitch and lateral motions respond in the sine mode. For both components, the third torsion mode prevails with the lateral pylon motions defined by fuselage twist. Further, the torsion shape resembles that of the ground shake test mode at 10.4 cps shown in Figure 64.

#### In-flight Forced Mode at 11.1 cps - Figure 64

The fuselage lateral-torsion mode corresponding to the peak response at 11.1 cps is compared to the ground shake test mode at 10.4 for lateral excitation. In flight the coupling motion decreases showing only localized fuselage motion at the shaker and engine pitch in the cosine mode. Compared to the ground test, the cosine mode shows first lateral bending of the fuselage with out-of-phase engine motion, and only rigid lateral motion of the pylon. Torsion motion does not agree, but using the sine mode the comparison is reasonable. The sine component of fuselage lateral bending compares well with the ground test; pylon lateral motions disagree being distinguished by a local reversal. It is of interest to note that, unlike the ground test, in-flight reversals of the pylon motion occur rather frequently.

#### In-flight Forced Mode at 13.2 cps - Figure 63

The in-flight response peak at 13.2 cps corresponds to a lateral-torsion fuselage mode with no significant engine motion. In the ground test, the comparable modal response occurs at 14.1 cps with lateral excitation. The ground test mode shows good shape agreement compared to the in-flight cosine mode. In the comparable shape, the first lateral bending mode is predominant with no vertical coupling; torsion of the aft fuselage results in rigid rotation of the aft pylon. Engine yaw and roll motion appear out-of-phase with the fuselage motion in both comparable modes.

#### In-flight Forced Mode at 13.75 cps - Figure 64

In flight the peak response at 13.75 cps corresponds to the lateral-torsion mode illustrated in Figure 64. The sine component exhibits the first lateral bending shape and a tendency toward the third torsion shape. No significant vertical coupling appears except for the engine longitudinal-pitch motion. Lateral hub motions are in phase resulting from a forward pylon reversal. In the less significant cosine response, the fuselage lateral mode remains, but is of lesser amplitude; the torsion motions exhibit the second flexible shape.

#### Conclusions

The testing techniques evolved for the performance of an in-flight shake test provide a powerful diagnostic tool for improving helicopter vibration environment. A large inertia hydraulic shaker was developed and tested to fulfill the specific requirements of the test. An analyzer system capable of separating the shaker response from the environmental vibration level of the helicopter consisted of a magnetic tape recorder and an electronic wave form analyzer. The techniques which were developed have proven the feasibility of the in-flight shake test as a routine method for determining the response characteristics of helicopters in-flight.

In-flight testing techniques developed herein were applied to the H-21 helicopter to obtain the fuselage response to vertical and lateral excitations. Ground shake testing of the same aircraft was performed with the same equipment prior to flight, and the results compared with flight data to evaluate multi-directional rotor coupling, flap and chord blade natural frequency effects, and rotor damping. In-flight shake testing of the aircraft was performed at three rotor speeds at a constant 80-knot forward speed.

Specific conclusions pertinent to the H-21 helicopter under the excitation of a lateral shaker located near the centerline between rotors are as follows:

1. A fuselage response is clearly evident at 5.5 cps corresponding to blade rigid body lag frequency plus rotor speed, i.e., fixed system blade lag frequency.
2. Fuselage modes whose frequencies are not near the fundamental flap bending frequencies of either forward or aft blades are not subject to rpm variations in-flight. (Blade frequencies differ by virtue of a 20-pound weight at 50% span in the forward blades.)
3. The fundamental lateral ground shake test natural frequencies are all shifted in flight as follows:

<u>Ground, cps</u>	<u>In Flight, cps</u>
8.4 to 8.9	9.2
10.4 to 10.8	11.1
14.0 to 14.2	13.2

In two cases the frequency shift is upward, in the third it is downward. Rotor effective mass coupling thus shifts ground modes, but not in one definite direction. The frequency shift to 13.2 cps is particularly significant because it places this mode nearly in resonance with the predominant three per rev forcing frequency of this three-bladed helicopter.

4. In-flight forward blade flap frequency agrees with the calculated value at 240 rpm, but is above the calculated value at 258 and 278 rpm by about 0.25 cps ( $0.06\Omega$ ).
5. In-flight aft blade flap frequencies do not follow the calculated values as consistently as the forward blade.

<u>Rotor rpm</u>	<u>In-flight Flap, cps</u>	<u>Calculated Flap, cps</u>
240	10.1	10.4
258	11.1	11.1
278	11.4	11.8

They agree at 258 rpm, but test is below calculated at 240 and 278 rpm. However, interpretation of the data in the light of about 0.25 cps overall instrumentation accuracy gives the likelihood of two peak responses at 258 rpm, the lower, at 10.8 cps, corresponds to blade flap, the higher to a nearby fuselage mode. Based on this supposition, the aft blade natural frequency is generally reduced by 0.25 cps ( $0.06\Omega$ ) from the calculated values.

6. The differences between in-flight test and calculated blade flap natural frequencies are probably due to the presence of the 10.4 to 10.8 cps ground fuselage mode in this vicinity. The blade frequency peaks generally follow the predicted upward trend with rotor rpm.
7. Calculated uncoupled blade natural frequencies, long an empirical guide to moderated vibration levels, must be viewed with the possibility that coupling with fuselage modes can vary them by 0.25 cps in either direction.
8. The response which shows nearest correspondence to the 14.8 cps calculated lag bending natural frequency -  $1\Omega$  is at 13.75 cps indicating a 1.0 cps ( $0.24\Omega$ ) downward shift in flight.

Similar conclusions are drawn regarding the results from vertical shaker excitation.

1. The ground fuselage modes at 8.1 to 8.4 cps and 9.0 to 9.5 cps remain unchanged in frequency during flight and show little rpm variation.
2. The 11.6 to 12.1 cps ground test mode increases to 12.6 cps at 240 and 258 rpm and to 12.2 cps at 278 rpm, resulting in a downtrend with rpm. This rpm effect attests to the importance of rotor effective mass coupling, but it is not clear why these frequencies decrease with rpm rather than increase with rpm as do the blade flap natural frequencies.
3. The 12.8 to 13.1 cps ground test mode shows a significant rotor speed effect in-flight with response varying from 14.0 cps at 240 rpm to 13.4 cps at 278 rpm. This mode is particularly important because of its closeness to the rotor third harmonic. As in the previous mode, it is not known why these frequencies decrease with rpm.
4. In-flight peak responses at 14.4, 14.5 cps show that this mode remains in about the same place as the ground mode at 14.2 to 14.7 cps.
5. In-flight peak responses at 15.2, 15.0 cps apparently represent a downward coupling of the 15.3 to 15.6 cps ground mode due to the forward blade fundamental lag bending -  $1\Omega$  mode.
6. Blade flap bending natural frequencies obtained in the flight test under vertical excitation follow an uptrend with rpm, but at a lesser rate than calculated. This is probably due to the influence of coupling with nearby fuselage modes. The blade modes obtained under vertical shaker excitation differ from those under lateral excitation, again verifying the powerful effect of the fuselage-blade relationships.
7. Despite the use of 300 pounds of shaker force in the vertical direction compared to 200 pounds in the lateral direction, response amplitudes of the blade flap modes are smaller under vertical excitation. This is evidently because (a) vertical excitation must excite the whole helicopter mass in order to transmit vertical excitation to the blades, while lateral excitation at the cabin floor rolls the fuselage and excites the blades in differential vertical motion on the right and left sides of the rotor, and (b) rotor damping is more effective in the vertical direction.

## SECTION VII

### A METHOD FOR THE PREDICTION OF COUPLED VERTICAL-LATERAL NATURAL AND FORCED MODES

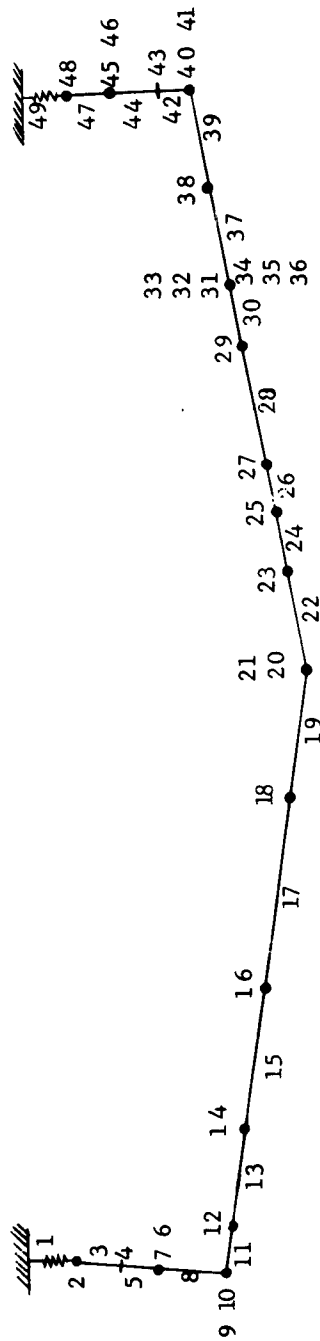
#### A. General

To improve correlation between analytical and shake test results, the Associated Matrix Method of Section III was expanded to include coupling between vertical and lateral motions. The general matrix program represents fuselage structural characteristics using either an elastic matrix or a frame racking matrix depending on the elastic characteristics of the section. The elastic matrix considers simple beam theory in both the lateral and vertical directions, but in addition, permits different elastic and neutral axis locations. The frame racking matrix permits beam bending in the vertical and lateral directions, but replaces pure beam torsional deflection by frame distortion under both direct torque load and laterally offset vertical load. Prior to the dynamic analysis, the adequacy of the analytical model was proven by theoretically duplicating the test deflections under applied load.

#### B. Vertical-Lateral Natural Mode Calculation

In the comparison of shake test results and matrix calculations of Section III, discrepancies existed which could not be explained on the basis of separate uncoupled vertical and lateral analyses. These differences were attributed to the structural coupling between vertical and lateral motions observed in the deflection test. In an effort to improve the correlation with test data, the Associated Matrix Program was expanded to a coupled vertical-lateral analysis, thereby permitting the inclusion of the coupled properties obtained in the deflection test. In this section, calculated natural frequencies and modes which reflect stiffness and mass coupling between vertical and lateral motions are presented for the H-21 helicopter and compared with the latest shake test data.

The matrix representation shown in Figure 65 is designed so as to be capable of simulating the test deflection data. The complex structural properties along the forward fuselage for each elastic section are shown in Figure 66. Each elastic section in the forward fuselage is typified by a frame racking matrix, which in addition to normal beam bending includes frame distortion. The results of a static deflection calculation for the forward fuselage under a 3600 lbs vertical rotor load are presented in Figure 67 and compared with the test data to justify the matrix representation. The aft fuselage is represented in the program by the elastic sections illustrated in Figure 68. Weight distribution for the dynamic model is shown in Figure 69, together with the fuselage reference axis. Mass properties are for the 13,200 lbs gross weight ballasted shake test configuration of H-21C No. 96. As a relatively important dynamic element, the engine is included in the matrix representation as an elastically supported mass using coupled engine natural modes and frequencies obtained from a shake test of the engine removed from the fuselage.



Item	Description	m	$I_{xx}$	$I_{yy}$	a	b	c	L	$A_x$	$A_y$	$A_z$	$I_G J_x$	$E I_y$	$E I_z$	$K_x$	$K_y$	$K_z$	$K_{\phi}$	$K_{\theta}$	$K_{\psi}$
1	Fwd. Rotor Bungee	1.9559	0	0	0	0	0	19.7	14.3	13.8	13.8	2.85	3.96	3.96	154	.053	.053	0	0	0
2	Fwd. Rotor Mass	1.9559	0	0	5	0	0	19.7	14.3	13.8	13.8	2.85	3.96	3.96	154	.053	.053	0	0	0
3	Rotor Shaft	1.9559	0	0	0	0	0	15.6	15.6	15.6	15.6	15.6	15.6	15.6	15.6	15.6	15.6	15.6	15.6	15.6
4	Rotor Shaft Spring	1.9559	0	0	0	0	0	15.6	15.6	15.6	15.6	15.6	15.6	15.6	15.6	15.6	15.6	15.6	15.6	15.6
5	Transmission Elastic Bay	1.9559	0	0	0	0	0	15.6	15.6	15.6	15.6	15.6	15.6	15.6	15.6	15.6	15.6	15.6	15.6	15.6
6	Transmission Mass	1.9559	0	0	0	0	0	15.6	15.6	15.6	15.6	15.6	15.6	15.6	15.6	15.6	15.6	15.6	15.6	15.6
7	Transmission Spring	1.9559	0	0	0	0	0	15.6	15.6	15.6	15.6	15.6	15.6	15.6	15.6	15.6	15.6	15.6	15.6	15.6
8	Fwd. Pylon Elastic Bay	1.9559	0	0	0	0	0	15.6	15.6	15.6	15.6	15.6	15.6	15.6	15.6	15.6	15.6	15.6	15.6	15.6
9	Bend, Fwd. Pylon	1.9559	0	0	0	0	0	15.6	15.6	15.6	15.6	15.6	15.6	15.6	15.6	15.6	15.6	15.6	15.6	15.6
10	Mass Station 100	4.5516	1962.1	3465.4	2259.4	-12.04	0	23	4.86	1.55	.91	407	1500	1500	1500	1500	1500	1500	1500	1500
11	Frame Racking Bay	0.80	0	0	0	0	0	40	4.86	1.55	.91	407	1500	1500	1500	1500	1500	1500	1500	1500
12	Mass Station 119.5	1.2674	181.99	335.22	318.87	3.46	11.05	60	4.63	1.21	2.41	557	669	669	669	669	669	669	669	669
13	Frame Racking Bay	0.8759	208.9	425.95	-9.46	6.28	-14.65	80	5.29	2.15	1.48	617	755	755	755	755	755	755	755	755
14	Mass Station 159.5	3.8563	605.3	1492.9	1441.9	18.53	8.11	54.5	5.62	1.98	2.13	796	755	755	755	755	755	755	755	755
15	Frame Racking Bay	1.047	89.49	96.30	6.77	-8.30	0	38.5	5.71	2.39	3.13	552	670	670	670	670	670	670	670	670
16	Mass Station 199.5	7.408	7044.2	3487.3	440.66	-5.24	0	31.0	5.76	2.39	3.13	552	670	670	670	670	670	670	670	670
17	Frame Racking Bay	.599	0	0	0	-4.5	0	21.0	5.81	2.39	3.13	552	670	670	670	670	670	670	670	670
18	Mass Station 243	.523	0	0	0	13.5	0	49.0	5.81	1.69	2.64	96	638	1000	1000	1000	1000	1000	1000	1000
19	Frame Racking Bay	.597	0	0	0	6.5	0	26.0	5.90	1.69	2.64	96	638	1000	1000	1000	1000	1000	1000	1000
20	Mass Station 299.5	31	Shift to Engine Axis																	
21	Frame Racking Bay	4.76	1009	995	959															
22	Mass Station 395	6405	40.27	1.71	39.35	19.42	-6.20	-10.84	40.5	5.83	2.19	1.52	64	740	204					
23	Frame Racking Bay	.415	0	0	0	24	0	5.5	51.5	4.57	1.23	1.88	36	378	86					
24	Mass Station 445	1.0539	1461.9	203.5	1567.2	10.03	0	2.08	14.0											
25	Frame Racking Bay	1.015	103	76	76	9.5	0	1.5	22.4											
26	Mass Station 494	1.705	0	0	0	-6.0	0	0	19.7	14.3	13.8	13.8	2.85	3.95	3.95	154	.053	.053	0	0
27	Frame Racking Bay																			
28	Mass Station 521																			
29	Frame Racking Bay																			
30	Mass Station 562																			
31	Frame Racking Bay																			
32	Mass Station 604																			
33	Frame Racking Bay																			
34	Mass Station 644																			
35	Frame Racking Bay																			
36	Mass Station 684																			
37	Frame Racking Bay																			
38	Mass Station 724																			
39	Frame Racking Bay																			
40	Mass Station 764																			
41	Frame Racking Bay																			
42	Mass Station 804																			
43	Frame Racking Bay																			
44	Mass Station 844																			
45	Frame Racking Bay																			
46	Mass Station 884																			
47	Frame Racking Bay																			
48	Mass Station 924																			
49	Frame Racking Bay																			

Figure 65 H-21 Vertical-Lateral Matrix Representation

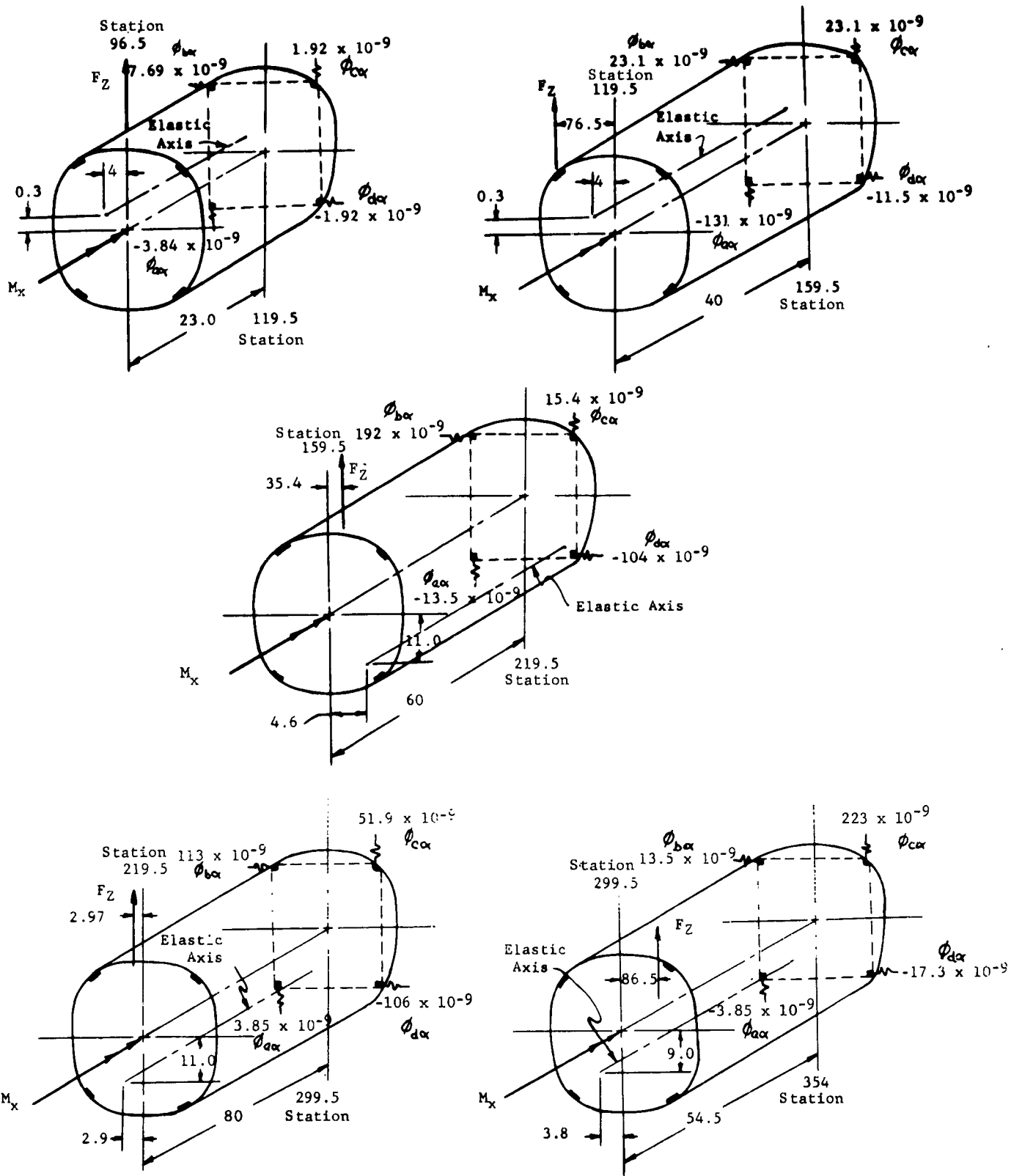


Figure 66 H-21 Forward Fuselage Elastic Properties





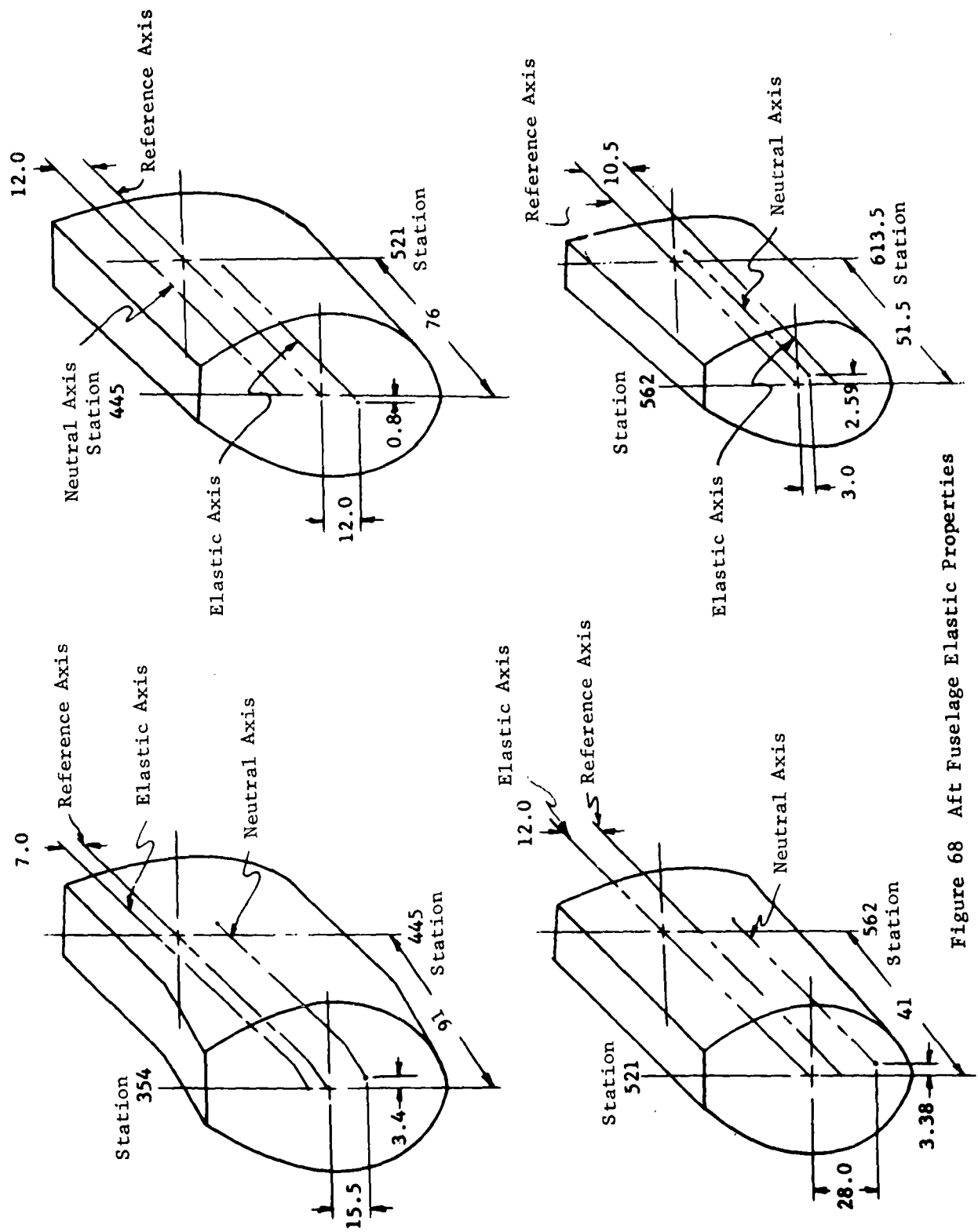
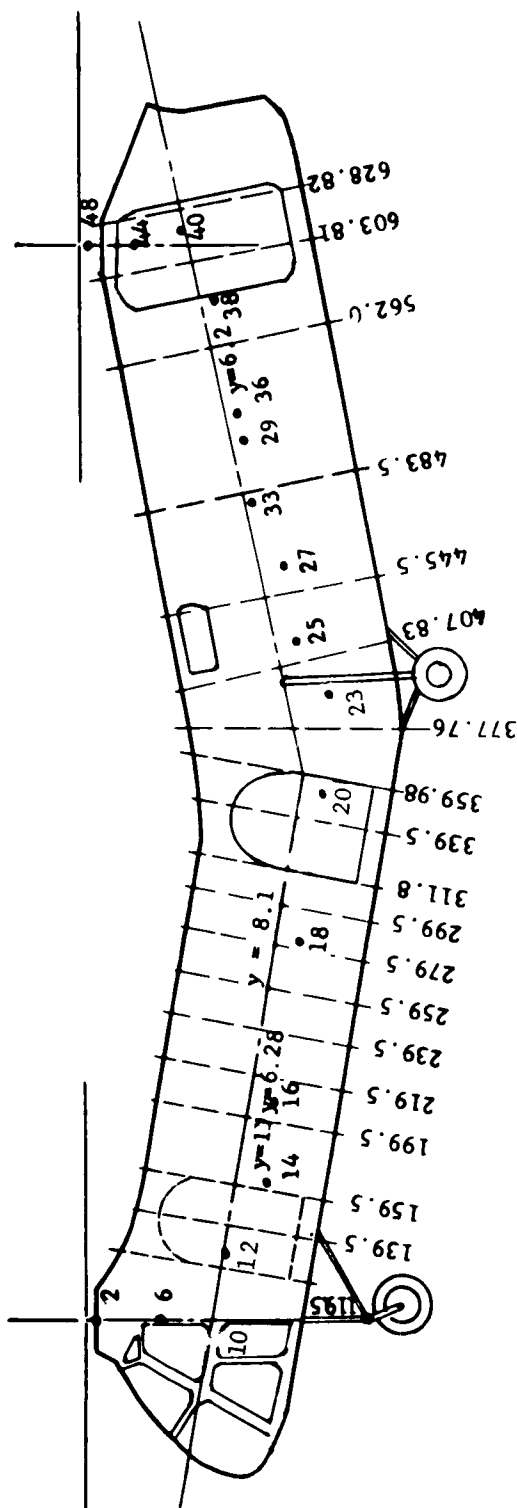


Figure 68 Aft Fuselage Elastic Properties



Matrix No.	Mass Lb-Sec <sup>2</sup> In.	Weight Lbs.	Inertia Lb-Sec <sup>2</sup> -In.				Matrix No.	Mass <sup>2</sup> Lb-Sec <sup>2</sup> In.	Weight Lbs.	Inertia Lb-Sec <sup>2</sup> -In.			
			I <sub>α</sub>	Roll I <sub>β</sub>	Pitch I <sub>γ</sub>	Yaw				I <sub>α</sub>	Roll I <sub>β</sub>	Pitch I <sub>γ</sub>	Yaw
2	1.9559	754					25	.599	231				
6	1.0549	407				61	27	.523	202				
10	4.5516	1758				2259.4	29	.597	230				
12	0.80	309	56	1962.1	3465.4		33	4.76	1838	1009	995	959	
14	1.2674	488	181.99	335.22	318.87		36	.6405	247	40.27	1.71	39.25	
16	0.8759	338	208.9	262.3	425.95		38	.415	160				
18	3.8563	1488	605.3	1492.9	1443.9		40	1.0539	407	1461.3	2035.0	1567.2	
20	1.047	404	89.49	96.3	6.77		44	1.015	392	103	76	76	
23	7.408	2860	7044.2	3487.3	4406.8		48	1.705	658				

Figure 69 Reference Axis Location and Weight Distribution

Coupled Vertical-Lateral Natural Mode Calculations - Using the stiffness properties illustrated in Figures 66 and 68 matrix calculations are performed, and the results shown in Figures 71 to 77. The frequency results are shown below compared to the corresponding shake test results.

<u>Mode</u>	<u>Matrix, CPS</u>	<u>Test, CPS</u>	<u>Figure</u>
First	7.37 (Normalized to engine)		71
Second	7.62	8.1	71
Third	8.45 (Normalized to engine)	8.4	72
Third	8.45 (Normalized to engine)	9.45	72
Fourth	9.58	9.45	73
Fourth	9.58	8.4	73
Fifth	8.85	10.4	74
Sixth	11.66	11.8	74
Seventh	12.16	11.9	75
Eighth	12.88	13.15	75
Ninth	14.53		76
Tenth	16.09	14.1	76
Eleventh	17.8	15.5	77
Twelfth	18.9		77

#### First Matrix Mode

Figure 71

The first calculated matrix mode of the fuselage at 7.37 cps results from the predominant yaw and roll suspension mode of the engine at 7.43 cps. The test response curves of the fuselage showed no peak response near this frequency, but a slight response of the engine vertical pickup is noted at 7.5 cps indicating the possible presence of this mode. It is reasonable to conclude that the generalized force input from the shaker located at Fuselage Station 312 was insufficient to excite this mode of nearly pure engine motion. In the absence of any peak fuselage response, but with strong indication of an engine suspension mode with very little fuselage coupling, it is considered that frequency and shape correlation is present by comparison with the engine shake test results.

#### Second Matrix Mode

Figure 71

Calculated at 7.62 cps, the second matrix mode shows the fundamental vertical bending shape of the fuselage with no lateral coupling motion except for yaw. This yaw motion of the engine results from coupling with the engine suspension mode at 7.43 cps. In the fuselage ground shake test the comparable vertical bending mode of the fuselage responds at 8.1 cps. The matrix mode compared with the test agrees quite well in shape, and somewhat less in frequency with a variation of 0.5 cps which is considered satisfactory. However, the test mode shows some aft pylon lateral motion and additional magnification of engine pitch motion not evident in the matrix mode.

#### Third Matrix Mode

Figure 72

The third calculated matrix mode of the fuselage at 8.45 cps is a predominant longitudinal-pitch mode of the engine. Comparison with the mode associated

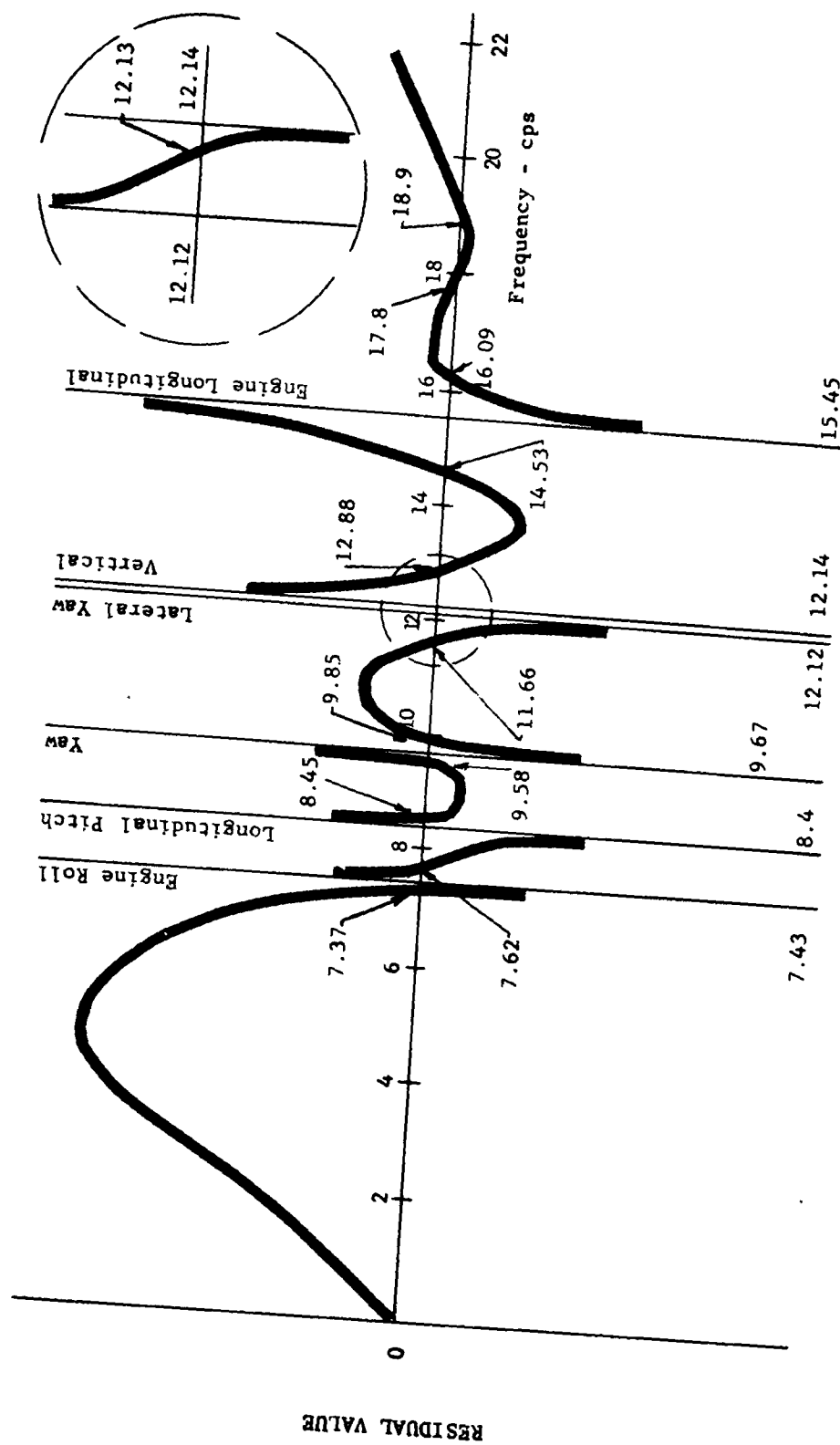


Figure 70 Matrix Residual Plot

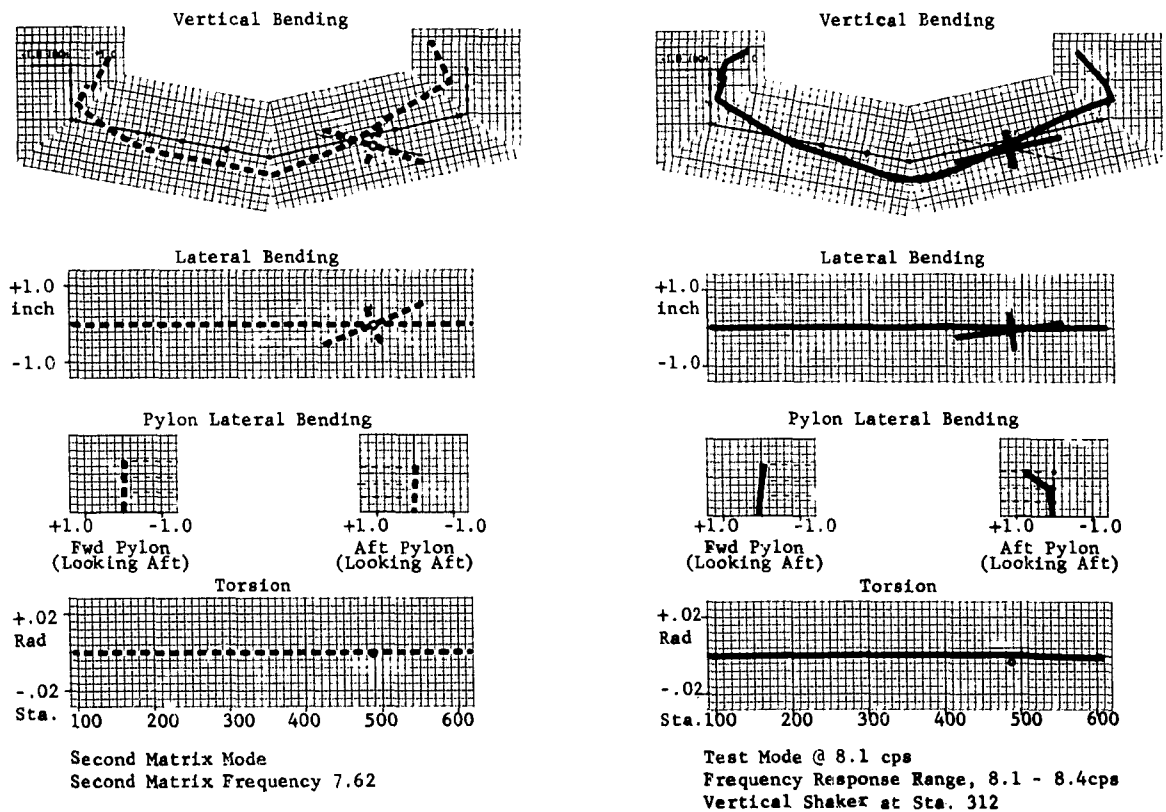
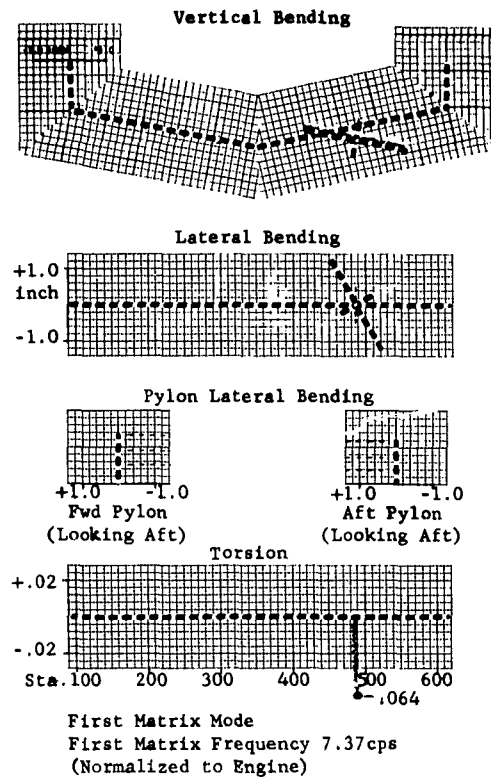


Figure 71 First and Second Matrix Modes

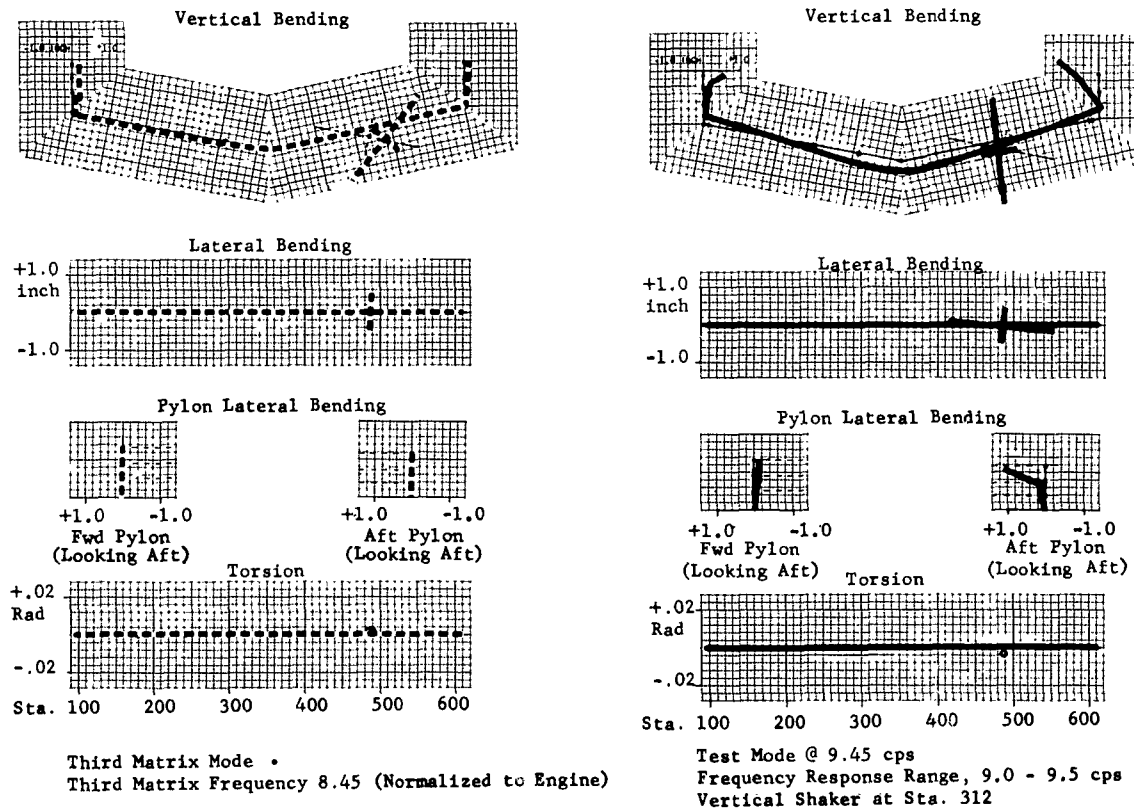
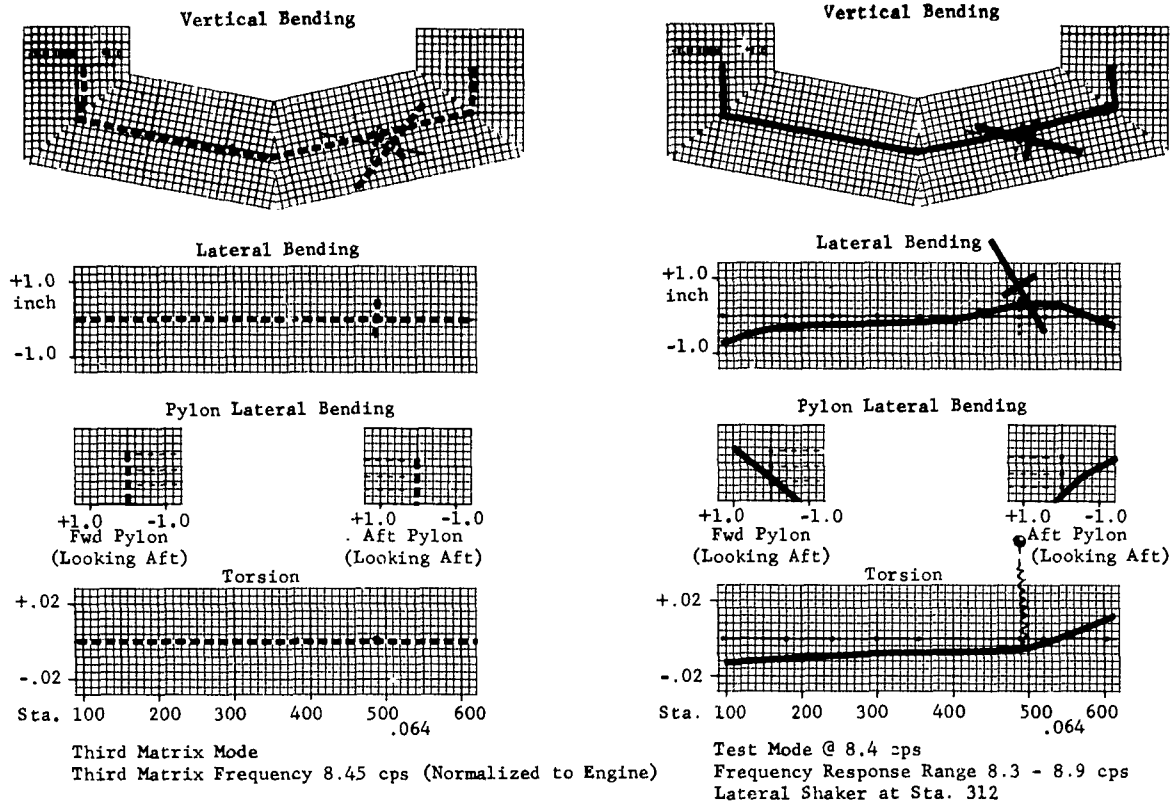


Figure 72 Third Matrix Mode

with the next higher peak response frequency at 8.4 cps provides excellent frequency agreement, but the calculated shape shows little resemblance to the test mode. However, with the engine test longitudinal-pitch mode at 8.4 cps, it is reasonable to expect a coupled fuselage engine mode near this frequency with a similar shape.

Further investigation of the third matrix mode includes comparison with the test mode at 9.45 cps which shows better shape comparison with mostly longitudinal-pitch motions, but the frequency match appears unacceptable. The engine-fuselage modal phase is reversed between analytical and test results, and further, the test mode shows significant fuselage response in the fundamental vertical bending mode. In attempting to understand the modal discrepancies which exist, consider the engine mode to be highly damped in the coupled system whereas in the matrix analysis no damping is included. Suppose, for example, that the rigid-engine fuselage frequency is at nearly the same location as the highly damped engine mode, then it would be expected that the fuselage frequency would remain unchanged, while the coupling effect would displace the engine mode to a higher frequency. It is hypothesized that the test shape remains as the fundamental lateral mode of the fuselage with a negligible frequency change from engine coupling, whereas in the matrix calculation the lack of damping permits the fuselage lateral mode to be displaced to the fourth matrix mode at 9.58 cps.

#### Fourth Matrix Mode

Figure 73

Calculated at 9.58 cps, the fourth matrix mode appears as the first lateral-torsion mode of the fuselage highly coupled to the engine. Continuing the frequency sequence from the ground shake test, this mode is compared to the test mode at 9.45 cps which provides an excellent frequency comparison, but shows no similarity in shape. As discussed previously, it appears that this matrix mode and the third matrix mode are reversed relative to test. Considering this reversal, the fourth matrix mode is compared to the test mode at 8.4 cps. This mode comparison is made acceptable in most respects by excluding the engine motion. Matrix calculations indicate more pitch and less torsion motion of the engine than test data. Also, yaw, pitch, and lateral motions occur out-of-phase from the measured data.

#### Fifth Matrix Mode

Figure 74

Similar to the fourth matrix mode with pitch and torsion of the engine, the fifth mode at 9.85 cps follows the pattern of the engine yaw mode at 9.67 cps, balanced by the fuselage shape of the preceding matrix mode. A comparison with the test mode at 10.4 cps shows fair frequency agreement and good engine motion agreement excepting the phase difference noted between pitch and yaw. However, the corresponding fuselage modes obtained from test and calculation indicate poor agreement.

#### Sixth Matrix Mode

Figure 74

The sixth calculated matrix mode of the fuselage at 11.66 cps shows a forward pylon longitudinal mode combined with vertical-yaw engine motion and a lesser



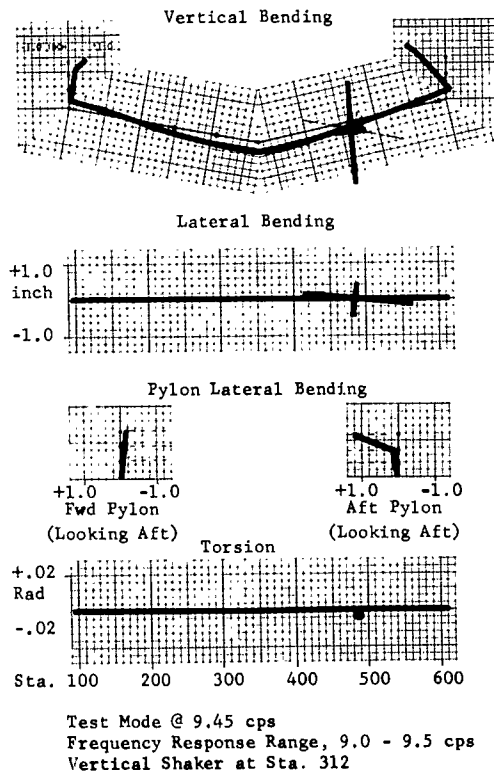
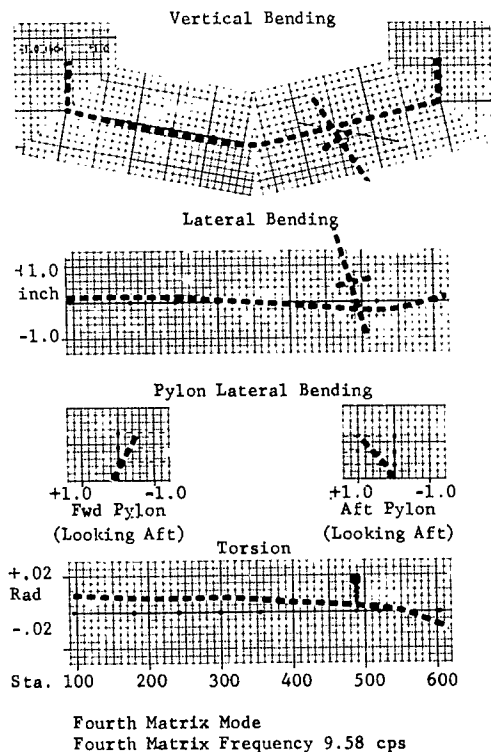
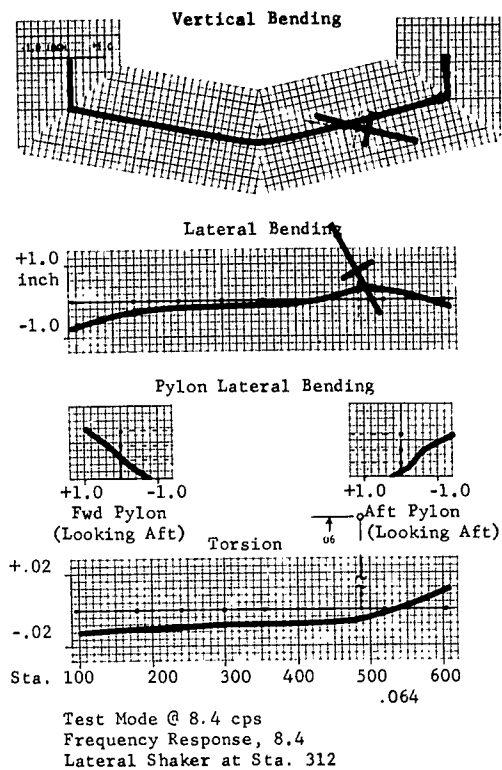
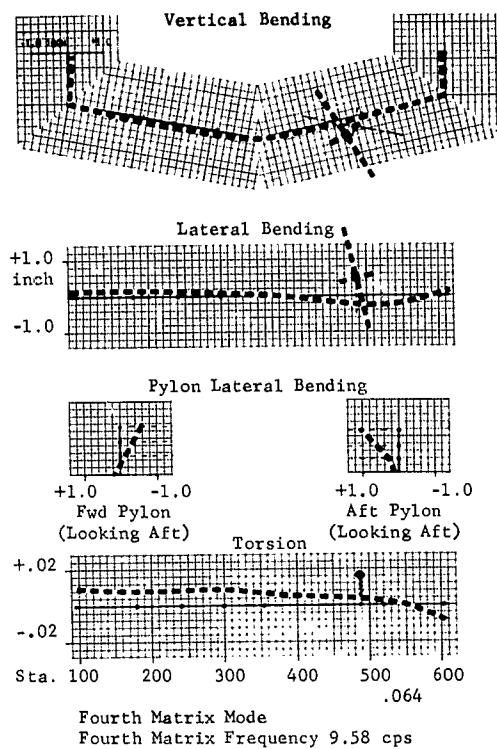


Figure 73 Fourth Matrix Mode

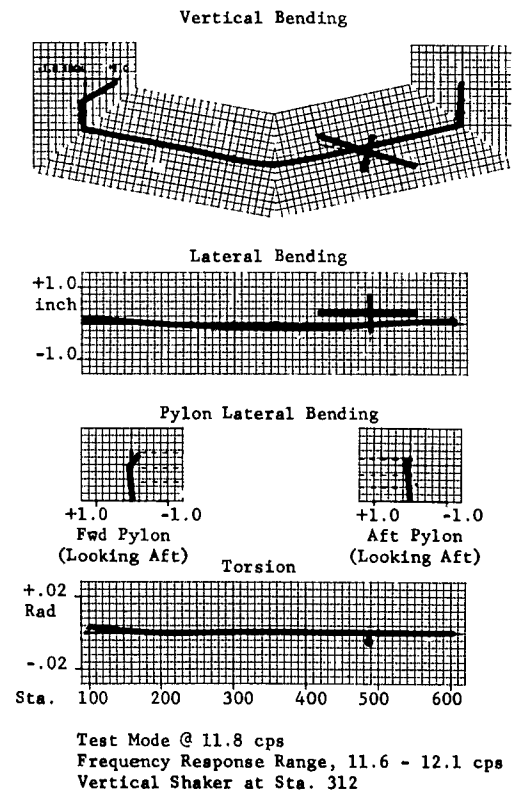
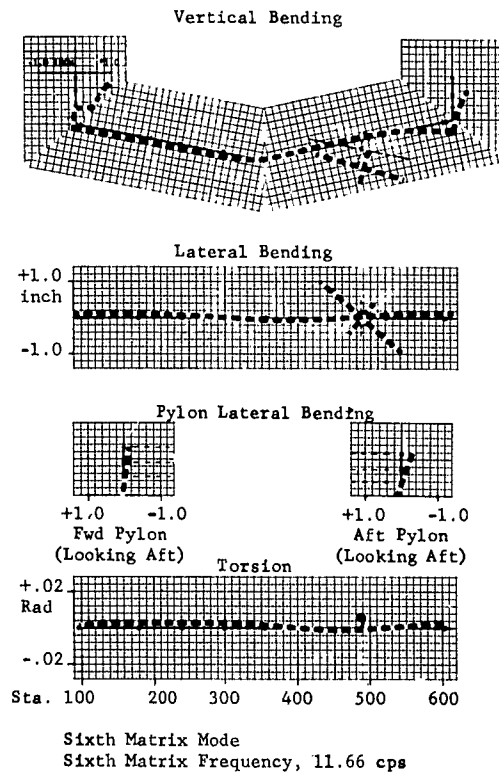
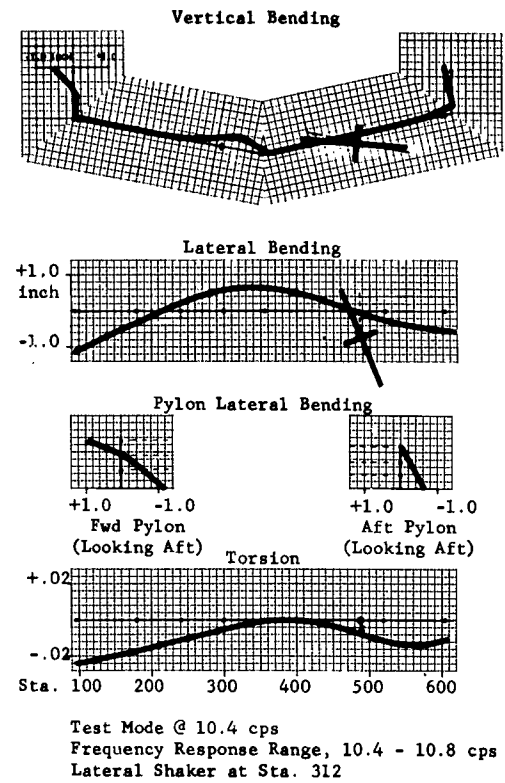
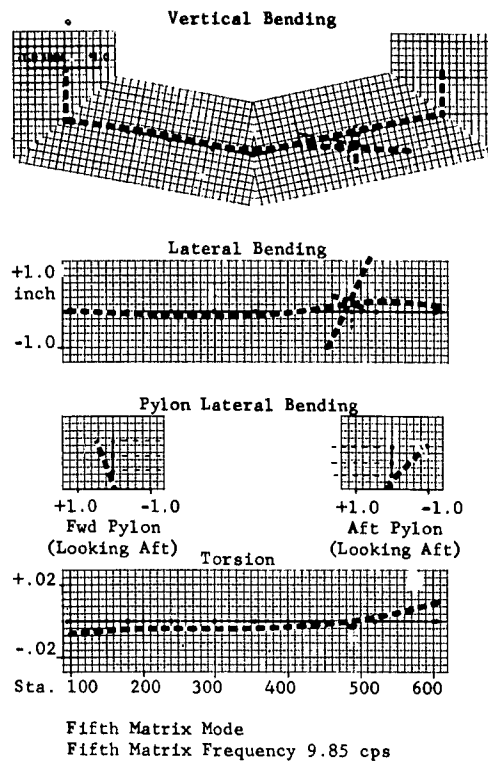


Figure 74 Fifth and Sixth Matrix Modes

amount of aft pylon motion. In the fuselage ground shake test the comparable mode at 11.8 cps provides an excellent frequency match, but only agrees in shape at the forward pylon with the engine and aft pylon motion being absent.

#### Seventh Matrix Mode

Figure 75

The shape of the seventh matrix mode at 12.13 cps resembles an engine lateral-yaw mode with the addition of fuselage motion, predominantly lateral bending and torsion. Comparison with the 11.9 cps test mode provides very good frequency correlation, and the engine modal shapes show good agreement, but along the fuselage the correlation tends to fluctuate. In the vertical and lateral bending motions and forward pylon motion, the mode shapes appear nearly identical. However, the aft pylon motion shows no agreement and the torsional shape from test is more complex than the calculated shape, although the phasing is in general agreement.

#### Eighth Matrix Mode

Figure 75

The eighth matrix mode at 12.88 cps is a predominant forward pylon longitudinal mode with coupling introducing lateral bending and torsion, together with yaw motion of the engine. The comparable mode from the fuselage ground shake test is 13.15 cps. Comparison with the test response shows very good frequency agreement, good shape agreement at the forward and aft pylons, but vertical fuselage and engine pitch motion are reversed between test and calculated results. In the coupled lateral bending and torsion motions the test, unlike the calculated results, shows no significant response except for engine yaw motion of approximately one-half the calculated value.

#### Ninth Matrix Mode

Figure 76

A test mode comparable to the ninth matrix mode at 14.53 cps was undefined by the ground shake test. However, it is quite possible that this mode exists, but with the shaker location at Station 312, a node point of the calculated mode, the generalized shaker force in this mode was close to zero and thus the mode was not excited using this shake test configuration. The calculated shape shows in-phase pylon motion, i.e., both pylons move aft simultaneously, engine pitch and yaw motions, and a small amount of aft pylon lateral motion.

#### Tenth Matrix Mode

Figure 76

The tenth matrix mode at 16.09 cps shows mostly lateral and torsion motions of the fuselage coupled with lateral, yaw and roll motion of the engine. A comparison to the test mode at 14.1 cps shows only marginal frequency agreement, and good agreement of fuselage motion with the exception of a 180° phase shift at the forward pylon. Also, good agreement in engine motion exists with large in-phase yaw and pitch motion. The matrix mode contains vertical and lateral engine motions whereas the test shows no similar response.

#### Eleventh Matrix Mode

Figure 77

In the eleventh matrix mode at 17.8 cps, the calculated shape shows a highly coupled system with the lateral bending shape of the same magnitude as the vertical bending response. Comparing with the test mode at 15.5 cps only

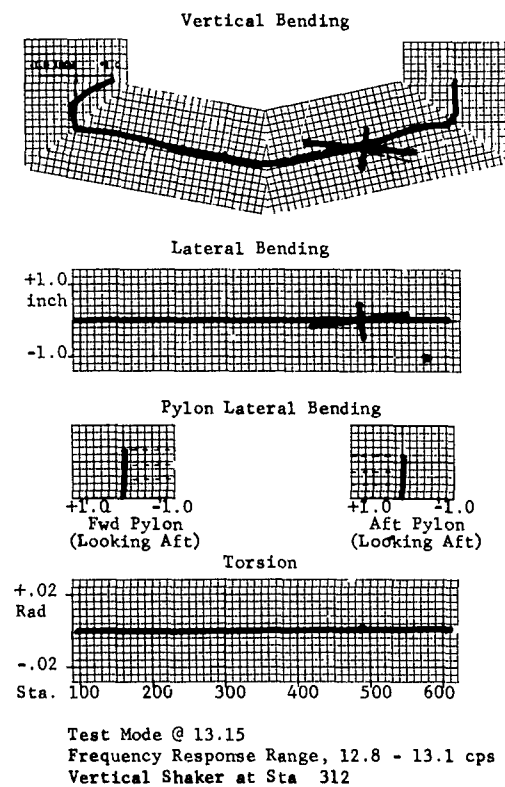
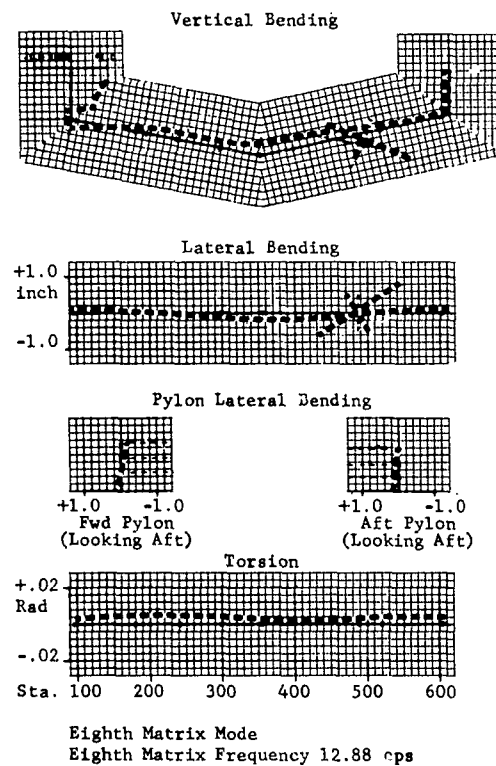
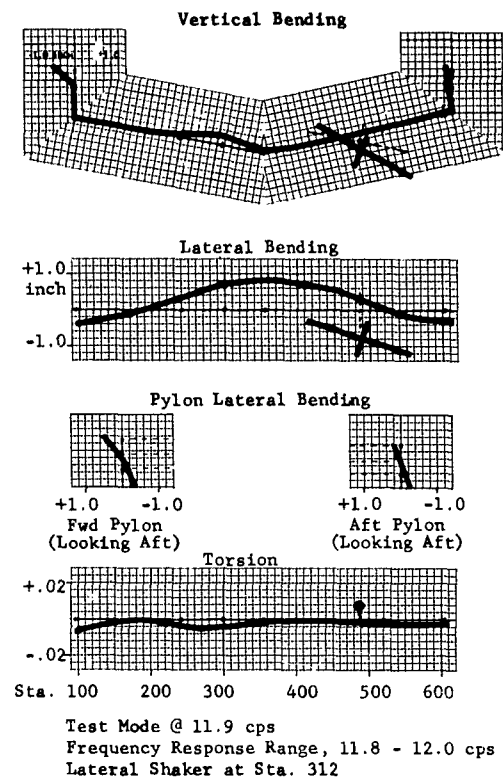
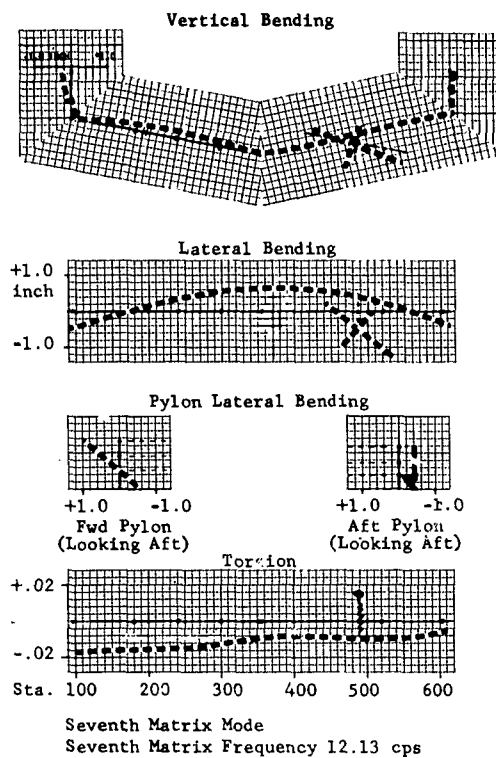


Figure 75 Seventh and Eighth Matrix Modes

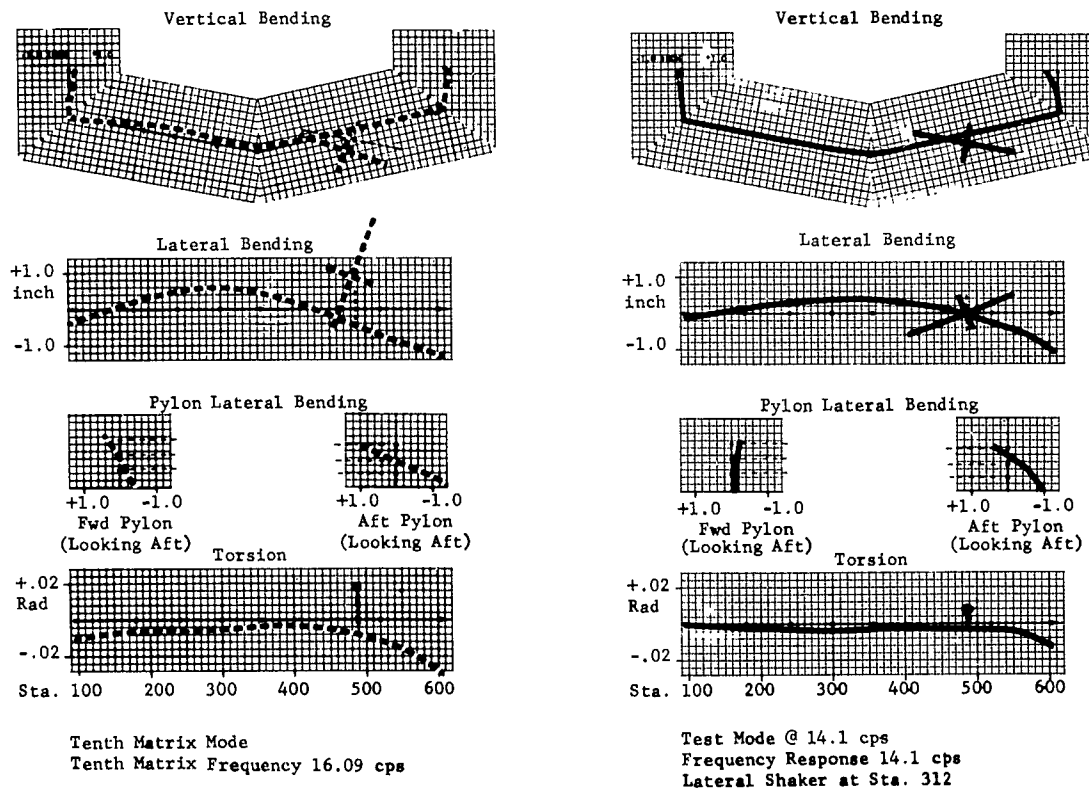
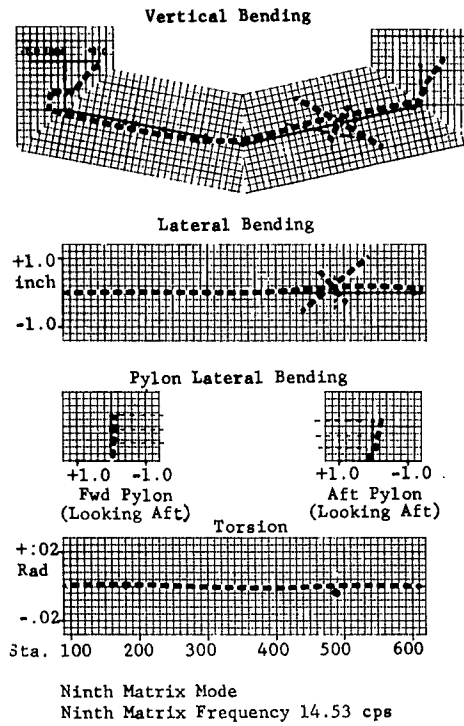


Figure 76 Ninth and Tenth Matrix Modes

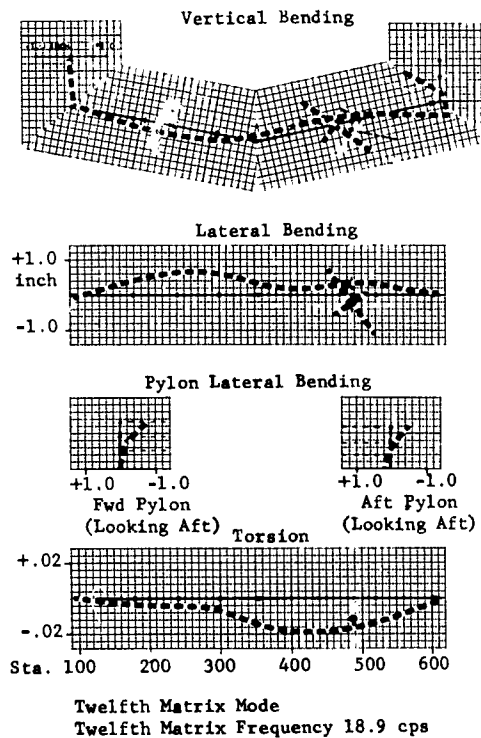
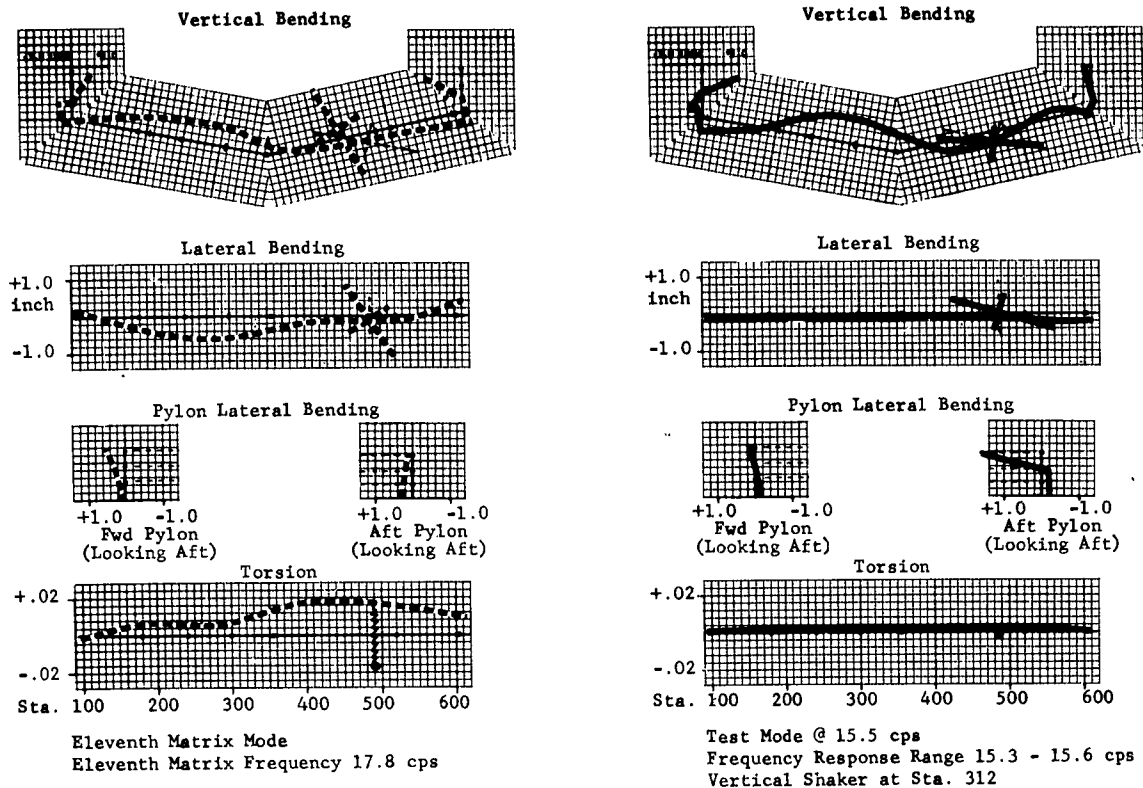


Figure 77 Eleventh and Twelfth Matrix Modes

a marginal frequency match exists; however, in the shape comparison the agreement is somewhat better. The vertical bending shape compares reasonably well, but the lateral and torsional test motions are negligible compared to the calculated values.

#### Twelfth Matrix Mode

#### Figure 77

The twelfth matrix mode was calculated at 18.9 cps, beyond the limit of available shake test data. The calculated shape shows aft pylon longitudinal motion with no corresponding forward pylon motion, equally large, flexible in-phase lateral pylon motion, and nearly zero torsion and lateral motions at both ends of the fuselage. In detail, the bending and torsion shapes increase toward mid-fuselage with the bending peaking at Station 250 and the torsion at Station 400.

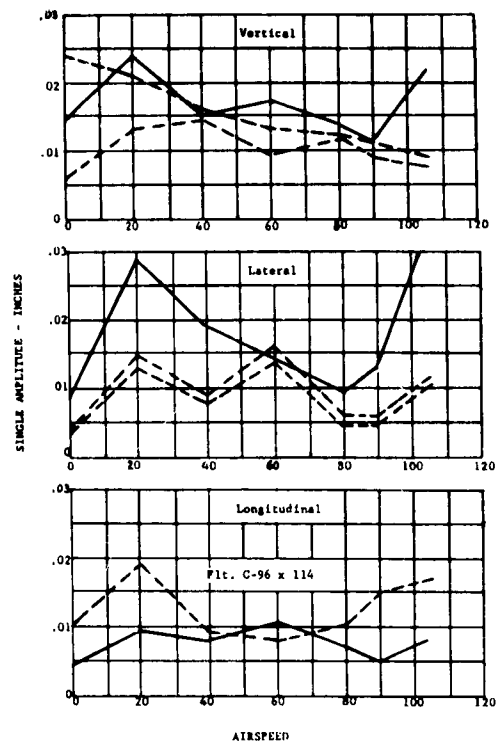
#### C. Forced Response with Measured Hub Loads

Calculated and measured cockpit floor amplitudes for the 40 and 90 knot rotor speed sweeps and the results of the airspeed sweep at a rotor speed of 258 rpm are shown in Figure 78. The calculated amplitudes are shown on each figure by a solid line, the test results are shown with a dotted line representing the upper and lower limits of a scatterband obtained by reading two cycles of data for each flight configuration. However, in the less significant longitudinal direction, the measured amplitudes include only one data point per run at comparable rpm and airspeed from flight C96X114.

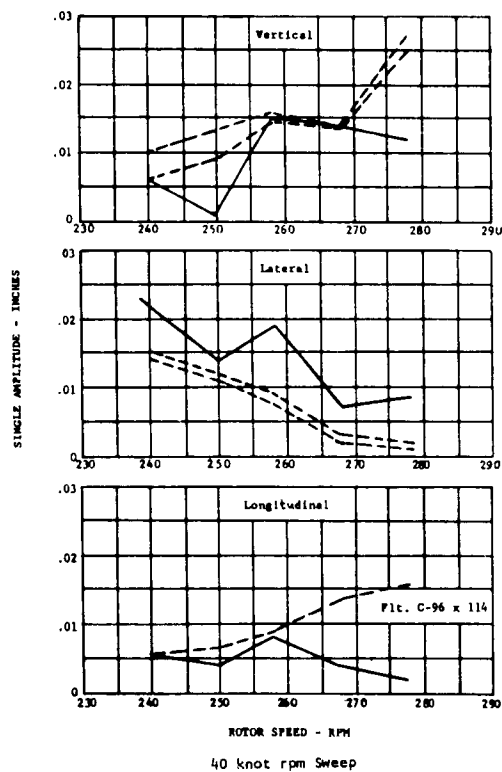
In the 40 knot airspeed sweep the calculated vertical response is identical to the measured values at three of the recorded rpm's. Below 258 rpm the calculated value decreases sharply while the measured amplitude continues in an upward trend. At 278 rpm the measured amplitude increases to a maximum while the calculated value remains nearly constant. Laterally, the calculated response is somewhat higher than the measured. In the longitudinal direction, the correlation is good excepting the 268 and 278 rpm data points which show the measured response increasing and the calculated response decreasing.

In the vertical direction, the 90 knot sweep shows better correlation than that shown in the 40 knot sweep. The calculated vertical motion is nearly within the range of measured response at all rpm's, except the maximum rotor speed of 278 rpm which shows the measured amplitude approximately twice the calculated value. The lateral response is identical at 240, 250 and 278 rpm, but poor at 258 and 268 rpm. In the 90 knot sweep, no correlation exists between the calculated and measured longitudinal motion. It is of interest to note that in the longitudinal motion low rpm ranges, where the least agreement exists, the measured longitudinal motions are nearly three times the values shown in the 40 knot sweep, but the calculated values show the same order of magnitude.

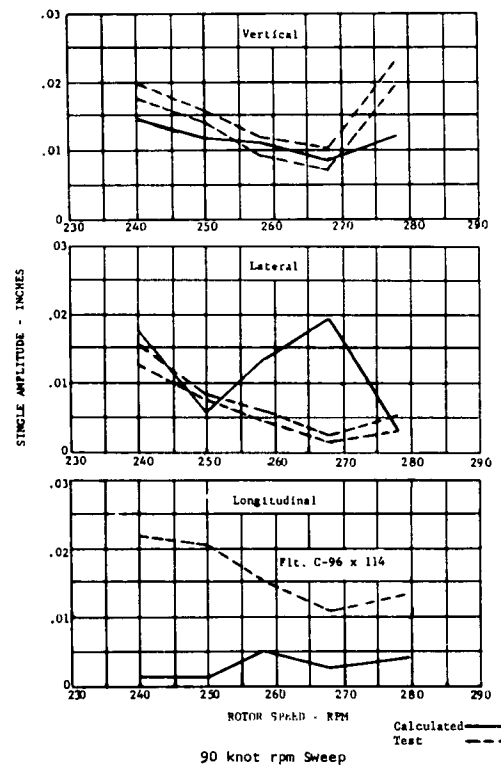
As in the rpm sweep, the vertical response again shows the best correlation with test data in the airspeed sweep. In general, the vertical motions remain nearly within the bounds of the measured data, except for the maximum airspeed point which shows the calculated value nearly twice the measured amplitude. Lateral and longitudinal results generally indicate the proper trend but do not compare as favorably in amplitude. In the lateral direction, the calculated values are generally about twice the measured values; in the longitudinal direction, the measured values are usually about twice the calculated values.



258 rpm Airspeed Sweep



40 knot rpm Sweep



90 knot rpm Sweep

Figure 78 Cockpit Floor Response



#### D. Conclusions

An analytical matrix program has been developed and presented for the calculation of coupled six degrees of freedom forced and natural modes of an elastic fuselage structure. As in the past uncoupled analyses, the matrix representation includes concentrated masses and inertias, distributed stiffness properties in bending, shear or torsion, local spring properties, a wandering elastic axis and uncoupled suspended masses. In addition to conventional beam elements, the program includes matrices representing (1) elastic sections with frame racking, (2) coupled six degree of freedom mass systems, and (3) forcing functions at any beam station. The method was programmed for a UNIVAC 1103A at Wright Field.

The method was applied to the H-21 helicopter fuselage to predict natural modes and in-flight forced responses. Stiffness properties were obtained from a deflection test performed earlier on the same fuselage. The matrix representation checked closely with the test deflection data when vertical-lateral deflections under a 3,600 lb vertical forward rotor load were calculated.

An effort was made in the early part of the next phase of the contract to define another significant unknown, the 1800 lb dynafocal suspended R2800 engine and accessory package. A shake test was conducted on the engine-dynafocal-truss assembly removed from the aircraft and attached to a concrete floor. Frequency response peaks and attendant mode shapes resulted at 7.43, 8.4, 9.67, 12.12, 12.14, and 15.45 cps, but in several instances the response peak bandwidths from different pickups varied by as much as 1/2 cps. These test modes were used in the matrix engine simulation.

This test-authenticated matrix simulation was next used to calculate natural modes of the fuselage at 13,200 lb gross weight with rotors replaced by equal weight rigid concentrated masses corresponding to a hung shake test configuration of the same aircraft, also conducted under Phase V. Twelve natural modes resulted in the range from 7 to 20 cps, six of which were related to the dynafocal engine suspension. Reasonable frequency agreement appeared between the calculated and test data, but mode shape agreement was not as favorable.

The first mode at 7.37 cps was engine roll and had no fuselage shake test counterpart because a single hydraulic shaker in the cabin did not excite this mode. First vertical bending was predominant in the second mode at 7.62 cps calculated, and compared closely in shape and frequency with an 8.1 cps test mode. The third mode at 8.45 cps was a predominant engine mode. Fourth matrix at 9.58 cps was fundamental lateral bending-torsion, corresponding in shape to a test mode at 8.4 cps. Fifth matrix at 9.35 cps was a mixture of engine and fuselage lateral bending-torsion. The calculated 11.66 cps sixth mode matched the second vertical bending-highly coupled with lateral bending-torsion shape of the 10.4 cps test mode. Seventh matrix at 12.13 cps, second lateral bending-torsion, was similar to an 11.9 cps test mode. Eighth to twelfth matrix modes at 12.83, 14.53, 16.09, 17.3 and 18.9 cps were more complex shapes.

Forced response calculations were performed using the H-21 matrix representation with applied  $3\Omega$  shaft loads obtained from the in-flight load measurement program. Comparison with measured cockpit floor response shows very good agreement in the vertical direction. During the airspeed sweep, nearly all the calculated amplitudes are within the measured data scatterband with the amplitude decreasing nearly uniformly from an average of .015 in. at hover to .010 in. at 90 knots. In the 40 knot rpm sweep excluding two rpm points, the calculations follow the measured data increasing from 0.01 in. at 258 rpm to .025 in. at 278 rpm. Showing identical trends, the 90 knots sweep amplitude decreases from .015 in. at 240 rpm to a minimum of .010 in. at 264 rpm and then, increases to a peak at .012 in.

In the lateral direction at the cockpit floor, the calculated response generally exhibits the proper trends but does not compare as well as the vertical in absolute magnitude. Excluding two data points at 258 and 268 rpm, the lateral motion during the 90 knots rpm sweep shows the same trends as the measured data, but with somewhat larger magnitude. In the airspeed sweep the response is similar to the vertical motion with a peak amplitude of .030 in. and in both the 40 and 90 knot rpm sweeps the amplitude decreases with rpm from .015 in. at 240 rpm to less than .005 in. at 278 rpm.

An effort at correlation of cockpit floor vibration and rotor loads was made. Longitudinal and lateral vibration levels generally follow the longitudinal and lateral force trends with airspeed, low in hover, an increase to transition, a drop toward 80 knots cruise and an increase at 105 knots. Vertical vibration for the airspeed run recorded is high at hover and transition, and then, drops with airspeed, so that it does not correlate consistently with any single force.

In the 40 knot rpm sweep, vertical and longitudinal cockpit floor motions increase with rpm, in concert with longitudinal load. In the 90 knot rpm sweep, the vibration levels are bucket shaped, being minimal at 265 rpm. A study of the measured load phasing along with calculated forced modes explained the bucket effect with speed. At low rotor speed, forward rotor longitudinal and aft rotor vertical forces were phased so as to cancel each other's cockpit motion effect, leaving the large forward rotor vertical force to produce a large vibration level. As rpm increased, the forward rotor vertical force reduced and the vibration level dropped to its minimum. Above 260 rpm, the phasing changed so that forward rotor longitudinal and aft rotor vertical forces were additive, and the vibration level increased again.

## SECTION VIII

### A METHOD FOR THE PREDICTION OF COUPLED VERTICAL-LATERAL MODES INCLUDING MULTI-DIRECTIONAL DAMPED ROTOR EFFECTIVE MASS

#### A. General

The Associated Matrix Method of Section VII was extended to include an analytical representation for a rotating rotor. The large inherent damping of the rotor made it necessary to double the matrix order to include the effect of rotor aerodynamic damping. In addition, engine damping and a reduced torsional stiffness were used in the final representation of the H-21 helicopter. Rotor and damped engine properties are shown in Figure 79.

The method was evaluated by simulating the in-flight shake test and comparing the analytical results with test results.

#### B. In-Flight Response at Normal Rotor Speed

Fuselage Response - Calculated in-flight fuselage response at normal rotor speed compared to measured response is presented in Figures 80 and 81 for vertical and lateral excitation respectively. Response curves present double amplitude motion in inches as ordinate against shaker frequency in cps as abscissa for four fuselage locations. For vertical excitation, response curves are included for longitudinal motion at the forward transmission, for vertical motion at the cockpit floor and Station 602 and for longitudinal motion at the aft transmission; for lateral excitation, response comparisons are presented for lateral motion at the cockpit floor, Station 359 W.L. 44, Station 602 and the aft transmission. Both test values and analytical response represent the resultant amplitude for a 200 lb vertical or lateral excitation at Station 312, the hydraulic shaker location.

The first noticeable in-flight test peak appears at 5.4 cps with lateral excitation in Figure 81 corresponding to the fixed system rigid lag frequency ( $\text{rigid lag} + 1\Omega$ ). This response peak is outside the frequency range used for analytical calculations. Cockpit floor vertical response shows the next higher frequency at 7.4 cps with no corresponding analytical response.

The fundamental vertical bending mode is calculated in the vicinity of 8.0 cps in Figure 80 which agrees with the peak area from test near 8.1 cps. However, the matrix response amplitude is much higher than the measured response. The next higher test response appears at 8.8 to 9.1 cps with vertical excitation, but no corresponding analytical peak exists. In the same frequency region, a response peak occurs with lateral excitation, but again analytical comparison is not apparent.

At 9.8 to 10.1 cps the next vertical test peak occurs with vertical excitation, showing measured peak response at Station 602 vertical and aft transmission longitudinal. Analytically, a similar peak occurs at the aft transmission. Similar test response is noted with lateral excitation for lateral motion at the cockpit floor. No corresponding analytical peak appears with lateral excitation.

# ENGINE PROPERTIES

Direction	Mass or Inertia lb-sec <sup>2</sup> /in. or lb-sec <sup>2</sup> -in.	Mode at 46.6 rad/sec	Mode at 52.7 rad/sec	Mode at 60.6 rad/sec	Mode at 76.1 rad/sec	Mode at 76.4 rad/sec	Mode at 97.0 rad/sec
Vertical(z)	4.76	+ .002	0	.001	-.001	-.0037	0
Pitch (φ)	995	0	-.00012	.00092	0	-.000057	.00013
Longitudinal(x)	4.76	0	.001	.001	-.004	.001	-.0121
Lateral(y)	4.76	0	0	-.001	-.0082	.001	0
Yaw(δ)	959	.001605	0	.000555	-.000685	-.000011	.000013
Roll(ε)	1009	.00253	0	-.00005	-.000017	.000036	0
Modal Test Damping (in. -lb-sec)		.048204	.000139	.001704	.004348	.000757	.003254

## ROTOR PROPERTIES FOR 258 RPM

### Aft Rotor

	Static Hub Lag	Static Hub Flap	Static Blade Lag	Static Blade Flap	Rigid Lag	1st Flex Lag	Rigid Flap	1st Flex Flap	2nd Flex Flap
Mass, lb-sec <sup>2</sup> /in.	.4782	.2547	.4108	.4853	.08807	+.1144	.09155	.09224	.0882
Inertia, lb-sec <sup>2</sup> -in.	47.82	12.48	6124.	6159.0	7.854	136.8	27.39	69.18	131.9
Frequency, rad/sec					.1342	-.09704	.1459	-.08844	.06231
1st Moment, $\sum m_i z_i$ or $\sum m_i y_i$					23.89	-1.349	24.42	-.4068	.2866
Prod. of Inertia, $\sum m_i z_i^2$ or $\sum m_i y_i^2$					.1982	3.718	2.463	1.383	1.925
Damping, $\sum C_i z_i$ or $\sum C_i y_i$									

### Fwd Rotor

	Static Hub Lag	Static Hub Flap	Static Blade Lag	Static Blade Flap	Rigid Lag	1st Flex Lag	Rigid Flap	1st Flex Flap	2nd Flex Flap
Mass, lb-sec <sup>2</sup> /in.	.4779	.2547	.4842	.5586	.1013	.1003	.1127	.08026	.1116
Inertia, lb-sec <sup>2</sup> -in.	47.79	12.48	7142.	7177.0	8.101	127.0	26.0	61.31	130.1
Frequency, rad/sec					.1647	-.09518	.1852	-.07677	.07918
1st Moment, $\sum m_i z_i$ or $\sum m_i y_i$					27.62	-1.323	30.09	-.3531	.3642
Prod. of Inertia, $\sum m_i z_i^2$ or $\sum m_i y_i^2$					.1932	2.281	2.59	1.025	2.024
Damping, $\sum C_i z_i$ or $\sum C_i y_i$									

Figure 79 Rotor and Engine Properties

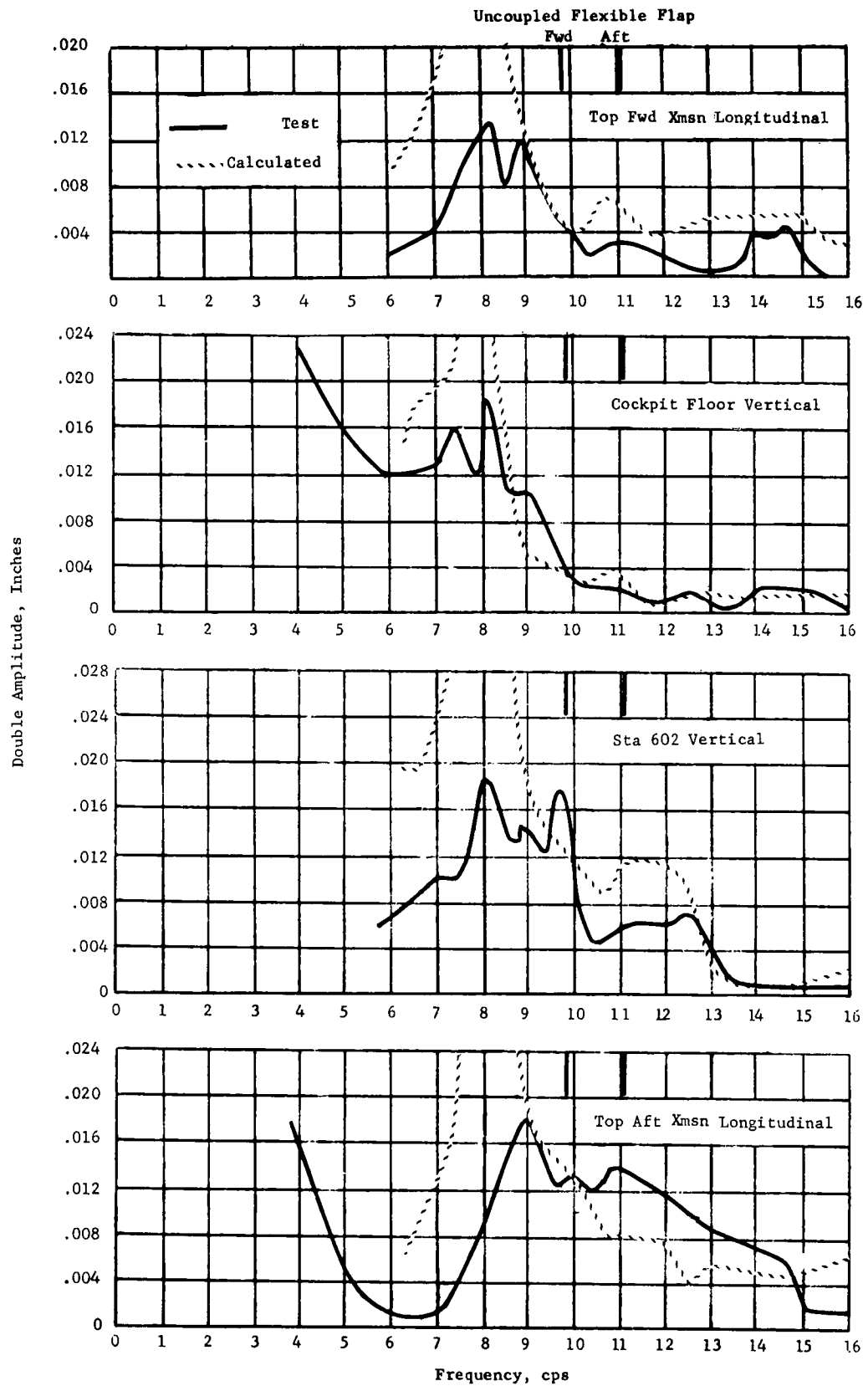


Figure 80 In-flight Response for 200 lb. Vertical Force at Station 312

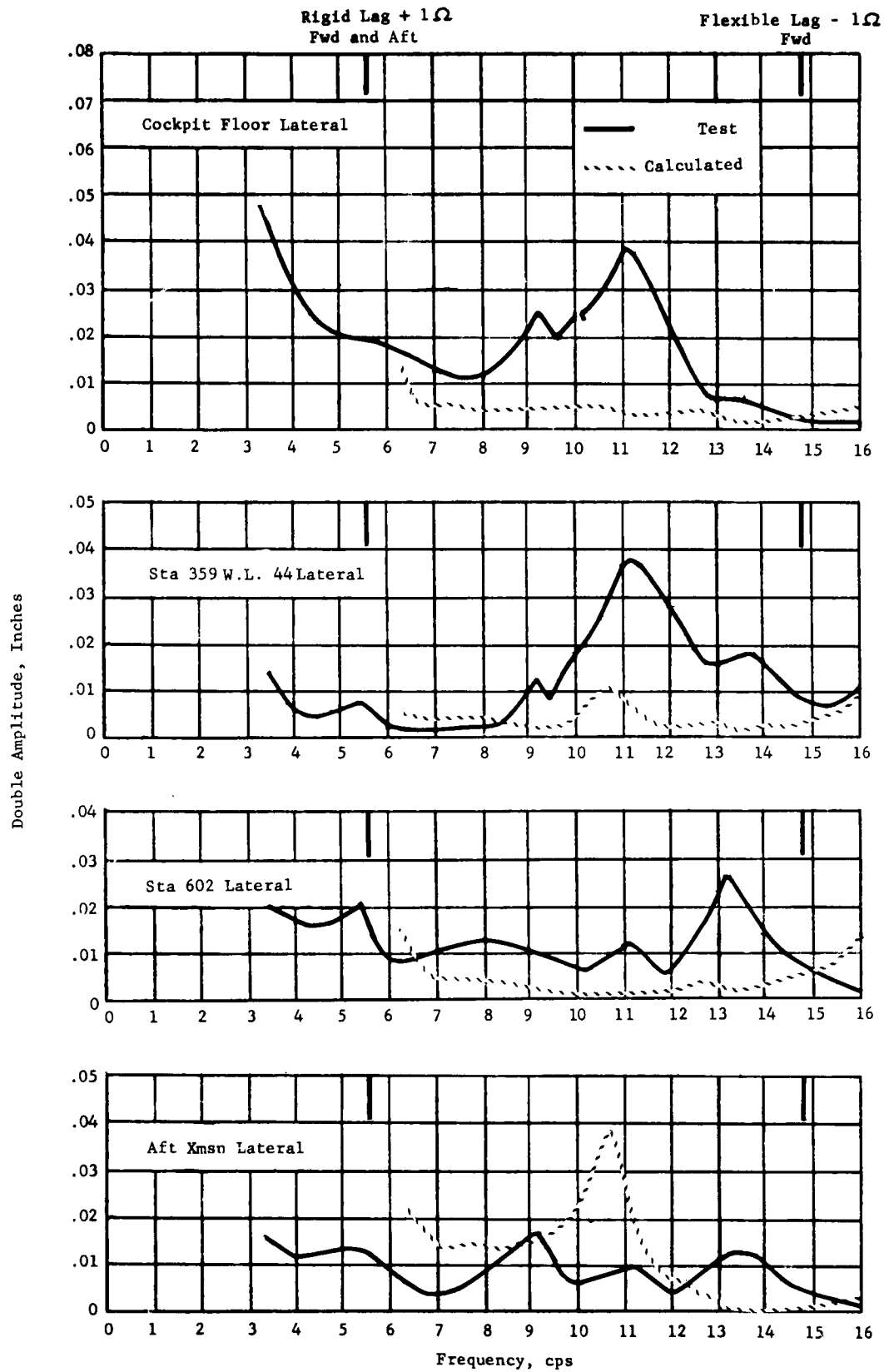


Figure 81 In-flight Response for 200 lb. Lateral Force at Station 312

The next significant test response region appears with vertical excitation at 10.8 to 11.2 cps and is evident at the forward transmission, Station 602 and the aft transmission. It corresponds to the analytical response at 10.8 to 11.3 cps for the forward transmission, cockpit floor and Station 602. In a closely related frequency region, measured data shows a major lateral response at 11.1 - 11.2 cps with peaks appearing at Station 602, aft transmission, cockpit floor and Station 359. This response can be compared with the analytical response at 10.5 - 10.8 cps.

Another important test response region with vertical excitation appears at 12.5 - 12.7 cps with correlative analytical peaks between 12.9 and 13.0 cps. Similar frequency peaks appear analytically with lateral excitation at 12.6 - 12.9 cps, but it is assumed that this response corresponds to the 13.2 - 13.7 cps response area in-flight. For vertical excitation, the forward transmission shows another in-flight test peak at 14.7 cps with a correlative analytical peak at 14.9 cps.

Blade Response - In conventional uncoupled analyses of rotors, a vertical oscillation along the rotor shaft axis will induce blade flap motions at the same frequency. Oscillation of the shaft bearings parallel to the rotor plane at a frequency  $\omega$  will induce blade lag motions at frequencies of  $(\omega + \Omega)$  and  $(\omega - \Omega)$ , where  $\Omega$  is the rotor speed. The present analysis treats the rotor as a fully coupled, aerodynamically damped system so that the blades respond in all directions to each uni-directional excitation. Thus vertical excitation along the shaft axis at  $\omega$  will induce blade flap at  $\omega$ ,  $\omega + \Omega$ ,  $\omega - \Omega$ , and blade lag, at  $\omega$ ,  $\omega + \Omega$ , and  $\omega - \Omega$ . Further, since the fuselage is also treated as a fully coupled system, a vertical shaker on the cabin floor will produce vertical, lateral and longitudinal vibratory motions at each rotor. A lateral shaker on the cabin floor will also produce vertical, lateral and longitudinal vibratory motions at each rotor. Thus the fuselage-blade system is coupled in many ways, so that blade response must be examined somewhat differently than in the past. The uncoupled blade frequencies for the H-21 metal blade at normal rotor speed are shown below for reference in the discussion of blade response:

<u>Rotor</u>	<u>Rotor Speed rpm</u>	<u>Rigid Flap, cps</u>	<u>Fundamental Flap Bending, cps</u>	<u>Rigid Lag Rotor Speed, cps</u>	<u>Fundamental Lag-Bending + Rotor Speed, cps</u>
Forward	258	4.4	9.8	5.6	14.8
Aft	258	4.4	11.1	5.6	17.5

Figure 82 provides a comparison between the resultant flap tip response at the forward and aft blades with vertical fuselage excitation. The response for the forward and aft blades appears similar, except that the peak at 9.5 cps for the forward blade appears at 10.4 cps for the aft blade. An examination of the blade response corresponding to these peaks reveals that the deflection is primarily in the first flap bending mode. It is apparent from the modal response that these peaks represent the coupled blade frequencies shifted downward from the 9.8 cps and 11.1 cps uncoupled frequencies shown above. The large response at 8.0 cps is the fundamental fuselage bending mode. The peaks at 11.0 for both forward and aft blades are due to the fuselage mode at this frequency. For further discussion only the forward blade response will be considered, noting that for the aft blade the peak due to the uncoupled blade flap frequency will occur approximately 1.0 cps higher.

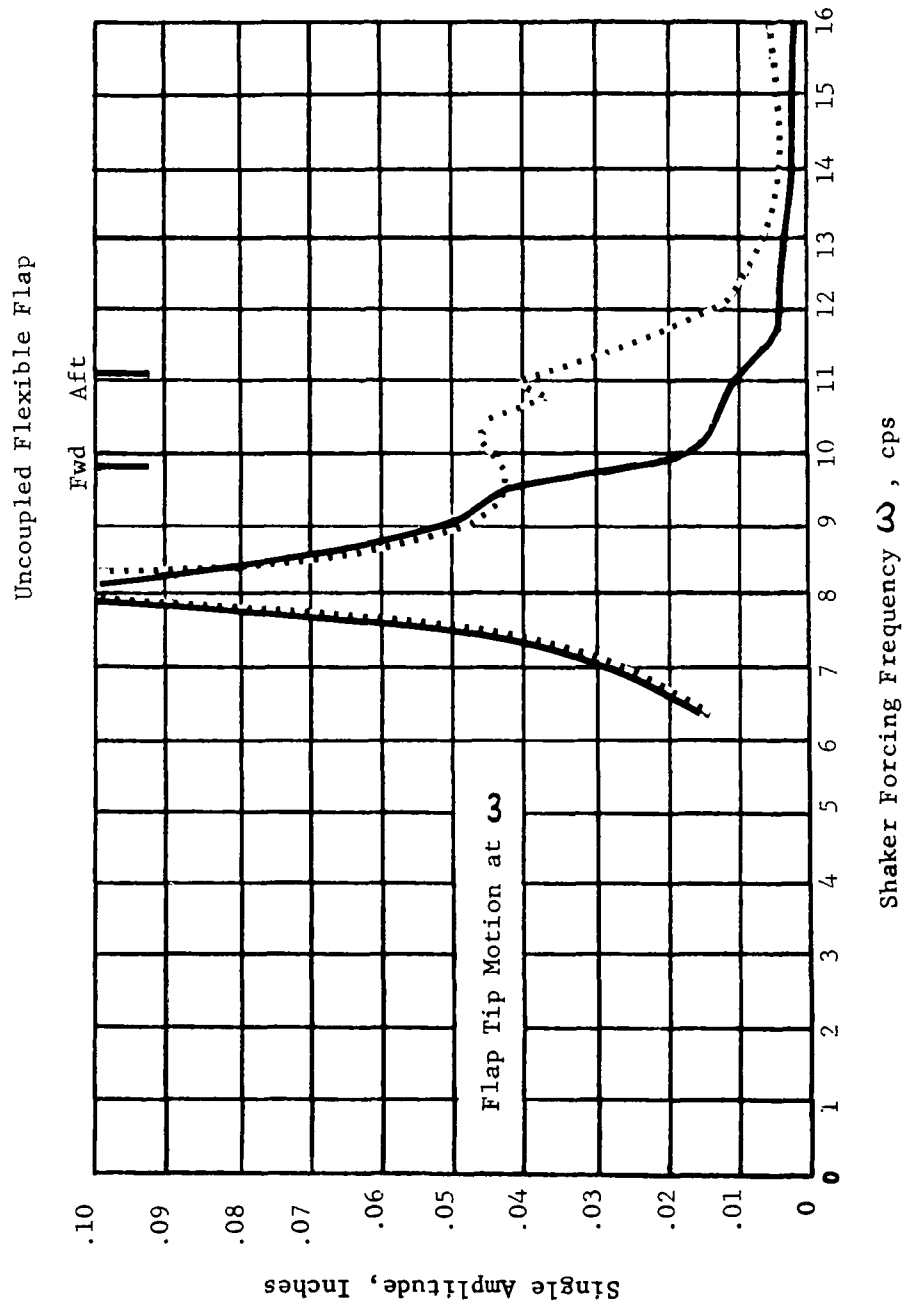


Figure 82 Comparison of Forward and Aft Blade Calculated Response at 258 rpm for 200 lb. Vertical Excitation at Station 312



Frequency response curves of the forward blade tip motion and the forward rotor head are presented in Figures 83 and 84 for vertical and lateral shaker excitation respectively. Individual plots on the figure give single amplitude in inches as ordinate, and shaker exciting frequency  $\omega$  as abscissa. The three columns represent response at  $\omega$ , the same as the shaker frequency, at  $(\omega - \Omega)$  the shaker frequency minus rotor speed and at  $(\omega + \Omega)$  the shaker frequency plus rotor speed. The rotor head motions occur only at  $\omega$ , the blade motions occur at  $\omega$ ,  $(\omega - \Omega)$  and  $(\omega + \Omega)$ . There are four rows in each figure, (1) blade flap sine component and rotor head vertical sine component motions, (2) blade flap cosine component and rotor head vertical cosine motions, (3) blade lag sine component and rotor head longitudinal and lateral sine component motions, and (4) blade lag cosine component and rotor head longitudinal and lateral cosine component motions. All blade motions are measured relative to the deflected disc; they do not contain rotor head motions.

As indicated previously, the blade will respond at  $\omega$ ,  $\omega - \Omega$ , and  $\omega + \Omega$ , under a shaking frequency  $\omega$ . For example, in Figure 83 the blade  $\omega$  flap sine motion in Column 1 at shaker forcing frequency of 9.0 cps is  $\pm 0.050$  inches. The blade flap  $(\omega - \Omega = 9.0 - 4.3 = 4.7 \text{ cps})$  sine motion in Column 2 at a shaker forcing frequency of 9.0 cps is  $\pm 0.002$  inches. The blade flap  $(\omega + \Omega = 9.0 + 4.3 = 13.3 \text{ cps})$  sine motion in Column 3 at a shaker forcing frequency of 9.0 cps is  $\pm 0.0075$  inches. Thus for a single shaker frequency of 9.0 cps the blade is forced at 4.7, 9.0 and 13.3 cps.

In Figure 83 under  $\omega$  response, the rotor head vertical sine motion indicates peaks at 7.8 and 8.2 cps. Blade flap sine motion follows the rotor head with its own peaks at 7.8 and 8.2 cps. Rotor head cosine motion peaks at 8.0 cps, the fundamental fuselage bending mode. Blade cosine flap motion also peaks at 8.0 cps indicating that the motion is induced by the fuselage mode. Blade cosine flap peaks at 9.5 cps; this is the coupled location of the first uncoupled blade flap bending mode which was at 9.8 cps.

The pair of sine and cosine  $(\omega - \Omega)$  blade flap plots bear a close relation to the  $(\omega)$  flap motions. Sine  $(\omega - \Omega)$  flap peaks at 8.0 and 9.5 cps corresponding to cosine  $(\omega)$  flap peaks. Cosine  $(\omega - \Omega)$  flap peaks at 7.7 and 8.2 cps corresponding to sine  $(\omega)$  flap peaks. The peak at 12.8 cps will be shown to be related to lateral fuselage motion. Peaks at 8.2 and 7.9 cps appear for  $(\omega + \Omega)$  flap sine and cosine respectively. These are also related to the 8.0 cps fuselage mode motion at the rotor head.

Rotor head longitudinal sine motion occurs at  $\omega$ , the shaker frequency, with maximums at 7.8, 8.3, 11.0 and 13.0 cps. Rotor head lateral sine motion peaks at 8.0, 10.0, 10.9, 12.0 and 13.0 cps. Rotor head longitudinal cosine motion peaks at 8.0, 10.4, 12.7 and 15.1 cps. Rotor head lateral cosine motion resonates at 7.7, 8.3, 9.8, 10.6 and 12.7 cps.

Blade lag sine at  $\omega$  follows the rotor head longitudinal cosine in the vicinity of 8.0 cps, and follows rotor head lateral sine motion elsewhere. Blade lag cosine at  $\omega$  follows rotor head longitudinal sine in the vicinity of 8.0 cps, and follows rotor head lateral cosine elsewhere. In other words, longitudinal hub motion induces blade lag motion  $90^\circ$  later, while lateral hub motion is felt instantly in phase.

Blade lag motions at  $(\omega - \Omega)$  generally follow their sine and cosine counterparts at  $(\omega)$ . However at 5.6 cps for  $(\omega - \Omega)$  the sine increases rapidly and the cosine drops to zero, indicating a nearly pure rigid lag mode. Note here that

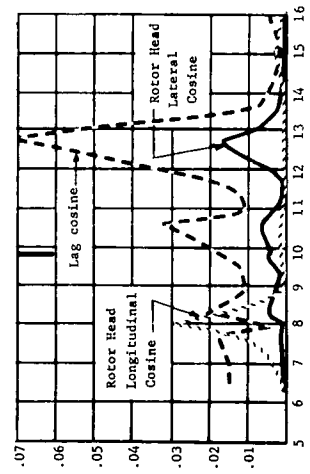
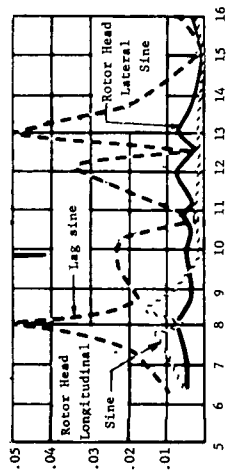
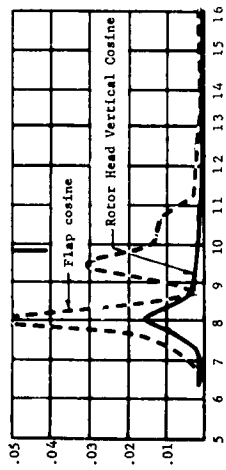
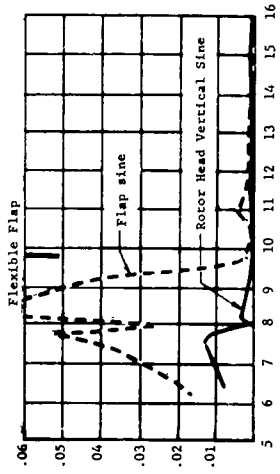
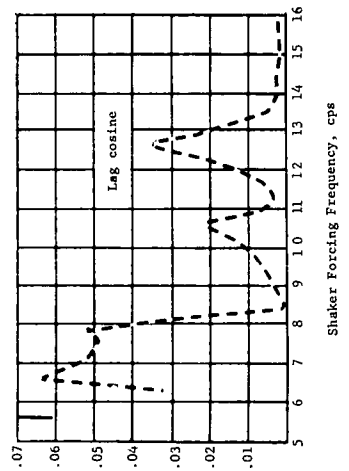
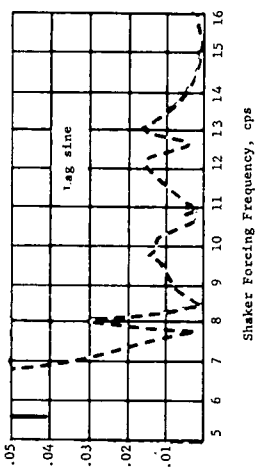
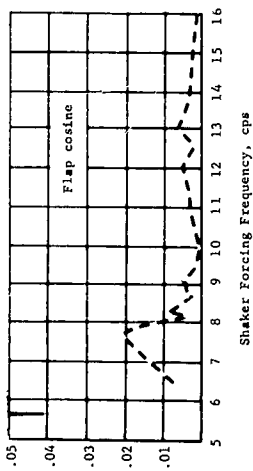
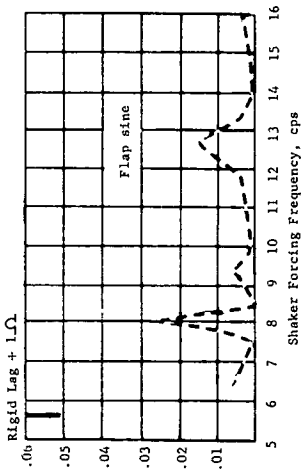
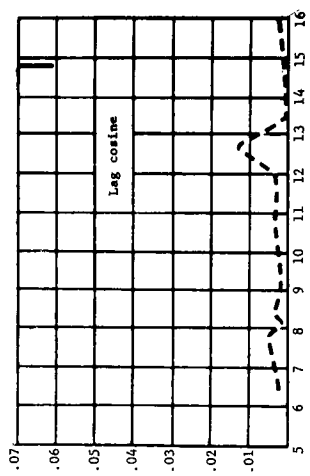
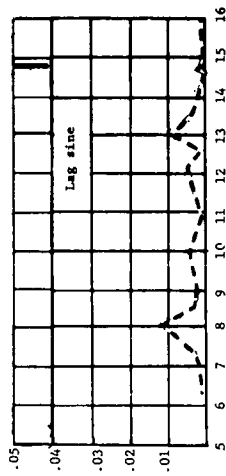
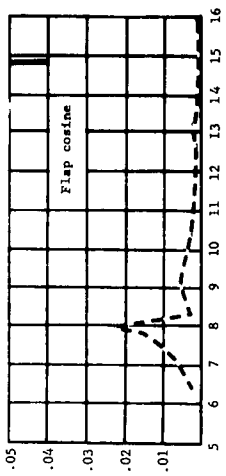
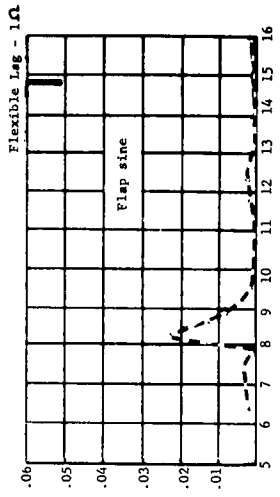
$\omega$  $\omega - \Omega$  $\omega + \Omega$ 

Figure 83 Forward Rotor Hub and Blade Tip Motions at 258 rpm under 200 lb Vertical Excitation at Station 312

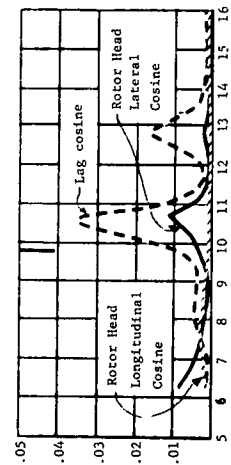
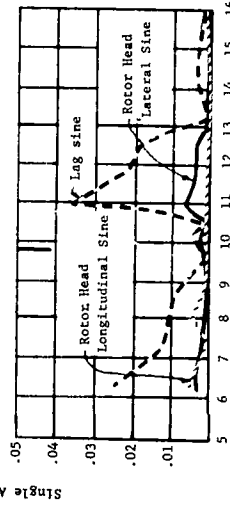
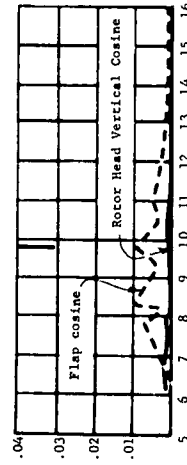
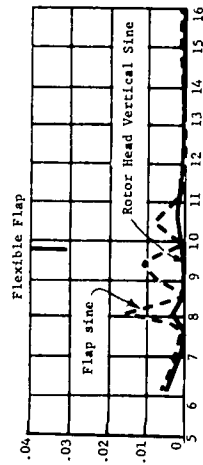
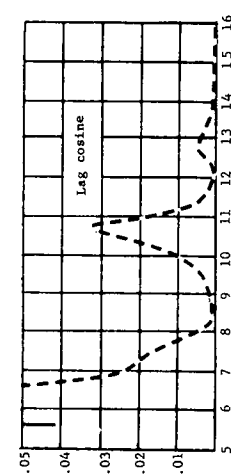
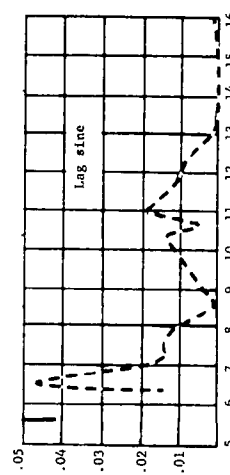
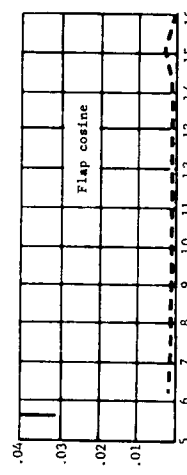
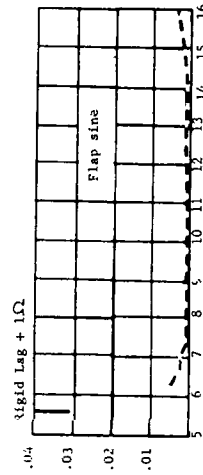
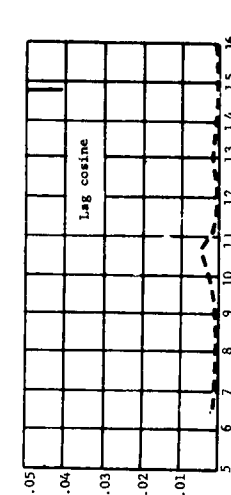
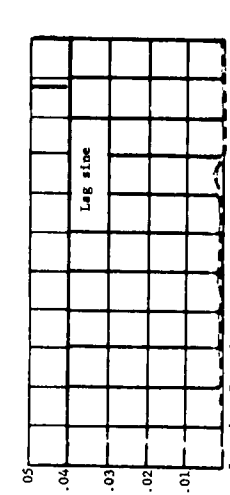
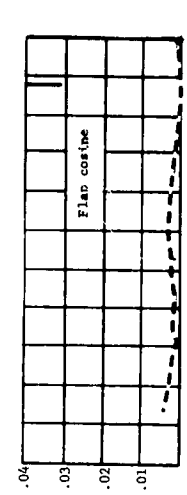
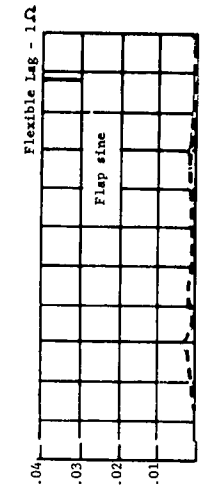
$\omega$  $\omega - \Omega$  $\omega + \Omega$ 

Figure 84 Forward Rotor Hub and Blade Tip Motions at 258 rpm under 200 lb Lateral Excitation at Station 312

when the forcing frequency is 5.6 cps,  $\omega - \Omega$  is  $5.6 - 4.3 = 1.3$  cps, which in turn is the uncoupled rigid body blade lag frequency. Blade lag motions at  $(\omega + \Omega)$  are again similar to the  $(\omega)$  component motions but of smaller magnitude; a peak at 14.8 cps in the  $(\omega + \Omega)$  plot is the only appearance of the first lag bending mode whose uncoupled frequency is also at 14.8 cps.

All the peaks described above are blade motions responding to fuselage peaks except blade rigid lag at 5.6 cps, blade first flap bending at 9.5 cps and blade first lag bending at 14.8 cps. Note again that the flap mode has been shifted 0.3 cps from its uncoupled location at 9.8 cps.

Figure 84 presents similar rotor head - blade calculations under a 200 lb lateral shaker force at Station 312. Rotor head vertical sine motions are similar but smaller than rotor head vertical cosine motions in Figure 83 under vertical shaker excitation. Rotor head vertical cosine motions are also similar but much smaller than rotor head vertical sine motions in Figure 83. As usual, blade flap at  $\omega$  follows the rotor head vertical peaks except at 9.5 cps where the blade flap bending resonance occurs. Flap motions at  $(\omega - \Omega)$  and  $(\omega + \Omega)$  under lateral excitation are negligible.

Rotor head longitudinal sine and cosine motions are very small under lateral shaker excitation. Rotor head lateral sine and cosine motions are more evident and cause blade lag motions in concert. At  $(\omega - \Omega)$  blade lag motions exhibit amplitudes generally as large as those at  $(\omega)$ . Peaks at  $(\omega - \Omega)$  are closely related to their respective sine and cosine  $(\omega)$  motions. Blade motion at  $(\omega + \Omega)$  is quite small.

Except for the first flap bending peak at 9.5 cps forcing frequency and for the first lag bending peak at 14.8 cps forcing frequency, all blade peaks described in Figures 83 and 84 represent predominant rigid blade motion. This indicates that unless the forcing frequency is near the uncoupled blade natural frequency, the fuselage (rotor head) motion induces primarily rigid blade modes.

Modal Response - Using the average frequency of peak response, the comparable in-flight test and analytical results are shown below.

<u>Excitation</u>	<u>In-flight Response Frequency, cps</u>	
	Matrix	Test
Lateral	5.6 (Blade Response)	5.6
Vertical	No corresponding response	7.5
Vertical	8.1	8.1
Vertical	Masked by the fundamental vertical response	9.1
Lateral	No corresponding response	9.2
Vertical	10.0 (Fuselage Response)	9.9
Lateral	9.5 (Blade Response)	10.05
Vertical	10.4 (Blade Response)	
Lateral	10.8	11.1
Vertical	11.0	11.0
Vertical	13.0	12.6
Lateral	12.8	13.4
Vertical	14.1 (Lateral Response)	14.0
Vertical	14.9	14.7
Vertical	14.9	15.2

For all cases shown above in which test modes are available, mode comparisons between test and calculated shapes have been prepared. Specific comparisons are made as follows.

<u>Excitation</u>	<u>In-flight Test, cps</u>	<u>In-flight Calculated, cps</u>	<u>Figure</u>
Vertical	8.1	8.1	85
Vertical	9.1		62
Lateral	9.2		61
Vertical	9.9	10.0	86
Lateral	10.05	9.5	87
Lateral	11.1	10.8	88
Lateral	13.4	12.8	89

Each figure illustrates the calculated shapes on the top and the test shapes on the bottom. Shapes in the left column are the cosine components, referred to the instant when the red blade is in its trail aft position. Shapes in the right column are the sine components, referred to the instant when the red blade is at a 90° advanced position. Fuselage vertical bending, lateral bending, pylon bending and fuselage torsion are shown in each plot. Blade motions are detailed along the top of the page; they are shown at the modal frequency  $\omega$  and at  $\omega + \Omega$  and  $\omega - \Omega$ .

#### In-Flight Response at 8.1 cps

Figure 85

The fundamental vertical mode in-flight at 8.1 cps shows excellent frequency correlation with the analytical response. Cosine response from analytical calculations compares reasonably well with both the sine and cosine fuselage response from test. Yaw motion of the engine is reversed from calculation for both the sine and cosine response. Engine pitch and forward pylon lateral response are clearly defined in the test, but show no significant matrix response. The analytical sine shape shows no significant response except for out-of-phase rigid lateral pylon motion.

#### In-Flight Response at 9.1 cps

Figure 62

Corresponding to a response peak with vertical excitation, the in-flight forced mode at 9.1 cps is a highly coupled vertical-lateral mode with relatively large engine motions. The cosine mode in-flight resembles the fundamental vertical bending mode, but the pylons show a longitudinal reversal. In-phase lateral motion of the pylons appears in the cosine component while out-of-phase pylon motion exists in the sine shape. Lateral, yaw and roll motions of the engine show significant response. No correlative analytical modes exist as the matrix peak is enveloped by the extremely large fundamental vertical response.

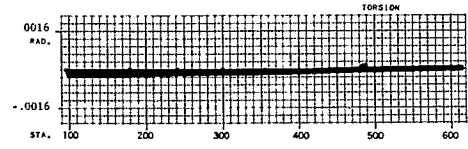
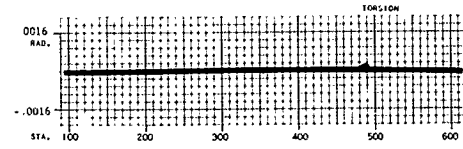
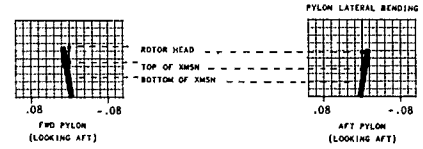
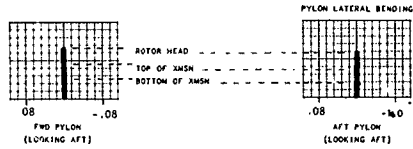
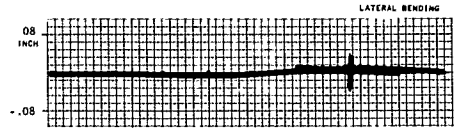
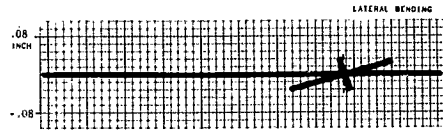
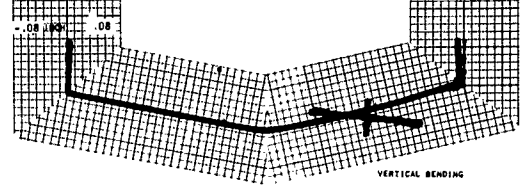
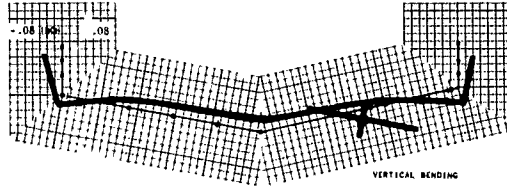
#### In-Flight Forced Mode at 9.2 cps

Figure 61

For lateral excitation, the in-flight test mode corresponding to the 9.2 cps response peak appears as a lateral-torsion mode of the fuselage strongly coupled to engine motion. Fuselage response includes first fuselage torsion out-of-phase with the engine, and fundamental fuselage lateral bending with in-phase engine motion and out-of-phase yaw motion. No significant coupling is noted with vertical-longitudinal motion of the fuselage, but the engine responds with vertical-pitch motion. Matrix calculations with lateral excitation produced no corresponding response.

# FWD ROTOR BLADE RESPONSE

	$\cos(\omega)$	$\sin(\omega)$	$\cos(\omega + \Omega)$	$\sin(\omega + \Omega)$	$\cos(\omega - \Omega)$	$\sin(\omega - \Omega)$	
Zb1	-2.6102E-03	6.3442E-02	2.1849E-02	-1.6036E-02	2.3144E-02	4.7076E-03	Rigid Flap
Zb2	-3.5575E-02	5.0829E-02	-8.0010E-04	6.4670E-04	-2.0230E-05	2.9575E-05	First Flexible Flap
Zb3	1.3922E-03	-3.4025E-03	-1.5382E-04	6.5723E-05	2.7747E-06	-4.3753E-06	Second Flexible Flap
Yb1	4.5142E-02	1.4502E-02	-8.4850E-03	+7.3813E-04	2.9431E-02	-1.8840E-02	Rigid Lag
Yb2	3.8877E-04	1.8052E-04	-2.8167E-03	-8.2940E-04	6.0505E-04	-2.8857E-04	First Flexible Lag
Zb TIP,IN	-3.6794E-02	1.1089E-01	2.0895E-02	-1.5323E-02	2.3129E-02	4.7320E-03	Sum Flap
Yb TIP,IN	4.5531E-02	7.4682E-02	-1.1302E-02	-1.5675E-03	3.0036E-02	-1.9137E-02	Sum Lag



In-flight Matrix Mode at 8.1 cps  
200 lb. Vertical Force, 258 rpm

In-flight Cosine Mode

In-flight Sine Mode

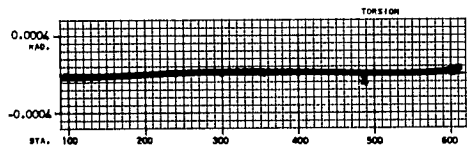
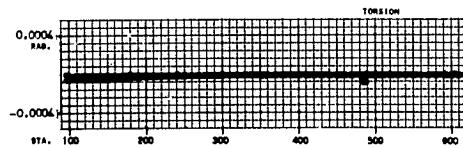
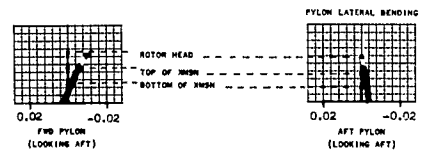
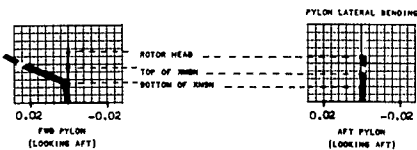
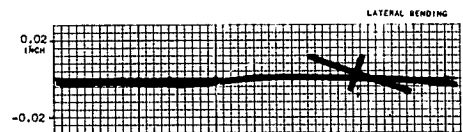
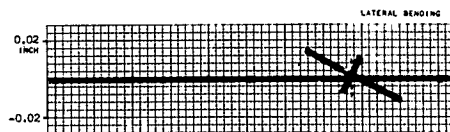
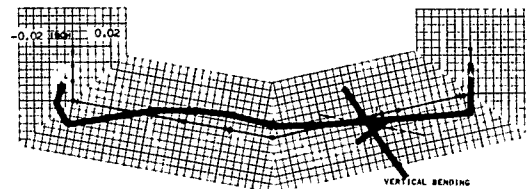
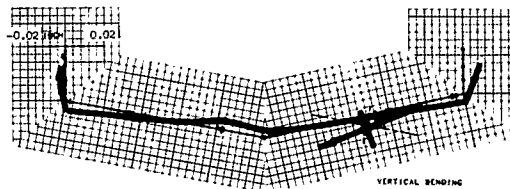


Figure 85 In-flight Test Mode at 8.1 cps - 300 lb Vertical Force,  
258 rpm Rotor Speed

#### In-Flight Forced Mode at 9.9 cps

Figure 86

The in-flight mode corresponding to the peak response at 9.9 cps with vertical excitation shows excellent frequency agreement with the comparable analytical mode at 10 cps. From test, the cosine mode continues with fundamental vertical motion, but in addition, shows highly coupled engine motion in all directions and lateral response of the aft pylon. Similar shape characteristics are apparent in the analytical sine response. However, the engine response is reduced and further, relatively large lateral motions exist for the forward and aft pylon.

Vertical, pitch and yaw of the engine together with aft pylon longitudinal pre-dominate in the measured sine response. Similarly, a large response of the engine appears in the analytical cosine mode, but the lateral and yaw motions are out-of-phase.

#### In-Flight Forced Mode at 10.05 cps

Figure 87

The coupled fuselage-forward blade flap bending mode corresponding to the peak response at 10.05 cps with lateral excitation is compared to the calculated mode at 9.5 cps. Since the analytical response is highly dependent on the blade frequency obtained by supplemental calculations and is not substantiated by test, the frequency correlation is considered to be acceptable. In both the test and matrix modes, the fuselage vertical-longitudinal motion is nonexistent except for small relative motion of the aft pylon in the calculated cosine mode and localized shaker motion from test results.

Engine motions appear similar in the yaw direction and out-of-phase laterally; pitch motion appears in the test response whereas calculations indicate significant torsion. A comparison of the cosine response shows out-of-phase pylon response and calculated fuselage lateral-torsion below that of the test. Aft pylon motion appears similar for the sine response, but no correlation exists for forward pylon lateral. In addition, no reasonable shape correlation exists for lateral-torsion response of the fuselage.

#### In-Flight Forced Mode at 11.1 cps

Figure 88

The in-flight fuselage lateral-torsion mode at 11.1 cps shows good frequency agreement with the calculated mode at 10.8 cps. Test cosine response contains first lateral bending of the fuselage with out-of-phase engine motion and rigid lateral motion of the pylons. Comparing this shape with the calculated cosine response indicates similar areas of response, but a phase reversal is evident for all motions with the exception of forward pylon lateral and torsion along the forward fuselage. Sine response from test compared to the analytical cosine response shows better shape correlation for lateral bending along the fuselage, but the lateral reversal shown for both the forward and aft pylon was not obtained by calculation. Lateral-yaw of the engine and fuselage rigid torsion, clearly evident in the matrix response, are not as significant in the test shapes.

#### In-Flight Forced Mode at 13.4 cps

Figure 89

The in-flight response peak at 13.4 cps corresponds to a lateral torsion fuselage mode with no significant engine motion. From matrix calculations, the comparable modal response occurs at 12.8 cps with lateral excitation. In the cosine mode, the lateral response shape appears similar, but out-of-phase between test and matrix;

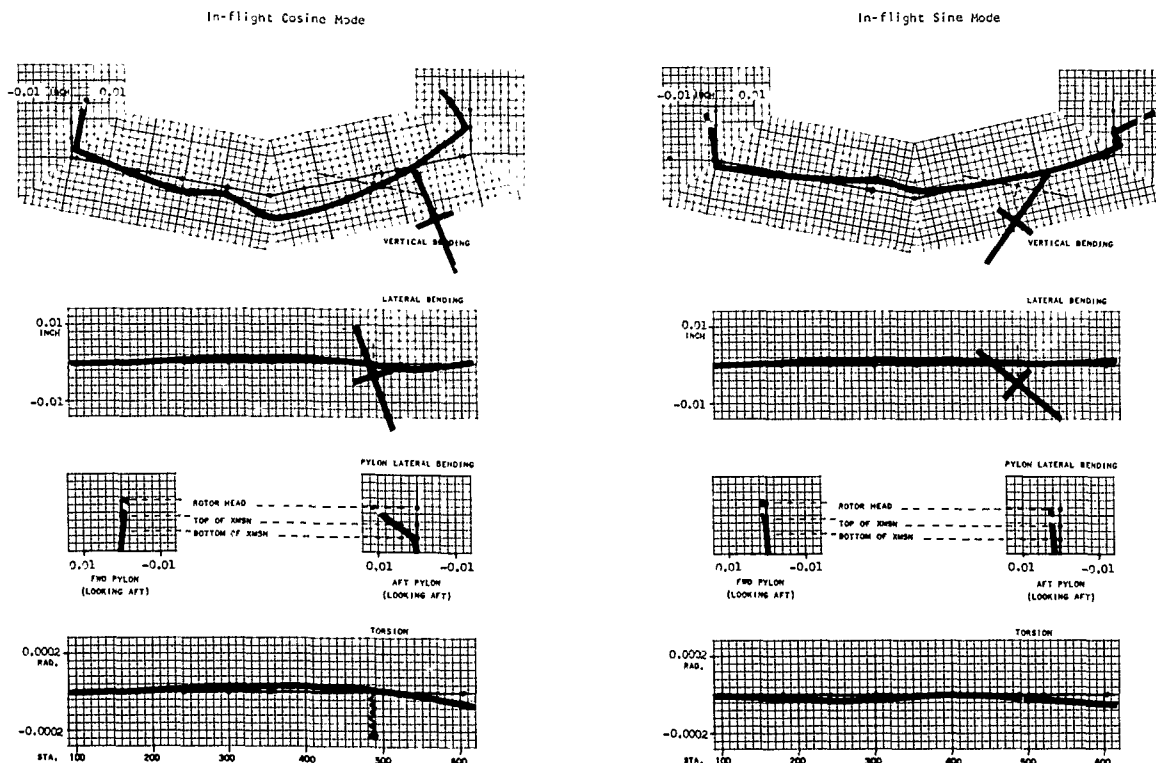
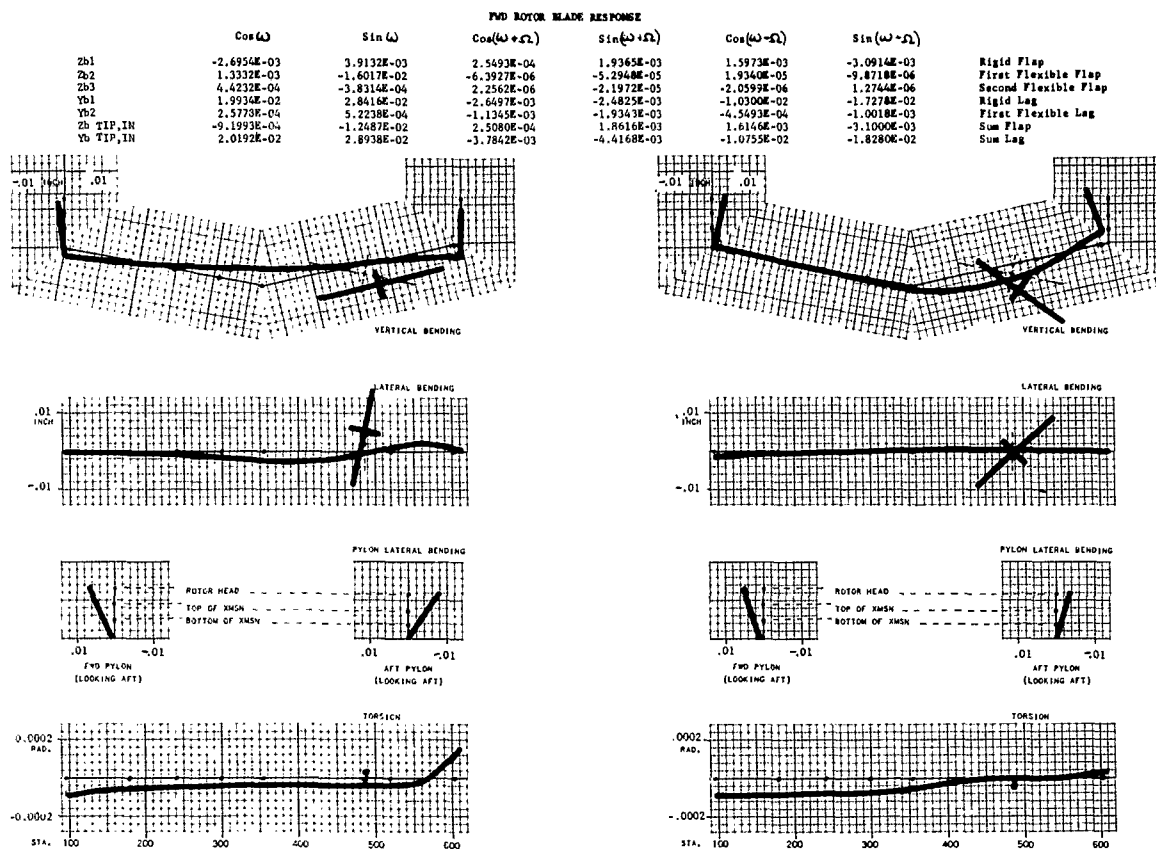
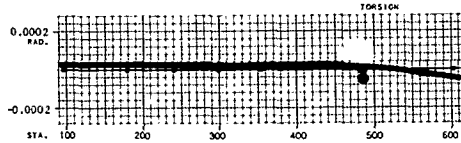
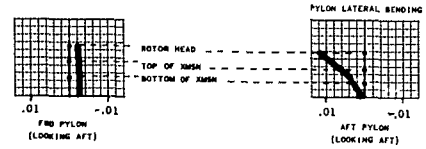
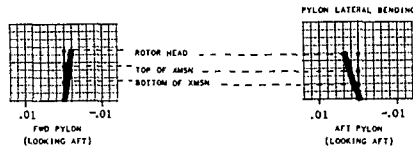
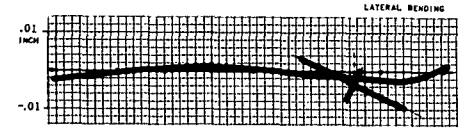
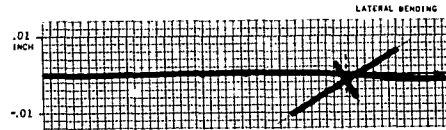
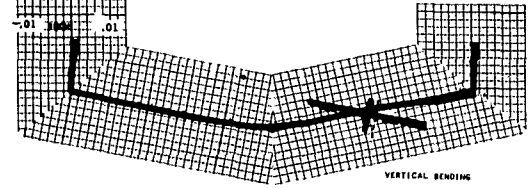
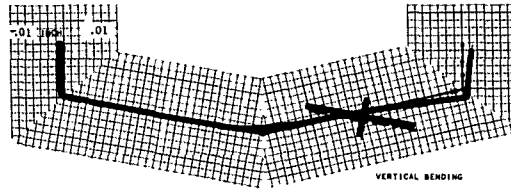


Figure 86 In-flight Test Mode at 9.9 cps - 300 lb Vertical Force, 258 rpm Rotor Speed



# FWD ROTOR BLADE RESPONSE

	$\cos(\omega)$	$\sin(\omega)$	$\cos(\omega + \Omega_1)$	$\sin(\omega + \Omega_1)$	$\cos(\omega - \Omega_1)$	$\sin(\omega - \Omega_1)$	
Zb1	-2.1460E-03	1.3038E-03	9.6042E-04	2.2277E-03	1.2975E-03	-1.4282E-03	Rigid Flap
Zb2	-6.8810E-03	-8.0444E-03	-2.8649E-05	-6.6354E-05	6.6392E-06	-7.0274E-08	First Flexible Flap
Zb3	2.3512E-04	-6.5983E-05	-3.9188E-04	-2.1643E-05	-8.3102E-07	5.8503E-08	Second Flexible Flap
Yb1	7.3933E-04	-7.0449E-03	4.1899E-04	7.6684E-04	7.9306E-03	4.3224E-03	Rigid Lag
Yb2	2.3399E-05	-9.3541E-05	1.0816E-04	4.2244E-04	2.9373E-04	2.0543E-04	First Flexible Lag
Zb TIP, IN	-8.7918E-03	-6.8068E-03	9.2803E-04	2.1397E-03	1.3053E-03	-1.4282E-03	Sum Flap
Yb TIP, IN	7.6273E-04	-7.1585E-03	5.2715E-04	1.1893E-03	8.2243E-03	4.5278E-03	Sum Lag



In-flight Matrix Mode @ 9.5 cps  
200 lb. Lateral Force, 258 rpm

In-flight Cosine Mode

In-flight Sine Mode

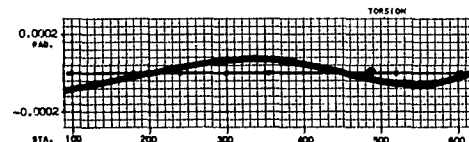
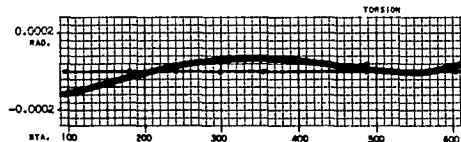
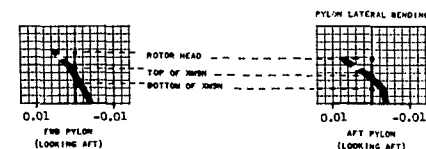
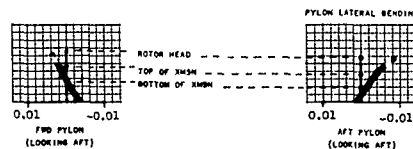
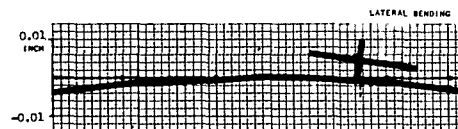
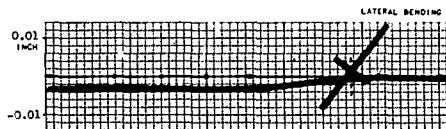
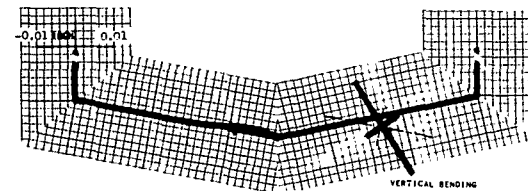
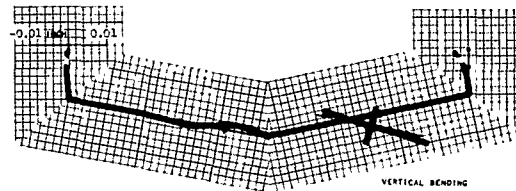


Figure 87 In-Flight Test Mode at 10.05 cps - 200 lb Lateral Force,  
258 rpm Rotor Speed

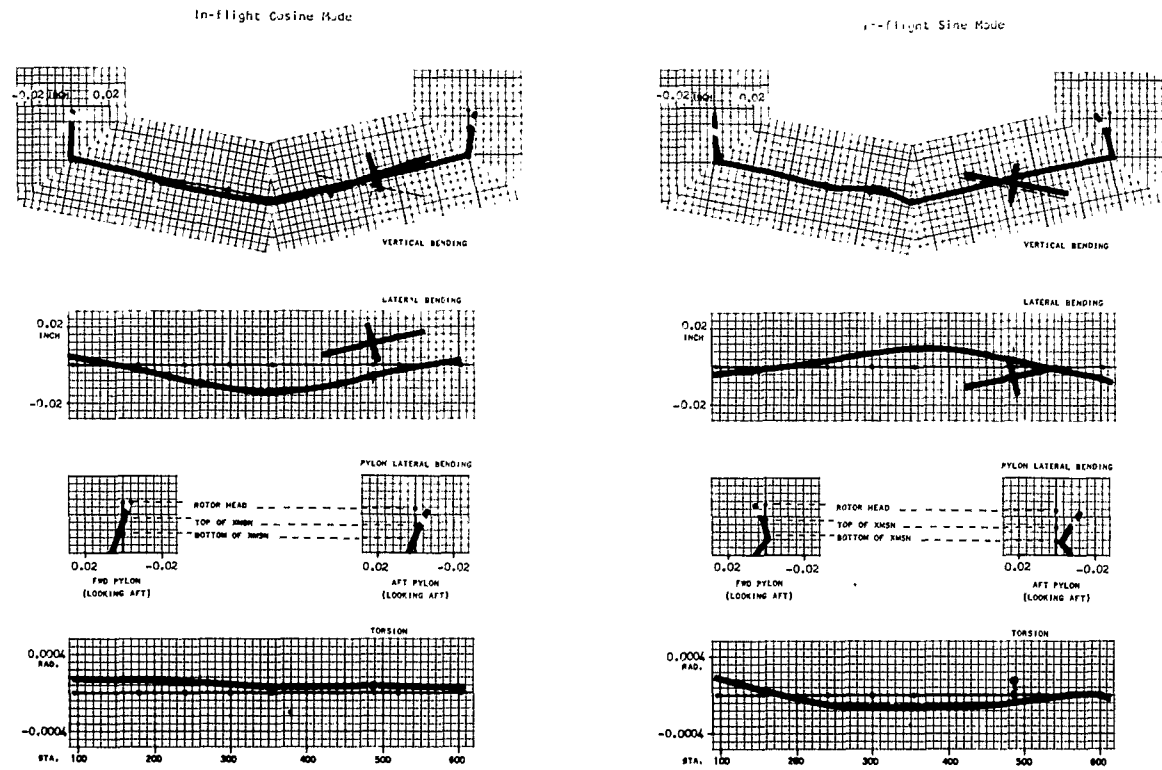
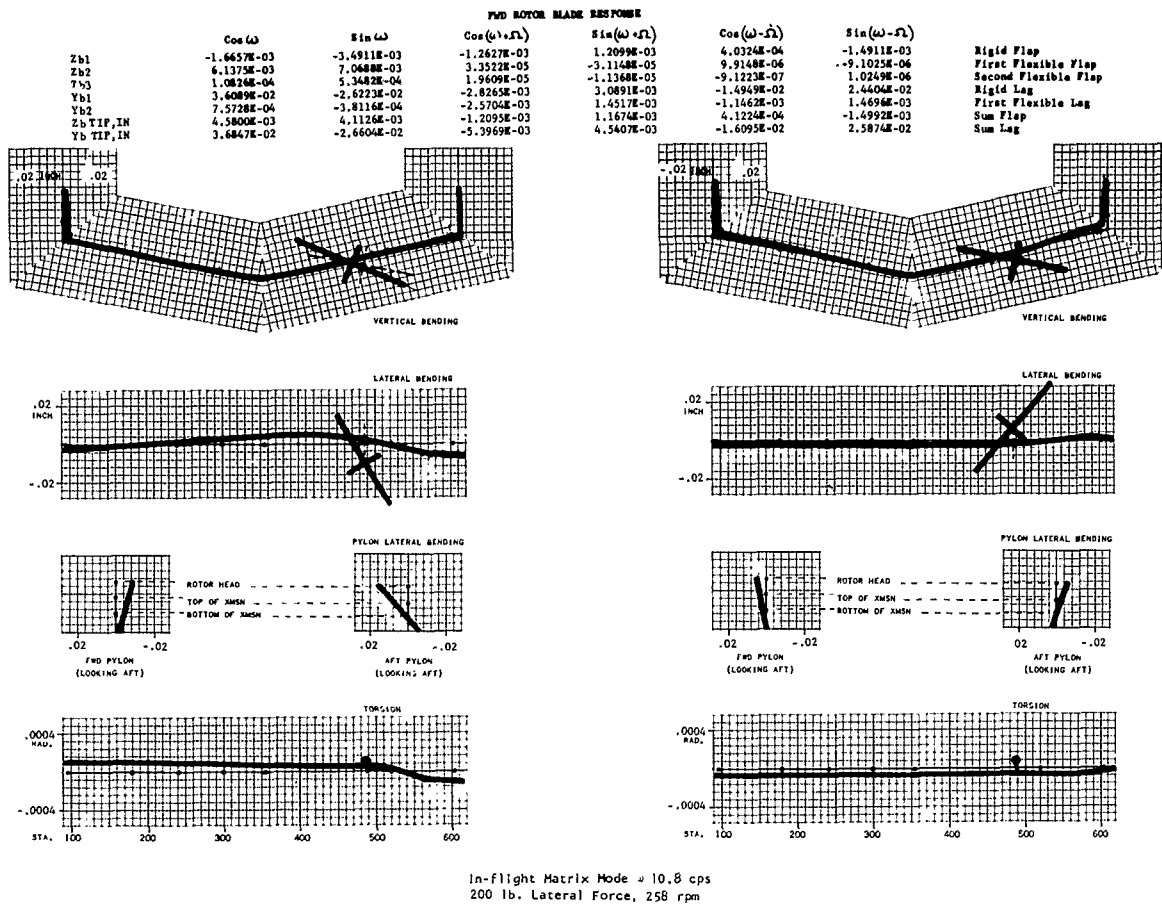
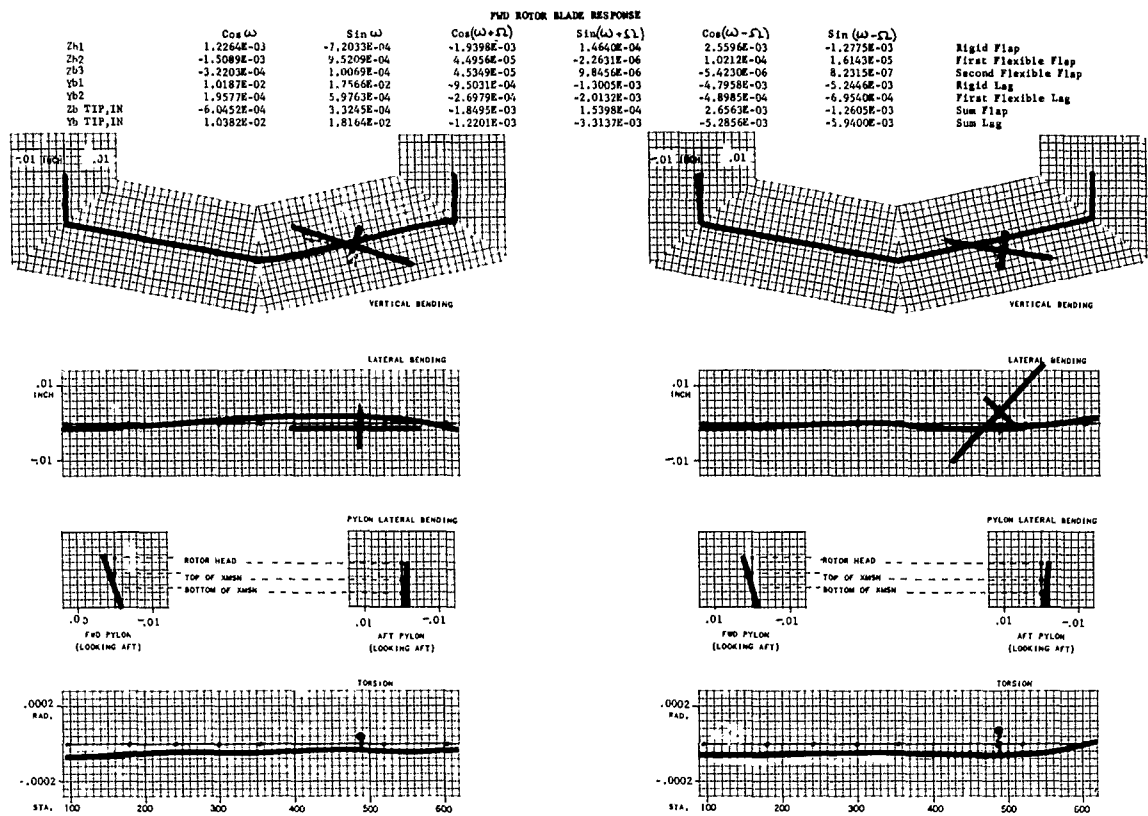


Figure 88 In-flight Test Mode at 11.1 cps - 200 lb Lateral Force, 258 rpm Rotor Speed



In-flight Matrix Mode : 12.7 cws  
200 lb. Lateral Force, 258 rpm

In-flight Cosine Mode

In-flight Sine Mode

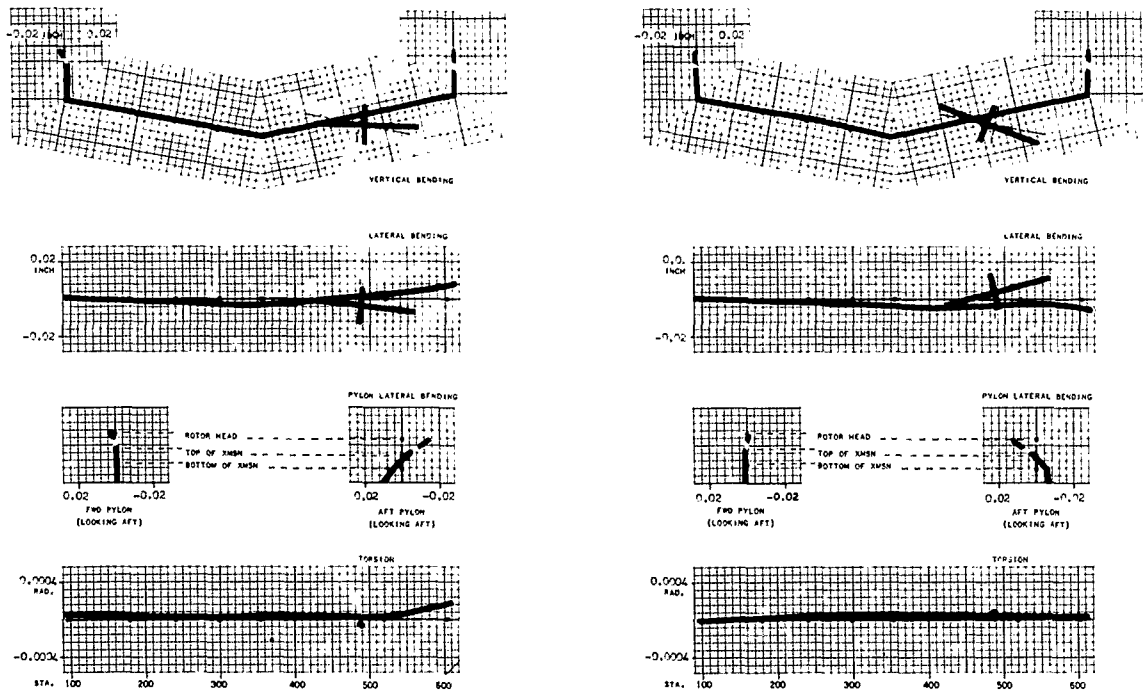


Figure 89 In-flight Test Mode at 13.2 cps - 200 Lateral Force,  
258 rpm Rotor Speed

fuselage torsion results in rigid aft pylon motion for test results whereas matrix response shows forward pylon motion. Engine yaw appears in the sine response for both test and matrix. However, no shape correlation is apparent for the fuselage sine response. No significant vertical coupling appears in either the test or matrix response.

### C. Effect of Rotor Speed

Frequency response curves for vertical and lateral excitation at rotor speeds of 240, 258, and 278 rpm are illustrated in Figure 90 for fuselage motion and in Figure 91 for blade motion. Calculated fuselage response curves are shown with the comparable Phase V test data for forward transmission longitudinal motion with a 300 lb vertical excitation and Station 359 W.L. 44 with a 200 lb lateral excitation. Blade response curves are presented in Figure 91 showing the flap tip deflection of the forward blade at the shaker frequency minus rotor speed for a 200 lb lateral excitation. No comparable blade test response is presented, for as in the Section VI in-flight test, blade response corresponding to shaker excitation could not be detected.

In Figure 90 the calculated forward transmission longitudinal response peaks at 7.9, 8.05, and 8.1 cps for 240, 258 and 278 rpm. Corresponding test peaks occur at 7.9, 8.2 and 8.1 cps. Therefore, only a slight, and not a clearly defined trend with rpm occurs at the 8.0 cps resonant area. For the 10.5 cps resonant area, the calculated forward transmission longitudinal response peaks at 10.4, 10.9 and 10.6 cps for 240, 258 and 278 rpm respectively, with corresponding test peaks at 10.7, 11.0 and 11.5 cps. Here there is significant peak variation with rpm, indicating coupling between fuselage and the aft rotor first flap bending mode. However, the calculated peak for 278 rpm, 10.6 cps, does not agree with the test trend, being below the resonant peak for 258 rpm at 11.0 instead of occurring above the 258 rpm peak. The test peaks near 9.0 cps are not reproduced analytically.

For lateral excitation, Station 359 calculated lateral response indicates only one response area between 10.0 and 10.7 cps for which the response peaks vary with rpm. The calculated peaks occur at 10.0, 10.7 and 10.2 cps for 240, 258 and 278 rpm respectively. No valid comparison with test can be obtained in this area because a large number of test peaks occupy this area.

In Figure 91 for vertical excitation, the flap response at  $\omega$  for the aft blade shows peaks at 9.5 for 240 rpm, at 10.4 for 258 rpm and at 11.0 cps for 278 rpm. These peaks indicate the coupled locations for the first flap bending mode located previously at 10.4, 11.1 and 11.8 cps for 240, 258 and 278 rpm respectively. The peaks near 8.0 cps are due to the fuselage fundamental mode described previously in Figure 90.

For lateral excitation at the bottom Figure 91, lag tip response at  $(\omega - \Omega)$  for the forward blade illustrates response which tends to peak at 5.2, 5.6 and 6.0 cps for 240, 258 and 278 rpm respectively. These peaks correspond to the uncoupled rigid lag mode at identical frequency locations. The resonant area between 10.0 and 10.7 cps corresponds to the fuselage response area described in Figure 90.

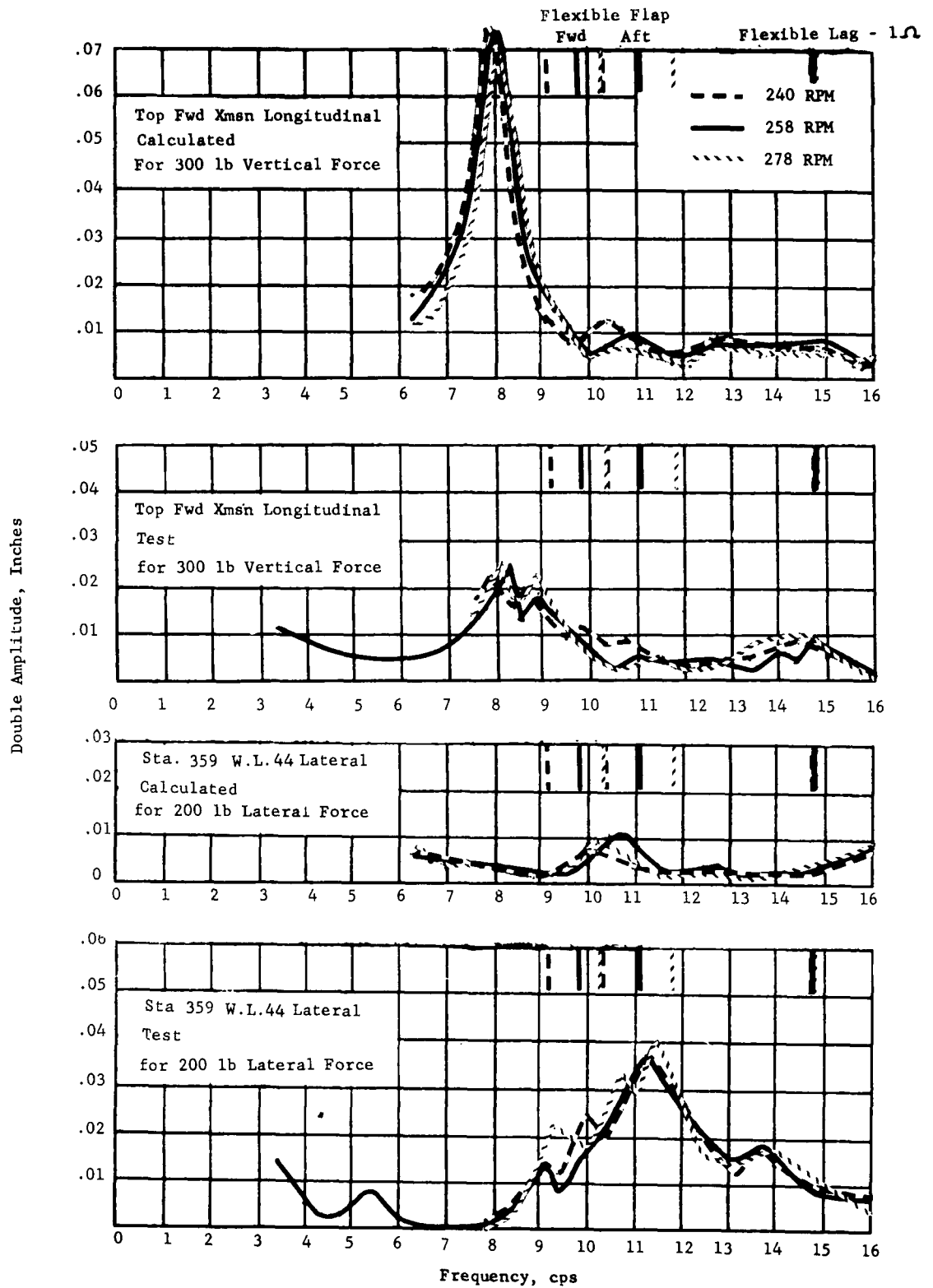


Figure 90 Comparison of In-flight Fuselage Response at 240, 258 and 278 rpm

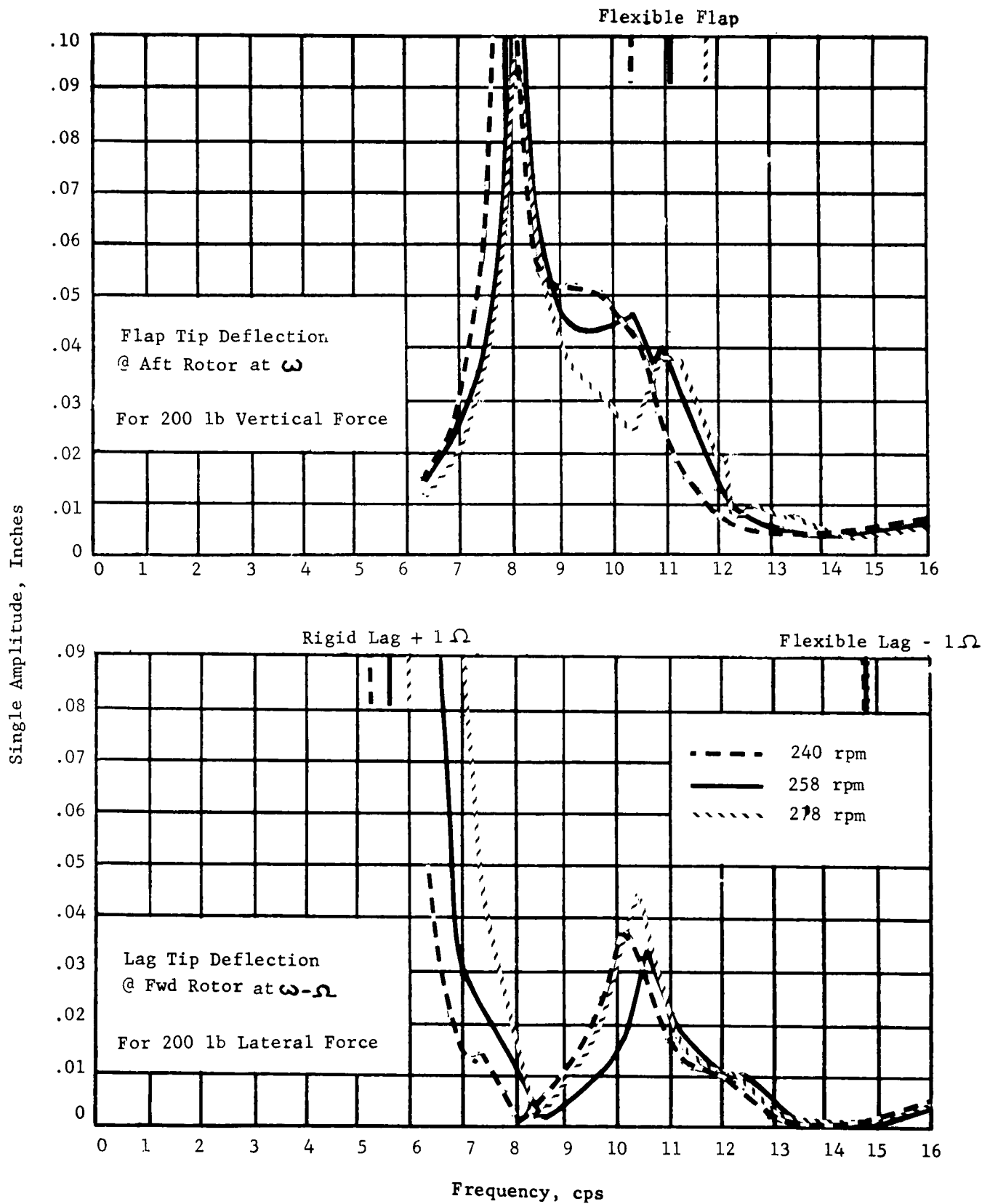


Figure 91 Comparison of In-flight Blade Tip Response at 240, 258 and 278 rpm for Fuselage Excitation

As a summary of rpm effects, the calculated in-flight response peaks obtained from Figures 90 and 91 are plotted in Figures 92 and 93 on spectra containing the blade uncoupled frequencies and the ground calculated resonant areas. Frequency in cps is plotted as the ordinate, and the rotor speed in rpm is plotted as the abscissa. Uncoupled frequencies are shown in the plots by solid lines. The ground calculated resonant areas are shown as horizontal bands because they are not related to rotor speed, and the calculated in-flight response peaks as points, "X", connected between rpm's by dashed lines.

In the frequency spectrum for vertical excitation, Figure 92, the ground calculated modes appear at 7.4 - 7.5 cps, at 9.7 - 9.9 cps, at 12.2 - 12.3 cps and at 15.0 - 15.2 cps. These results were obtained from the analytical ground shake simulation described previously in Reference 8. With the addition of rotors, the in-flight calculated response is no longer independent of rotor speed. However, the rotor speed effect is small for the in-flight modes near 8.0 cps and 15.0 cps.

The change between static and dynamic representation of the rotor does influence the location of the resonant frequencies. The fundamental vertical bending mode shifted approximately 0.5 cps from the 7.4 - 7.5 cps ground calculated to the 7.9 - 8.1 cps in-flight calculated. The in-flight mode at 12.6 - 12.9 cps also has shifted upward from the 12.2 - 12.3 cps ground mode. This mode also exhibits a trend with rpm, shifting the frequency location downward with an increase in rotor speed.

Because of fuselage coupling the blade frequencies for the first flap bending mode shift from the uncoupled frequency location. Thus for the forward blade, the peaks at 8.9, 9.5, and 9.7 cps, for 240, 258 and 278 rpm respectively, have shifted from the uncoupled frequency locations at 9.2, 9.8 and 10.4. For the aft blade, the peaks at 9.2, 10.4 and 11.0 cps moved down from the uncoupled frequencies at 10.4, 11.1 and 11.8 cps. The calculated in-flight mode defined at 10.4 cps for 240 rpm, at 10.9 for 258 rpm and at 10.6 cps for 278 rpm is related to the calculated ground mode at 9.7 - 9.9 cps. This in-flight mode, in addition to the frequency shift due to the change in the effective mass of the rotor between ground and in-flight representation, is also highly coupled with the aft blade first flap bending mode as evidenced by frequency changes due to rotor speed. Between 240 and 265 rpm, the frequency increases with an increase in rotor speed, but for rotor speeds greater than 265 rpm, the frequency decreases sharply with an rpm increase.

In the frequency spectrum for lateral excitation, Figure 93, the ground calculated modes appear at 9.2 - 9.4 cps, at 11.4 - 11.8 cps, and at 14.5 - 15.0 cps. The effect of rotor speed is negligible on the in-flight calculated modes at 12.7 and 14.1 cps. Because of the difference between static and dynamic representations of the rotor, these modes have shifted in frequency from 11.4 - 11.8, and 14.5 - 15.0 cps ground modes. The in-flight mode defined by 10.0 cps at 240 rpm, by 10.7 at 258 rpm and by 10.2 cps at 278 rpm is a highly coupled fuselage-blade mode which also appears strongly with vertical excitation at slightly higher frequency.

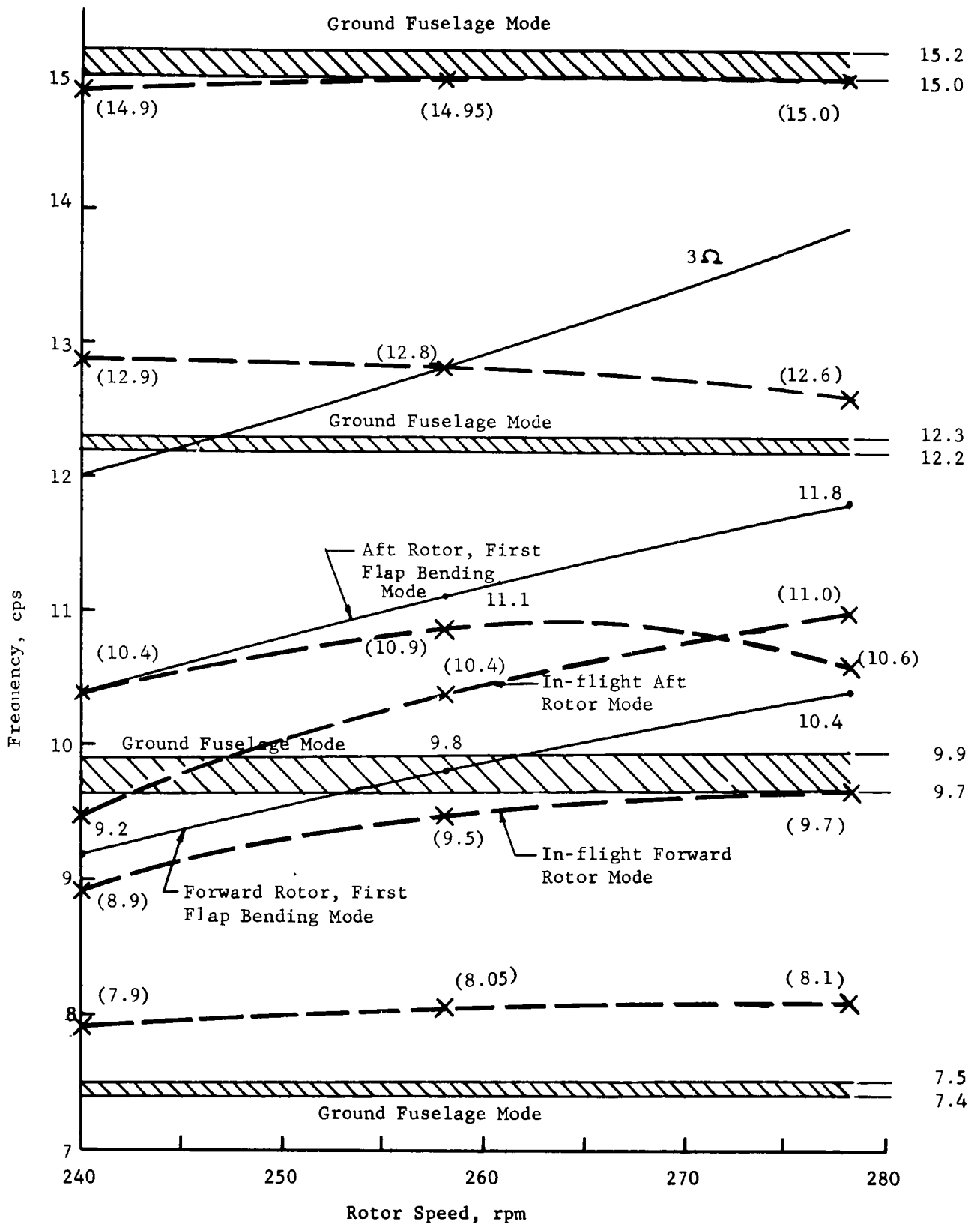


Figure 92 Calculated Frequency Response with Vertical Excitation.



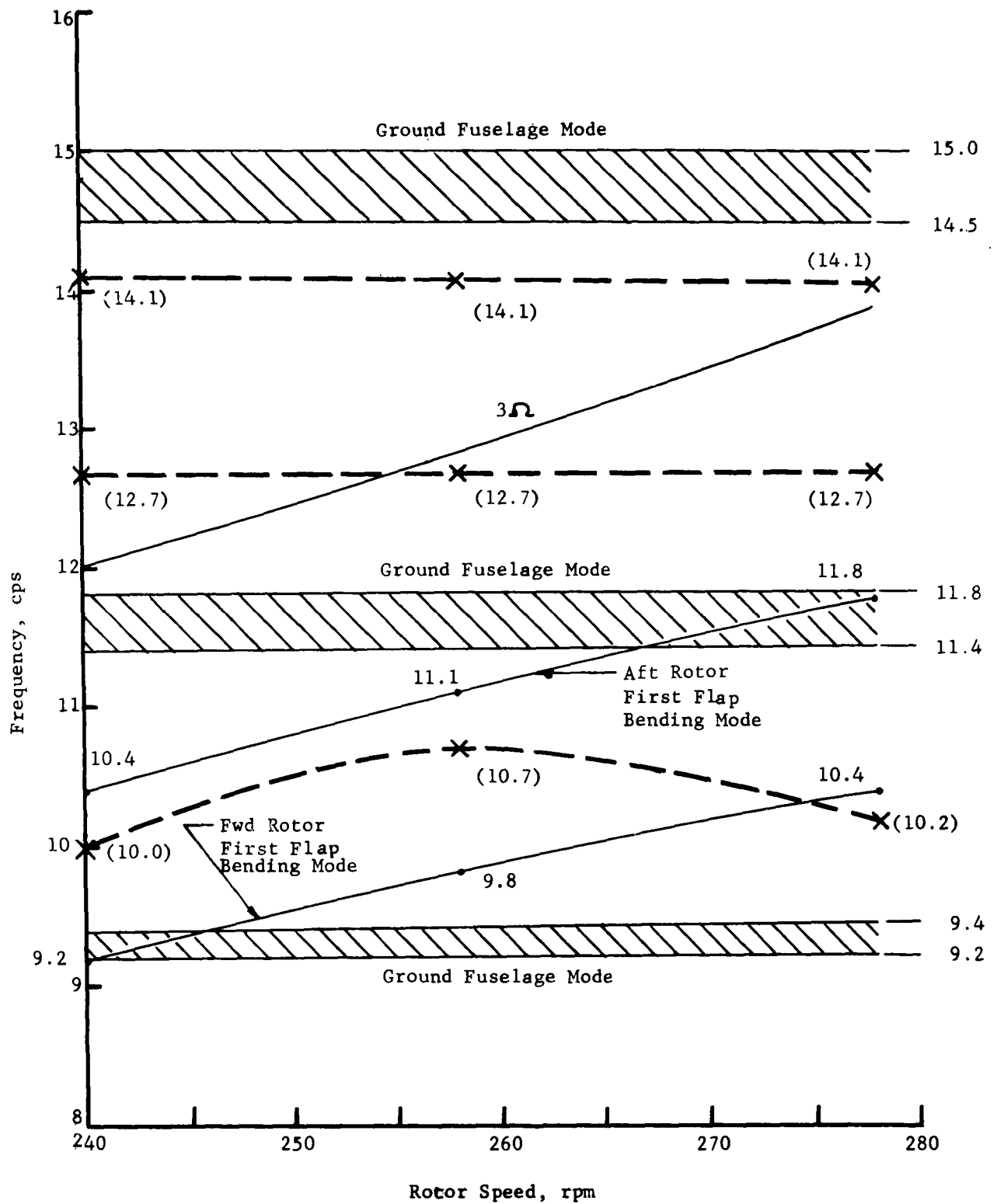



Figure 93 Calculated Frequency Response with Lateral Excitation

#### D. Third Harmonic Forced Response with Measured Hub Loads

Forced mode calculations were performed for the H-21 using the analytical model previously described and measured third harmonic shaft loads. Forced mode shapes were calculated for the flight conditions shown below:

<u>Rotor Speed Sweep</u>		<u>Air Speed Sweep</u>	
<u>Rotor Speed, rpm</u>	<u>Air Speed, knots</u>	<u>Air Speed, knots</u>	<u>Rotor Speed, rpm</u>
240	40 and 90	0	258
250	40 and 90	20	
258	40 and 90	40	
268	40 and 90	60	
278	40 and 90	80	
		90	
		105	258

For each of the preceding flight conditions, the forced mode is calculated but not plotted as a necessary step in obtaining the 3/rev cockpit floor response. These resultant or maximum vibratory amplitudes at the cockpit floor are presented and compared with measured third harmonic amplitudes from Reference 12.

All measured vibration data was recorded simultaneously with hub load measurements during Flight C96X124. No longitudinal motion was obtained. Calculated and measured cockpit floor amplitudes for the 40 and 90 knot rotor speed sweeps and for the air-speed sweep at a rotor speed of 258 are presented in Figure 94. The calculated amplitudes are shown on each figure by a solid line; the test results are shown with a dotted line representing the upper and lower limits of a scatterband obtained by reading two cycles of data for each flight configuration.

The airspeed sweep at 258 rpm shows reasonable correlation. Good trend and amplitude agreement exists between vertical and lateral test and computed cockpit floor response. For the 40 knot rpm sweep vertical calculated response is identical in general trend to the measured response, though smaller in amplitude. The lateral response does not compare well, being much higher at 278 rpm, and lower in the low rpm range than the test response. Only at 268 rpm is there good comparison between lateral test and calculated amplitudes. The 90 knot rpm sweep shows a test and analytical correlation which is opposite the one indicated at 40 knots; very good lateral agreement exists, while the vertical agreement is poor.

#### E. Forced Response to Independently Applied Rotor Forces

Fuselage response to 200 lb vertical, lateral and longitudinal cosine forces applied independently at each rotor head are presented to illustrate the relative effectiveness of each force in exciting the fuselage. Forced modes at  $3\Omega$  for forward and

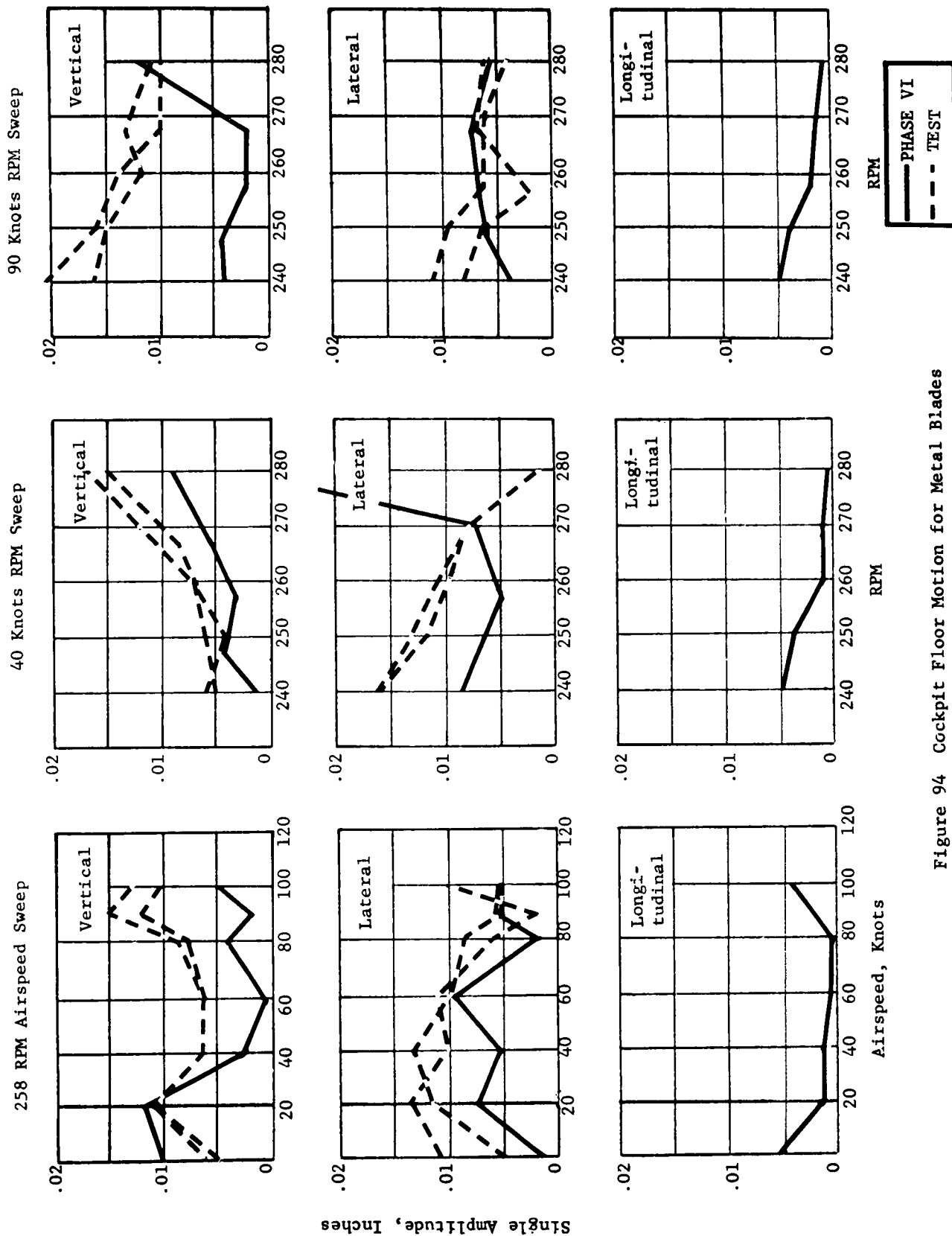


Figure 94 Cockpit Floor Motion for Metal Blades

aft rotor vertical forces, lateral forces, and longitudinal forces are compared in Figures 95, 96, and 97 respectively. Each figure presents forced modes due to longitudinal, lateral or vertical force at the forward and aft rotors. The in-phase, cosine mode shape is on top of the sheet and the 90° out-of-phase, sine, mode appears below the in-phase mode. Forward rotor 3Ω excitation is on the left side while the aft rotor 3Ω force is on the right side.

Figure 95 illustrates fuselage amplitudes under vertical loads at 3Ω at the forward and aft rotors. The left column shows the motion under a 200 lb instantaneous download at the forward rotor; the upper figure is the motion in phase with the force; the lower figure is 90° out of phase with the force. The right column is a similar study for an instantaneous vertical upload at the aft rotor. Note that vertical cockpit floor amplitudes for the forward rotor vertical force are two times that for an aft rotor force of the same magnitude. Out of phase response is small at the cockpit floor, but large in the aft fuselage and for the engine. Lateral cockpit floor motions are about a quarter of the longitudinal motions.

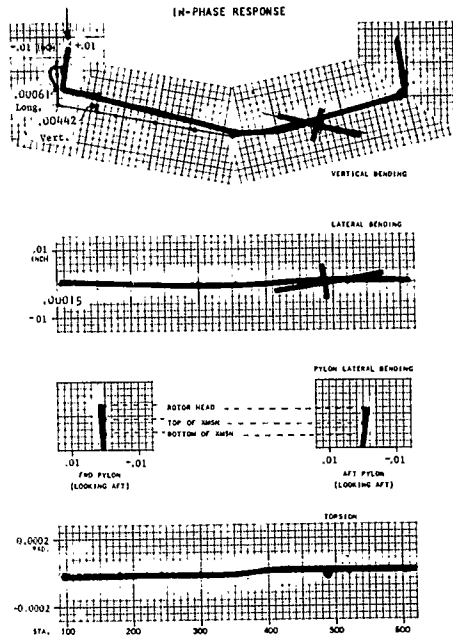
The 3Ω response to lateral individual forces at the forward and aft rotors in Figure 96 indicates that the fuselage motion due to the forward rotor excitation is nearly a mirror image of the response due to aft rotor excitation. Therefore, the lateral cockpit floor response is of opposite sign. The lateral in-phase motion is the only significant response with the vertical-longitudinal response being small. The force at the aft rotor excites larger lateral and yaw engine motion than the forward rotor force.

A 200 lb longitudinal force at the forward rotor in Figure 97, excites primarily longitudinal motion of the forward pylon about the cockpit floor station. Cockpit floor longitudinal and vertical motions are also present with the longitudinal motion of .00079 in. being larger than the .00061 in. amplitude produced by vertical forward rotor force. Note that forward and aft longitudinal forces acting in opposite directions will produce vertical and longitudinal cockpit floor motion of the same sign. The aft rotor force excites large vertical out of phase motion of the engine.

Summarizing cockpit floor response,

Force	Cockpit Floor Motion, Inches					
	Vertical, + Up		Lateral, + Right		Longitudinal, + Aft	
	In-Phase	Out of Phase	In-Phase	Out of Phase	In-Phase	Out of Phase
Forward Rotor						
200 lb Vertical, Up	-.00442	+.00004	-.00015	-.00001	-.00061	-.00001
200 lb Lateral, Right	-.00003	-.00008	-.00868	-.00018	-.00057	-.00004
200 lb Longitudinal, Aft	-.0042	-.00239	+.00035	-.00038	-.00079	-.0004

FORCED RESPONSE  
200 LBS. VERTICAL @ FWD. ROTOR



FORCED RESPONSE  
200 LBS. VERTICAL @ AFT ROTOR

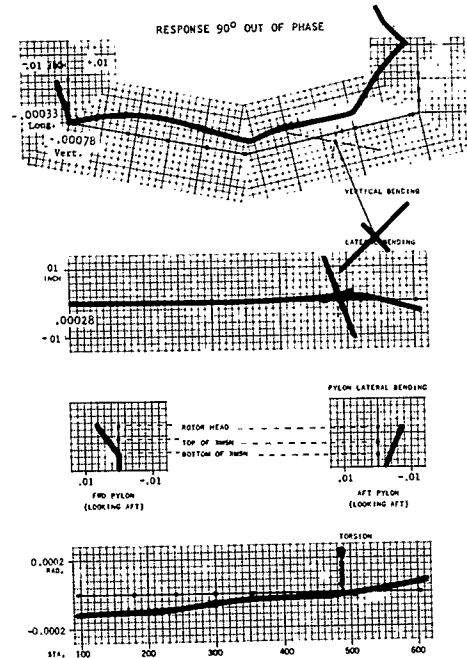
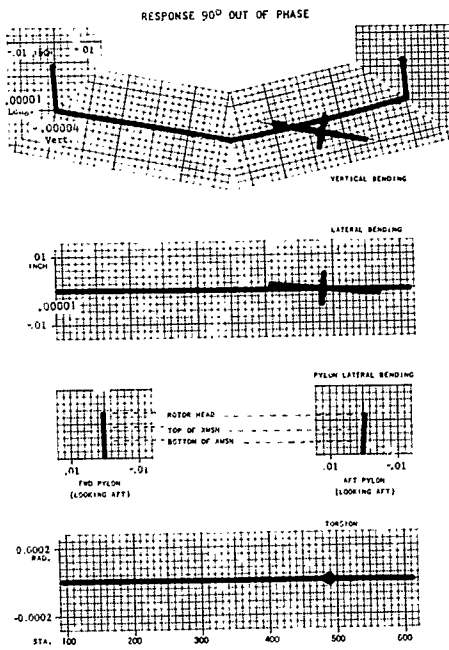
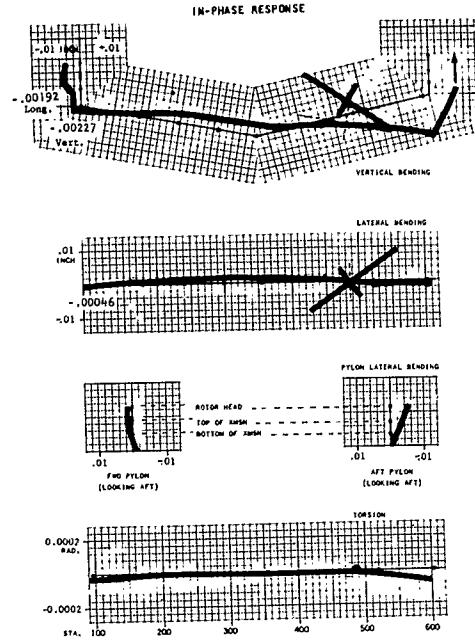
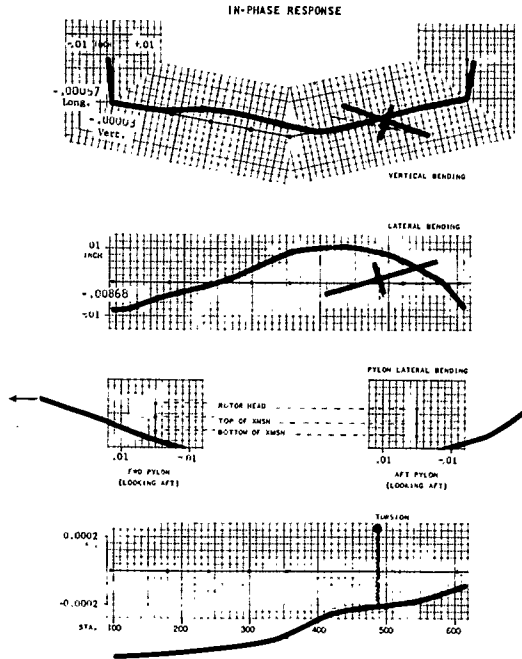


Figure 95 Forced Response - Vertical Unit Loads

FORCED RESPONSE  
200 LBS. LATERAL @ FWD ROTOR



FORCED RESPONSE  
200 LBS. LATERAL @ AFT ROTOR

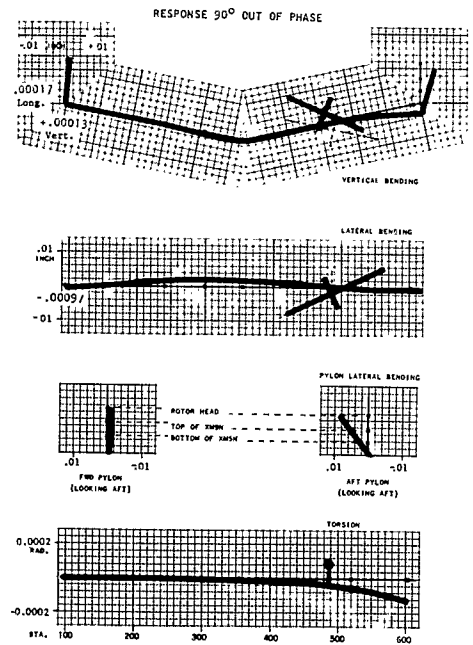
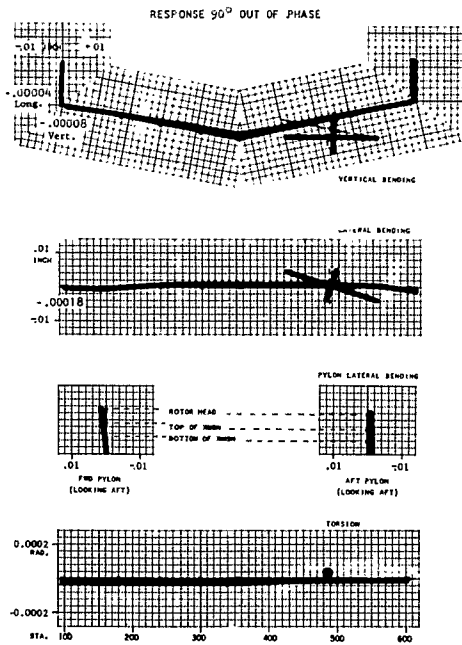
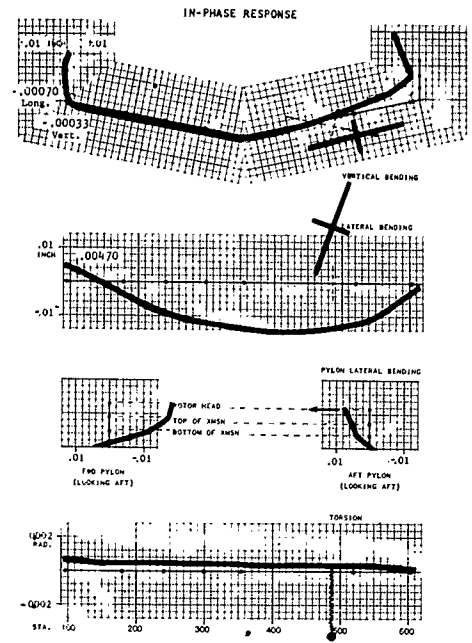
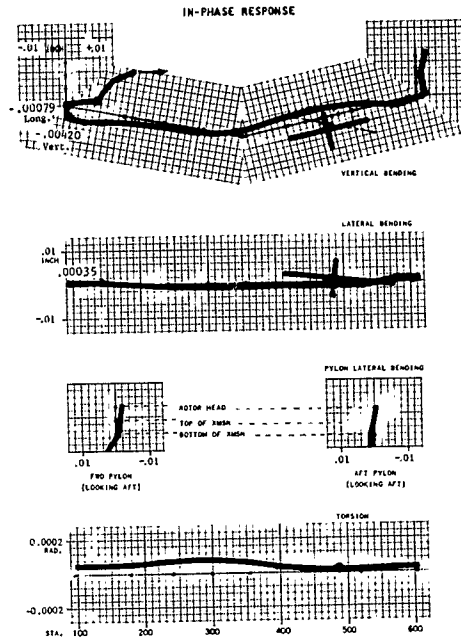


Figure 96 Forced Response - Lateral Unit Loads

FORCED RESPONSE  
200 LBS. LONGITUDINAL @ FWD ROTOR



FORCED RESPONSE  
200 LBS. LONGITUDINAL @ AFT ROTOR

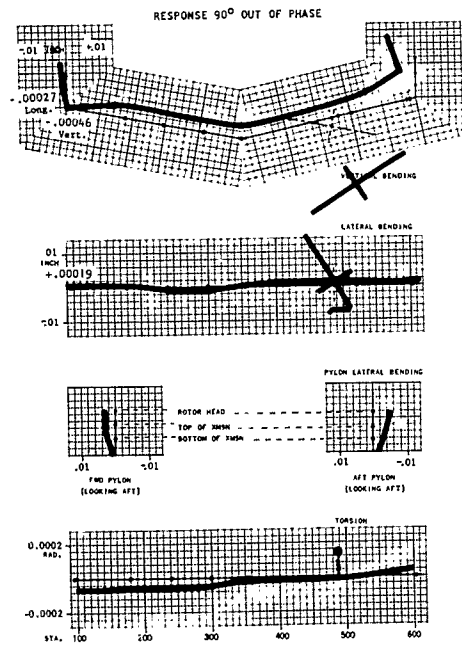
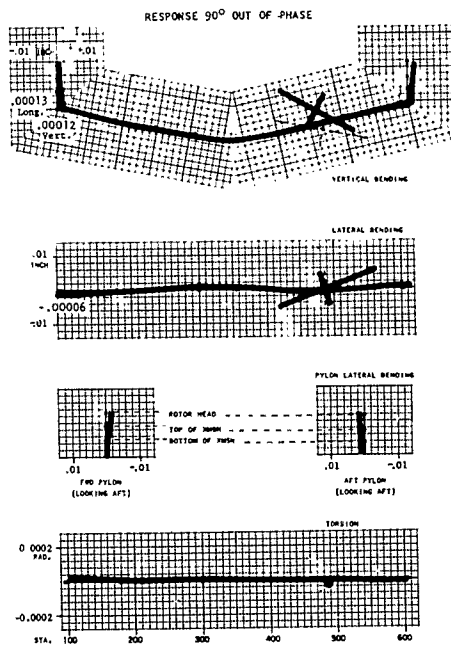
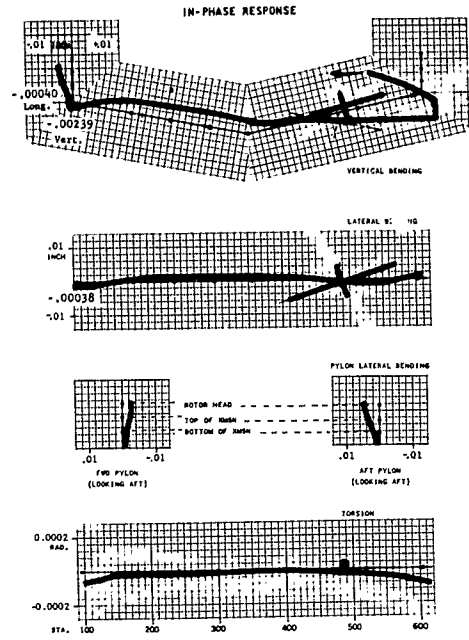


Figure 97 Forced Response - Longitudinal Unit Loads

Cockpit Floor Motion, Inches

Force	Vertical, + Up		Lateral, + Right		Longitudinal, + Aft	
	In-Phase*	Out of Phase	In-Phase	Out of Phase	In-Phase	Out of Phase
Aft Rotor						
200 lb Vertical, Up	-.00227	-.00078	-.00046	.00028	-.00192	-.00033
200 lb Lateral, Right	-.00033	+.00013	+.00470	-.00097	-.0007	.00017
200 lb Longitudinal, Aft	+.00239	+.00046	+.00038	-.0019	+.0004	+.00027

\* In phase or  $90^{\circ}$  out of phase with respect to the exciting force.

The table shows directly that vertical and longitudinal forces at either rotor produce nearly equal vertical motion and that forward rotor forces generally produce twice the cockpit floor motion that aft rotor forces produce.

#### F. Conclusions

An Associated Matrix analysis was developed for the calculation of the natural modes and forced response of a helicopter including six degrees of freedom for each mass element, structural damping and multidirectional rotor effective masses. This analysis is an extension of an earlier 13th order method without damping. The matrix representation includes concentrated masses and inertias, distributed stiffness properties in bending, shear and torsion, elastic sections to permit frame racking, local concentrated springs, a wandering elastic axis, uncoupled suspended mass, coupled suspended mass representing an engine mounted on damped dynafocal mounts, and a rotor effective mass containing flap and lag, and rigid and flexible rotor blade motions. Each matrix is of 26th order, allowing six real and imaginary motions and internal loads, and a real and imaginary external load. The method was programmed for the IBM 7090 computer at Wright Field.

The application of the procedure was to the H-21 helicopter in an in-flight shake test configuration for which directly comparable test data was available. The difference between ground and in-flight configurations is the addition of rotors, which for analytical calculations are represented by a fully coupled rotor effective mass matrix. Two sets of calculations were made, one with a vertical shaker at the mid-cabin, the second with a lateral shaker at the mid-cabin.

1. The calculated peak response frequencies generally show good agreement with the response peaks from test.

<u>Excitation</u>	<u>Matrix, cps</u>	<u>Test, cps</u>	<u>Excitation</u>	<u>Matrix, cps</u>	<u>Test, cps</u>
Lateral	5.6	5.6	Lateral	10.8	11.1
Vertical	---	7.5	Vertical	11.0	11.0
Vertical	8.1	8.1	Vertical	13.0	12.6
Lateral	---	9.2	Lateral	12.8	13.4
Vertical	---	9.1	Vertical	14.1	14.0
Vertical	10.0	9.9	Vertical	14.9	14.7
Lateral	9.5	10.05	Vertical	14.9	15.2
Vertical	10.4				



2. The amplitudes of the calculated shaker forced motions under vertical excitation are larger than the corresponding test amplitudes near the fundamental 8.1 cps vertical mode. Above this region, the calculated amplitudes for most of the fuselage stations are only slightly above the corresponding test amplitudes.
3. Calculated fuselage amplitudes under lateral shaker excitation, unlike those for vertical excitation, are nearly always below the comparable test data, with one exception. The calculated lateral transmission motion at 10.8 cps is much larger than the amplitude measured during the in-flight shake test.
4. The test peaks at 7.5 cps under vertical excitation and at 9.2 cps under lateral excitation have no corresponding calculated response. The mode calculated at 9.2 cps is the fundamental lateral bending mode.
5. Variations of rotor damping have most influence on forced amplitudes for frequencies near the fundamental vertical mode at 8.0 cps. The amplitudes decrease rapidly when the damping is increased from  $\frac{1}{2}$  normal (calculated) to normal, but a further increase to  $1\frac{1}{2}$  normal produces only a negligible reduction.
6. ( $\omega$ ) excitations at the rotor shaft induce blade flap, and lag oscillations at  $\omega$ ,  $\omega + \Omega$  (rotor speed) and  $\omega - \Omega$ . The blades respond in all directions to uni-directional excitation at all three frequencies.
7. A damped blade resonance can be produced whenever any one of the three frequencies  $\omega$ ,  $\omega + \Omega$ , or  $\omega - \Omega$  correspond with a coupled fuselage-blade mode.
8. The flap response at  $\omega$  follows in-phase vertical rotor hub motion. Flap response at  $\omega - \Omega$  follows the vertical rotor hub motion  $90^\circ$  later.
9. The lag response at  $\omega$ ,  $\omega - \Omega$ , and  $\omega + \Omega$  follows the lateral rotor hub motion in-phase, and follows the longitudinal rotor hub motion  $90^\circ$  later.
10. The peak frequencies which appear, namely, blade rigid lag, blade first flap bending and first lag bending, are due to blade dynamics and not to rotor hub motions.

Effect of rotor speed conclusions:

1. Several of the calculated ground modes shift frequency in flight. Some exhibit a uniform shift, nearly independent of rotor speed, while others vary natural frequency with rotor speed.
2. Under vertical mid-cabin shaker excitation, the calculated 7.4 - 7.5 cps ground mode moves to 7.9 - 8.1 cps. The ground mode at 12.2 - 12.3 ranges from 12.9 to 12.6 cps with increasing rotor speed; the ground mode at 15.0 - 15.2 cps moves to 14.9 - 15.0 cps in-flight.
3. The forward blade uncoupled flap frequency moves from 9.2 to 10.4 cps as rotor speed varies from 240 to 278 rpm. The calculated coupled fuselage-blade modes are shifted downward to 8.9, 9.5, and 9.7 cps, a maximum shift of 0.16 per rev.
4. The aft blade uncoupled flap frequency shifts downward from 10.4 to 9.2 at 240 rpm and from 11.8 to 11.0 cps at 278 rpm, a maximum shift of 0.28 per rev.

Rotor order forced calculations were performed for the H-21 helicopter applying 3 $\Omega$  shaft loads obtained from the in-flight load measurement program with metal blades. Measured cockpit floor vibration data recorded simultaneously with the load data is used for comparison. Conclusions specific to third harmonic rotor order excitation for metal blades are as follows:

#### Metal Blades

1. For the airspeed sweep, the calculated and test single amplitudes at the cockpit floor average:

	<u>Vertical</u>	<u>Lateral</u>	<u>Longitudinal</u>
Calculated	0.005"	.007"	.003"
Test	0.009"	.009"	Not available

2. For vertical cockpit floor motion, the calculated trend with rpm at 40 knots compares well with the corresponding test trend, with the calculated amplitudes being slightly below the test amplitudes. For the 40 knot rpm sweep, the trend between test and calculated values is similar up to 268 rpm, but at 278 rpm, the sharp calculated uptrend is not reflected in test.
3. For the 40 knot rpm sweep the calculated lateral cockpit floor motion is similar to test but smaller up to 268 rpm. For rpm greater than 268, the calculated amplitudes go up, while the test amplitudes continue to decrease. For the 90 knot rpm sweep, the lateral cockpit floor amplitudes have no clear trend with rpm, nevertheless, the test and calculated amplitudes are generally equal.

#### Independently Applied Rotor Forces

1. Cockpit floor motions in all directions are twice as large for forward rotor forces as they are for aft rotor forces.
2. Equal vertical or longitudinal forces at either rotor produce nearly equal cockpit floor motion in all directions.
3. Vertical excitation in the same direction at the forward and aft rotors produces cockpit floor motions of the same sign in the vertical direction; the opposite is true for lateral and longitudinal forces.
4. Out of phase cockpit floor response is small.
5. Aft rotor forces induce large engine motion, usually out of phase.

## SECTION IX

### CONCLUSIONS

A comprehensive research program covering many facets of tandem rotor helicopter fuselage vibration has been conducted. Analytical portions consisted of the development of methods for the prediction of natural frequencies and forced modes; test portions of the program determined fuselage stiffness properties, rotor shaft vibratory loads and in-flight natural frequencies, modes and vibration levels. The information obtained here has proven to be invaluable in the development cycles of the present generation of military helicopters.

The initial analytical effort, Phase I, used generalized coordinate coupling to predict changes in natural frequencies and modes resulting from changes in mass and stiffness properties.

1. An inherent advantage of this method is that data from ground shake tests, which are a part of most aircraft development, and weight data which must be known, may be utilized directly without resort to the stiffness estimates which must accompany the creation of lumped mass analytical models.
2. For mass changes only, the coupling method was accurate, but rigid body modes had to be included, especially for the lower frequency modes nearest the "zero" frequency rigid body modes.
3. For stiffness changes only, the coupling procedure did not function as effectively. Rigid body modes made no contribution whatever, so that the three straight-forward modes which were useful in the mass case were of no assistance.

Next, an uncoupled method for the prediction of fuselage natural modes and frequencies from design mass and stiffness data was developed under Phase IIa.

1. The method was shown to be operationally simple and capable of representing a multitude of fuselage properties including (1) discrete lumped masses and moments of inertia, (2) suspended lumped masses and moments of inertia, (3) bends permitting the selected elastic axis to follow the general fuselage shape, (4) sections of elastic beam which permitted inclusion of bending, shear, axial, and torsional stiffness properties, (5) concentrated springs which simulate the attachment of large local mass and inertia items to the fuselage structure, and (6) ground springs which permit attachment of the vibrating body to an external ground.
2. For large helicopter fuselage cross sections where normal cutouts such as cabin entrance doors were only a small portion of the overall peripheral size, it was possible to obtain good agreement with test using separate vertical and lateral analyses.

3. Certain patterns appeared in the fuselage modes with reasonable consistency. In vertical bending, the first mode was predominantly simple beam bending, so that the bending stiffness estimate was most important here. The second vertical bending mode consisted of anti-symmetric pylon motions along with a second bending mode of the fuselage proper. This mode was particularly dependent on the estimate of the rotor transmission attachment spring rates. Third and higher modes reflected all the stiffness properties, and were less a function of any single property. In the lateral cases, torsional stiffness predominated in the first mode, and either lateral bending or rotor transmission roll attachment in the second mode. Higher modes were dependent on a mixture of all the properties as in the vertical case.

4. The addition of a flexibly mounted engine disturbed the mode pattern somewhat. For modes in which engine motion was not dominant, the fuselage mode patterns were still applicable.

5. For small helicopter fuselage cross sections where normal cutouts were a large portion of the overall peripheral size, the separate vertical and lateral treatment was shown to be inadequate. In such cases, important coupling appeared between vertical and lateral directions, so that a fully coupled, six degree of freedom analysis was necessary.

A load deflection test, Phase IIb, was performed on the H-21 to obtain stiffness characteristics and check them against the calculated stiffness values used in Phase IIa. Stiffness properties were determined for fuselage vertical and lateral bending and transverse shear; fuselage torsion; transmission vertical, lateral, pitch and roll restraints relative to the fuselage; and rotor shaft pitch and roll spring restraints relative to the transmission.

1. Substantial coupling was found between vertical bending and torsion due to the large asymmetrically located cabin doors. Such coupling had always been neglected in dynamic calculations for helicopter fuselages.
2. Torsional deformation of the cabin structure involved appreciable racking of the fuselage frames, and was not definable by the simple Saint Venant torsion theory.
3. Vertical bending and shear stiffness of the forward fuselage, and to a lesser extent the aft fuselage, were nonlinear above a certain load level.
4. Cross sectional distortion of many of the fuselage frames for loads at the rotor shafts was substantial.
5. Calculated values were generally judged to be reasonably accurate for purposes of preliminary dynamic analysis of the fuselage. Exceptions were torsional stiffness including the location of the elastic axis, and lateral bending stiffness in the engine hatch and forward cabin areas.

A rotor load measurement program was conducted in Phase III, giving for the first time a complete picture of all the steady and oscillatory loads acting in the rotor shafts.

1. Shaft strain gage instrumentation had average accuracies of 6% for steady and 4% for oscillating load.
2. Steady loads checked against known data, that is, the total lift at both rotors checked closely against takeoff gross weight, and the torque total agreed with known power requirements. Forward and aft rotor torques were equal in hover, but in forward flight the aft rotor averaged 2.5 times the forward rotor; the torque differential was shown to be reacted by a measured lateral couple at the two rotors.
3. First harmonic fixed system results indicated that the in-plane loads were of appreciable magnitude, but vertical loads were always small.
4. Second harmonic fixed system loads were small with respect to other harmonics.
5. With a three bladed helicopter, third harmonic vibration levels are usually the dominant portion of the vibration environment, so that measured third harmonic loads are particularly important. Longitudinal shaft loads were the largest, averaging 800 lb at the forward rotor and 1300 lb at the aft; lateral loads averaged 250 and 500 lb forward and aft respectively; vertical loads averaged 200 and 400 lb forward and aft respectively. Both roll and pitch moments averaged 2500 in lb at the forward rotor and 5000 in lb at the aft rotor.
6. Third harmonic vertical loads arise from direct addition of the vertical components of third harmonic blade root flap shears. Third harmonic in-plane loads come from second and fourth harmonic blade root lag shears and from horizontal components of second and fourth harmonic blade root normal flap shears. The measured second and fourth harmonic resultant rotating loads were the same in the longitudinal and lateral directions; in the rotating system these directions refer to the master hub spline azimuth and its perpendicular.
7. Second harmonic rotating loads averaged 500 lb at the forward rotor, 900 lb at the aft rotor. They displayed a tendency toward the high hover, low cruise force levels characteristic of third harmonic vibration levels. Fourth harmonic rotating loads averaged 250 lb at the forward rotor, and 500 lb at the aft rotor. In converting to the fixed third harmonic system, second and fourth add to produce large longitudinal loads and subtract to produce small lateral loads.
8. Longitudinal and lateral cockpit floor vibration levels followed the longitudinal and lateral force trends with airspeed. Vertical vibration did not correlate consistently with any single force.

The testing techniques evolved for the performance of an in-flight shake test in Phase II provide a powerful diagnostic tool for improving helicopter vibration environment. The techniques which were developed have proven the feasibility of the in-flight shake test as a routine method for determining the response characteristics of helicopters in-flight. Ground shake testing of the H-21 was performed with the same equipment prior to flight, and the results compared with flight data to evaluate multi-directional rotor coupling, flap and chord blade natural frequency effects and rotor damping.

Specific conclusions pertinent to the H-21 helicopter under the excitation of a lateral shaker located near the centerline between rotors are as follows:

1. A fuselage response was clearly evident at 5.5 cps corresponding to blade rigid body lag frequency plus rotor speed, i.e., fixed system blade lag frequency.
2. Fuselage modes whose frequencies were not near the fundamental flap bending frequencies of either forward or aft blades were not subject to rpm variations in flight. (Blade frequencies differed by virtue of a 20 pound weight at 50% span in the forward blades.)
3. The fundamental lateral ground shake test natural frequencies were all shifted in-flight as follows:

<u>Ground, CPS</u>	<u>In-Flight, CPS</u>
8.4 to 8.9	9.2
10.4 to 10.8	11.1
14.0 to 14.2	13.2

In two cases the frequency shift was upward, in the third it was downward. Rotor effective mass coupling thus shifted ground modes, but not in one definite direction. The frequency shift from 14.0 to 13.2 cps was particularly significant because it placed this mode nearly in resonance with the predominant three per rev forcing frequency of this three-bladed helicopter.

4. The in-flight forward blade fundamental flap bending natural frequency agreed with the calculated value of 240 rpm, but was above the calculated value at 258 rpm and 278 rpm by about 0.25 cps ( $0.06\Omega$ ).

5. The in-flight aft blade fundamental flap bending natural frequency was generally reduced by 0.25 cps ( $0.06\Omega$ ) from the calculated values.

6. The blade flap bending natural frequency peaks generally follow the predicted upward trend with rotor rpm.

7. Calculated uncoupled blade natural frequencies, long an empirical guide to moderate vibration levels, must be viewed with recognition that coupling with fuselage modes can vary them by 0.25 cps in either direction.

Similar conclusions were drawn regarding the results from vertical shaker excitation.

1. The ground fuselage modes at 8.1 to 8.4 cps and 9.0 to 9.5 cps remained unchanged in frequency during flight and showed little rpm variation.

2. The 11.6 to 12.1 cps ground test mode increased to 12.6 cps at 240 and 258 rpm and to 12.2 cps at 278 rpm, resulting in a downtrend with rpm. This rpm effect attests to the importance of rotor effective mass coupling.

3. The 12.8 to 13.1 cps ground test mode showed a significant rotor speed effect in-flight, with response varying from 14.0 cps at 240 rpm to 13.4 cps at 278 rpm. This mode was particularly important because of its closeness to the rotor third harmonic.

4. In-flight peak responses at 14.4, 14.5 cps showed that this mode remained in about the same place as the ground mode at 14.2 to 14.7 cps.

5. In-flight peak responses at 15.2, 15.0 cps represented a downward coupling of the 15.3 to 15.6 ground mode due to the forward blade fundamental lag bending -  $1\Omega$  mode.

6. Blade flap bending natural frequencies obtained in the flight test under vertical excitation followed an uptrend with rpm, but at a lesser rate than calculated. This was again due to the influence of coupling with nearby fuselage modes. The blade modes obtained under vertical shaker excitation differed from those under lateral excitation, again verifying the powerful effect of the fuselage blade relationships.

7. Despite the use of 300 lb of shaker force in the vertical direction compared to 200 lb in the lateral direction, response amplitudes of the blade flap modes were smaller under vertical excitation. This is evidently because (a) vertical excitation must excite the whole helicopter mass in order to transmit vertical excitation to the blades, while lateral excitation at the cabin floor rolls the fuselage and excites the blades in differential vertical motion on the right and left sides of the rotor, and (b) rotor damping is more effective in the vertical direction.

As a result of the Phase IIb load-deflection test, the analytical matrix analysis of Phase IIa was extended in Phase IIc to include vertical-lateral coupling and frame racking. Six degrees of freedom were used to calculate free and forced modes of the fuselage.

1. A static deflection calculation using the fuselage matrix representation agreed closely with the test deflection data when vertical - lateral deflections under a 3600 lb vertical forward rotor load were calculated.

2. Twelve natural modes were calculated in the range from 7 to 20 cps, six of which were related to the dynafocal engine suspension. Reasonable frequency agreement appeared between the calculated and test data, but mode shape agreement was not as favorable.

3. The first mode at 7.37 cps was engine roll and had no fuselage shake test counterpart because a single hydraulic shaker in the cabin did not excite this mode. First vertical bending was predominant in the second mode at 7.62 cps calculated, and compared closely in shape and frequency with an 8.1 cps test mode. The third mode at 8.45 cps was a predominant engine mode. Fourth matrix at 9.58 cps was fundamental lateral bending - torsion, corresponding in shape to a test mode at 8.4 cps. Fifth matrix at 9.85 cps was a mixture of engine and fuselage lateral bending - torsion. The calculated 11.66 cps sixth mode matched the second vertical bending, highly coupled with the lateral bending-torsion shape of the

10.4 cps test mode. Seventh matrix at 12.13 cps, second lateral bending-torsion, was similar to an 11.9 cps test mode. Eighth to twelfth matrix modes at 12.88, 14.53, 16.09, 17.8 and 18.9 cps were more complex shapes.

4. Forced response calculations were performed using measured third harmonic shaft loads from Phase III. Comparison with measured cockpit floor vibration showed good agreement in the vertical direction. In the lateral direction at the cockpit floor the calculated vibration generally exhibited the same trends as the test data, but did not compare as well as the vertical in absolute magnitude.

As a further development of the Associated Matrix Method for the calculation of the natural modes and forced response of a helicopter, structural damping and multi-directional rotor effective masses were added to the matrix representation used in Phase IIc and IV. The procedure was applied to the H-21 helicopter in an in-flight shake test configuration for which directly comparable test data was available.

1. The calculated peak response frequencies showed good agreement with response peaks from test.

2. The amplitudes of shaker forced motions under vertical excitation were calculated to be larger than the corresponding test amplitudes, especially at the fundamental mode. Calculated fuselage amplitudes under lateral shaker excitation, unlike those for vertical excitation, were nearly always below the comparable test data.

3. Excitations,  $\omega$ , at the rotor shaft induced blade flap and lag oscillations at  $\omega$ ,  $(\omega + \Omega)$  (rotor speed) and  $(\omega - \Omega)$ . The blades responded in all directions to uni-directional excitation at all three frequencies.

4. A damped blade resonance was produced whenever any one of the three frequencies  $\omega$ ,  $(\omega + \Omega)$ , or  $(\omega - \Omega)$  corresponded with a coupled fuselage-blade mode.

5. Blade flap response at  $\omega$  followed vertical rotor hub motion in-phase, and followed the longitudinal rotor hub motion  $90^\circ$  later.

6. Blade lag response at  $\omega$ ,  $(\omega - \Omega)$ , and  $(\omega + \Omega)$  followed the lateral rotor hub motion in-phase, and followed the longitudinal rotor hub motion  $90^\circ$  later.

7. Peak frequencies appeared which were due to blade dynamics and not to rotor hub motions, namely; blade rigid lag, blade first flap bending and first lag bending.

8. Several of the calculated ground modes shifted frequency in-flight. Some exhibited a uniform shift, nearly independent of rotor speed, while others varied natural frequency with rotor speed.



9. The forward blade uncoupled flap frequency moved from 9.2 to 10.4 cps as rotor speed varied from 240 to 278 rpm. The calculated coupled fuselage-blade modes were shifted downward to 8.9, 9.5 and 9.7 cps, a maximum shift of  $0.16 \Omega$ .

10. The aft blade uncoupled flap frequency shifted downward from 10.4 to 9.2 cps at 240 rpm and from 11.8 to 11.0 cps at 278 rpm, a maximum shift of  $0.28 \Omega$ .

## REFERENCES

1. Air Force Contract AF33(616)-5240, Theoretical Analysis and Calculations for a Method of Computing the Response of Tandem Rotor Helicopters to Rotor Induced Vibratory Forces, May 27, 1957.
2. Loewy, R.G., Yntema, R.T., Gabel, R. A Study of Tandem Helicopter Fuselage Vibration; Phase I, A Method for the Prediction of Natural Mode and Frequency Changes Accompanying Changes in Fuselage Mass and Stiffness, Boeing-Vertol, Report R-160, October 1958.
3. Loewy, R.G., Yntema, R.T., Gabel, R. A Study of Tandem Helicopter Fuselage Vibration; Phase IIa, A Method for the Prediction of Natural Modes and Frequencies from Design Mass and Stiffness Data, Boeing-Vertol, Report R-181, February 1960.
4. Yntema, R.T., Manger, D. A Study of Tandem Helicopter Fuselage Vibration; Phase IIb, Load Deflection Tests on an H-21 Helicopter Fuselage to Determine Stiffness Characteristics, Boeing-Vertol, Report R-180, April 1959.
5. Yntema, R.T., Gable, R., Ricks, R.G. A Study of Tandem Helicopter Fuselage Vibration; Phase III, In-Flight Measurement of Steady and Oscillatory Rotor Shaft Loads, Boeing-Vertol, Report R-238, February 1961.
6. Yntema, R.T., Gabel, R., Ricks, R.G. A Study of Tandem Helicopter Fuselage Vibration ; Phase IIc and IV, A Method for the Prediction of Coupled Vertical-Lateral Natural and Forced Modes, Boeing-Vertol, Report R-246, April 1961.
7. Yntema, R.T., Gabel, R., Ricks, R.G., Reed, D.A. A Study of Tandem Helicopter Fuselage Vibration ; Phase V, In-Flight Shake Test, Boeing-Vertol, Report R-259, September 1961.
8. Ricks, R.G., Shyprykevich, P., Gabel, R., A Study of Tandem Helicopter Fuselage Vibration; Phase VI, A Method for the Prediction of Coupled Vertical-Lateral Modes Including Multidirectional Damped Rotor Effective Mass, Boeing-Vertol, Report R-274, April 1962.
9. Grant, William. A Study of Tandem Helicopter Fuselage Vibration; Phase VII, Correlation Between Measured Helicopter Vibration Data and Pilot Comments, Boeing-Vertol, Report R-225, December 1960.
10. Targoff, W.P. "The Associated Matrices of Bending and Coupled Bending-Torsion Vibrations," Journal of the Aeronautical Sciences, January 1947.
11. Yeates, J.E., Jr., Brooks, G.W., Houbolt, J. C. Flight and Analytical Methods for Determining the Coupled Vibration Response of Tandem Helicopter, NACA Report 1326, 1957.
12. Ricks, R.G., Shyprykevich, P., Gabel, R. Smyers, D.J. In-Flight Measurement of Helicopter Rotor Shaft Loads Under Control Cyclic Trim Variations, Boeing-Vertol, Report R-262, August 1961.

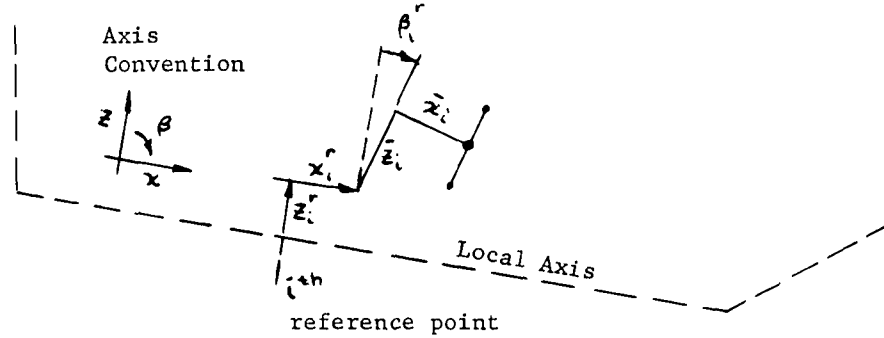
APPENDIX A  
DERIVATION OF THE GENERALIZED  
COORDINATE COUPLING EQUATIONS

## Vertical - Longitudinal Coupling Analysis

### Kinetic Energy

Consider a fuselage section having mass  $m_i$  and pitching mass moment of inertia  $I_i$  located from a reference point  $i$  on a local axis by components  $\bar{x}_i$  and  $\bar{z}_i$ , parallel and perpendicular to the local axis. Displacements  $x_i^r$ ,  $z_i^r$  and  $\beta_i^r$  in a natural mode ( $r$ ) at the reference point  $i$  are assumed to be known.

Displacement of the mass  $m_i$  due to motion in the  $r^{\text{th}}$  mode, written in the local axis convention, are



$$\begin{aligned} x_{LA} &= x_i^r + \bar{z}_i \beta_i^r \\ z_{LA} &= z_i^r - \bar{x}_i \beta_i^r \\ \beta_{LA} &= \beta_i^r \end{aligned} \quad \text{For small values of } \beta_i^r \quad (1)$$

Introduce the generalized modal coordinate  $H_r$  and determine the component velocities by differentiating with respect to time.

$$\begin{aligned} \dot{x}_{LA} &= [x_i^r + \bar{z}_i \beta_i^r] \dot{H}_r \\ \dot{z}_{LA} &= [z_i^r - \bar{x}_i \beta_i^r] \dot{H}_r \\ \dot{\beta}_{LA} &= \dot{\beta}_i^r \dot{H}_r \end{aligned} \quad (2)$$

From equations (2) the Kinetic Energy may be written for any two modes  $H_r$  and  $H_s$  (or it may be extended for any number of modes).

If the modes  $H_r$  and  $H_s$  were true natural modes, no terms would result in the Kinetic Energy expression that involved the product  $H_r H_s$  and the original mass distribution. Products should arise, however, from terms involving the added mass distribution and these products will lead to the necessary coupling between the modes resulting from added mass. The use of experimental information results in coupling terms with the original mass distribution and these terms are omitted from the final equations.

The remaining terms involving the original mass distribution are the coefficients of  $\frac{1}{2} \dot{H}_r^2$  and  $\frac{1}{2} \dot{H}_s^2$ . These coefficients are called the effective masses  $M_{eff}^r$  and  $M_{eff}^s$ . They represent the mass which, placed at the points at which  $H_r$  and  $H_s$  are normalized (i.e. unity), would have the kinetic energy of the whole structure in that mode.

### Potential Energy

Potential energy, in beam deformation problems, is composed of the fibre strain energy which alternately stores and returns energy to the kinetic form during an oscillation. From deformation theory, such strain energy may come from bending deflection, tensile deflection, shear deflection, and twist deflection. For the vertical bending fuselage beam, only the first three are applicable. They are classically stated as

$$\begin{aligned} V_b &= \frac{1}{2} \int \left( \frac{M}{EI} \right)^2 EI dx && \text{Bending} \\ V_s &= \frac{1}{2} \int \left( \frac{V}{GA} \right)^2 GA dx && \text{Shear} \\ V_t &= \frac{1}{2} \int \left( \frac{P}{AE} \right)^2 AE dx && \text{Tension} \end{aligned}$$

where

- $V$  = potential energy
- $x$  = longitudinal beam location, in.
- $z$  = vertical deflection, in.
- $E$  = Modulus of elasticity, #/in<sup>2</sup>
- $I$  = cross sectional moment of inertia, in<sup>4</sup>
- $G$  = shear modulus of elasticity, #/in<sup>2</sup>
- $A$  = cross sectional area, in<sup>2</sup>
- $M$  = bending moment, in.-#
- $V$  = Vertical shear, #
- $P$  = axial tension, #

If a change in section property is made, an increment of potential energy is added to the total, and continuing with the use of two illustrative modes, which may later be extended to a general number of modes, the modes  $r$  and  $s$  are introduced into the potential energy expressions. This may be done by letting the total moment, shear, or tension,  $M$ ,  $V$ ,  $P$  be composed of loadings in each mode.

$$V_0 + \Delta V_0 + \frac{1}{2} \int_0^l \left( \frac{M^r H_r + M^s H_s}{EI} \right)^2 EI dx + \frac{1}{2} \int_l^{l+1} \left( \frac{M^r H_r + M^s H_s}{EI} \right)^2 \Delta EI dx$$

Bending

$$V_s + \Delta V_s = \frac{1}{2} \int_0^l \left( \frac{V^r H_r + V^s H_s}{GA} \right)^2 GA dx + \frac{1}{2} \int_l^{l+1} \left( \frac{V^r H_r + V^s H_s}{GA} \right)^2 \Delta GA dx$$

Shear

$$V_t + \Delta V_t = \frac{1}{2} \int_0^l \left( \frac{P^r H_r + P^s H_s}{EA} \right)^2 EA dx + \frac{1}{2} \int_l^{l+1} \left( \frac{P^r H_r + P^s H_s}{EA} \right)^2 \Delta EA dx$$

Tension

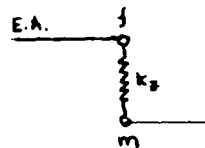
Local springs may be included in the equations of motion by first considering their potential energy contributions. The spring may be in series with the main progression of the beam length, or elastic axis, or may be a branch, system supporting a local mass.

#### Spring Joint

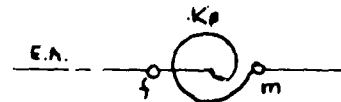
Tension  
Member



Shear  
Member

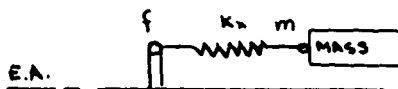


Moment  
Member



#### Suspension Spring

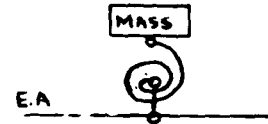
Tension  
Direction



Shear  
Direction



Pitch  
Direction



If  $x_f$ ,  $z_f$  and  $\phi_f$  define the motion of the spring support on the main fuselage beam in the local axial, vertical, and pitch directions, and  $x_m$ ,  $z_m$  and  $\phi_m$  define the motion of the other end of the spring joint or the motion of the sprung mass in the corresponding directions, then the potential energy may be written as,

$$\begin{aligned} V_L + \Delta V_L &= \frac{1}{2} (K_x + \Delta K_x) (\chi_m^r - \chi_f^r) H_r + (\chi_m^s - \chi_f^s) H_s \\ &+ \frac{1}{2} (K_z + \Delta K_z) (z_m^r - z_f^r) H_r + (z_m^s - z_f^s) H_s \\ &+ \frac{1}{2} (K_\theta + \Delta K_\theta) (\theta_m^r - \theta_f^r) H_r + (\theta_m^s - \theta_f^s) H_s \end{aligned}$$

As described under the kinetic energy section, the orthogonality condition between normal modes demands that all products of the form  $H_r H_s$  involving only the original stiffness distributions must sum to zero. Consequently, such terms in the potential energy are eliminated. As with the Kinetic Energy, the coefficients of  $\frac{1}{2} H^2$  that involve the original stiffnesses are called  $K_{eff}^r$  and  $K_{eff}^s$ .

The Potential Energy expression is further simplified by evaluating the integrals containing stiffness changes. The moment at any point in a bay is expressed in terms of the inertia loads at one end of the bay.

#### Equations of Motion

Fulfillment of the appropriate terms in the Lagrange equation

$$\frac{d}{dt} \left( \frac{\partial T}{\partial \dot{H}} \right) - \frac{\partial T}{\partial H} + \frac{\partial V}{\partial H} = 0$$

### H<sub>r</sub> Equation of Motion

$$\begin{aligned}
 & - \left\{ M_{\text{eff}}^r + m_a [(\bar{\chi}_a^r + \bar{z}_a \beta_a^r)^2 + (\bar{z}_a^r - \bar{\chi}_a \beta_a^r)^2] + I_a \beta_a^{r^2} \right\} \bar{H}_r \\
 & - \left\{ m_a [(\bar{\chi}_a^r + \bar{z}_a \beta_a^r)(\bar{\chi}_a^s + \bar{z}_a \beta_a^s) + (\bar{z}_a^r - \bar{\chi}_a \beta_a^r)(\bar{z}_a^s - \bar{\chi}_a \beta_a^s)] + I_a \beta_a^r \beta_a^s \right\} \bar{H}_s \\
 & + \left\{ \omega_r^2 M_{\text{eff}}^r + \left[ M_s^r \ell_s - M_s^r V_f^r \ell_s^2 + V_f^r \frac{\ell_s^3}{3} \right] \frac{\Delta EI}{(EI)^2} + V_f^r \ell_s \frac{\Delta GA}{(GA)^2} + P_s^r \ell_s \frac{\Delta EA}{(EA)^2} \right. \\
 & \quad \left. + \Delta K_x (\chi_m^r - \chi_s^r)^2 + \Delta K_z (z_m^r - z_s^r)^2 + \Delta K_\theta (\theta_m^r - \theta_f^r)^2 \right\} \frac{\bar{H}_r}{\omega^2} \\
 & + \left\{ (M_s^r M_s^s \ell_s - M_s^r V_f^s \frac{\ell_s^2}{2} - M_s^s V_f^r \frac{\ell_s^2}{2} + V_f^r V_f^s \frac{\ell_s^3}{3}) \frac{\Delta EI}{(EI)^2} + V_f^r V_f^s \ell_s \frac{\Delta GA}{(GA)^2} + P_s^r P_s^s \ell_s \frac{\Delta EA}{(EA)^2} \right. \\
 & \quad \left. + \Delta K_x (\chi_m^r - \chi_s^r)(\chi_m^s - \chi_s^s) + \Delta K_z (z_m^r - z_s^r)(z_m^s - z_s^s) + \Delta K_\theta (\theta_m^r - \theta_f^r)(\theta_m^s - \theta_f^s) \right\} \frac{\bar{H}_s}{\omega^2} = 0
 \end{aligned}$$

### H<sub>s</sub> Equation of Motion

$$\begin{aligned}
 & - \left\{ M_{\text{eff}}^s + m_a [(\bar{\chi}_a^s + \bar{z}_a \beta_a^s)^2 + (\bar{z}_a^s - \bar{\chi}_a \beta_a^s)^2] + I_a \beta_a^{s^2} \right\} \bar{H}_s \\
 & - \left\{ m_a [(\bar{\chi}_a^r + \bar{z}_a \beta_a^r)(\bar{\chi}_a^s + \bar{z}_a \beta_a^s) + (\bar{z}_a^r - \bar{\chi}_a \beta_a^r)(\bar{z}_a^s - \bar{\chi}_a \beta_a^s)] + I_a \beta_a^r \beta_a^s \right\} \bar{H}_r \\
 & + \left\{ \omega_s^2 M_{\text{eff}}^s + \left[ M_s^s \ell_s - M_s^s V_f^s \ell_s^2 + V_f^s \frac{\ell_s^3}{3} \right] \frac{\Delta EI}{(EI)^2} + V_f^s \ell_s \frac{\Delta GA}{(GA)^2} + P_s^s \ell_s \frac{\Delta EA}{(EA)^2} \right. \\
 & \quad \left. + \Delta K_x (\chi_m^s - \chi_s^s)^2 + \Delta K_z (z_m^s - z_s^s)^2 + \Delta K_\theta (\theta_m^s - \theta_f^s)^2 \right\} \frac{\bar{H}_s}{\omega^2} \\
 & + \left\{ (M_s^r M_s^s \ell_s - M_s^r V_f^s \frac{\ell_s^2}{2} - M_s^s V_f^r \frac{\ell_s^2}{2} + V_f^r V_f^s \frac{\ell_s^3}{3}) \frac{\Delta EI}{(EI)^2} + V_f^r V_f^s \ell_s \frac{\Delta GA}{(GA)^2} + P_s^r P_s^s \ell_s \frac{\Delta EA}{(EA)^2} \right. \\
 & \quad \left. + \Delta K_x (\chi_m^r - \chi_s^r)(\chi_m^s - \chi_s^s) + \Delta K_z (z_m^r - z_s^r)(z_m^s - z_s^s) + \Delta K_\theta (\theta_m^r - \theta_f^r)(\theta_m^s - \theta_f^s) \right\} \frac{\bar{H}_r}{\omega^2} = 0
 \end{aligned}$$



The pattern of these equations is now evident, and a general form of one equation (r) from a set containing any number of degrees of freedom n, may be written. The expression permits any number of mass changes (p) and stiffness changes (q), and provides for coupling with all other equations of the set.

#### General Form of the r<sup>th</sup> Equation of Motion

$$\begin{aligned}
 & - \sum_s^n \left\{ \delta_{rs} M_{eff}^r + \sum_a^p m_a \left[ (\dot{x}_a^r + \bar{z}_a \beta_a^r)(\dot{x}_a^s + \bar{z}_a \beta_a^s) + (\dot{z}_a^r + \bar{x}_a \beta_a^r)(\dot{z}_a^s + \bar{x}_a \beta_a^s) \right] + \sum_d^q I_d \beta_d^r \beta_d^s \right\} H_s \\
 & + \sum \left\{ \delta_{rs} \omega_r^2 M_{eff}^r + \sum_f^v \left[ M_f^r M_f^s l_f - M_f^r V_f^s l_f^2 - M_f^s V_f^r l_f^2 + V_f^r V_f^s l_f^3 \right] \frac{\Delta E I_f}{(E I_f)^2} \right. \\
 & \left. + \sum_f^v \left[ V_f^r V_f^s l_f \right] \frac{\Delta G A_f}{(G A_f)^2} + \sum_f^v \left[ P_f^r P_f^s l_f \right] \frac{\Delta E A_f}{(E A_f)^2} + \sum_f^q \Delta K_{x_f} [(\dot{x}_m^r - \dot{x}_f^r)(\dot{x}_m^s - \dot{x}_f^s)] \right. \\
 & \left. + \sum_f^q \Delta K_{z_f} [(\dot{z}_m^r - \dot{z}_f^r)(\dot{z}_m^s - \dot{z}_f^s)] + \sum_f^q \Delta K_{\theta_f} [(\dot{\theta}_m^r - \dot{\theta}_f^r)(\dot{\theta}_m^s - \dot{\theta}_f^s)] \right\} \frac{\bar{H}_s}{\omega^2} = 0
 \end{aligned}$$

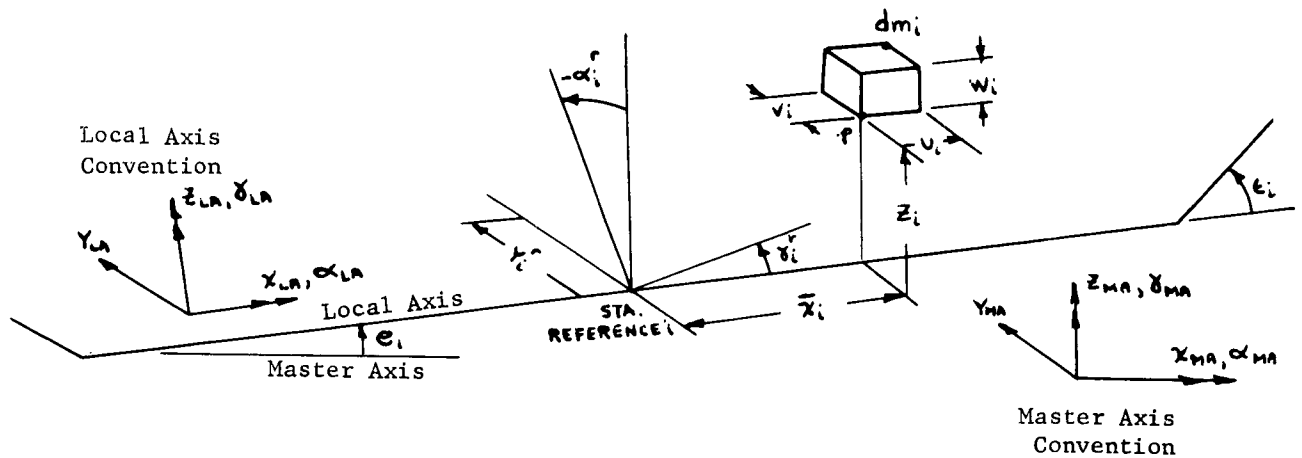
where  $\delta_{rs} = 1$  when  $r = s$

$\delta_{rs} = 0$  when  $r \neq s$

and where the summation  $\sum_s^n$  includes r.

#### D. Lateral-Torsion Coupling Analysis

Consider an elemental mass particle  $dm_i$  located from a reference point p by the distances u, v, w parallel to the x, y, and z local axes. Point p is itself located from reference point i on the local axis by components  $\bar{x}_i$  and  $\bar{z}_i$  parallel to the local axis system. Displacements  $y_i^{(r)}$ ,  $\delta_i^{(r)}$  and  $\alpha_i^{(r)}$  in a natural mode (r) at the reference point i are assumed to be known.



Component locations of the particle  $dm_i$  from reference point  $i$  in the local axis system after motions in the  $r^{\text{th}}$  mode are,

$$x_{LA} = \bar{x}_i - v_i \delta_i^r$$

$$y_{LA} = y_i^r + (\bar{x}_i + u_i) \delta_i^r - (\bar{z}_i + w_i) \alpha_i^r$$

$$z_{LA} = v_i \alpha_i^r$$

Following similar steps to those outlined for the Vertical Longitudinal Analysis yields the Kinetic Energy.

### Potential Energy

#### Beam Strain

Contributions to the potential energy in the lateral bending-torsion case come from lateral bending strain, lateral shear strain, and torsional strain. Writing these for the basic beam and for a change in each of these stiffness properties.

$$\text{Lateral Bending } V_0 + \Delta V_0 = \frac{1}{2} \int_0^L \left( \frac{M_i}{EI_i} \right)^2 EI_i dx + \frac{1}{2} \int_0^L \left( \frac{M_i}{EI_i} \right)^2 \Delta EI_i dx$$

$$\text{Lateral Shear } V_s + \Delta V_s = \frac{1}{2} \int_0^L \left( \frac{V_i}{GA_i} \right)^2 GA_i dx + \frac{1}{2} \int_0^L \left( \frac{V_i}{GA_i} \right)^2 \Delta GA_i dx$$

$$\text{Twist } V_t + \Delta V_t = \frac{1}{2} \int_0^L \left( \frac{T}{GJ} \right)^2 GJ dx + \frac{1}{2} \int_0^L \left( \frac{T}{GJ} \right)^2 \Delta GJ dx$$

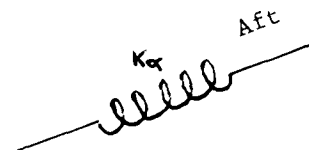
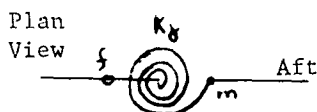
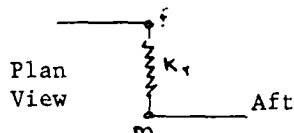
where

V	= potential energy, #-in.	A <sub>L</sub>	= lateral cross sectional area, in. <sup>2</sup>
x	= longitudinal beam location, in.	M <sub>L</sub>	= lateral bending moment, in. -#
E	= Modulus of Elasticity, #/in. <sup>2</sup>	V <sub>L</sub>	= lateral shear, #
I <sub>L</sub>	= lateral cross sectional moment of inertia, in. <sup>4</sup>	T	= torque, in.-#
G	= Shear Modulus of Elasticity, #/in. <sup>2</sup>		

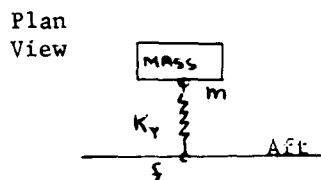
### Local Springs

Local springs which can contribute to the potential energy are of the following types.

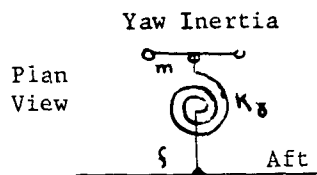
#### Spring Joint



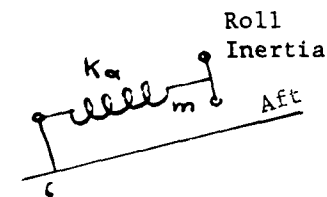
### Suspension Springs



Lateral Spring



Yaw Spring



Roll Spring

If  $y_f, \delta_f, \alpha_f$  define the motion of the spring support on the main fuselage beam in the local lateral, yaw, and roll directions, and  $y_m, \delta_m, \alpha_m$  define the motion of the other end of the spring joint or the motion of the sprung mass, then the potential energy is,

$$V + \Delta V = \frac{1}{2} (K_y + \Delta K_y) (y_m - y_f)^2 + \frac{1}{2} (K_\delta + \Delta K_\delta) (\delta_m - \delta_f)^2 + \frac{1}{2} (K_\alpha + \Delta K_\alpha) (\alpha_m - \alpha_f)^2$$

Following similar steps to those outlined for the Vertical Longitudinal Analysis yields the Potential Energy.

#### Equations of Motion

The Lagrange equation now yields.

#### H<sub>r</sub> Equation of Motion

$$\begin{aligned} & - \left\{ M_{eff}^r + m_a [\bar{y}_a \delta_a^r - \bar{z}_a \alpha_a^r + Y_a^r] + I_{\delta a} \delta_a^{r^2} + I_{\alpha a} \alpha_a^{r^2} \right\} \bar{H}_r \\ & - \left\{ m_a [(\bar{y}_a \delta_a^r - \bar{z}_a \alpha_a^r + Y_a^r)(\bar{y}_a \delta_a^r - \bar{z}_a \alpha_a^r + Y_a^r)] + I_{\delta a} \delta_a^r \delta_a^s + I_{\alpha a} \alpha_a^r \alpha_a^s \right\} \bar{H}_s \\ & + \left\{ \omega_r^2 M_{eff}^r + \left[ M_{i,1}^r l_1 + M_{i,1}^r V_{i,1}^r l_1^2 + V_{i,1}^r \frac{l_1^3}{3} \right] \frac{\Delta EI_i}{(EI_i)^2} + V_{i,1}^r l_1 \frac{\Delta GA_i}{(GA)^2} + T_i^r l_1 \frac{\Delta GJ}{(GJ)^2} \right. \\ & \quad \left. + \Delta K_y (Y_m^r - Y_f^r)^2 + \Delta K_\delta (\delta_m^r - \delta_f^r)^2 + \Delta K_\alpha (\alpha_m^r - \alpha_f^r)^2 \right\} \frac{\bar{H}_r}{\omega^2} \\ & \left\{ \left[ M_{i,1}^r M_{i,1}^s l_1 + M_{i,1}^r V_{i,1}^s \frac{l_1^2}{2} + M_{i,1}^s V_{i,1}^r \frac{l_1^2}{2} + V_{i,1}^r V_{i,1}^s \frac{l_1^3}{3} \right] \frac{\Delta EI_i}{(EI_i)^2} + V_{i,1}^r V_{i,1}^s l_1 \frac{\Delta GA_i}{(GA)^2} + T_i^r T_i^s l_1 \frac{\Delta GJ}{(GJ)^2} \right. \\ & \quad \left. + \Delta K_y (Y_m^r - Y_f^r)(Y_m^s - Y_f^s) + \Delta K_\delta (\delta_m^r - \delta_f^r)(\delta_m^s - \delta_f^s) + \Delta K_\alpha (\alpha_m^r - \alpha_f^r)(\alpha_m^s - \alpha_f^s) \right\} \frac{\bar{H}_r}{\omega^2} = 0 \end{aligned}$$

### H<sub>s</sub> Equation of Motion

$$\begin{aligned}
 & - \left\{ M_{\text{eff}}^s + m_d \left[ \bar{x}_d \delta_d^s - \bar{z}_d \alpha_d^s + \gamma_d^s \right]^2 + I_{\delta d} \delta_d^s + I_{\alpha d} \alpha_d^s \right\} \bar{H}_s \\
 & - \left\{ m_d \left[ (\bar{x}_d \delta_d^s - \bar{z}_d \alpha_d^s + \gamma_d^s) (\bar{x}_d \delta_d^r - \bar{z}_d \alpha_d^r + \gamma_d^r) \right] + I_{\delta d} \delta_d^s \delta_d^r + I_{\alpha d} \alpha_d^s \alpha_d^r \right\} \bar{H}_r \\
 & + \left\{ \omega_s^2 M_{\text{eff}}^s + \left[ M_{i,j}^s \ell_j + M_{i,j}^s V_{i,j}^s \ell_j^2 + V_{i,j}^s \frac{\ell_j^3}{3} \right] \frac{\Delta E I_i}{(E I_i)^2} + V_{i,j}^s \ell_j \frac{\Delta G A_i}{(G A_i)^2} + T_j^s \ell_j \frac{\Delta G J_i}{(G J_i)^2} \right\} \frac{\bar{H}_s}{\omega^2} \\
 & + \left\{ \Delta K_Y (\gamma_m^s - \gamma_f^s)^2 + \Delta K_\delta (\delta_m^s - \delta_f^s)^2 + \Delta K_\alpha (\alpha_m^s - \alpha_f^s)^2 \right\} \frac{\bar{H}_s}{\omega^2} \\
 & + \left\{ \left[ M_{i,j}^s M_{i,j}^r \ell_j + M_{i,j}^s V_{i,j}^r \frac{\ell_j^2}{2} + M_{i,j}^r V_{i,j}^s \frac{\ell_j^2}{2} + V_{i,j}^s V_{i,j}^r \frac{\ell_j^3}{3} \right] \frac{\Delta E I_i}{(E I_i)^2} + V_{i,j}^s V_{i,j}^r \frac{\Delta G A_i}{(G A_i)^2} + T_j^s T_j^r \frac{\Delta G J_i}{(G J_i)^2} \right\} \frac{\bar{H}_r}{\omega^2} = 0 \\
 & + \left\{ \Delta K_Y (\gamma_m^s - \gamma_f^s) (\gamma_m^r - \gamma_f^r) + \Delta K_\delta (\delta_m^s - \delta_f^s) (\delta_m^r - \delta_f^r) + \Delta K_\alpha (\alpha_m^s - \alpha_f^s) (\alpha_m^r - \alpha_f^r) \right\} \frac{\bar{H}_r}{\omega^2} = 0
 \end{aligned}$$

The pattern of these equations is now evident, and a general form of one equation (r) from a set containing any number of degrees of freedom n, may be written. The expression permits any number of mass changes (p) and stiffness changes (q), and provides for coupling with all other equations of the set.

### General Form of the r<sup>th</sup> Equation of Motion

$$\begin{aligned}
 & - \sum_s^n \left\{ \partial_{rs} M_{\text{eff}}^r + \sum_d^p m_d \left[ (\bar{x}_d \delta_d^r - \bar{z}_d \alpha_d^r + \gamma_d^r) (\bar{x}_d \delta_d^s - \bar{z}_d \alpha_d^s + \gamma_d^s) \right] + \sum_d^p I_{\delta d} \delta_d^r \delta_d^s + \sum_d^p I_{\alpha d} \alpha_d^r \alpha_d^s \right\} H_s \\
 & + \sum_s^n \left\{ \delta_{rs} \omega_r^2 M_{\text{eff}}^r + \sum_j^q \left[ M_{i,j}^r M_{i,j}^s \ell_j + M_{i,j}^r V_{i,j}^s \frac{\ell_j^2}{2} + M_{i,j}^s V_{i,j}^r \frac{\ell_j^2}{2} + V_{i,j}^r V_{i,j}^s \frac{\ell_j^3}{3} \right] \frac{\Delta E I_i}{(E I_i)^2} \right. \\
 & + \sum_j^q \left[ V_{i,j}^r V_{i,j}^s \ell_j \frac{\Delta G A_i}{(G A_i)^2} + \sum_j^q (T_j^r T_j^s \ell_j) \frac{\Delta G J_i}{(G J_i)^2} + \sum_j^q \Delta K_Y [(\gamma_m^r - \gamma_f^r) (\gamma_m^s - \gamma_f^s)] \right. \\
 & \left. \left. + \sum_j^q \Delta K_\delta [(\delta_m^r - \delta_f^r) (\delta_m^s - \delta_f^s)] + \sum_j^q \Delta K_\alpha [(\alpha_m^r - \alpha_f^r) (\alpha_m^s - \alpha_f^s)] \right] \right\} \frac{\bar{H}_s}{\omega^2} = 0
 \end{aligned}$$

## APPENDIX B

### UNCOUPLED MODE ASSOCIATED MATRIX DERIVATION AND METHOD OF SOLUTION

## Fuselage Modes Analysis

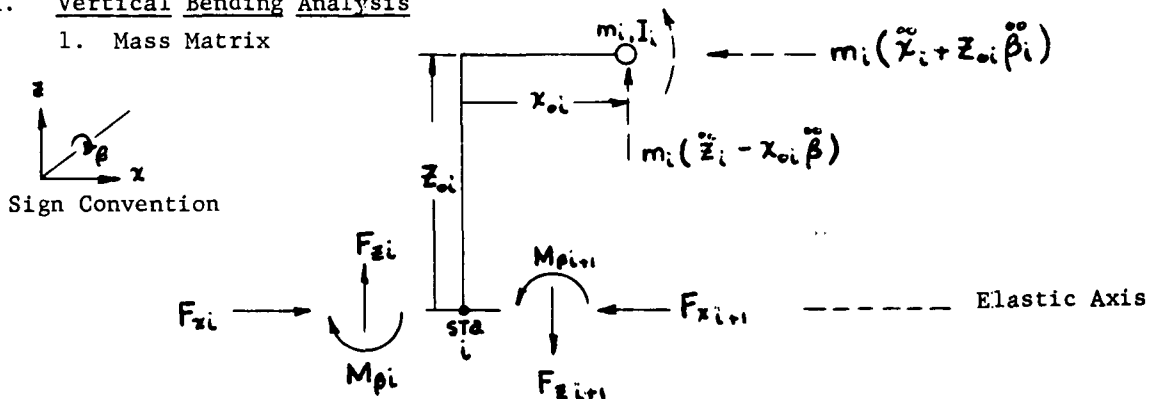
The method used for the calculation of the fuselage natural modes is based on the method of Associated Matrices, as presented in Reference 10. This is in essence a formalized Holzer or Myklestad lumped parameter procedure which has been found to be convenient in many aircraft applications. Structures are represented by a series of matrices of several types representing for example, (1) stations with discrete lumped masses and mass moments of inertia (2) sections of weightless elastic beam, which permit inclusion of bending, shear, tension and torsional stiffness properties, (3) bends, permitting the selected elastic beam axis to follow the general fuselage shape, and (4) concentrated springs which simulate the attachment of large local mass and inertia items to the fuselage structure, such as the helicopter rotor transmissions.

For fuselage vertical bending modes, three degrees of freedom are described by the matrix terms; vertical displacement, longitudinal displacement, and pitch rotation. For lateral-torsion modes, three other degrees of freedom are described by the matrix terms; lateral displacement, roll rotation and yaw rotation. The structure is separated into lumped parameter form and a matrix representation prepared for each property. The matrices are assembled into an array to simulate a progression from one end of the fuselage beam to the other. Starting with a set of load and deflection boundary conditions at one end of the fuselage beam, namely the top of the forward rotor, successive multiplication of numerical matrices is performed to reach the other end of the beam. For this operation, a trial frequency  $\omega$  is used, which, by the conventional harmonic motion assumption, applies an acceleration to each mass and inertia item, resulting in an applied load and moment distribution on the beam. At the other end of the beam, a second set of boundary conditions are enforced; by successive trials, frequencies are found which satisfy the boundaries and are therefore the natural frequencies being sought.

When the natural frequency  $\omega_n$  is determined, one further matrix multiplication of the system is required; the value and an assumed unit deflection at one boundary are used to obtain a detailed listing of the intermediate results of each matrix multiplication, thus providing the natural mode shapes corresponding to  $\omega_n$ . This listing contains displacements, rotations, shears, moments and torques at each station along the structure. In practice, the extensive matrix multiplications are performed on a digital computer and lead to rapid solutions.

### A. Vertical Bending Analysis

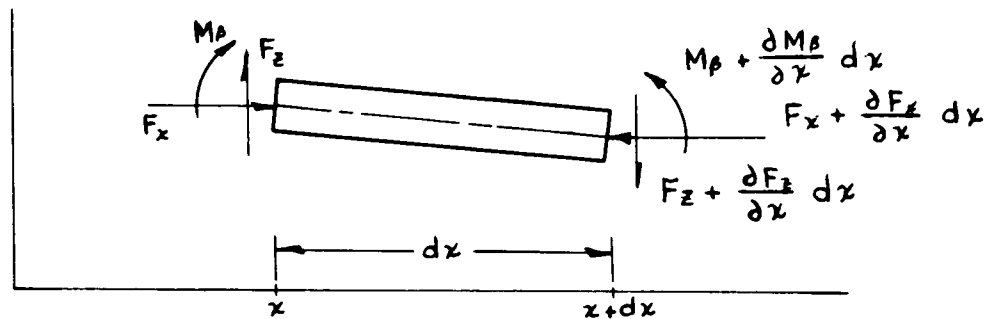
#### 1. Mass Matrix



$$\begin{bmatrix} F_z \\ M_\theta \\ F_x \\ x \\ \beta \\ z \end{bmatrix}_{i+1} = \begin{bmatrix} 1 & * & & & -m_i \omega^2 z_{oi} & m_i \omega^2 \\ * & 1 & & m_i \omega^2 z_{oi} & m_i \omega^2 z_{oi}^2 + m_i \omega^2 z_{oi} + I \rho_i \omega^2 & -m_i \omega^2 z_{oi} \\ & & 1 & m_i \omega^2 & m_i \omega^2 z_{oi} & \\ & & & 1 & & \\ & & & & 1 & \\ & & & & & 1 \end{bmatrix} \begin{bmatrix} F_z \\ M_\theta \\ F_x \\ x \\ \beta \\ z \end{bmatrix}_i$$

\* Blank Space Denotes Zero Element

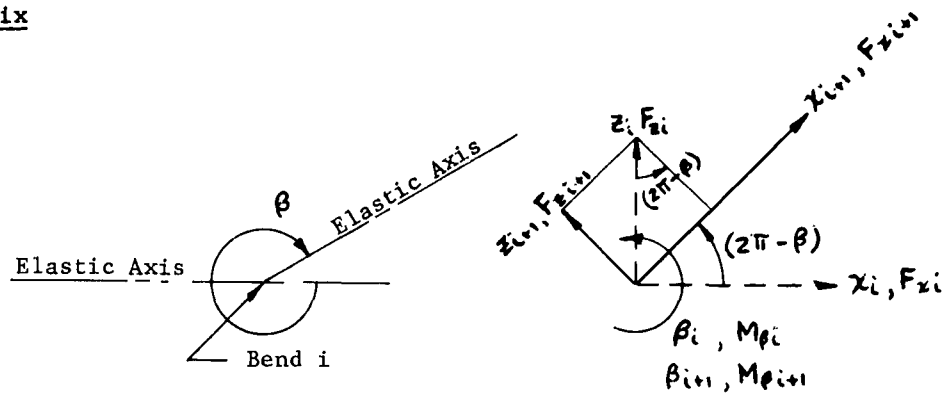
### Elastic Matrix



$$\begin{bmatrix} F_z \\ M_\theta \\ F_x \\ x \\ \beta \\ z \end{bmatrix}_{i+1} = \begin{bmatrix} 1 & & & & & \\ l_i & 1 & & & Q l_i & \\ & & 1 & & & \\ & & -\frac{l_i}{AE} & 1 & & \\ -\frac{l_i^2}{2EI} & -\frac{l_i}{EI} & & & 1 & \\ \frac{l_i^3}{6EI} - \frac{l_i}{AG} & \frac{l_i^2}{2EI} & & & -l_i & 1 \end{bmatrix} \begin{bmatrix} F_z \\ M_\theta \\ F_x \\ x \\ \beta \\ z \end{bmatrix}_i$$

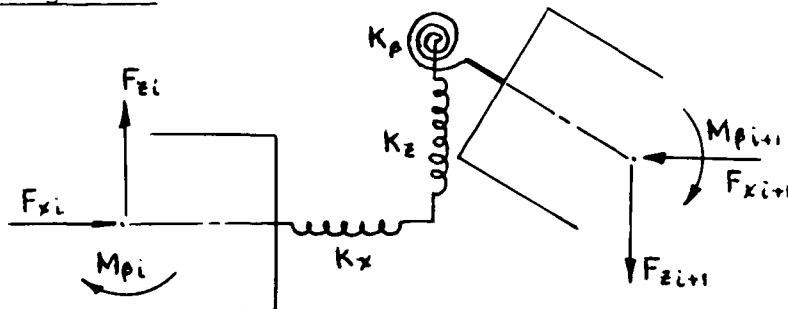


## Bend Matrix



$$\begin{bmatrix} F_z \\ M_\theta \\ F_x \\ x \\ \beta \\ z \end{bmatrix}_{i+1} = \begin{bmatrix} \cos \beta & & \sin \beta & & & \\ & 1 & & & & \\ -\sin \beta & & \cos \beta & & & \\ & & & \cos \beta & & -\sin \beta \\ & & & & 1 & \\ & & & \sin \beta & & \cos \beta \end{bmatrix} \begin{bmatrix} F_z \\ M_\theta \\ F_x \\ x \\ \beta \\ z \end{bmatrix}_i$$

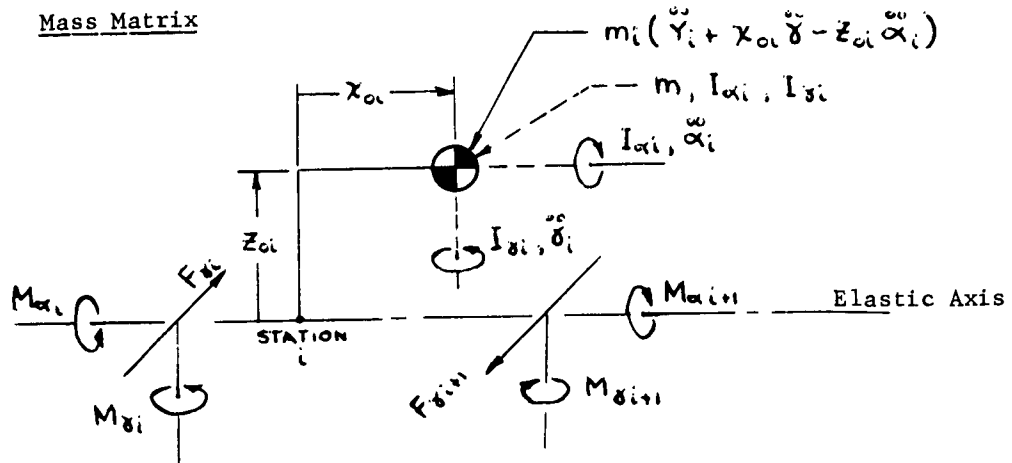
## Concentrated Spring Matrix



$$\begin{bmatrix} F_z \\ M_\theta \\ F_x \\ x \\ \beta \\ z \end{bmatrix}_{i+1} = \begin{bmatrix} 1 & & & & & \\ & 1 & & & & \\ & & 1 & & & \\ & & -\frac{1}{K_x} & 1 & & \\ & -\frac{1}{K_p} & & & 1 & \\ -\frac{1}{K_z} & & & & & 1 \end{bmatrix} \begin{bmatrix} F_z \\ M_\theta \\ F_x \\ x \\ \beta \\ z \end{bmatrix}_i$$

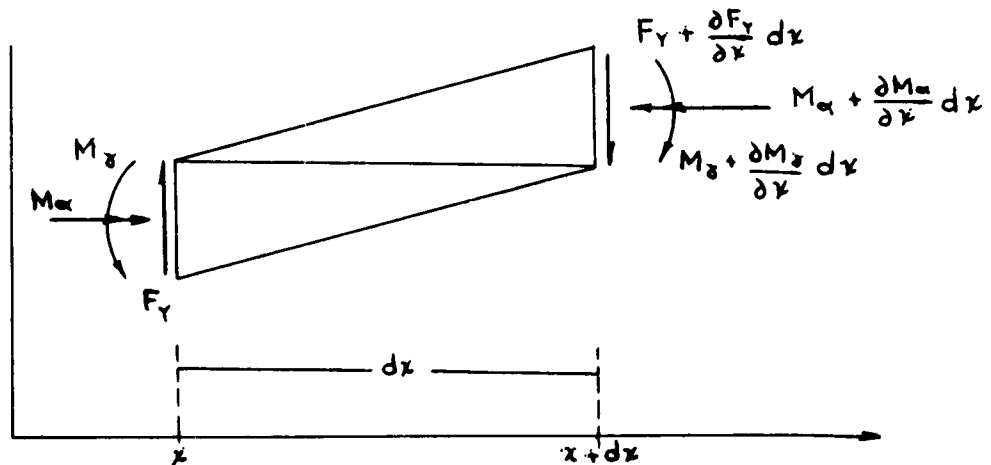
## B. Lateral-bending-torsion Analysis

### Mass Matrix



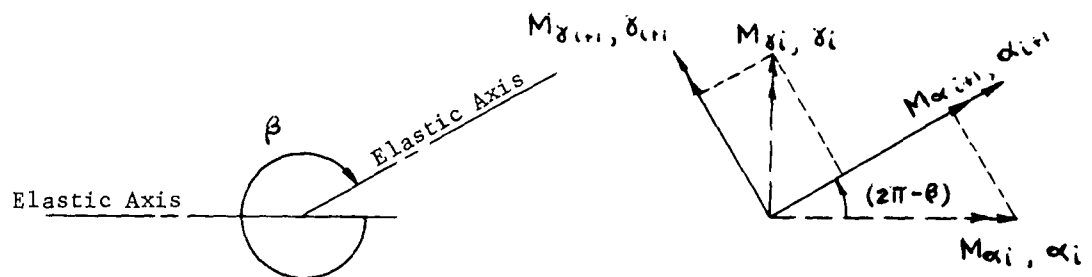
$$\begin{bmatrix} F_Y \\ M_\delta \\ M_\alpha \\ \alpha \\ \delta \\ Y \end{bmatrix}_{i+1} = \begin{bmatrix} 1 & & & -m_i \omega^2 z_{oi} & m_i \omega^2 x_{oi} & m_i \omega^2 \\ & 1 & & -m_i \omega^2 x_{oi} z_{oi} & (m_i z_{oi}^2 + I_{\beta i}) \omega^2 & m_i \omega^2 x_{oi} \\ & & 1 & (m_i x_{oi}^2 + I_{\alpha i}) \omega^2 & -m_i \omega^2 x_{oi} z_{oi} & -m_i \omega^2 z_{oi} \\ & & & 1 & & \\ & & & & 1 & \\ & & & & & 1 \end{bmatrix} \begin{bmatrix} F_Y \\ M_\delta \\ M_\alpha \\ \alpha \\ \delta \\ Y \end{bmatrix}_i$$

### Elastic Matrix



$$\begin{bmatrix} F_Y \\ M_\theta \\ M_\alpha \\ \alpha \\ \delta \\ Y \end{bmatrix}_{i+1} = \begin{bmatrix} 1 & & & & & \\ -l_i & 1 & & & & -Q l_i \\ & & 1 & & & \\ & & -\frac{l_i}{GJ} & 1 & & \\ \frac{l_i^2}{2EI} & -\frac{l_i}{EI} & & & 1 & \\ \frac{l_i^2}{6EI} - \frac{l_i}{AG} & -\frac{l_i^2}{2EI} & & & l_i & 1 \end{bmatrix} \begin{bmatrix} F_Y \\ M_\theta \\ M_\alpha \\ \alpha \\ \delta \\ Y \end{bmatrix}_i$$

Bend Matrix



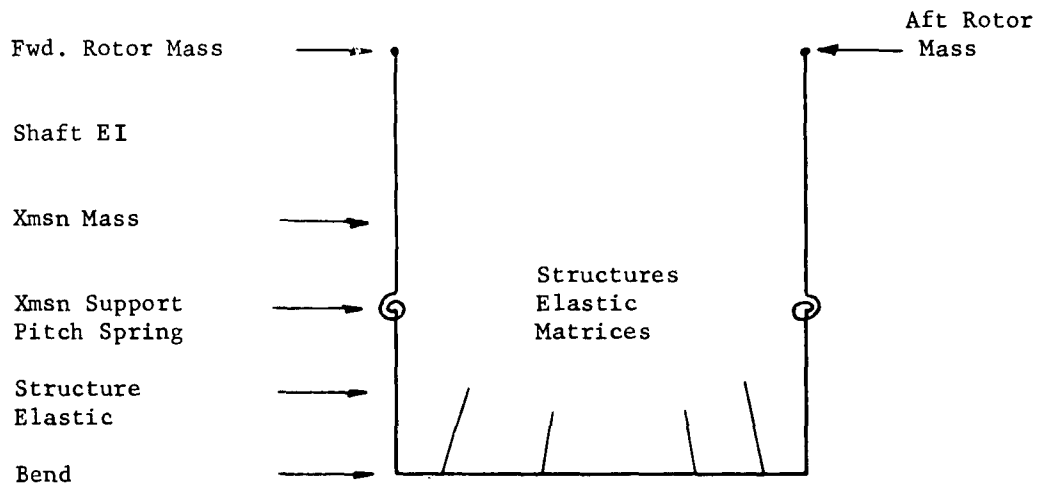
$$\begin{bmatrix} F_Y \\ M_\theta \\ M_\alpha \\ \alpha \\ \delta \\ Y \end{bmatrix}_{i+1} = \begin{bmatrix} 1 & & & & & \\ & \cos \beta & \sin \beta & & & \\ & -\sin \beta & \cos \beta & & & \\ & & & \cos \beta & -\sin \beta & \\ & & & \sin \beta & \cos \beta & \\ & & & & & 1 \end{bmatrix} \begin{bmatrix} F_Y \\ M_\theta \\ M_\alpha \\ \alpha \\ \delta \\ Y \end{bmatrix}_i$$

### Concentrated Spring Matrix

$$\begin{bmatrix} F_Y \\ M_\delta \\ M_\alpha \\ \alpha \\ \delta \\ Y \end{bmatrix}_{i+1} = \begin{bmatrix} 1 & & & & & \\ & 1 & & & & \\ & & 1 & & & \\ & & & -\frac{1}{K_\alpha} & 1 & \\ & & & & & 1 \\ & -\frac{1}{K_Y} & & & & \\ & & & & & & 1 \end{bmatrix} \begin{bmatrix} F_Y \\ M_\delta \\ M_\alpha \\ \alpha \\ \delta \\ Y \end{bmatrix}_i$$

### Method of Solution

These matrices are now "building blocks" from which a dynamic representation of the helicopter fuselage may be constructed. For example, a fuselage "U-beam" may appear as an assemblage of matrices.



The boundary conditions for such a beam are that the loads  $F_x$ ,  $F_z$ ,  $M_\theta$  just before the forward rotor mass and just after the aft rotor mass are zero, in other words a "free-free" beam. Even ground springs do not affect the boundaries, because they are taken to act just before the boundaries are reached. Matrix multiplications from forward rotor to aft rotor are conducted repeatedly for trial frequencies of  $\omega$  until the boundary conditions are met. Note that since the forward end boundary conditions  $F_x=F_y=M_\theta=0$  appear in the single column end matrix, and since only  $F_x$ ,  $F_y$ ,  $M_\theta$  need be determined for comparison with the aft end boundary conditions, it is then necessary to use only the terms shown below for the frequency calculations.

$$\begin{bmatrix} F_z \\ M_\theta \\ F_x \\ \chi \\ \beta \\ z \end{bmatrix} = \begin{bmatrix} & & & a_{14} & a_{15} & a_{16} \\ & & & a_{24} & a_{25} & a_{26} \\ & & & a_{34} & a_{35} & a_{36} \\ & & & & & \\ & & & & & \\ & & & & & \\ & & & & & \end{bmatrix} \begin{bmatrix} 0 \\ 0 \\ 0 \\ \chi \\ \beta \\ z \end{bmatrix}$$

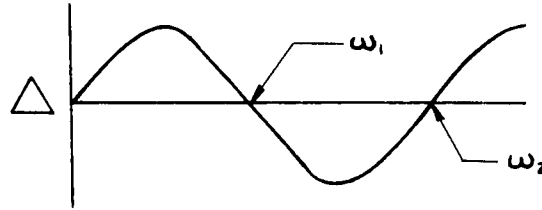
Aft End

Fwd End

Repeated trials of frequency  $\omega$  are made, and each one of the nine values  $a_{14}$  through  $a_{36}$  obtained numerically. To meet the boundary requirement, the residual  $\Delta$  of the matrix array must be zero.

$$\Delta = \begin{bmatrix} a_{14} & a_{15} & a_{16} \\ a_{24} & a_{25} & a_{26} \\ a_{34} & a_{35} & a_{36} \end{bmatrix} = 0$$

In practice, the residual may be plotted vs. the frequency trials, and when



a zero intersection occurs, a natural frequency  $\omega_1, \omega_2, \dots, \omega_n$  is determined. To obtain the mode shape accompanying each natural frequency  $\omega_n$  the unknown deflection boundary conditions are first calculated, using the same elements,

$$\begin{bmatrix} 0 \\ 0 \\ 0 \end{bmatrix} = \begin{bmatrix} F_x \\ M_\theta \\ F_z \end{bmatrix} = \begin{bmatrix} a_{14} & a_{15} & a_{16} \\ a_{24} & a_{25} & a_{26} \\ a_{34} & a_{35} & a_{36} \end{bmatrix} \begin{bmatrix} X \\ \theta \\ Z \end{bmatrix}$$

Aft Fwd

An arbitrary unit end deflection is now selected, usually

$$\begin{bmatrix} 0 \\ 0 \\ 0 \end{bmatrix} = \begin{bmatrix} a_{14} & a_{15} & a_{16} \\ a_{24} & a_{25} & a_{26} \\ a_{34} & a_{35} & a_{36} \end{bmatrix} \begin{bmatrix} X \\ \theta \\ 1.0 \end{bmatrix}$$

Fwd

So that in equation form, this becomes

$$a_{14}X + a_{15}\theta = -a_{16}$$

$$a_{24}X + a_{25}\theta = -a_{26}$$

and a determinant solution gives,

$$X = \frac{\begin{vmatrix} -a_{16} & a_{15} \\ -a_{26} & a_{25} \end{vmatrix}}{\begin{vmatrix} a_{14} & a_{15} \\ a_{24} & a_{25} \end{vmatrix}} \quad \theta = \frac{\begin{vmatrix} a_{14} & -a_{16} \\ a_{25} & -a_{26} \end{vmatrix}}{\begin{vmatrix} a_{14} & a_{15} \\ a_{24} & a_{25} \end{vmatrix}}$$

The complete column matrix of forward end boundary conditions is now known. By successive multiplication and print-out of each matrix, starting with the known end column, the complete mode shape in both load and deflection is obtained for every station along the fuselage. The procedure is repeated until all frequencies and modes within a desired range are obtained. Solution of the lateral bending-torsion case is obtained in a similar manner.

## APPENDIX C

### COUPLED MODE ASSOCIATED MATRIX DERIVATION AND METHOD OF SOLUTION

#### Associated Matrix Procedure

For fuselage vertical-lateral bending modes, six degrees of freedom are described by the matrix terms; longitudinal, lateral and vertical displacement, roll, pitch and yaw rotation. The structure is separated into lumped parameter form and a matrix representation prepared for each property. The matrices are assembled into an array to simulate a progression from one end of the fuselage beam to the other. Starting with a set of load and deflection boundary conditions at one end of the beam, the top of the forward rotor, successive multiplication of numerical matrices is performed to reach the other end of the beam. For this operation, a trial frequency,  $\omega$ , is used, which, by the conventional harmonic motion assumption, applies an acceleration to each mass and inertia item, resulting in an applied load and moment distribution on the beam. At the other end of the beam, a second set of boundary conditions are enforced; by successive trials, frequencies are found which satisfy the boundaries and are, therefore, the natural frequencies being sought. Each trial matrix multiplication produces a non-zero residual; when this value is at or very near zero, the natural frequency is established.

When the natural frequency,  $\omega_n$ , is determined, one further matrix multiplication of the system is required; this  $\omega_n$  value and an assumed unit deflection at one boundary is used to obtain a detailed listing of the intermediate results of each matrix multiplication, thus providing the natural mode shapes corresponding to  $\omega_n$ . This listing contains displacements, rotations, forces and moments at each station along the structure. In practice, the extensive matrix multiplications are performed on a digital computer and lead to a rapid solution.



## Elastic Matrix

The general elastic matrix for a weightless beam element undergoing deflections in the vertical plane was derived in Appendix B.

$$\begin{array}{c} \begin{array}{c} F_z \\ M_\beta \\ F_x \\ X \\ \beta \\ Z \end{array} \\ \begin{array}{c} n+1 \end{array} \end{array} = \begin{array}{c} \begin{array}{cccccc} 1 & 0 & 0 & 0 & 0 & 0 \\ l_i & 1 & 0 & 0 & Q l_i & 0 \\ 0 & 0 & 1 & 0 & 0 & 0 \\ 0 & 0 & -l_i/AE & 1 & 0 & 0 \\ -l_i^2/2EI_y & -l_i/EI_y & 0 & 0 & 1 & 0 \\ l_i^3/6EI_y - l_i/AG & l_i^2/2EI_y & 0 & 0 & -l_i & 1 \end{array} \\ \begin{array}{c} n \end{array} \end{array} \begin{array}{c} \begin{array}{c} F_z \\ M_\beta \\ F_x \\ X \\ \beta \\ Z \end{array} \end{array}$$

The elastic matrix for a weightless beam element undergoing deflections in the lateral plane was also derived in Appendix B.

$$\begin{array}{c} \begin{array}{c} F_y \\ M_\gamma \\ M_\alpha \\ \alpha \\ \gamma \\ y \end{array} \\ \begin{array}{c} n+1 \end{array} \end{array} = \begin{array}{c} \begin{array}{cccccc} 1 & 0 & 0 & 0 & 0 & 0 \\ -l_i & 1 & 0 & 0 & -Q l_i & 0 \\ 0 & 0 & 1 & 0 & 0 & 0 \\ 0 & 0 & -l_i/GI_x & 1 & 0 & 0 \\ l_i^2/2EI_z & -l_i/EI_z & 0 & 0 & 1 & 0 \\ l_i^3/6EI_z - l_i/AG & -l_i^2/2EI_z & 0 & 0 & l_i & 1 \end{array} \\ \begin{array}{c} n \end{array} \end{array} \begin{array}{c} \begin{array}{c} F \\ M_\gamma \\ M_\alpha \\ \alpha \\ \gamma \\ y \end{array} \end{array}$$

The effect of the axial force  $Q$  in the above matrices will be neglected in the formation of the coupled elastic matrix because experience has proved it to have little effect. The first step in forming the coupled matrix is the writing of a twelfth order matrix containing both the above uncoupled components in their proper diagonal positions.

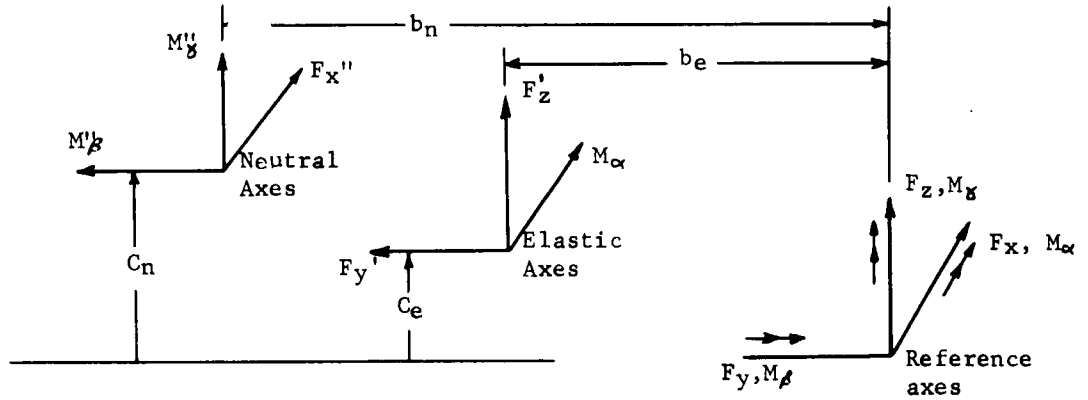
[ E3 ]

$F_z$	$M_\beta$	$F_x$	$X$	$\beta$	$Z$	$F_y$	$M_\gamma$	$M_\alpha$	$\alpha$	$\gamma$	$y$	n
1												
L	1											
		1										
			$1$									
			$-\frac{L}{A_x E}$									
$-\frac{L^2}{2EI_y}$	$-\frac{L}{EI_y}$											
$\frac{L^3}{6EI_y} - \frac{L}{A_z G}$	$\frac{L^2}{2EI_y}$				$1$							
					$-L$							
						$1$						
							$-L$					
								$1$				
									$-\frac{L}{GJ_x}$	$1$		
											$-\frac{L}{EI_z}$	
											$-\frac{L^2}{2EI_z}$	
											$\frac{L^3}{6EI_z} - \frac{L}{A_z G}$	
												$1$

where

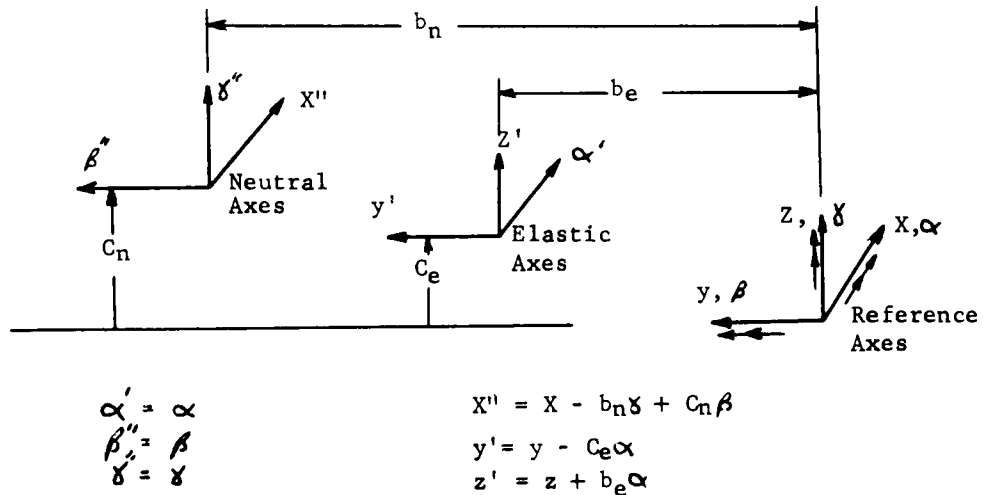
$A_x$  = Longitudinal Area  
 $A_z$  = Vertical Shear Area  
 $A_y$  = Lateral Shear Area

Pitching moment, yawing moment, and axial longitudinal load are shifted from the reference axis system through the distance  $b_n$ ,  $c_n$  to the neutral axis prior to calculation of the resulting deflections in the elastic matrix. Similarly, vertical and lateral loads and rolling moment (fuselage torsion) are shifted from the reference axes to the shear center axis  $b_e$ ,  $c_e$  as shown below:



$$\begin{aligned}
 \text{Therefore } F'_y &= F_y & F''_x &= F_x \\
 F'_z &= F_z & M''_\delta &= M + b_n F_x \\
 M'_\alpha &= M_\alpha - b_e F_z + c_e F_y & M''_\beta &= M_\beta - c_n F_x
 \end{aligned}$$

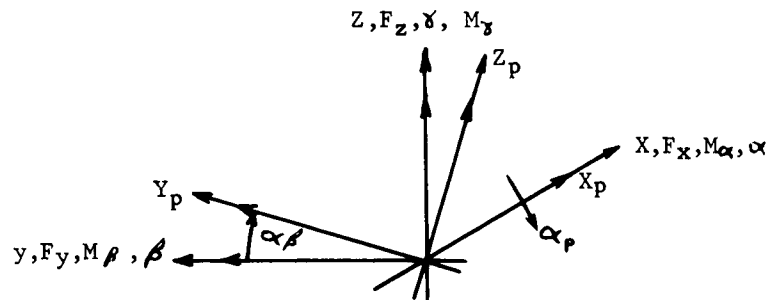
Similarly the linear and angular deflections are transformed to their respective set of axes.



Thus the transfer matrix of forces and displacements from the reference axes to the shear center and neutral axes is  $[E_1]$

$$\begin{bmatrix} F'_z \\ M''_\beta \\ F''_x \\ X'' \\ \beta'' \\ Z' \\ F'_y \\ M''_\gamma \\ M'_\alpha \\ \alpha' \\ \gamma'' \\ y' \end{bmatrix}_{n', n''} = \begin{bmatrix} 1 & & & & & & & & & & & \\ & 1 & -C_n & & & & & & & & & \\ & & 1 & & & & & & & & & \\ & & & 1 & C_n & & & & & & -b_n & \\ & & & & 1 & & & & & & & \\ & & & & & 1 & & & & & b_e & \\ & & & & & & 1 & & & & & \\ & & & & & & & 1 & & & & \\ & & & & & & & & 1 & & & \\ -b_e & & & & & & C_e & & 1 & & & \\ & & & & & & & & & 1 & & \\ & & & & & & & & & & -C_e & 1 \end{bmatrix} \begin{bmatrix} F_z \\ M \\ F_x \\ X \\ \beta \\ Z \\ F_y \\ M_\gamma \\ M_\alpha \\ \alpha \\ \gamma \\ y \end{bmatrix}_n$$

In order to write the bending equations without considering additional stiffness coupling terms, the axis system is oriented to the principal axes.



$$X_p = X$$

$$Y_p = Y \cos \alpha_p + Z \sin \alpha_p$$

$$Z_p = -Y \sin \alpha_p + Z \cos \alpha_p$$

$$F_x = F_x$$

$$F_{y_p} = F_y \cos \alpha_p + F_z \sin \alpha_p$$

$$F_{z_p} = -F_y \sin \alpha_p + F_z \cos \alpha_p$$

$$\alpha_p = \alpha$$

$$\beta_p = \beta \cos \alpha_p + \gamma \sin \alpha_p$$

$$\gamma_p = -\beta \sin \alpha_p + \gamma \cos \alpha_p$$

$$M_{\alpha_p} = M_{\alpha}$$

$$M_{\beta_p} = M_{\beta} \cos \alpha_p + M_{\gamma} \sin \alpha_p$$

$$M_{\gamma_p} = M_{\beta} \sin \alpha_p + M_{\gamma} \cos \alpha_p$$



Thus, the triple matrix product,

$$\begin{bmatrix} E_3 \end{bmatrix} \begin{bmatrix} E_2 \end{bmatrix} \begin{bmatrix} E_1 \end{bmatrix} = \begin{bmatrix} \text{Elastic} \\ \text{Matrix} \end{bmatrix} \times \begin{bmatrix} \text{Rotation} \\ \text{Matrix} \end{bmatrix} \times \begin{bmatrix} \text{Translation} \\ \text{Matrix} \end{bmatrix}$$

will relate the forces and displacements at station n with those at (n + 1) with respect to the principal - neutral and principal - elastic axes of the elastic beam. Since the forces and displacements must be with respect to the reference axes in order to continue with the associated matrix method, a rotation and translation opposite to those derived previously are required

$$\begin{aligned} \text{Thus } \begin{bmatrix} E_5 \end{bmatrix} \times \begin{bmatrix} E_4 \end{bmatrix} \times \begin{bmatrix} E_3 \end{bmatrix} \times \begin{bmatrix} E_2 \end{bmatrix} \times \begin{bmatrix} E_1 \end{bmatrix} &= \\ &= \begin{bmatrix} \text{Return} \\ \text{Trans-} \\ \text{lation} \\ \text{Matrix} \end{bmatrix} \times \begin{bmatrix} \text{Return} \\ \text{Rotation} \\ \text{Matrix} \end{bmatrix} \times \begin{bmatrix} \text{Elastic} \\ \text{Matrix} \end{bmatrix} \times \begin{bmatrix} \text{Rotation} \\ \text{Matrix} \end{bmatrix} \times \begin{bmatrix} \text{Translation} \\ \text{Matrix} \end{bmatrix} \end{aligned}$$

will relate the forces and displacements at station n with those at station (n + 1) with respect to the reference axes.

The required matrices to return to the reference axes are as follows:

Return Rotation Matrix

$$\begin{bmatrix} F_z \\ M_\beta \\ F_x \\ X \\ \beta \\ Z \\ F_y \\ M_\gamma \\ M_\alpha \\ \alpha \\ \gamma \\ y \end{bmatrix}_{n+1} = \begin{bmatrix} \cos \alpha_p & & & & & & & & & & & \\ & \cos \alpha_p & & & & & & & & & & \\ & & 1 & & & & & & & & & \\ & & & 1 & & & & & & & & \\ & & & & \cos \alpha_p & & & & & & & \\ & & & & & \cos \alpha_p & & & & & & \\ & & & & & & \cos \alpha_p & & & & & \\ & -\sin \alpha_p & & & & & & \cos \alpha_p & & & & \\ & & \sin \alpha_p & & & & & & \cos \alpha_p & & & \\ & & & -\sin \alpha_p & & & & & & 1 & & \\ & & & & & & & & & & 1 & \\ & & & & & & & & & & & \cos \alpha_p \\ & & & & & & & & & & & & \sin \alpha_p \\ & & & & & & & & & & & & & -\sin \alpha_p \\ & & & & & & & & & & & & & & \cos \alpha_p \end{bmatrix}_{n'}$$



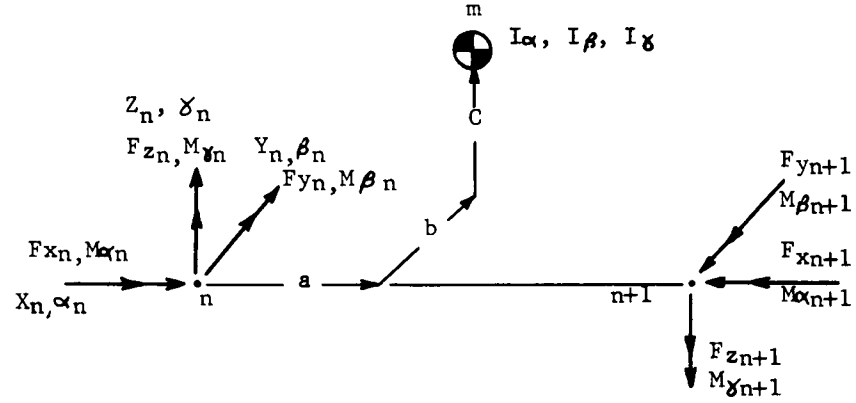
Return Translation Matrix

$$\begin{bmatrix} F_z \\ M_\beta \\ F_x \\ X \\ \beta \\ Z \\ F_y \\ M_\gamma \\ M_\alpha \\ \alpha \\ \gamma \\ y \end{bmatrix}_{n+1} = \begin{bmatrix} 1 & & & & & & & & & & & \\ & 1 & & & & & & & & & & \\ & & C_N & & & & & & & & & \\ & & & 1 & & & & & & & & \\ & & & & 1 & & & & & & & \\ & & & & & -C_N & & & & & & \\ & & & & & & 1 & & & & & \\ & & & & & & & 1 & & & & \\ & & & & & & & & 1 & & & \\ & & & & & & & & & -b_E & & \\ & & & & & & & & & & b_N & \\ & & & & & & & & & & & 1 \end{bmatrix} \begin{bmatrix} F_z \\ M_\beta \\ F_x \\ X \\ \beta \\ Z \\ F_y \\ M_\gamma \\ M_\alpha \\ \alpha \\ \gamma \\ y \end{bmatrix}_n$$

[illegible]

### Mass Matrix

Consider a mass  $m$  whose position is known with respect to the reference axes of an arbitrary section  $n$ . Associated with the mass are the inertial properties  $I_\alpha$ ,  $I_\beta$  and  $I_\gamma$  about its centroid. These masses and inertias, accelerated by harmonic oscillations, produce inertial loads on the beam structure.



$$\begin{aligned}\sum F_x = 0 &= F_{xn} + m\omega^2(X_n + C\beta_n - b\gamma_n) - F_{xn+1} \\ \sum F_y = 0 &= F_{yn} + m\omega^2(y_n - C\alpha_n + a\gamma_n) - F_{yn+1} \\ \sum F_z = 0 &= F_{zn} + m\omega^2(Z_n + b\alpha_n - a\beta_n) - F_{zn+1} \\ \sum M_\alpha = 0 &= M_{\alpha n} - m\omega^2(y_n - C\alpha_n + a\gamma_n)C + m\omega^2(Z_n + b\alpha_n - a\beta_n)b \\ &\quad + I_\alpha\omega^2\alpha_n - M_{\beta n+1} \\ \sum M_\beta = 0 &= M_{\beta n} + m\omega^2(X_n + C\beta_n - b\gamma_n)C - m\omega^2(Z_n + b\alpha_n - a\beta_n)a \\ &\quad + I_\beta\omega^2\beta_n - M_{\beta n+1} \\ \sum M_\gamma = 0 &= M_{\gamma n} - m\omega^2(X_n + C\beta_n - b\gamma_n)b + m\omega^2(y_n - C\alpha_n + a\gamma_n)a \\ &\quad + I_\gamma\omega^2\gamma_n - M_{\gamma n+1}\end{aligned}$$

Deflections are unchanged across the mass stations. The final matrix form is

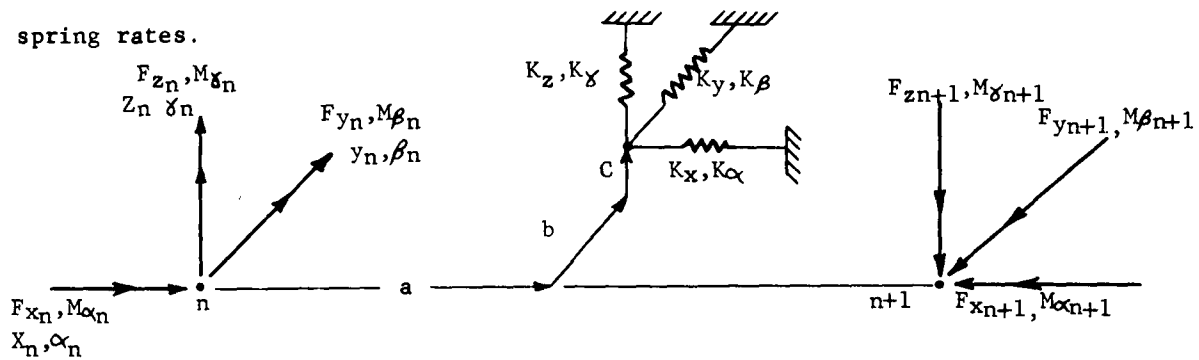
### Mass Matrix

+

### Ground Spring Matrix

A mathematical device which permits simulation of ground shake tests, in which the aircraft is suspended from the roof trusses of a hangar building, is the ground spring matrix. Suppose a station,  $n$ , has its six degrees of freedom partially restrained by springs, then these external springs induce additional loads on the vibrating structure in proportion to the motion amplitude and spring rates.

spring rates.



$$F_x = 0 = F_{x_n} - K_x(X_n + C\beta_n - b\delta_n) - F_{x_{n+1}}$$

$$F_y = 0 = F_{y_n} - K_y(y_n - C\alpha_n + a\delta_n) - F_{y_{n+1}}$$

$$F_z = 0 = F_{z_n} - K_z(Z_n + b\alpha_n - a\beta_n) - F_{z_{n+1}}$$

$$M_\alpha = 0 = M\alpha_n + K_y(y_n - C\alpha_n + a\delta_n)C - K_z(Z_n + b\alpha_n - a\beta_n)b \\ - K_\alpha\alpha_n - M\alpha_{n+1}$$

$$M_\beta = 0 = M\beta_n - K_x(X_n + C\beta_n - b\delta_n)C + K_z(Z_n + b\alpha_n - a\beta_n)a \\ - K_\beta\beta_n - M\beta_{n+1}$$

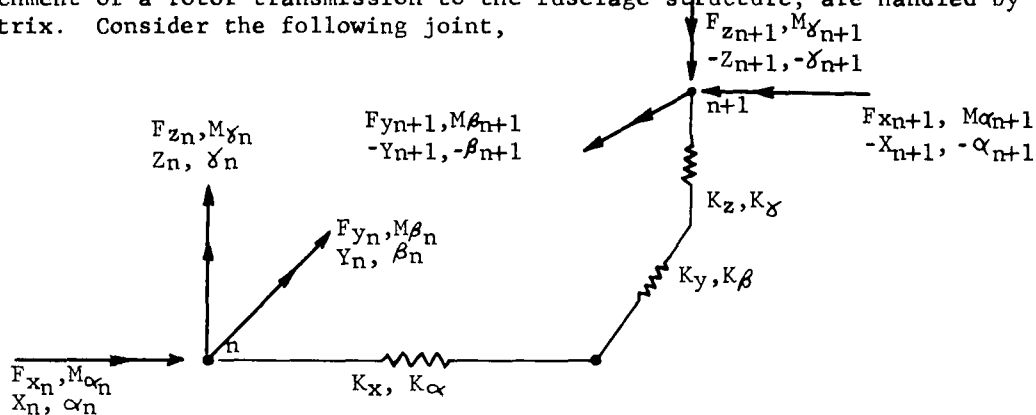
$$M_\gamma = 0 = M\gamma_n + K_x(X_n + C\beta_n - b\delta_n)b - K_y(y_n - C\alpha_n + a\delta_n) \\ - K_\gamma\gamma_n - M\gamma_{n+1}$$

Ground Spring Matrix

$$\begin{bmatrix} F_z \\ M_\beta \\ F_x \\ X \\ \beta \\ Z \\ F_y \\ M_\gamma \\ M_\alpha \\ \alpha \\ \gamma \\ y \end{bmatrix}^{n+1} = \begin{bmatrix} 1 & & & & & & & & & & & \\ & 1 & & & & & & & & & & \\ & & 1 & & & & & & & & & \\ & & & 1 & & & & & & & & \\ & & & & 1 & & & & & & & \\ & & & & & 1 & & & & & & \\ & & & & & & 1 & & & & & \\ & & & & & & & 1 & & & & \\ & & & & & & & & 1 & & & \\ & & & & & & & & & 1 & & \\ & & & & & & & & & & 1 & \\ & & & & & & & & & & & 1 \end{bmatrix} \begin{bmatrix} F_z \\ M_\beta \\ F_x \\ X \\ \beta \\ Z \\ F_y \\ M_\gamma \\ M_\alpha \\ \alpha \\ \gamma \\ y \end{bmatrix}^n$$

### Concentrated Spring Matrix

Concentrated springs between adjacent fuselage beam sections, such as the attachment of a rotor transmission to the fuselage structure, are handled by a matrix. Consider the following joint,



Since no force generation occurs across the spring joint the forces at stations  $n$  and  $n + 1$  are equal. Deflections change because of the action of forces on the springs. At joint  $n$ ,

$$\sum F_x = 0 = F_{x_n} - K_x(X_n - X_{n+1})$$

$$\sum F_y = 0 = F_{y_n} - K_y(Y_n - Y_{n+1})$$

$$\sum F_z = 0 = F_{z_n} - K_z(Z_n - Z_{n+1})$$

$$\sum M_\alpha = 0 = M_{\alpha_n} - K_\alpha(\alpha_n - \alpha_{n+1})$$

$$\sum M_\beta = 0 = M_{\beta_n} - K_\beta(\beta_n - \beta_{n+1})$$

$$\sum M_\gamma = 0 = M_{\gamma_n} - K_\gamma(\gamma_n - \gamma_{n+1})$$

Solving these equations for the displacements at station  $n+1$ , the concentrated spring matrix is,

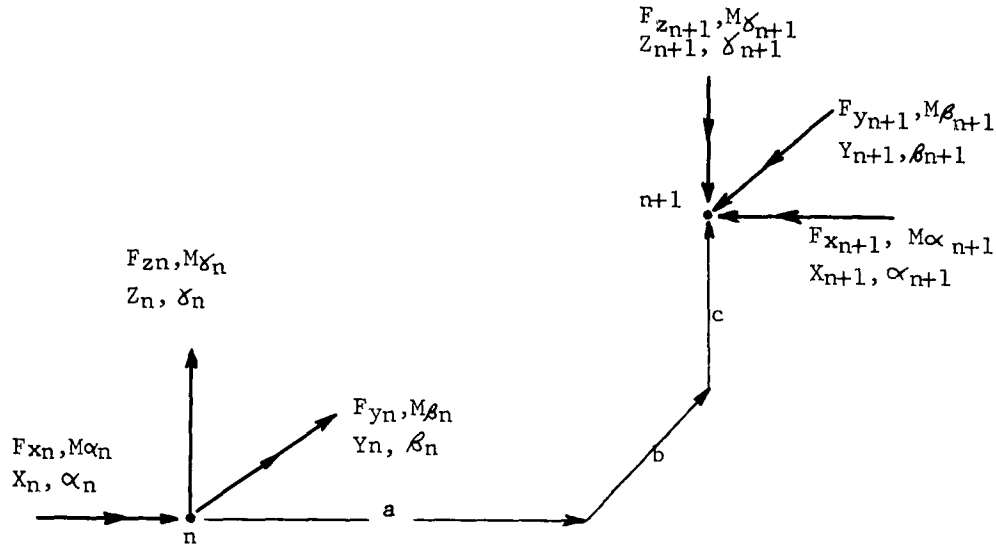
# Concentrated Spring Matrix

$$\begin{bmatrix} F_z \\ M_\beta \\ F_x \\ X \\ \beta \\ Z \\ F_y \\ M_\gamma \\ M_\alpha \\ \alpha \\ \gamma \\ y \end{bmatrix}^{n+1} = \begin{bmatrix} 1 & & & & & & & & & & & \\ & 1 & & & & & & & & & & \\ & & 1 & & & & & & & & & \\ & & & 1 & & & & & & & & \\ & & & & 1 & & & & & & & \\ & & & & & 1 & & & & & & \\ & & & & & & 1 & & & & & \\ & & & & & & & 1 & & & & \\ & & & & & & & & 1 & & & \\ & & & & & & & & & 1 & & \\ & & & & & & & & & & 1 & \\ & & & & & & & & & & & 1 \end{bmatrix}^n$$



### Shift Matrix

To permit a change of position of the reference axes a shift matrix is employed to covert loads and deflections from one axis orientation to another.



$$F_{x_{n+1}} = F_{x_n}$$

$$\alpha_{n+1} = \alpha_n$$

$$F_{y_{n+1}} = F_{y_n}$$

$$\beta_{n+1} = \beta_n$$

$$F_{z_{n+1}} = F_{z_n}$$

$$\gamma_{n+1} = \gamma_n$$

$$M_{\alpha_{n+1}} = M_{\alpha_n} - b_0 F_{z_n} + c_0 F_{y_n}$$

$$X_{n+1} = X_n = b_0 \gamma_n + c_0 \beta_n$$

$$M_{\beta_{n+1}} = M_{\beta_n} - c_0 F_{x_n} + a_0 F_{z_n}$$

$$Y_{n+1} = Y_n - c_0 \alpha_n + a_0 \gamma_n$$

$$M_{\gamma_{n+1}} = M_{\gamma_n} + b_0 F_{x_n} - a_0 F_{y_n}$$

$$Z_{n+1} = Z_n + b_0 \alpha_n - a_0 \beta_n$$

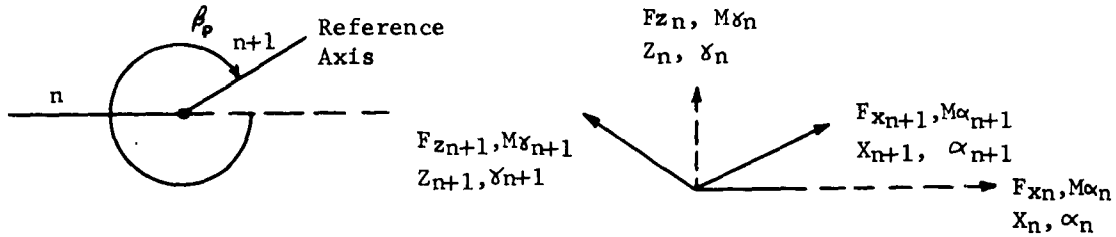
Thus the shift matrix

Shift Matrix

$$\begin{bmatrix} F_z \\ M_\theta \\ F_x \\ X \\ \beta \\ Z \\ F_y \\ M_y \\ M_\alpha \\ \alpha \\ \gamma \\ y \end{bmatrix}^n = \begin{bmatrix} 1 & & & & & & & & & & & \\ & a & & & & & & & & & & \\ & & 1 & & & & & & & & & \\ & & & -c & & & & & & & & \\ & & & & 1 & & & & & & & \\ & & & & & l & & & & & & \\ & & & & & & c & & & & & \\ & & & & & & & l & & & & \\ & & & & & & & & -a & & & \\ & & & & & & & & & l & & \\ & & & & & & & & & & b & \\ & & & & & & & & & & & l \\ & & & & & & & & & & & & 1 \\ & & & & & & & & & & & & & -b \\ & & & & & & & & & & & & & & 1 \\ & & & & & & & & & & & & & & & a \\ & & & & & & & & & & & & & & & & -c \\ & & & & & & & & & & & & & & & & & l \\ & & & & & & & & & & & & & & & & & & 1 \end{bmatrix}^{n+1}$$

### Bend Matrix

To permit a change of direction of the elastic axis, a bend matrix is employed to convert loads and deflections from one axis orientation to another



In progressing from left to right, the bend angle is defined as clockwise from an extension of the initial axis past the bend.

$$X_{n+1} = X_n \cos \beta_p - Z_n \sin \beta_p$$

$$Z_{n+1} = Z_n \cos \beta_p + X_n \sin \beta_p$$

$$Y_{n+1} = Y_n$$

$$\alpha_{n+1} = \alpha_n \cos \beta_p - \delta_n \sin \beta_p$$

$$\delta_{n+1} = \delta_n \cos \beta_p + \alpha_n \sin \beta_p$$

$$\beta_{n+1} = \beta_n$$

$$F_{x_{n+1}} = F_{x_n} \cos \beta_p - F_{z_n} \sin \beta_p$$

$$F_{z_{n+1}} = F_{z_n} \cos \beta_p + F_{x_n} \sin \beta_p$$

$$F_{y_{n+1}} = F_{y_n}$$

$$M_{\alpha_{n+1}} = M_{\alpha_n} \cos \beta_p - M_{\delta_n} \sin \beta_p$$

$$M_{\delta_{n+1}} = M_{\delta_n} \cos \beta_p + M_{\alpha_n} \sin \beta_p$$

$$M_{\beta_{n+1}} = M_{\beta_n}$$

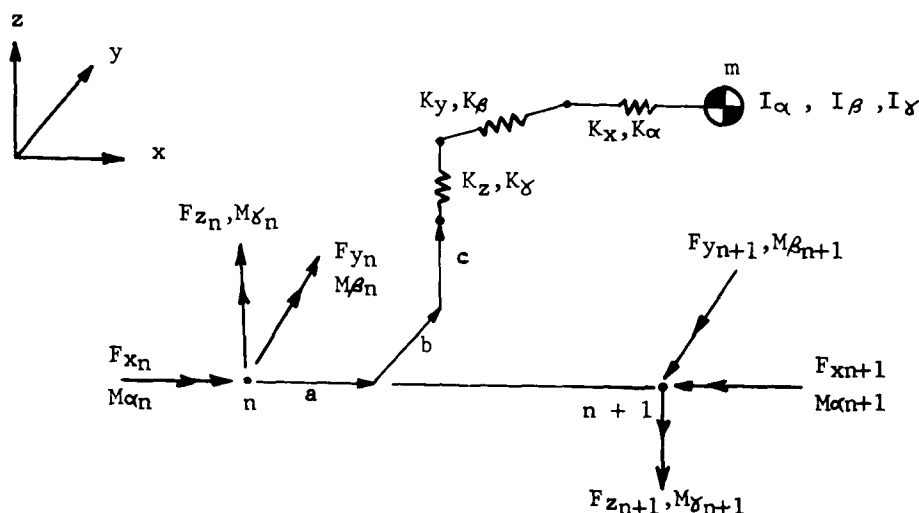
Vertical Bend Matrix

$$\begin{bmatrix} F_z \\ M_\beta \\ F_x \\ X \\ \beta \\ Z \\ F_y \\ M_\gamma \\ M_\alpha \\ \alpha \\ \gamma \\ y \end{bmatrix}_{n+1} = \begin{bmatrix} \cos \beta_p & \sin \beta_p & & & & & & & & & & \\ & 1 & & & & & & & & & & \\ & & \cos \beta_p & & & & & & & & & \\ & & & -\sin \beta_p & & & & & & & & \\ & & & & 1 & & & & & & & \\ & & & & & \cos \beta_p & & & & & & \\ & & & & & \sin \beta_p & & & & & & \\ & & & & & & 1 & & & & & \\ & & & & & & & \cos \beta_p & \sin \beta_p & & & \\ & & & & & & & & \cos \beta_p & & & \\ & & & & & & & & & -\sin \beta_p & & \\ & & & & & & & & & & \cos \beta_p & \\ & & & & & & & & & & \sin \beta_p & \\ & & & & & & & & & & & 1 \end{bmatrix} \begin{bmatrix} F_z \\ M_\beta \\ F_x \\ X \\ \beta \\ Z \\ F_y \\ M_\gamma \\ M_\alpha \\ \alpha \\ \gamma \\ y \end{bmatrix}_n$$

## Sprung Mass Matrices

Consider a mass,  $m$ , whose position is known with respect to the axes at an arbitrary station,  $n$ . Associated with the mass are the inertial properties  $I_\alpha$ ,  $I_\beta$ ,  $I_\gamma$  about its centroid. In addition, the mass is mounted on six simple springs which act in the same directions as the general displacements. These masses and inertias, accelerated by harmonic oscillations, produce inertial loads on the beam structure.

(a) Uncoupled System



$$\sum F_x = 0 = F_{x_n} + m\mu_x\omega^2(x + c\beta - b\gamma) - F_{x_{n+1}}$$

$$\sum F_y = 0 = F_{y_n} + m\mu_y\omega^2(y - c\alpha + a\gamma) - F_{y_{n+1}}$$

$$\sum F_z = 0 = F_{z_n} + m\mu_z\omega^2(z + b\alpha - a\beta) - F_{z_{n+1}}$$

$$\sum M_\alpha = 0 = M_{\alpha_n} - m\mu_y\omega^2(y - c\alpha + a\gamma)c + m\mu_z\omega^2(z + b\alpha - a\beta)b + I_\alpha\mu_\alpha\omega^2\alpha - M_{\alpha_{n+1}}$$

$$\sum M_\beta = 0 = M_{\beta_n} + m\mu_x\omega^2(x + c\beta - b\gamma)c - m\mu_z\omega^2(z + b\alpha - a\beta)a + I_\beta\mu_\beta\omega^2\beta - M_{\beta_{n+1}}$$

$$\sum M_\gamma = 0 = M_{\gamma_n} - m\mu_x\omega^2(x + c\beta - b\gamma)b + m\mu_y\omega^2(y - c\alpha + a\gamma)a + I_\gamma\mu_\gamma\omega^2\gamma - M_{\gamma_{n+1}}$$

Where from simple spring-mass theory,  $\mathcal{U}$  represents the amplification factors of the system

$$\mathcal{U}_x = \frac{1}{1 - \left(\frac{\omega}{\omega_x}\right)^2}$$

$$\mathcal{U}_\alpha = \frac{1}{1 - \left(\frac{\omega}{\omega_\alpha}\right)^2}$$

$$\mathcal{U}_y = \frac{1}{1 - \left(\frac{\omega}{\omega_y}\right)^2}$$

$$\mathcal{U}_\beta = \frac{1}{1 - \left(\frac{\omega}{\omega_\beta}\right)^2}$$

$$\mathcal{U}_z = \frac{1}{1 - \left(\frac{\omega}{\omega_z}\right)^2}$$

$$\mathcal{U}_\gamma = \frac{1}{1 - \left(\frac{\omega}{\omega_\gamma}\right)^2}$$

and

$$\omega_x^2 = \frac{K_x}{m}$$

$$\omega_\alpha^2 = \frac{K_\alpha}{I_\alpha}$$

$$\omega_y^2 = \frac{K_y}{m}$$

$$\omega_\beta^2 = \frac{K_\beta}{I_\beta}$$

$$\omega_z^2 = \frac{K_z}{m}$$

$$\omega_\gamma^2 = \frac{K_\gamma}{I_\gamma}$$

Thus, since the displacements at stations  $n$  and  $n + 1$  are equal the matrix is



(b) The coupled force relationship (effective mass matrix), let mass properties be denoted as follows:

$$\begin{array}{ll} M = m_1 & M = m_4 \\ I_\beta = m_2 & I_\gamma = m_5 \\ M = m_3 & I_\alpha = m_6 \end{array}$$

Let mass motion be denoted as follows (with respect to fuselage):

$$\begin{array}{ll} z_e = e_1 & y_e = e_4 \\ \beta_e = e_2 & \gamma_e = e_5 \\ x_e = e_3 & \alpha_e = e_6 \end{array}$$

Let fuselage motion and external forces be denoted as follows:

$$\begin{array}{llll} z = f_1 & y = f_4 & F_z = -Q_1 & F_y = -Q_4 \\ \beta = f_2 & \gamma = f_5 & M_\beta = -Q_2 & F_\gamma = -Q_5 \\ x = f_3 & \alpha = f_6 & F_x = -Q_3 & F_\alpha = -Q_6 \end{array}$$

Let mass frequencies and modes be denoted as follows:

$$\omega_r \begin{cases} e_1^{(r)}, e_4^{(r)} \\ e_2^{(r)}, e_5^{(r)} \\ e_3^{(r)}, e_6^{(r)} \end{cases} \quad \begin{matrix} r^{\text{th}} \text{ mode} \\ (r = 1, 2, 3, 4, 5, 6) \end{matrix}$$

Let the mass motion with respect to fuselage be represented as the sum of all normal modes

$$e_i = \sum_{r=1}^6 e_i^{(r)} H_r$$

Where  $H_r$  is the generalized coordinate in the  $r^{\text{th}}$  mode.



The total kinetic energy of the mass and of the fuselage displacements due to external forces and moments is,

$$T = \frac{1}{2} \sum_{i=1}^6 m_i (\dot{f}_i + \dot{e}_i)^2$$

By substitution, the kinetic energy becomes

$$T = \frac{1}{2} \sum_{r=1}^6 m_i (\dot{f}_i + \sum_{r=1}^6 e_i^{(r)} \dot{H}_r)^2$$

or

$$T = \frac{1}{2} \sum_{r=1}^6 m_i (\dot{f}_i^2 + 2 \dot{f}_i \sum_{r=1}^6 e_i^{(r)} \dot{H}_r + \sum_{r=1}^6 e_i^{(r)^2} \dot{H}_r^2)$$

The total potential energy of system is

$$V = \frac{1}{2} \sum_{r=1}^6 K_r H_r^2$$

where  $K_r$  = Effective Spring In  $r^{th}$  Mode

since by orthogonality of normal modes

$$\sum_{i=1}^6 m_i e_i^{(r)} e_i^{(s)} = 0 \text{ for } r \neq s$$

The lagrange equations of motion are as follows:

$$f_i : m_i \ddot{f}_i + \sum_{r=1}^6 m_i e_i^{(r)} \ddot{H}_r = -Q_i$$

$$H_r : M_r \ddot{H}_r + K_r H_r + \sum_{j=1}^6 m_j e_j^{(r)} \ddot{f}_j = 0$$

where

$$M_r = \sum_{i=1}^6 m_i e_i^{(r)^2}$$

Solving for  $H_r$

assuming  $f_j = f_{j0} e^{i\omega t}$  (Harmonic Motion)

$$H_r = \frac{\sum_{j=1}^6 m_j e_j^{(r)} f_{j0}}{M_r \left( \frac{\omega_r^2}{\omega^2} - 1 \right)}$$

Substituting in  $f_i$  equation

$$m_i f_i^{\infty} + \sum_{r=1}^6 \frac{\sum_{j=1}^6 m_i m_j e_i^{(r)} e_j^{(r)} f_j^{\infty}}{M_r \left( \frac{\omega_r^2}{\omega^2} - 1 \right)} = -Q_i$$

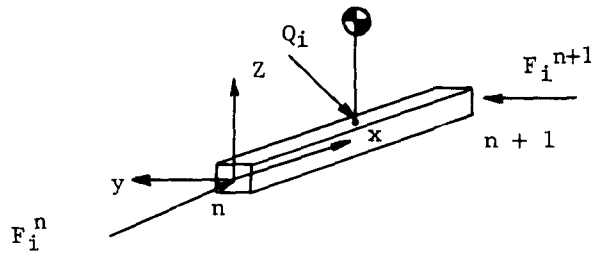
for simplicity the equation is written

$$m_i f_i^{\infty} + \Delta m_{ij} f_j^{\infty} = -Q_i$$

Since harmonic motion is assumed

$$m_i f_i \omega^2 + \Delta m_{ij} f_j \omega^2 = Q_i$$

A schematic free body diagram of the effective mass - fuselage combination between stations  $n$  and  $n+1$



where  $F_i^n$  and  $F_i^{n+1}$  are the six components of force at station  $n$  and  $n+1$  respectively

$$\sum F_i = 0 = F_i^n + Q_i - F_i^{n+1}$$

$$\text{or } F_i^{n+1} = F_i^n + m_i f_i \omega^2 + \Delta m_{ij} f_j \omega^2$$

Since the position vector of station  $n+1$  with respect to station  $n$  is small, the six displacement components at the two stations are equal. Thus the "coupled mass matrix" is written as follows:

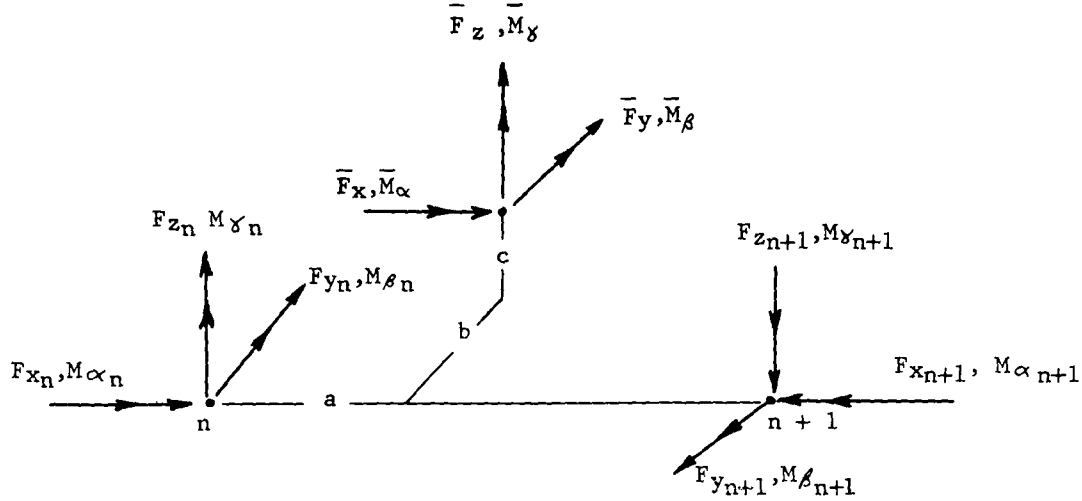
\_\_\_\_\_



\_\_\_\_\_

### Force Matrix

A mathematical device which permits simulation of a forcing function placed anywhere along the fuselage of an aircraft is the force matrix. Suppose a station,  $n$ , is subjected to a forcing function having six components, then these external forces induce additional loads on the vibrating structure.



$$\sum F_x = 0 = F_{x_n} + \bar{F}_x - F_{x_{n+1}}$$

$$\sum F_y = 0 = F_{y_n} + \bar{F}_y - F_{y_{n+1}}$$

$$\sum F_z = 0 = F_{z_n} + \bar{F}_z - F_{z_{n+1}}$$

$$\sum M_\alpha = 0 = M_{\alpha_n} - c\bar{F}_y + b\bar{F}_z - M_{\alpha_{n+1}} + \bar{M}_\alpha$$

$$\sum M_\beta = 0 = M_{\beta_n} - c\bar{F}_x - a\bar{F}_z - M_{\beta_{n+1}} + \bar{M}_\beta$$

$$\sum M_\gamma = 0 = M_{\gamma_n} - b\bar{F}_x + a\bar{F}_y - M_{\gamma_{n+1}} + \bar{M}_\gamma$$

In general, the forcing function,  $\bar{F}_{ij}$ , is of the form

$$\bar{F} = F_0 + F_1 \cos \psi_n + F_2 \sin \psi_n$$

where  $\psi_n$  is the harmonic azimuth angle.

Since the forcing function must be added to the inertial and elastic loads of the fuselage independent of the basic boundary column, the matrix is extended to include a 13th row and column. As an example in the force matrix shown on the following page, increasing the loads at station  $h + 1$  is possible by the addition of forcing functions in the 13th column which are added to the modal column by an independent coordinate  $Q$ .

Using this 13 x 13 force matrix requires that all the previously derived matrices be padded from 12 x 12 to 13 x 13.

$$\begin{bmatrix} 12 \times 1 \\ Q \end{bmatrix} = \begin{bmatrix} 12 \times 12 \\ 0 \end{bmatrix} \begin{bmatrix} 0 \\ 12 \times 12 \\ 0 \end{bmatrix} \begin{bmatrix} 0 \\ 12 \times 1 \\ Q \end{bmatrix}$$

The diagram illustrates the padding of a 12x12 matrix to a 13x13 matrix. The leftmost vector is a 13x1 column with a 12x1 block and a Q element. This is equal to the product of a 13x13 matrix and a 13x1 vector. The 13x13 matrix is shown as a 12x12 block with a 0 at the bottom-left, and a column with 0 at the top and 0 at the bottom. The 13x1 vector is shown as a 12x1 block with a Q element at the bottom.

Force Matrix

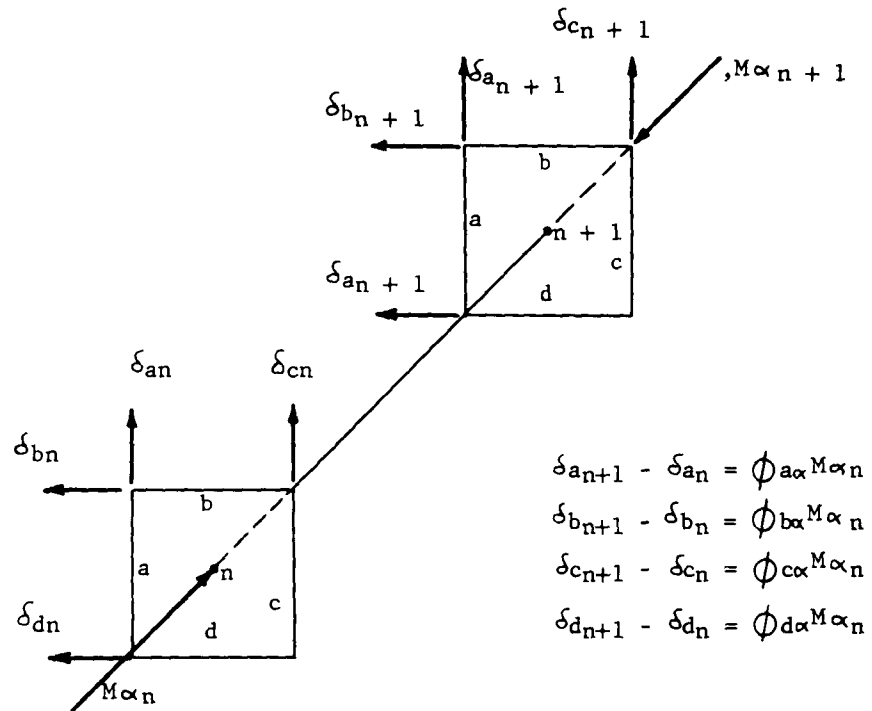
$F_z$	$M_\beta$	$F_x$	X	$\beta$	Z	$F_y$	$M_\gamma$	$M_\alpha$	$\alpha$	$\gamma$	y	Q
1												
	1											
		1										
			1									
				1								
					1							
						1						
							1					
								1				
									1			
										1		
											1	
												1

$F_{ux}, F_{uy}, F_{uz}$  ----Unit Forces (lb)  
 $M_{u\alpha}, M_{u\beta}, M_{u\gamma}$  ----Unit Moments (In. #)  
 $F_{cx}, F_{cy}, F_{cz}$  ----Cos Force Coefficients (#)  
 $M_{c\alpha}, M_{c\beta}, M_{c\gamma}$  ----Cos Moment Coefficients (In. #)

$F_{sx}, F_{sy}, F_{sz}$  ----Sin Force Coefficients (#)  
 $M_{s\alpha}, M_{s\beta}, M_{s\gamma}$  ----Sin Moment Coefficients (In. #)  
 $\psi_n$  ----Harmonic Azimuth (deg.)  
 $a_f, b_f, c_f$  ----Long, Lat. & Vert. Force Locations (In.)

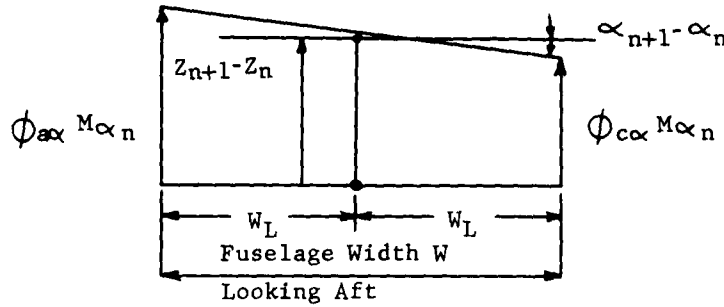
### Frame Racking Matrix

From deflection tests of the H-21 helicopter it was noted that frame racking occurs in the vertical and lateral directions in the "constant section" portion of the fuselage. If elementary beam theory is used in conjunction with test data an elastic matrix which describes the force-displacement relationship in the "constant section" may be derived.



The deflections  $\delta_{an}$ ,  $\delta_{bn}$ ,  $\delta_{cn}$ ,  $\delta_{dn}$ ,  $\delta_{an+1}$ ,  $\delta_{bn+1}$ ,  $\delta_{cn+1}$ ,  $\delta_{dn+1}$  came from test data for a unit torsional moment,  $M_{\alpha n}$  thus from the above equations the racking coefficients  $\phi_{a\alpha}$ ,  $\phi_{b\alpha}$ ,  $\phi_{c\alpha}$  and  $\phi_{d\alpha}$  were computed.

Having the racking coefficients for relative translations in the vertical direction enables calculation of the relative vertical translation at any point in the fuselage and the relative rotation about the longitudinal axis.



Thus

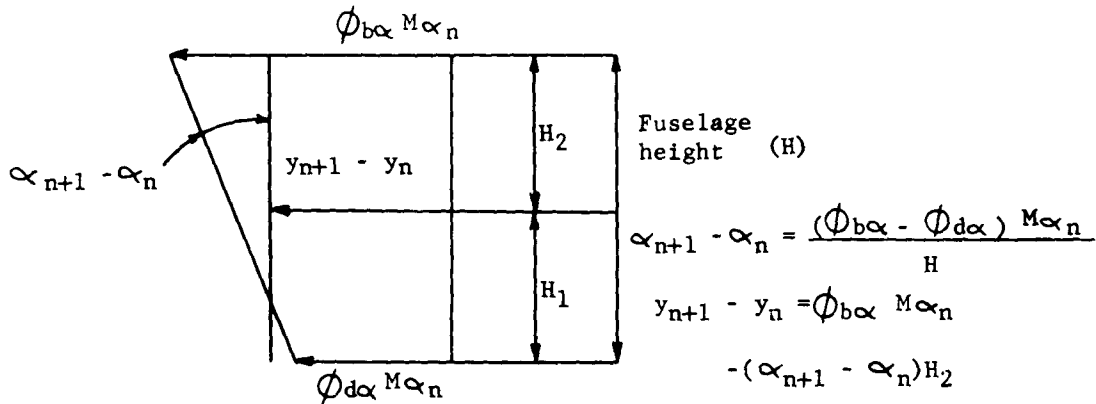
$$\alpha_{n+1} - \alpha_n = \frac{(\phi_{a\alpha} - \phi_{c\alpha}) M \alpha_n}{W}$$

$$Z_{n+1} - Z_n = \phi_{c\alpha} M \alpha_n + (\alpha_{n+1} - \alpha_n) W_L$$

Replacing the relative rotation in the above equation

$$Z_{n+1} - Z_n = \left(1 - \frac{W_L}{W}\right) \phi_{c\alpha} M \alpha_n + \frac{W_L}{W} \phi_{a\alpha} M$$

Likewise, using the lateral racking coefficients



Placing the relative rotation in the above equation

$$y_{n+1} - y_n = \left(1 - \frac{H_2}{H}\right) \phi_{b\alpha} M \alpha_n + \frac{H_2}{H} \phi_{d\alpha} M \alpha_n$$

Thus, if the equations for vertical and lateral translation and longitudinal rotation are added to the equations comprising the existing elastic matrix, the result is an elastic matrix which includes frame racking.



$$[E_2]$$

$F_z$	$M_\beta$	$F_x$	$X$	$\beta$	$Z$	$F_y$	$M_\gamma$	$M_\alpha$	$\alpha$	$\gamma$	$y$	$Q$
-------	-----------	-------	-----	---------	-----	-------	------------	------------	----------	----------	-----	-----

11

[illegible]

[illegible]

Where

$$A = \left[ \frac{\phi_{a\alpha} - \phi_{c\alpha}}{W} \right] \text{ or } \left[ \frac{\phi_{d\alpha} - \phi_{b\alpha}}{H} \right]$$

The frame racking matrix in the lateral and vertical direction is used with the neutral axis and shear center axis shift matrices developed earlier. The subdivided elastic matrix can be written as,

$$\begin{bmatrix} \bar{E} \end{bmatrix} = \begin{bmatrix} \bar{E}_3 \end{bmatrix} \begin{bmatrix} \bar{E}_2 \end{bmatrix} \begin{bmatrix} \bar{E}_1 \end{bmatrix}$$

Input required for the  $\bar{E}_1$ ,  $\bar{E}_2$ ,  $\bar{E}_3$  matrices shown on the following pages.

$b_n$ , Dist. from the ref. axis to the neutral axis in the y direction (in.)  
 $c_n$ , Dist. from the ref. axis to the neutral axis in the z direction (in.)  
 $A_x$ , Axial Compression area (in<sup>2</sup>)  
 $A_y$ , effective shear area in the y direction (in<sup>2</sup>)  
 $A_z$ , effective shear area in the z direction (in<sup>2</sup>)  
 $I_y$ , Bending stiffness about the y axis (in<sup>4</sup>)  
 $I_z$ , Bending stiffness about the z axis (in<sup>4</sup>)  
 $E$ , Bending modulus (#/in<sup>2</sup>)  
 $G$ , Shear modulus (#/in<sup>2</sup>)  
 $L$ , Elastic bay length (in)  
 $\phi_{d\alpha}$ , Linear deflection at the right side of the frame from a unit moment (1/#)  
 $\phi_{b\alpha}$ , Linear deflection at the top section of the frame from a unit moment (1/#)  
 $\phi_{c\alpha}$ , Linear deflection at the left side of the frame from a unit moment (1/#)  
 $\phi_{d\alpha}$ , Linear deflection at the bottom section of the frame from a unit moment (1/#)  
 $W$ , Lateral distance between longerons (in.)  
 $W_1$ , Lateral distance from the reference axis to the right longeron (in.)  
 $H$ , Vertical distance between longerons (in.)  
 $H_2$ , Vertical distance from the reference axis to the upper longeron (in.)

$$\begin{bmatrix} \bar{E}_1 \end{bmatrix}$$

$F_z$	$M_\beta$	$F_x$	$X$	$\beta$	$Z$	$F_y$	$M_\gamma$	$M_\alpha$	$\alpha$	$\gamma$	$y$	$Q$
-------	-----------	-------	-----	---------	-----	-------	------------	------------	----------	----------	-----	-----

=

1												1
	1	$-C_N$										
		1										
			1	$C_N$								
				1								
					1							
						1						
							1					
								1				
									1			
										1		
											1	

$F_z$	$M_\beta$	$F_x$	$X$	$\beta$	$Z$	$F_y$	$M_\gamma$	$M_\alpha$	$\alpha$	$\gamma$	$y$	$Q$
-------	-----------	-------	-----	---------	-----	-------	------------	------------	----------	----------	-----	-----

$\begin{bmatrix} \bar{E}_3 \end{bmatrix}$

$F_z$	$M_\beta$	$F_x$	$X$	$\beta$	$Z$	$F_y$	$M_\gamma$	$M_\alpha$	$\alpha$	$\gamma$	$y$	$Q$
-------	-----------	-------	-----	---------	-----	-------	------------	------------	----------	----------	-----	-----

$n+1$

=

1												
	1	$C_N$										
		1										
			1	$-C_N$								
				1								
					1							
						1						
							1					
								1				
									1			
										1		
											1	
												1

$n$

$F_z$	$M_\beta$	$F_x$	$X$	$\beta$	$Z$	$F_y$	$M_\gamma$	$M_\alpha$	$\alpha$	$\gamma$	$y$	$Q$
-------	-----------	-------	-----	---------	-----	-------	------------	------------	----------	----------	-----	-----

## Frame Racking Matrix (Collapsed)

[illegible]

## Method of Solution for Coupled Matrix Program

### Method of Solution - Free Vibration

These matrices are now "building blocks" from which a dynamic representation of the helicopter fuselage may be constructed.

The boundary conditions for such a representative helicopter fuselage are that the loads  $F_x$ ,  $F_y$ ,  $F_z$ ,  $M_\alpha$ ,  $M_\beta$  and  $M_\gamma$  just before the forward rotor mass and just after the aft rotor mass are zero, that is a "free-free" beam. Even ground springs do not affect the boundary conditions, because they are taken to act on the fuselage side before the boundaries are reached. Matrix multiplications from the forward to aft rotor are conducted repeatedly for trial frequencies, until the boundary conditions are met.. Note that since the forward end boundary conditions,  $F_x = F_y = F_z = M_\alpha = M_\beta = M_\gamma = 0$  appear in the single column end matrix, and since only these forces need be determined for comparison with the aft end boundary conditions, it is then necessary to use only the terms shown on the next page in the final collapsed matrix for the frequency calculation.

Note that the element values are symbolized in the following description by  $a_{14}$ ,  $a_{15}$ ,  $a_{16}$  etc. These represent numerical values present in specific row-column locations after collapsing of the matrix assemblage. Their content is dependent on the matrix arrangement for a particular application and on the frequency being considered.

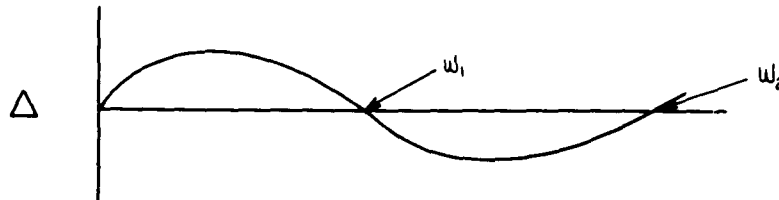
$F_z$			$a_{14}$	$a_{15}$	$a_{16}$			$a_{110}$	$a_{111}$	$a_{112}$	0
M			$a_{24}$	$a_{25}$	$a_{26}$			$a_{210}$	$a_{211}$	$a_{212}$	0
$F_x$			$a_{34}$	$a_{35}$	$a_{36}$			$a_{310}$	$a_{311}$	$a_{312}$	0
X											X
$\beta$											$\beta$
Z											Z
$F_y$			$a_{74}$	$a_{75}$	$a_{76}$			$a_{710}$	$a_{711}$	$a_{712}$	0
M			$a_{84}$	$a_{85}$	$a_{86}$			$a_{810}$	$a_{811}$	$a_{812}$	0
M			$a_{94}$	$a_{95}$	$a_{96}$			$a_{910}$	$a_{911}$	$a_{912}$	0
$\alpha$											$\alpha$
$\gamma$											$\gamma$
y											y

Aft End
Fwd End

Repeated trials of frequency,  $\omega$ , are made, and each one of the thirty-six terms shown above are obtained numerically. To meet the boundary requirement, the residual,  $\Delta$ , of the matrix array must be zero.

$$\Delta = \begin{array}{|c|c|c|c|c|c|} \hline a_{14} & a_{15} & a_{16} & a_{110} & a_{111} & a_{112} \\ \hline a_{24} & a_{25} & a_{26} & a_{210} & a_{211} & a_{212} \\ \hline a_{34} & a_{35} & a_{36} & a_{310} & a_{311} & a_{312} \\ \hline a_{74} & a_{75} & a_{76} & a_{710} & a_{711} & a_{712} \\ \hline a_{84} & a_{85} & a_{86} & a_{810} & a_{811} & a_{812} \\ \hline a_{94} & a_{95} & a_{96} & a_{910} & a_{911} & a_{912} \\ \hline \end{array} = 0$$

In practice, the residual may be plotted against the frequency trials, and when



a zero intersection occurs, natural frequencies  $\omega_1, \omega_2, \dots, \omega_n$  are determined.

For each natural mode, it is desirable to normalize in terms of the largest relative linear deflection value which exist at the ends of the beam. Now, calculating the relative linear deflections at both ends of the beam:

Rewriting the collapsed matrix with the zero columns removed;

$$\begin{bmatrix} 0 \\ 0 \\ 0 \\ X \\ \beta \\ Z \\ 0 \\ 0 \\ 0 \\ \alpha \\ \gamma \\ y \end{bmatrix} = \begin{bmatrix} a_{14} & a_{15} & a_{16} & a_{1\bar{0}} & a_{1\bar{1}} & a_{1\bar{2}} \\ a_{24} & a_{25} & a_{26} & a_{2\bar{0}} & a_{2\bar{1}} & a_{2\bar{2}} \\ a_{34} & a_{35} & a_{36} & a_{3\bar{0}} & a_{3\bar{1}} & a_{3\bar{2}} \\ a_{44} & a_{45} & a_{46} & a_{4\bar{0}} & a_{4\bar{1}} & a_{4\bar{2}} \\ a_{54} & a_{55} & a_{56} & a_{5\bar{0}} & a_{5\bar{1}} & a_{5\bar{2}} \\ a_{64} & a_{65} & a_{66} & a_{6\bar{0}} & a_{6\bar{1}} & a_{6\bar{2}} \\ a_{74} & a_{75} & a_{76} & a_{7\bar{0}} & a_{7\bar{1}} & a_{7\bar{2}} \\ a_{84} & a_{85} & a_{86} & a_{8\bar{0}} & a_{8\bar{1}} & a_{8\bar{2}} \\ a_{94} & a_{95} & a_{96} & a_{9\bar{0}} & a_{9\bar{1}} & a_{9\bar{2}} \\ a_{\bar{0}4} & a_{\bar{0}5} & a_{\bar{0}6} & a_{\bar{0}\bar{0}} & a_{\bar{0}\bar{1}} & a_{\bar{0}\bar{2}} \\ a_{\bar{1}4} & a_{\bar{1}5} & a_{\bar{1}6} & a_{\bar{1}\bar{0}} & a_{\bar{1}\bar{1}} & a_{\bar{1}\bar{2}} \\ a_{\bar{2}4} & a_{\bar{2}5} & a_{\bar{2}6} & a_{\bar{2}\bar{0}} & a_{\bar{2}\bar{1}} & a_{\bar{2}\bar{2}} \end{bmatrix} \begin{bmatrix} X \\ \beta \\ Z \\ \alpha \\ \gamma \\ y \end{bmatrix}$$

Aft Rotor                      Fwd Rotor

Using the aft rotor load equations,

$$\begin{bmatrix} 0 \\ 0 \\ 0 \\ 0 \\ 0 \\ 0 \end{bmatrix} = \begin{bmatrix} a_{14} & a_{15} & a_{16} & a_{1\bar{0}} & a_{1\bar{1}} & a_{1\bar{2}} \\ a_{24} & a_{25} & a_{26} & a_{2\bar{0}} & a_{2\bar{1}} & a_{2\bar{2}} \\ a_{34} & a_{35} & a_{36} & a_{3\bar{0}} & a_{3\bar{1}} & a_{3\bar{2}} \\ a_{74} & a_{75} & a_{76} & a_{7\bar{0}} & a_{7\bar{1}} & a_{7\bar{2}} \\ a_{84} & a_{85} & a_{86} & a_{8\bar{0}} & a_{8\bar{1}} & a_{8\bar{2}} \\ a_{94} & a_{95} & a_{96} & a_{9\bar{0}} & a_{9\bar{1}} & a_{9\bar{2}} \end{bmatrix} \begin{bmatrix} X \\ \beta \\ Z \\ \alpha \\ \gamma \\ y \end{bmatrix}$$

Fwd Rotor

Solving for the fwd rotor deflections in terms of;

$$\begin{bmatrix} X \\ \beta \\ Z \\ \alpha \\ \gamma \end{bmatrix} = -y \begin{bmatrix} a_{14} & a_{15} & a_{16} & a_{1\bar{0}} & a_{1\bar{1}} \\ a_{24} & a_{25} & a_{26} & a_{2\bar{0}} & a_{2\bar{1}} \\ a_{34} & a_{35} & a_{36} & a_{3\bar{0}} & a_{3\bar{1}} \\ a_{74} & a_{75} & a_{76} & a_{7\bar{0}} & a_{7\bar{1}} \\ a_{84} & a_{85} & a_{86} & a_{8\bar{0}} & a_{8\bar{1}} \end{bmatrix} \cdot \begin{bmatrix} a_{1\bar{2}} \\ a_{2\bar{2}} \\ a_{3\bar{2}} \\ a_{7\bar{2}} \\ a_{8\bar{2}} \end{bmatrix}$$

Fwd Rotor                      -1



or letting  $y = 1$ , and then rewriting the equations

$$\begin{bmatrix} X \\ \beta \\ Z \\ \alpha \\ \gamma \\ y \end{bmatrix} = - \begin{bmatrix} a_{14} & a_{15} & a_{16} & a_{10} & a_{11} & \\ a_{24} & a_{25} & a_{26} & a_{20} & a_{21} & \\ a_{34} & a_{35} & a_{36} & a_{30} & a_{31} & \\ a_{74} & a_{75} & a_{76} & a_{70} & a_{71} & \\ a_{84} & a_{85} & a_{86} & a_{80} & a_{81} & \\ & & & & & -1 \end{bmatrix} \begin{bmatrix} a_{12} \\ a_{22} \\ a_{32} \\ a_{72} \\ a_{82} \\ 1 \end{bmatrix}$$

Fwd Rotor

Solving for the aft rotor deflections,

$$\begin{bmatrix} X \\ \beta \\ Z \\ \alpha \\ \gamma \\ y \end{bmatrix} = - \begin{bmatrix} a_{44} & a_{45} & a_{46} & a_{40} & a_{41} & a_{42} \\ a_{54} & a_{55} & a_{56} & a_{50} & a_{51} & a_{52} \\ a_{64} & a_{65} & a_{66} & a_{60} & a_{61} & a_{62} \\ a_{04} & a_{05} & a_{06} & a_{00} & a_{01} & a_{02} \\ a_{14} & a_{15} & a_{16} & a_{10} & a_{11} & a_{12} \\ a_{24} & a_{25} & a_{26} & a_{20} & a_{21} & a_{22} \end{bmatrix} \cdot \begin{bmatrix} a_{14} & a_{15} & a_{16} & a_{10} & a_{11} & \\ a_{24} & a_{25} & a_{26} & a_{20} & a_{21} & \\ a_{34} & a_{35} & a_{36} & a_{30} & a_{31} & \\ a_{74} & a_{75} & a_{76} & a_{70} & a_{71} & \\ a_{84} & a_{85} & a_{86} & a_{80} & a_{81} & \\ & & & & & -1 \end{bmatrix} \begin{bmatrix} a_{12} \\ a_{22} \\ a_{32} \\ a_{72} \\ a_{82} \\ 1 \end{bmatrix}$$

Aft Rotor

The program inspects the linear deflections calculated as shown above and continues the normalizing procedure relative to the linear deflection with the largest magnitude. The normalization in terms of any linear deflection can be performed by adjusting the fwd. rotor boundary conditions.

Forward Rotor

$$\begin{matrix} x \\ \begin{bmatrix} X \\ \beta \\ Z \\ \alpha \\ \gamma \\ y \end{bmatrix} \end{matrix} = \frac{1}{X} \begin{matrix} \begin{bmatrix} X \\ \beta \\ Z \\ \alpha \\ \gamma \\ y \end{bmatrix} \end{matrix}$$

Fwd Rotor Column

$$\begin{matrix} y \\ \begin{bmatrix} X \\ \beta \\ Z \\ \alpha \\ \gamma \\ y \end{bmatrix} \end{matrix} = 1 \begin{matrix} \begin{bmatrix} X \\ \beta \\ Z \\ \alpha \\ \gamma \\ y \end{bmatrix} \end{matrix}$$

Fwd Rotor Column

Fwd Rotor

$$\begin{array}{c} \underline{Z} \\ \begin{bmatrix} X \\ \beta \\ Z \\ \alpha \\ \gamma \\ y \end{bmatrix} = \frac{1}{Z} \begin{bmatrix} X \\ \beta \\ Z \\ \alpha \\ \gamma \\ y \end{bmatrix} \end{array}$$

Fwd Rotor Column      Fwd Rotor

Aft Rotor

$$\begin{array}{c} \underline{X} \\ \begin{bmatrix} X \\ \beta \\ Z \\ \alpha \\ \gamma \\ y \end{bmatrix} = \frac{1}{X} \begin{bmatrix} X \\ \beta \\ Z \\ \alpha \\ \gamma \\ y \end{bmatrix} \end{array} \quad \begin{array}{c} -1 \\ \begin{bmatrix} a_{44} & a_{45} & a_{46} & a_{40} & a_{41} & a_{42} \\ a_{54} & a_{55} & a_{56} & a_{50} & a_{51} & a_{52} \\ a_{64} & a_{65} & a_{66} & a_{60} & a_{61} & a_{62} \\ a_{04} & a_{05} & a_{06} & a_{00} & a_{01} & a_{02} \\ a_{14} & a_{15} & a_{16} & a_{10} & a_{11} & a_{12} \\ a_{24} & a_{25} & a_{26} & a_{20} & a_{21} & a_{22} \end{bmatrix} \end{array} \quad \begin{array}{c} -1 \\ \begin{bmatrix} X \\ \beta \\ Z \\ \alpha \\ \gamma \\ y \end{bmatrix} \end{array}$$

Fwd Rotor Column      Aft Rotor

$$\begin{array}{c} \underline{Z} \\ \begin{bmatrix} X \\ \beta \\ Z \\ \alpha \\ \gamma \\ y \end{bmatrix} = \frac{1}{Z} \begin{bmatrix} X \\ \beta \\ Z \\ \alpha \\ \gamma \\ y \end{bmatrix} \end{array} \quad \begin{array}{c} -1 \\ \begin{bmatrix} a_{44} & a_{45} & a_{46} & a_{40} & a_{41} & a_{42} \\ a_{54} & a_{55} & a_{56} & a_{50} & a_{51} & a_{52} \\ a_{64} & a_{65} & a_{66} & a_{60} & a_{61} & a_{62} \\ a_{04} & a_{05} & a_{06} & a_{00} & a_{01} & a_{02} \\ a_{14} & a_{15} & a_{16} & a_{10} & a_{11} & a_{12} \\ a_{24} & a_{25} & a_{26} & a_{20} & a_{21} & a_{22} \end{bmatrix} \end{array} \quad \begin{array}{c} -1 \\ \begin{bmatrix} X \\ \beta \\ Z \\ \alpha \\ \gamma \\ y \end{bmatrix} \end{array}$$

Fwd Rotor Column      Aft Rotor

$$\begin{array}{c} \underline{\quad} \\ \begin{bmatrix} X \\ \beta \\ Z \\ \alpha \\ \gamma \\ y \end{bmatrix} = \frac{1}{\quad} \begin{bmatrix} X \\ \beta \\ Z \\ \alpha \\ \gamma \\ y \end{bmatrix} \end{array} \quad \begin{array}{c} -1 \\ \begin{bmatrix} a_{44} & a_{45} & a_{46} & a_{40} & a_{41} & a_{42} \\ a_{54} & a_{55} & a_{56} & a_{50} & a_{51} & a_{52} \\ a_{64} & a_{65} & a_{66} & a_{60} & a_{61} & a_{62} \\ a_{04} & a_{05} & a_{06} & a_{00} & a_{01} & a_{02} \\ a_{14} & a_{15} & a_{16} & a_{10} & a_{11} & a_{12} \\ a_{24} & a_{25} & a_{26} & a_{20} & a_{21} & a_{22} \end{bmatrix} \end{array} \quad \begin{array}{c} -1 \\ \begin{bmatrix} X \\ \beta \\ Z \\ \alpha \\ \gamma \\ y \end{bmatrix} \end{array}$$

Fwd Rotor Column      Aft Rotor

# Forced Vibration

Forced mode shapes can be obtained by collapsing the matrix array representing the fuselage into a single matrix considering the unknown frequency,  $\omega$  as the frequency of forced excitation. Including the known magnitude of the shaking loads in the fuselage system the single matrix for the entire fuselage becomes,

$F_z$	$a_{11}$	$a_{12}$	$a_{13}$	$a_{14}$	$a_{15}$	$a_{16}$	$a_{17}$	$a_{18}$	$a_{19}$	$a_{10}$	$a_{11}$	$a_{12}$	$a_{13}$	$F_z$
$M_\beta$	$a_{21}$	$a_{22}$	$a_{23}$	$a_{24}$	$a_{25}$	$a_{26}$	$a_{27}$	$a_{28}$	$a_{29}$	$a_{20}$	$a_{21}$	$a_{22}$	$a_{23}$	$M_\beta$
$F_x$	$a_{31}$	$a_{32}$	$a_{33}$	$a_{34}$	$a_{35}$	$a_{36}$	$a_{37}$	$a_{38}$	$a_{39}$	$a_{30}$	$a_{31}$	$a_{32}$	$a_{33}$	$F_x$
$X$	$a_{41}$	$a_{42}$	$a_{43}$	$a_{44}$	$a_{45}$	$a_{46}$	$a_{47}$	$a_{48}$	$a_{49}$	$a_{40}$	$a_{41}$	$a_{42}$	$a_{43}$	$X$
$\beta$	$a_{51}$	$a_{52}$	$a_{53}$	$a_{54}$	$a_{55}$	$a_{56}$	$a_{57}$	$a_{58}$	$a_{59}$	$a_{50}$	$a_{51}$	$a_{52}$	$a_{53}$	$\beta$
$Z$	$a_{61}$	$a_{62}$	$a_{63}$	$a_{64}$	$a_{65}$	$a_{66}$	$a_{67}$	$a_{68}$	$a_{69}$	$a_{60}$	$a_{61}$	$a_{62}$	$a_{63}$	$Z$
$F_y$	$a_{71}$	$a_{72}$	$a_{73}$	$a_{74}$	$a_{75}$	$a_{76}$	$a_{77}$	$a_{78}$	$a_{79}$	$a_{70}$	$a_{71}$	$a_{72}$	$a_{73}$	$F_y$
$M_\gamma$	$a_{81}$	$a_{82}$	$a_{83}$	$a_{84}$	$a_{85}$	$a_{86}$	$a_{87}$	$a_{88}$	$a_{89}$	$a_{80}$	$a_{81}$	$a_{82}$	$a_{83}$	$M_\gamma$
$M_\alpha$	$a_{91}$	$a_{92}$	$a_{93}$	$a_{94}$	$a_{95}$	$a_{96}$	$a_{97}$	$a_{98}$	$a_{99}$	$a_{90}$	$a_{91}$	$a_{92}$	$a_{93}$	$M_\alpha$
$\alpha$	$a_{01}$	$a_{02}$	$a_{03}$	$a_{04}$	$a_{05}$	$a_{06}$	$a_{07}$	$a_{08}$	$a_{09}$	$a_{00}$	$a_{01}$	$a_{02}$	$a_{03}$	$\alpha$
$\gamma$	$a_{11}$	$a_{12}$	$a_{13}$	$a_{14}$	$a_{15}$	$a_{16}$	$a_{17}$	$a_{18}$	$a_{19}$	$a_{10}$	$a_{11}$	$a_{12}$	$a_{13}$	$\gamma$
$y$	$a_{21}$	$a_{22}$	$a_{23}$	$a_{24}$	$a_{25}$	$a_{26}$	$a_{27}$	$a_{28}$	$a_{29}$	$a_{20}$	$a_{21}$	$a_{22}$	$a_{23}$	$y$
$Q$	$a_{31}$	$a_{32}$	$a_{33}$	$a_{34}$	$a_{35}$	$a_{36}$	$a_{37}$	$a_{38}$	$a_{39}$	$a_{30}$	$a_{31}$	$a_{32}$	$a_{33}$	$Q$

Aft Rotor

Fwd Rotor

To solve for the unknown quantities at the forward rotor, consider the boundary conditions of the forward and aft rotor as part of its corresponding column matrix and then, simplify the solution. As an example, consider a free-free beam; the boundary conditions are defined by making all external loads equal to zero. Therefore, the matrix can be written as,

0	$a_{14}$	$a_{15}$	$a_{16}$	$a_{1\bar{0}}$	$a_{1\bar{1}}$	$a_{1\bar{2}}$	$a_{1\bar{3}}$	X
0	$a_{24}$	$a_{25}$	$a_{26}$	$a_{2\bar{0}}$	$a_{2\bar{1}}$	$a_{2\bar{2}}$	$a_{2\bar{3}}$	$\beta$
0	$a_{34}$	$a_{35}$	$a_{36}$	$a_{3\bar{0}}$	$a_{3\bar{1}}$	$a_{3\bar{2}}$	$a_{3\bar{3}}$	Z
X	$a_{44}$	$a_{45}$	$a_{46}$	$a_{4\bar{0}}$	$a_{4\bar{1}}$	$a_{4\bar{2}}$	$a_{4\bar{3}}$	$\alpha$
$\beta$	$a_{54}$	$a_{55}$	$a_{56}$	$a_{5\bar{0}}$	$a_{5\bar{1}}$	$a_{5\bar{2}}$	$a_{5\bar{3}}$	$\gamma$
Z	$a_{64}$	$a_{65}$	$a_{66}$	$a_{6\bar{0}}$	$a_{6\bar{1}}$	$a_{6\bar{2}}$	$a_{6\bar{3}}$	y
0	$a_{74}$	$a_{75}$	$a_{76}$	$a_{7\bar{0}}$	$a_{7\bar{1}}$	$a_{7\bar{2}}$	$a_{7\bar{3}}$	Q
0	$a_{84}$	$a_{85}$	$a_{86}$	$a_{8\bar{0}}$	$a_{8\bar{1}}$	$a_{8\bar{2}}$	$a_{8\bar{3}}$	
0	$a_{94}$	$a_{95}$	$a_{96}$	$a_{9\bar{0}}$	$a_{9\bar{1}}$	$a_{9\bar{2}}$	$a_{9\bar{3}}$	
$\alpha$	$a_{04}$	$a_{05}$	$a_{06}$	$a_{0\bar{0}}$	$a_{0\bar{1}}$	$a_{0\bar{2}}$	$a_{0\bar{3}}$	
$\gamma$	$a_{14}$	$a_{15}$	$a_{16}$	$a_{1\bar{0}}$	$a_{1\bar{1}}$	$a_{1\bar{2}}$	$a_{1\bar{3}}$	
y	$a_{24}$	$a_{25}$	$a_{26}$	$a_{2\bar{0}}$	$a_{2\bar{1}}$	$a_{2\bar{2}}$	$a_{2\bar{3}}$	
Q	$a_{34}$	$a_{35}$	$a_{36}$	$a_{3\bar{0}}$	$a_{3\bar{1}}$	$a_{3\bar{2}}$	$a_{3\bar{3}}$	

Now, the general solution considers only the equations which are equal to zero. Therefore the boundary conditions can be represented by six linear equations. The matrix for the free-free beam becomes,

0	$a_{14}$	$a_{15}$	$a_{16}$	$a_{1\bar{0}}$	$a_{1\bar{1}}$	$a_{1\bar{2}}$	$a_{1\bar{3}}$	X
0	$a_{24}$	$a_{25}$	$a_{26}$	$a_{2\bar{0}}$	$a_{2\bar{1}}$	$a_{2\bar{2}}$	$a_{2\bar{3}}$	$\beta$
0	$a_{34}$	$a_{35}$	$a_{36}$	$a_{3\bar{0}}$	$a_{3\bar{1}}$	$a_{3\bar{2}}$	$a_{3\bar{3}}$	Z
0	$a_{74}$	$a_{75}$	$a_{76}$	$a_{7\bar{0}}$	$a_{7\bar{1}}$	$a_{7\bar{2}}$	$a_{7\bar{3}}$	$\alpha$
0	$a_{84}$	$a_{85}$	$a_{86}$	$a_{8\bar{0}}$	$a_{8\bar{1}}$	$a_{8\bar{2}}$	$a_{8\bar{3}}$	$\gamma$
0	$a_{94}$	$a_{95}$	$a_{96}$	$a_{9\bar{0}}$	$a_{9\bar{1}}$	$a_{9\bar{2}}$	$a_{9\bar{3}}$	y
								Q

The 6 x 6 boundary condition matrix may be obtained directly by considering only the elements common to rows of zero boundary at the aft rotor and to columns of non-zero boundary condition at fwd rotor. Considering the use of this procedure in the free-free beam case:

0				$a_{14}$	$a_{15}$	$a_{16}$				$a_{1\bar{0}}$	$a_{1\bar{1}}$	$a_{1\bar{2}}$	$a_{1\bar{3}}$	0
0				$a_{24}$	$a_{25}$	$a_{26}$				$a_{2\bar{0}}$	$a_{2\bar{1}}$	$a_{2\bar{2}}$	$a_{2\bar{3}}$	0
0				$a_{34}$	$a_{35}$	$a_{36}$				$a_{3\bar{0}}$	$a_{3\bar{1}}$	$a_{3\bar{2}}$	$a_{3\bar{3}}$	0
X														X
$\beta$														$\beta$
Z														Z
0	=			$a_{74}$	$a_{75}$	$a_{76}$				$a_{7\bar{0}}$	$a_{7\bar{1}}$	$a_{7\bar{2}}$	$a_{7\bar{3}}$	0
0				$a_{84}$	$a_{85}$	$a_{86}$				$a_{8\bar{0}}$	$a_{8\bar{1}}$	$a_{8\bar{2}}$	$a_{8\bar{3}}$	0
0				$a_{94}$	$a_{95}$	$a_{96}$				$a_{9\bar{0}}$	$a_{9\bar{1}}$	$a_{9\bar{2}}$	$a_{9\bar{3}}$	0
$\alpha$														$\alpha$
$\gamma$														$\gamma$
y														y
Q														Q

Aft Rotor Fwd Rotor

Continuing, the matrix can be rewritten in terms of Q which is a known value for the free-free beam,

$$\begin{bmatrix} a_{14} & a_{15} & a_{16} & a_{1\bar{0}} & a_{1\bar{1}} & a_{1\bar{2}} \\ a_{24} & a_{25} & a_{26} & a_{2\bar{0}} & a_{2\bar{1}} & a_{2\bar{2}} \\ a_{34} & a_{35} & a_{36} & a_{3\bar{0}} & a_{3\bar{1}} & a_{3\bar{2}} \\ a_{74} & a_{75} & a_{76} & a_{7\bar{0}} & a_{7\bar{1}} & a_{7\bar{2}} \\ a_{84} & a_{85} & a_{86} & a_{8\bar{0}} & a_{8\bar{1}} & a_{8\bar{2}} \\ a_{94} & a_{95} & a_{96} & a_{9\bar{0}} & a_{9\bar{1}} & a_{9\bar{2}} \end{bmatrix} \cdot \begin{bmatrix} X \\ \beta \\ Z \\ \alpha \\ \gamma \\ y \end{bmatrix} = -Q \begin{bmatrix} a_{1\bar{3}} \\ a_{2\bar{3}} \\ a_{3\bar{3}} \\ a_{7\bar{3}} \\ a_{8\bar{3}} \\ a_{9\bar{3}} \end{bmatrix}$$

The equations can now be solved for the unknown values by inversion of the square matrix. The solution for the free-free beam can be written as,

$$\begin{bmatrix} X \\ \beta \\ Z \\ \alpha \\ \gamma \\ y \end{bmatrix} = -Q^{-1} \begin{bmatrix} a_{1\bar{3}} \\ a_{2\bar{3}} \\ a_{3\bar{3}} \\ a_{7\bar{3}} \\ a_{8\bar{3}} \\ a_{9\bar{3}} \end{bmatrix}$$

Following evaluation of the fwd rotor boundary conditions the forced mode shape at each station is obtained by progressive matrix multiplication and print-out starting with the known column elements.

APPENDIX D

COUPLED, DAMPED MODE ASSOCIATED MATRIX  
DERIVATION AND METHOD OF SOLUTION

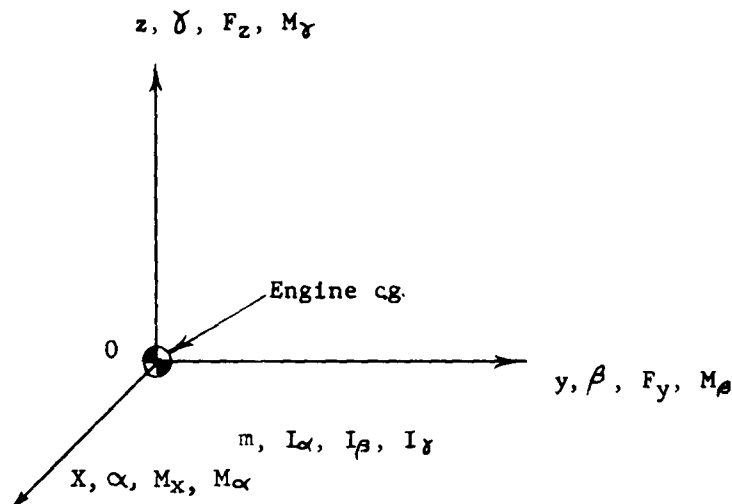
#### A. Matrices Derived in Appendix C

The matrices previously derived in Appendix C in a 13 x 13 form are expanded to a 26 x 26 form to obtain damped response. The matrices are presented in the following order:

- (1) discrete mass, (2) suspended mass, (3) shift, (4) vertical bend,
- (5) elastic, (6) frame racking, (7) concentrated spring, (8) ground spring, (9) force

#### B. Development of Engine Matrix and Engine Response

Consider an engine flexibly mounted to a fuselage system. The mass properties of the engine and its center of gravity are shown.



$x, y, z$	Fuselage Translational Displacements
$\alpha, \beta, \gamma$	Fuselage Angular Displacements
$F_x, F_y, F_z$	Fuselage Forces
$M_\alpha, M_\beta, M_\gamma$	Fuselage Moments
$m, I_\alpha, I_\beta, I_\gamma$	Engine Mass Properties

Now assume the engine center of gravity is displaced in six directions and in the same sense as fuselage displacements.

$x_e, y_e, z_e$	Engine Translational Displacements
$\alpha_e, \beta_e, \gamma_e$	Engine Angular Displacements



MASS MATRIX

$F_z$	$M_\beta$	$F_x$	$x$	$\beta$	$z$	$F_y$	$M_\gamma$	$M_\alpha$	$\alpha$	$\gamma$	$Q$	$F_z$	$M_\beta$	$F_x$	$x$	$\beta$	$z$	$F_y$	$M_\gamma$	$M_\alpha$	$\alpha$	$\gamma$	$Q$
1																							
	1																						
		1																					
			1																				
				1																			
					1																		
						1																	
							1																
								1															
									1														
										1													
											1												
												1											
													1										
														1									
															1								
																1							
																	1						
																		1					
																			1				
																				1			
																					1		
																						1	
																							1



# SHIFT MATRIX

P	M <sub>P</sub>	P <sub>z</sub>	x	y	z	P <sub>y</sub>	M <sub>y</sub>	M <sub>z</sub>	α	β	γ	Q	P <sub>x</sub>	M <sub>x</sub>	P <sub>x</sub>	x	y	z	P <sub>y</sub>	M <sub>y</sub>	M <sub>z</sub>	α	β	γ	Q
1																									1
a	1	-c																							
		1																							
			1	c																					
				1																					
					1																				
						1																			
							1																		
								1																	
									1																
										1															
											1														
												1													
													1												
														1											
															1										
																1									
																	1								
																		1							
																			1						
																				1					
																					1				
																						1			
																							1		
																								1	
																									1

VERTICAL BEND MATRIX

$E_z$	$H_y$	$E_x$	$X$	$\beta$	$Z$	$E_y$	$H_x$	$H_z$	$\alpha$	$\gamma$	$Q$	$E_z$	$H_y$	$E_x$	$X$	$\beta$	$Z$	$E_y$	$H_x$	$H_z$	$\alpha$	$\gamma$	$Q$
$\cos \beta$		$\sin \beta$																					1
	1																						
$-\sin \beta$		$\cos \beta$																					
			$\cos \beta$	$-\sin \beta$																			
				1																			
		$\sin \beta$		$\cos \beta$																			
					1																		
						$\cos \beta$	$\sin \beta$																
						$-\sin \beta$	$\cos \beta$																
								$\cos \beta$	$-\sin \beta$														
										$\cos \beta$	$\sin \beta$												
										$\sin \beta$	$\cos \beta$												
												1											
													1										
														1									
															$\cos \beta$	$-\sin \beta$							
																	$\cos \beta$	$\sin \beta$					
																			$\cos \beta$	$-\sin \beta$			
																					$\cos \beta$	$\sin \beta$	
																							1

[illegible]

[illegible]

$E$	$M_A$	$F_K$	$X$	$\beta$	$Z$	$F_2$	$M_f$	$M_m$	$\alpha$	$\gamma$	$y$	$Q$	$E$	$M_f$	$F_K$	$X$	$\beta$	$Z$	$F_2$	$M_f$	$M_m$	$\alpha$	$\gamma$	$y$	$Q$
-----	-------	-------	-----	---------	-----	-------	-------	-------	----------	----------	-----	-----	-----	-------	-------	-----	---------	-----	-------	-------	-------	----------	----------	-----	-----

CONCENTRATED SPRING MATRIX

$F_z$	$M_y$	$F_x$	$x$	$\theta$	$z$	$F_y$	$M_x$	$M_z$	$\alpha$	$\gamma$	$y$	$Q$	$F_z$	$M_y$	$F_x$	$x$	$\theta$	$z$	$F_y$	$M_x$	$M_z$	$\alpha$	$\gamma$	$y$	$Q$
1																									1
	1																								
		1																							
			1																						
				1																					
					1																				
						1																			
							1																		
								1																	
									1																
										1															
											1														
												1													
													1												
														1											
															1										
																1									
																	1								
																		1							
																			1						
																				1					
																					1				
																						1			
																							1		
																								1	
																									1

GROUND SPINING MATRIX

$P_z$	$M_y$	$P_x$	$x$	$\rho$	$z$	$P_y$	$M_x$	$M_z$	$\alpha$	$\beta$	$\gamma$	$Q$	$P_z$	$M_y$	$P_x$	$x$	$\rho$	$z$	$P_y$	$M_x$	$M_z$	$\alpha$	$\beta$	$\gamma$	$Q$
1																									1
	1																								
		1																							
			1																						
				1																					
					1																				
						1																			
							1																		
								1																	
									1																
										1															
											1														
												1													
													1												
														1											
															1										
																1									
																	1								
																		1							
																			1						
																				1					
																					1				
																						1			
																							1		
																								1	
																									1



**FORCE MATRIX**

[illegible]

For simplicity, let

$m_1 = m$	$f_1 = z$	$e_1 = z$	$F_1 = F_z$
$m_2 = I_\theta$	$f_2 = \theta$	$e_2 = \theta_e$	$F_2 = M_\theta$
$m_3 = m$	$f_3 = x$	$e_3 = x_e$	$F_3 = F_x$
$m_4 = m$	$f_4 = y$	$e_4 = y_e$	$F_4 = F_y$
$m_5 = I_\gamma$	$f_5 = \gamma$	$e_5 = \gamma_e$	$F_5 = M_\gamma$
$m_6 = I_\alpha$	$f_6 = \alpha$	$e_6 = \alpha_e$	$F_6 = M_\alpha$

The kinetic energy of the system is

$$T = 1/2 \sum_i m_i (\dot{f}_i + \dot{e}_i)^2$$

Natural frequencies and normal modes of the engine are introduced:

$r$  Engine Mode Number

$\omega_r$  Engine Natural Frequency

$e_i^{(r)}$  Engine Normal Modes

Engine displacements are written in terms of normal modes and generalized coordinates.

$$e_i = \sum_r e_i^{(r)} H_r$$

Where  $H_r$  is the engine generalized coordinate ignoring damping, the Lagrange operations readily yields the equations of motion for the oscillating system.

$$\begin{aligned} f_i: \quad m_i \ddot{f}_i + \sum_r \sigma_i^{(r)} \ddot{H}_r &= F_i \\ H_r: \quad M_r \ddot{H}_r + K_r H + \sum_i \sigma_i^{(r)} \ddot{f}_i &= 0 \end{aligned}$$

where

$$\begin{aligned} M_r &= \sum_i m_i e_i^{(r)2} \\ K_r &= M_r \omega_r^2 \\ \sigma_i^{(r)} &= m_i e_i^{(r)} \end{aligned}$$

Dampers are denoted by  $C_i$ . Damping energy is given by

$$D = 1/2 \sum_i C_i \dot{e}_i^2$$

The final equations of motion including damping are

$$\begin{aligned} f_i: \quad m_i \ddot{f}_i + \sum_r \sigma_i^{(r)} \ddot{H}_r &= F_i \\ H_r: \quad M_r \ddot{H}_r + C_r \dot{H}_r + K_r H_r + \sum_i \sigma_i^{(r)} \ddot{f}_i &= 0 \end{aligned}$$

Intermodal coupling due to damping is omitted.

Since  $f_i$  is of the form:

$$\text{then } f_i = f_{ic} \cos \omega t + f_{is} \sin \omega t$$

$$H_r = H_{rc} \cos \omega t + H_{rs} \sin \omega t$$

where

$$\begin{aligned} H_{rc} &= \sum_i \frac{\sigma_i^{(r)}}{M_r} \left[ \frac{\omega^2}{(\omega_r^2 - \omega^2)^2 + (\lambda_r \omega)^2} \right] [(\omega_r^2 - \omega^2) f_{ic} - (\lambda_r \omega) f_{is}] \\ H_{rs} &= \sum_i \frac{\sigma_i^{(r)}}{M_r} \left[ \frac{\omega^2}{(\omega_r^2 - \omega^2)^2 + (\lambda_r \omega)^2} \right] [(\omega_r^2 - \omega^2) f_{is} + (\lambda_r \omega) f_{ic}] \end{aligned}$$

$$\omega_r^2 = \frac{K_r}{M_r}$$

$$C_r = \sum_i m_i e_i^{(r)^2} \quad \lambda_r = \frac{C_r}{M_r}$$

Substituting,

$$\begin{aligned} f_i: \quad m_i \ddot{f}_i &= \sum_r \sigma_i^{(r)} \sum_{j=1}^6 \frac{\sigma_j^{(r)}}{M_r} \left[ \frac{\omega^4}{(\omega_r^2 - \omega^2)^2 + (\lambda_r \omega)^2} \right] [(\omega_r^2 - \omega^2) f_{jc} - (\lambda_r \omega) f_{js}] \cos \omega t \\ &- \sum_r \sigma_i^{(r)} \sum_{j=1}^6 \frac{\sigma_j^{(r)}}{M_r} \left[ \frac{\omega^4}{(\omega_r^2 - \omega^2)^2 + (\lambda_r \omega)^2} \right] [(\omega_r^2 - \omega^2) f_{js} + (\lambda_r \omega) f_{jc}] \sin \omega t = F_i \end{aligned}$$

Or

$$\begin{aligned} f_i: \quad F_{ic} + \sum_{j=1}^6 (a_{ij} f_{jc} - b_{ij} f_{js}) &= 0 \\ F_{is} + \sum_{j=1}^6 (b_{ij} f_{jc} + a_{ij} f_{js}) &= 0 \end{aligned}$$

where

$$\begin{aligned} a_{ij} &= m_i \omega^2 + \sum_r \frac{\sigma_i^{(r)} \sigma_j^{(r)}}{M_r} \left[ \frac{\omega^4}{(\omega_r^2 - \omega^2)^2 + (\lambda_r \omega)^2} \right] (\omega_r^2 - \omega^2) \\ b_{ij} &= \sum_r \frac{\sigma_i^{(r)} \sigma_j^{(r)}}{M_r} \left[ \frac{\omega^4}{(\omega_r^2 - \omega^2)^2 + (\lambda_r \omega)^2} \right] (\lambda_r \omega) \end{aligned}$$

$$m_{ij} = m_i \quad \text{For } i = j \quad ; \quad m_{ij} = 0 \quad \text{For } i \neq j$$

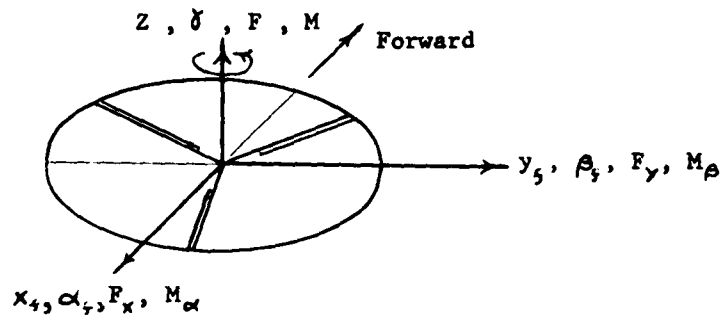
## ENGINE MATRIX

$F_{2c}$	$M_{\beta c}$	$F_{xc}$	$\beta_c$	$Z_c$	$F_{yc}$	$M_{\gamma c}$	$\alpha_c$	$\delta_c$	$\gamma_c$	$1$	$F_{2s}$	$M_{\beta s}$	$F_{xs}$	$x_s$	$\beta_s$	$Z_s$	$F_{ys}$	$M_{\gamma s}$	$\alpha_s$	$\delta_s$	$\gamma_s$	$1$		
1			$a_{13}$	$a_{12}$	$a_{11}$		$a_{16}$	$a_{15}$	$a_{14}$					$-b_{13}$	$-b_{12}$	$-b_{11}$				$-b$	$-b$	$-b$		
	1		$a_{23}$	$a_{22}$	$a_{21}$		$a_{26}$	$a_{25}$	$a_{24}$					$-b_{23}$	$-b_{22}$	$-b_{21}$				$-b$	$-b$	$-b$		
		1	$a_{33}$	$a_{32}$	$a_{31}$		$a_{36}$	$a_{35}$	$a_{34}$					$-b_{33}$	$-b_{32}$	$-b_{31}$				$-b$	$-b$	$-b$		
			1																					
				1																				
			$a_{43}$	$a_{42}$	$a_{41}$	1	$a_{46}$	$a_{45}$	$a_{44}$					$-b_{43}$	$-b_{42}$	$-b_{41}$				$-b$	$-b$	$-b$		
			$a_{53}$	$a_{52}$	$a_{51}$		$a_{56}$	$a_{55}$	$a_{54}$					$-b_{53}$	$-b_{52}$	$-b_{51}$				$-b$	$-b$	$-b$		
			$a_{63}$	$a_{62}$	$a_{61}$		$a_{66}$	$a_{65}$	$a_{64}$					$-b_{63}$	$-b_{62}$	$-b_{61}$				$-b$	$-b$	$-b$		
							1																	
								1																
									1															
			$b_{13}$	$b_{12}$	$b_{11}$		$b_{16}$	$b_{15}$	$b_{14}$			1		$a_{13}$	$a_{12}$	$a_{11}$				$a_{43}$	$a_{42}$	$a_{41}$		
			$b_{23}$	$b_{22}$	$b_{21}$		$b_{26}$	$b_{25}$	$b_{24}$				1	$a_{23}$	$a_{22}$	$a_{21}$				$a_{53}$	$a_{52}$	$a_{51}$		
			$b_{33}$	$b_{32}$	$b_{31}$		$b_{36}$	$b_{35}$	$b_{34}$					1	$a_{33}$	$a_{32}$	$a_{31}$				$a_{63}$	$a_{62}$	$a_{61}$	
															1									
																1								
			$b_{43}$	$b_{42}$	$b_{41}$		$b_{46}$	$b_{45}$	$b_{44}$					$a_{43}$	$a_{42}$	$a_{41}$	1			$a_{46}$	$a_{45}$	$a_{44}$		
			$b_{53}$	$b_{52}$	$b_{51}$		$b_{56}$	$b_{55}$	$b_{54}$					$a_{53}$	$a_{52}$	$a_{51}$		1		$a_{56}$	$a_{55}$	$a_{54}$		
			$b_{63}$	$b_{62}$	$b_{61}$		$b_{66}$	$b_{65}$	$b_{64}$					$a_{63}$	$a_{62}$	$a_{61}$			1	$a_{66}$	$a_{65}$	$a_{64}$		
																				1				
																					1			
																						1		
																							1	

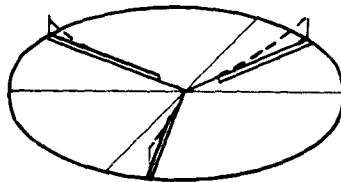
### C. Rotor Matrix Derivation

#### Rotor System Modes

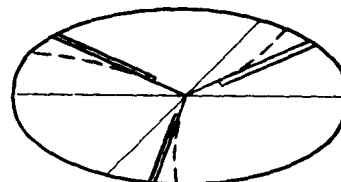
Consider a three-blade rotating hub which is displaced  $x, y, z, \alpha, \beta, \gamma$ , in the fixed system by the force vector  $F_x, F_y, F_z, M_\alpha, M_\beta, M_\gamma$ .



Also allow each flexible blade to flap and lag.



Flapping Blades  
in Vertical Plane



Lagging Blades  
in Horizontal Plane

The complete forces and moments at the rotor hub are

$$F_x = F_{xc} \cos \omega t + F_{xs} \sin \omega t$$

$$F_y = F_{yc} \cos \omega t + F_{ys} \sin \omega t$$

$$F_z = F_{zc} \cos \omega t + F_{zs} \sin \omega t$$

$$M_\alpha = M_{\alpha c} \cos \omega t + M_{\alpha s} \sin \omega t$$

$$M_\beta = M_{\beta c} \cos \omega t + M_{\beta s} \sin \omega t$$

$$M_\gamma = M_{\gamma c} \cos \omega t + M_{\gamma s} \sin \omega t$$

The forced response is

$$x = x_c \cos \omega t + x_s \sin \omega t$$

$$y = y_c \cos \omega t + y_s \sin \omega t$$

$$z = z_c \cos \omega t + y_c \sin \omega t$$

$$\alpha = \alpha_c \cos \omega t + \alpha_s \sin \omega t$$

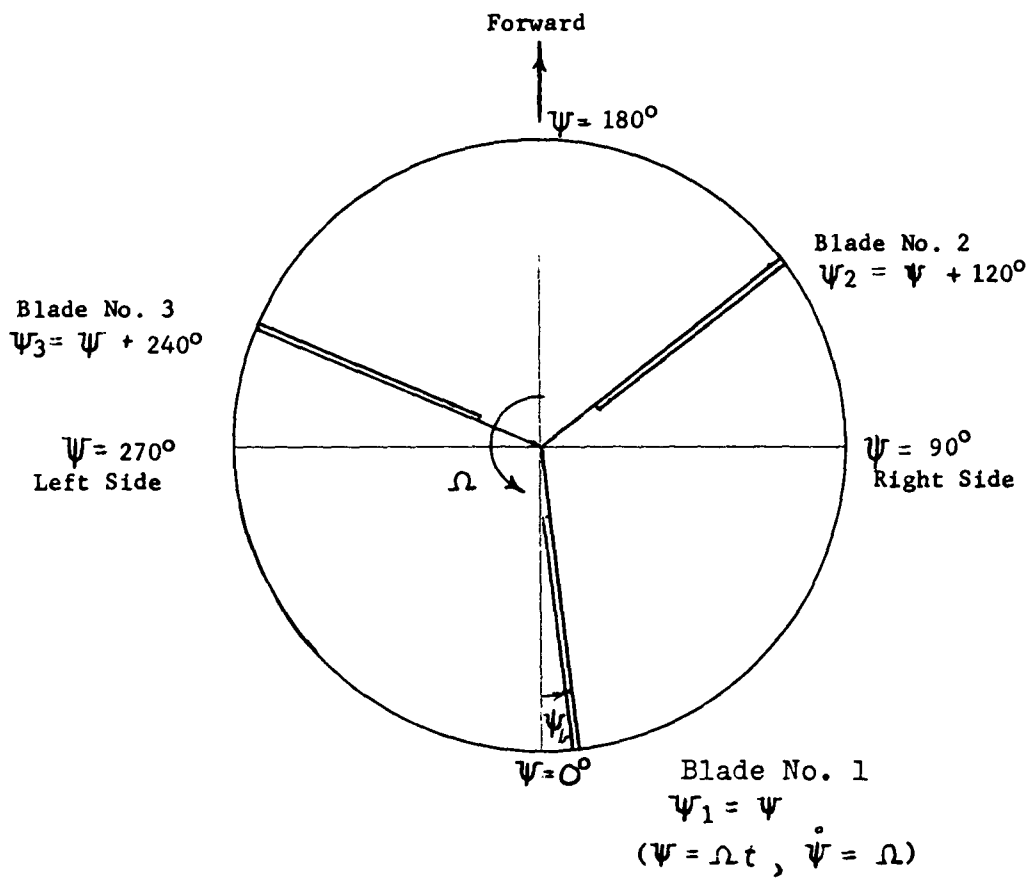
$$\beta = \beta_c \cos \omega t + \beta_s \sin \omega t$$

$$\delta = \delta_c \cos \omega t + \delta_s \sin \omega t$$

Note that frequency of exciting forces and displacements at rotor hub both occur at forced frequency  $\omega$ .

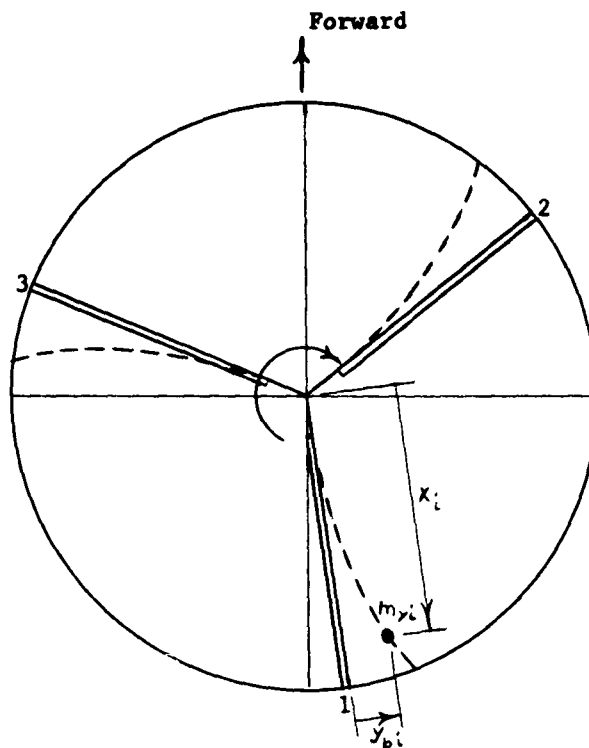
Symbols, sign convention and blade number pattern are shown in plan view of rotor system.

#### FIXED BLADE



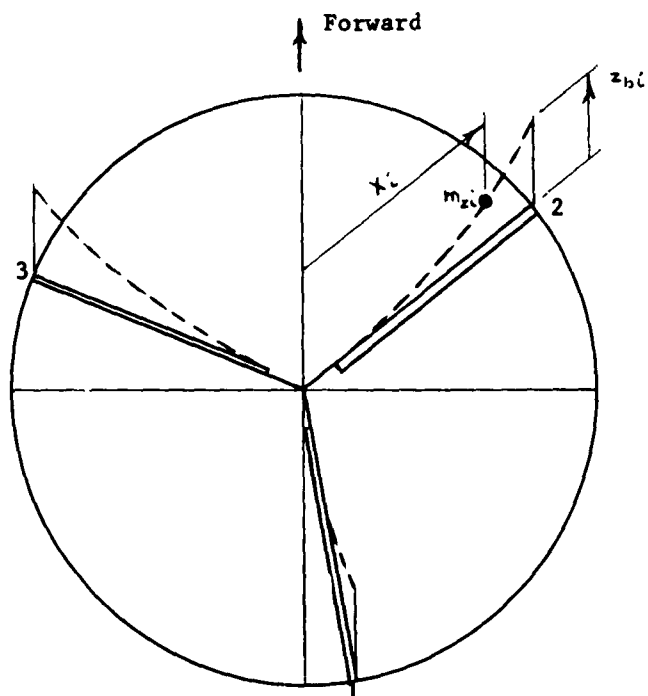
$\psi_b$  = Azimuth Position of Blade Number b

# Lagging Blades



$y_{bi}$  = Total lag bending of blade number  $b$  at mass station  $i$

## Flapping Blades



$z_{bi}$  = Total flap bending of blade number  $b$  at mass station  $i$

The general displacements of mass  $m_i$  are

$$\begin{aligned}x_i &= x_i \cos \beta \cos \gamma \cos \psi_b + x - (x_i \delta + y_{bi}) \sin \psi_b - \delta y_{bi} \cos \psi_b + z_{bi} \beta \\y_i &= x_i \cos \alpha \cos \gamma \sin \psi_b + y + (x_i \delta + y_{bi}) \cos \psi_b - \delta y_{bi} \sin \psi_b - z_{bi} \alpha \\z_i &= z_{bi} + Z + x_i \alpha \sin \psi_b - x_i \beta \cos \psi_b\end{aligned}$$

Terms of higher order than two are omitted since they do not produce linear terms in the final equations of motion. In addition, small angle assumptions of the form

$$\begin{aligned}\cos \Theta &= 1 \\ \sin \Theta &= \Theta\end{aligned}$$

are valid here except in the first terms of the displacements. Cosines are retained because no oscillation variable is present to increase its order to three, i.e.

$$\alpha \cos \Theta = \alpha (1 - 1/2 \Theta^2) \approx \alpha$$

The velocities are obtained by differentiating.

$$\begin{aligned}\dot{x}_i &= -x_i \Omega \cos \beta \cos \gamma \sin \psi_b + \dot{x} - (x_i \dot{\delta} + \dot{y}_{bi}) \sin \psi_b - \Omega (x_i \delta + y_{bi}) \cos \psi_b \\ &\quad - (\delta \dot{y}_{bi}) \cos \psi_b + \Omega \delta y_{bi} \sin \psi_b + (\beta \dot{z}_{bi}) \\ \dot{y}_i &= x_i \Omega \cos \alpha \cos \gamma \cos \psi_b + \dot{y} + (x_i \dot{\delta} + \dot{y}_{bi}) \cos \psi_b - \Omega (x_i \delta + y_{bi}) \sin \psi_b \\ &\quad - (\delta \dot{y}_{bi}) \sin \psi_b - \Omega \delta y_{bi} \cos \psi_b - (\alpha \dot{z}_{bi}) \\ \dot{z}_i &= \dot{z} + \dot{z}_{bi} + x_i (\Omega \alpha - \dot{\beta}) \cos \psi_b + x_i (\Omega \beta + \dot{\alpha}) \sin \psi_b\end{aligned}$$

Normal modes of the rotor blade in flap and lag motion are included by the substitution

$$\begin{aligned}z_{bi} &= \sum_r z_i^{(r)} Z_{br} \\ y_{bi} &= \sum_r y_i^{(r)} Y_{br}\end{aligned}$$

The blade generalized coordinates are  $Z_{br}$  and  $Y_{br}$ . For simplicity, only the 2<sup>th</sup> mode is shown in the kinetic energy.



$$\sum_b \cos \psi_b = 0$$

$$\sum_b \cos (\omega t + \psi_b) = 0$$

$$\sum_b \sin \psi_b = 0$$

$$\sum_b \sin (\omega t + \psi_b) = 0$$

$$\sum_b \cos^2 \psi_b = 3/2$$

$$\sum_b \cos (\omega t - \psi_b) = 0$$

$$\sum_b \sin^2 \psi_b = 3/2$$

$$\sum_b \sin (\omega t - \psi_b) = 0$$

$$\cos \omega t \cos \psi_b = 1/2 \cos (\omega t + \psi_b) + 1/2 \cos (\omega t - \psi_b)$$

$$\cos \omega t \sin \psi_b = 1/2 \sin (\omega t + \psi_b) - 1/2 \sin (\omega t - \psi_b)$$

$$\sin \omega t \cos \psi_b = 1/2 \sin (\omega t + \psi_b) + 1/2 \sin (\omega t - \psi_b)$$

$$\sin \omega t \sin \psi_b = -1/2 \cos (\omega t + \psi_b) + 1/2 \cos (\omega t - \psi_b)$$

$$\sum_b \cos \omega t \cos \psi_b = 0$$

$$\sum_b \sin \omega t \cos \psi_b = 0$$

$$\sum_b \cos (\omega t + \psi_b) \cos = 3/2 \cos \omega t$$

$$\sum_b \sin (\omega t + \psi_b) \cos = 3/2 \sin \omega t$$

$$\sum_b \cos (\omega t - \psi_b) \cos = 3/2 \cos \omega t$$

$$\sum_b \sin (\omega t - \psi_b) \cos = 3/2 \sin \omega t$$

$$\sum_b \cos \omega t \sin \psi_b = 0$$

$$\sum_b \sin \omega t \sin \psi_b = 0$$

$$\sum_b \cos (\omega t + \psi_b) \sin \psi_b = -3/2 \sin \omega t$$

$$\sum_b \sin (\omega t + \psi_b) \sin \psi_b = 3/2 \cos \omega t$$

$$\sum_b \cos (\omega t - \psi_b) \sin \psi_b = 3/2 \sin \omega t$$

$$\sum_b \sin (\omega t - \psi_b) \sin \psi_b = -3/2 \cos \omega t$$

The kinetic energy of three (3) blades is

$$T = \frac{1}{2} \sum_b \sum_i m_i (\dot{x}_f^2 + \dot{y}_f^2 + \dot{z}_f^2)$$

In the final expression for the kinetic energy, only the second order terms are retained. Also, terms of individual blades which cancel when summed around the azimuth are dropped. The kinetic energy becomes

$$\begin{aligned} T = & \frac{1}{2} \left\{ 3m_z \dot{Z}^2 + \frac{3}{2} \bar{I}_z (\dot{\alpha}^2 + \dot{\beta}^2 + 2\Omega \dot{\alpha} \dot{\beta} - 2\Omega \dot{\alpha} \dot{\beta}) \right\} \\ & + \frac{1}{2} \sum_b \left\{ \bar{I}_{zr} \dot{Z}_{br}^2 + 2\sigma_{zr} \dot{Z} \dot{Z}_{br} + 2\sigma_{xzr} (\dot{\alpha} \dot{Z}_{br} - \Omega \dot{\beta} Z_{br}) \sin \psi_b \right. \\ & \quad \left. - 2\sigma_{xzr} (\dot{\beta} \dot{Z}_{br} + \Omega \dot{\alpha} Z_{br}) \cos \psi_b \right\} \\ & + \frac{1}{2} \left\{ 3m_y (\dot{x}^2 + \dot{y}^2) + 3\bar{I}_y \dot{\gamma}^2 \right\} \\ & + \frac{1}{2} \sum_b \left\{ \bar{I}_{yr} \dot{Y}_{br}^2 + 2\sigma_{xyr} \dot{\gamma} \dot{Y}_{br} \right. \\ & \quad \left. - 2\sigma_{yrx} (\dot{Y}_{br} \sin \psi_b + \Omega Y_{br} \cos \psi_b) \right. \\ & \quad \left. + 2\sigma_{yry} (\dot{Y}_{br} \cos \psi_b - \Omega Y_{br} \sin \psi_b) \right\} \end{aligned}$$

The LaGrange equations representing coupled hub-blade motion are shown

$$\begin{aligned} Z : & \quad 3m_z \ddot{Z} + \sigma_{zr} \sum_b \ddot{Z}_{br} = F_z \\ \alpha : & \quad \frac{3}{2} \bar{I}_z (\ddot{\alpha} + 2\Omega \dot{\beta}) + \sigma_{xzr} \sum_b (\ddot{Z}_{br} + \Omega^2 Z_{br}) \sin \psi_b = M_\alpha \\ \beta : & \quad \frac{3}{2} \bar{I}_z (\ddot{\beta} - 2\Omega \dot{\alpha}) - \sigma_{xzr} \sum_b (\ddot{Z}_{br} + \Omega^2 Z_{br}) \cos \psi_b = M_\beta \\ Z_{br} : & \quad \bar{I}_{zr} \ddot{Z}_{br} + K_{zr} Z_{br} + \sigma_{zr} \ddot{Z} + \sigma_{xzr} (\ddot{\alpha} + 2\Omega \dot{\beta}) \sin \psi_b - \sigma_{xzr} (\dot{\beta} - 2\Omega \dot{\alpha}) \cos \psi_b = 0 \\ x : & \quad 3m_y \ddot{x} - \sigma_{yrx} \frac{d^2}{dt^2} \sum_b Y_{br} \sin \psi_b = F_x \\ y : & \quad 3m_y \ddot{y} + \sigma_{yry} \frac{d^2}{dt^2} \sum_b Y_{br} \cos \psi_b = F_y \\ \gamma : & \quad 3\bar{I}_y \ddot{\gamma} + \sigma_{xyr} \sum_b \ddot{Y}_{br} = M_\gamma \\ Y_{br} : & \quad \bar{I}_{yr} \ddot{Y}_{br} + K_{yr} Y_{br} + \sigma_{xyr} \ddot{\gamma} - \sigma_{yrx} \ddot{x} \sin \psi_b + \sigma_{yry} \ddot{y} \cos \psi_b = 0 \end{aligned}$$

Solution of a linear-differential equation of the second order without damping term:

$$\ddot{x} + \omega_x^2 x = A \cos \omega t + B \sin \omega t$$

$$x = \frac{A}{\omega_x^2 - \omega^2} \cos \omega t + \frac{B}{\omega_x^2 - \omega^2} \sin \omega t$$

Solution including damping term:

$$\ddot{x} + \lambda \dot{x} + \omega_x^2 x = A \cos \omega t + B \sin \omega t$$

$$x = \frac{A(\omega_x^2 - \omega^2) - B(\lambda \omega)}{(\omega_x^2 - \omega^2)^2 + (\lambda \omega)^2} \cos \omega t + \frac{B(\omega_x^2 - \omega^2) + A(\lambda \omega)}{(\omega_x^2 - \omega^2)^2 + (\lambda \omega)^2} \sin \omega t$$

Solution of flap generalized coordinate  $Z_{br}$  :

$$\ddot{I}_{Zr} Z_{br} + K_{Zr} Z_{br} + \sigma_{Zr} \ddot{Z} + \sigma_{xzr} (\ddot{\alpha} + 2\Omega \dot{\beta}) \sin \psi_b - \sigma_{xzr} (\ddot{\beta} - 2\Omega \dot{\alpha}) \cos \psi_b = 0$$

$$\ddot{I}_{Zr} Z_{br} + K_{Zr} Z_{br} + \sigma_{Zr} (-\omega^2 Z_c \cos \omega t - \omega^2 Z_s \sin \omega t) + \sigma_{xzr} \left\{ \begin{array}{l} -\omega^2 \alpha_c \cos \omega t \sin \psi_b - \omega^2 \alpha_s \sin \omega t \sin \psi_b \\ -2\Omega \omega \beta_c \sin \omega t \sin \psi_b + 2\Omega \omega \beta_s \cos \omega t \sin \psi_b \\ +\omega^2 \beta_c \cos \omega t \cos \psi_b + \omega^2 \beta_s \sin \omega t \cos \psi_b \\ -2\Omega \omega \alpha_c \sin \omega t \cos \psi_b + 2\Omega \omega \alpha_s \cos \omega t \cos \psi_b \end{array} \right\} = 0$$

$$\ddot{I}_{Zr} Z_{br} + K_{Zr} Z_{br} = \sigma_{Zr} (\omega^2 Z_c \cos \omega t + \omega^2 Z_s \sin \omega t) + \sigma_{xzr} \left\{ \begin{array}{l} -\frac{1}{2} \omega (\omega + 2\Omega) (\alpha_s + \beta_c) \cos(\omega t + \psi_b) \\ +\frac{1}{2} \omega (\omega + 2\Omega) (\alpha_c - \beta_s) \sin(\omega t + \psi_b) \\ +\frac{1}{2} \omega (\omega - 2\Omega) (\alpha_s - \beta_c) \cos(\omega t - \psi_b) \\ -\frac{1}{2} \omega (\omega - 2\Omega) (\alpha_c + \beta_s) \sin(\omega t - \psi_b) \end{array} \right\}$$

$$\begin{aligned}
Z_{br} = & \frac{\sigma_{zr}}{\bar{I}_{zr}} \left[ \frac{\omega^2}{\omega_{zr}^2 - \omega^2} \right] Z_c \cos \omega t \\
& + \frac{\sigma_{zr}}{\bar{I}_{zr}} \left[ \frac{\omega^2}{\omega_{zr}^2 - \omega^2} \right] Z_s \sin \omega t \\
& - \frac{1}{2} \frac{\sigma_{xzr}}{\bar{I}_{zr}} \left[ \frac{\omega(\omega + 2\Omega)}{\omega_{zr}^2 - (\omega + \Omega)^2} \right] (\alpha_s + \beta_c) \cos(\omega t + \psi_b) \\
& + \frac{1}{2} \frac{\sigma_{xzr}}{\bar{I}_{zr}} \left[ \frac{\omega(\omega + 2\Omega)}{\omega_{zr}^2 - (\omega + \Omega)^2} \right] (\alpha_c - \beta_s) \sin(\omega t + \psi_b) \\
& + \frac{1}{2} \frac{\sigma_{xzr}}{\bar{I}_{zr}} \left[ \frac{\omega(\omega - 2\Omega)}{\omega_{zr}^2 - (\omega - \Omega)^2} \right] (\alpha_s - \beta_c) \cos(\omega t - \psi_b) \\
& - \frac{1}{2} \frac{\sigma_{xzr}}{\bar{I}_{zr}} \left[ \frac{\omega(\omega - 2\Omega)}{\omega_{zr}^2 - (\omega - \Omega)^2} \right] (\alpha_c + \beta_s) \sin(\omega t - \psi_b)
\end{aligned}$$

Solution of lag generalized coordinate  $Y_{br}$  :

$$\begin{aligned}
\bar{I}_{yr} \ddot{Y}_{br} + K_{yr} Y_{br} + \sigma_{xyr} \ddot{x} - \sigma_{yr} \ddot{x} \sin \psi_b \\
+ \sigma_{yr} \ddot{y} \cos \psi_b = 0
\end{aligned}$$

$$\begin{aligned}
\bar{I}_{yr} \ddot{Y}_{br} + K_{yr} Y_{br} + \sigma_{xyr} (-\omega^2 x_c \cos \omega t - \omega^2 x_s \sin \omega t) \\
+ \sigma_{yr} \left\{ \begin{aligned} & \omega^2 x_c \cos \omega t \sin \psi_b + \omega^2 x_s \sin \omega t \sin \psi_b \\ & - \omega^2 y_c \cos \omega t \cos \psi_b - \omega^2 y_s \sin \omega t \cos \psi_b \end{aligned} \right\} = 0
\end{aligned}$$

$$\begin{aligned}
\bar{I}_{yr} \ddot{Y}_{br} + K_{yr} Y_{br} = \sigma_{xyr} (\omega^2 x_c \cos \omega t + \omega^2 x_s \sin \omega t) \\
+ \sigma_{yr} \left\{ \begin{aligned} & \frac{1}{2} \omega^2 (x_s + y_c) \cos(\omega t + \psi_b) \\ & - \frac{1}{2} \omega^2 (x_c - y_s) \sin(\omega t + \psi_b) \\ & - \frac{1}{2} \omega^2 (x_s - y_c) \cos(\omega t - \psi_b) \\ & + \frac{1}{2} \omega^2 (x_c + y_s) \sin(\omega t - \psi_b) \end{aligned} \right\}
\end{aligned}$$

$$\begin{aligned}
Y_{br} = & \frac{\sigma_{xyr}}{\bar{I}_{yr}} \left[ \frac{\omega^2}{\omega_{yr}^2 - \omega^2} \right] \gamma_c \cos \omega t + \frac{\sigma_{xyr}}{\bar{I}_{yr}} \left[ \frac{\omega^2}{\omega_{yr}^2 - \omega^2} \right] \gamma_s \sin \omega t \\
& + \frac{1}{2} \frac{\sigma_{yr}}{\bar{I}_{yr}} \left[ \frac{\omega^2}{\omega_{yr}^2 - (\omega + \Omega)^2} \right] (x_s + y_c) \cos(\omega t + \psi_b) \\
& - \frac{1}{2} \frac{\sigma_{yr}}{\bar{I}_{yr}} \left[ \frac{\omega^2}{\omega_{yr}^2 - (\omega + \Omega)^2} \right] (x_c - y_s) \sin(\omega t + \psi_b) \\
& - \frac{1}{2} \frac{\sigma_{yr}}{\bar{I}_{yr}} \left[ \frac{\omega^2}{\omega_{yr}^2 - (\omega - \Omega)^2} \right] (x_s - y_c) \cos(\omega t - \psi_b) \\
& + \frac{1}{2} \frac{\sigma_{yr}}{\bar{I}_{yr}} \left[ \frac{\omega^2}{\omega_{yr}^2 - (\omega - \Omega)^2} \right] (x_c + y_s) \sin(\omega t - \psi_b)
\end{aligned}$$

Let

$$\begin{aligned}
Y_b = & A \cos \omega t + B \sin \omega t \\
& + C \cos(\omega t + \psi_b) + D \sin(\omega t + \psi_b) \\
& + E \cos(\omega t - \psi_b) + F \sin(\omega t - \psi_b)
\end{aligned}$$

Then

$$\begin{aligned}
\sum_b Y_b &= 3A \cos \omega t + 3B \sin \omega t \\
\sum_b Y_b \cos \psi_b &= \frac{3}{2}(C + E) \cos \omega t + \frac{3}{2}(D + F) \sin \omega t \\
\sum_b Y_b \sin \psi_b &= \frac{3}{2}(D - F) \cos \omega t + \frac{3}{2}(-C + E) \sin \omega t
\end{aligned}$$

evaluation of integrals:

$$\sum_b^{\infty} Z_{br} = -3 \frac{\sigma_{zr}}{\bar{I}_{zr}} \left[ \frac{\omega^4}{\omega_{zr}^2 - \omega^2} \right] (Z_c \cos \omega t + Z_s \sin \omega t)$$

$$\begin{aligned}
\sum_b^{\infty} (Z_{br} + \Omega^2 Z_{br}) \cos \psi_b = & \\
& + \frac{3}{4} \frac{\sigma_{xzr}}{\bar{I}_{zr}} \left\{ \left[ \frac{(\omega^2 + 2\Omega\omega)^2}{\omega_{zr}^2 - (\omega + \Omega)^2} \right] (\alpha_s + \beta_c) - \left[ \frac{(\omega^2 - 2\Omega\omega)^2}{\omega_{zr}^2 - (\omega - \Omega)^2} \right] (\alpha_s - \beta_c) \right\} \cos \omega t \\
& - \frac{3}{4} \frac{\sigma_{xzr}}{\bar{I}_{zr}} \left\{ \left[ \frac{(\omega^2 + 2\Omega\omega)^2}{\omega_{zr}^2 - (\omega + \Omega)^2} \right] (\alpha_c - \beta_s) - \left[ \frac{(\omega^2 - 2\Omega\omega)^2}{\omega_{zr}^2 - (\omega - \Omega)^2} \right] (\alpha_c + \beta_s) \right\} \sin \omega t
\end{aligned}$$

$$\sum_b^{\infty} (Z_{br} + \Omega Z_{br}) \sin \psi_b =$$

$$- \frac{3}{4} \frac{\sigma_{xzr}}{\bar{I}_{zr}} \left\{ \left[ \frac{(\omega^2 + 2\Omega\omega)^2}{\omega_{zr}^2 - (\omega + \Omega)^2} \right] (\alpha_c - \beta_s) + \left[ \frac{(\omega^2 - 2\Omega\omega)^2}{\omega_{zr}^2 - (\omega - \Omega)^2} \right] (\alpha_c + \beta_s) \right\} \cos \omega t$$

$$- \frac{3}{4} \frac{\sigma_{xzr}}{\bar{I}_{zr}} \left\{ \left[ \frac{(\omega^2 + 2\Omega\omega)^2}{\omega_{zr}^2 - (\omega + \Omega)^2} \right] (\alpha_s + \beta_c) + \left[ \frac{(\omega^2 - 2\Omega\omega)^2}{\omega_{zr}^2 - (\omega - \Omega)^2} \right] (\alpha_s - \beta_c) \right\} \sin \omega t$$

$$\sum_b^{\infty} Y_{br} = -3 \frac{\sigma_{xyr}}{\bar{I}_{yr}} \left[ \frac{\omega^4}{\omega_{yr}^2 - \omega^2} \right] (\gamma_c \cos \omega t + \gamma_s \sin \omega t)$$

$$\frac{d^2}{dt^2} \sum_b Y_{br} \cos \psi_b =$$

$$- \frac{3}{4} \frac{\sigma_{yr}}{\bar{I}_{yr}} \left\{ \left[ \frac{\omega^4}{\omega_{yr}^2 - (\omega + \Omega)^2} \right] (x_s + y_c) - \left[ \frac{\omega^4}{\omega_{yr}^2 - (\omega - \Omega)^2} \right] (x_s - y_c) \right\} \cos \omega t$$

$$+ \frac{3}{4} \frac{\sigma_{yr}}{\bar{I}_{yr}} \left\{ \left[ \frac{\omega^4}{\omega_{yr}^2 - (\omega + \Omega)^2} \right] (x_c - y_s) - \left[ \frac{\omega^4}{\omega_{yr}^2 - (\omega - \Omega)^2} \right] (x_c + y_s) \right\} \sin \omega t$$

$$\frac{d^2}{dt^2} \sum_b Y_{br} \sin \psi_b =$$

$$+ \frac{3}{4} \frac{\sigma_{yr}}{\bar{I}_{yr}} \left\{ \left[ \frac{\omega^4}{\omega_{yr}^2 - (\omega + \Omega)^2} \right] (x_c - y_s) + \left[ \frac{\omega^4}{\omega_{yr}^2 - (\omega - \Omega)^2} \right] (x_c + y_s) \right\} \cos \omega t$$

$$+ \frac{3}{4} \frac{\sigma_{yr}}{\bar{I}_{yr}} \left\{ \left[ \frac{\omega^4}{\omega_{yr}^2 - (\omega + \Omega)^2} \right] (x_s + y_c) + \left[ \frac{\omega^4}{\omega_{yr}^2 - (\omega - \Omega)^2} \right] (x_s - y_c) \right\} \sin \omega t$$

Eliminating blade coordinates  $Z_{br}$  and  $Y_{br}$ , the resulting equations express hub forces and moments in terms of hub displacements only.

$$Z : 3m_z \ddot{Z} - 3 \frac{\sigma_{zr}}{\bar{I}_{zr}} \left[ \frac{\omega^4}{\omega_{zr}^2 - \omega^2} \right] (Z_c \cos \omega t + Z_s \sin \omega t) = F_z$$

$$\alpha : \frac{3}{2} \bar{I}_z (\ddot{\alpha} + 2\Omega \dot{\beta})$$

$$\begin{aligned}
& -\frac{3}{4} \frac{\sigma_{xzr}^2}{\bar{I}_{zr}} \left\{ \left[ \frac{(\omega^2 + 2\Omega\omega)^2}{\omega_{zr}^2 - (\omega + \Omega)^2} \right] (\alpha_c - \beta_s) + \left[ \frac{(\omega^2 - 2\Omega\omega)^2}{\omega_{zr}^2 - (\omega - \Omega)^2} \right] (\alpha_c + \beta_s) \right\} \cos \omega t \\
& -\frac{3}{4} \frac{\sigma_{xzr}^2}{\bar{I}_{zr}} \left\{ \left[ \frac{(\omega^2 + 2\Omega\omega)^2}{\omega_{zr}^2 - (\omega + \Omega)^2} \right] (\alpha_s + \beta_c) + \left[ \frac{(\omega^2 - 2\Omega\omega)^2}{\omega_{zr}^2 - (\omega - \Omega)^2} \right] (\alpha_s - \beta_c) \right\} \sin \omega t = M_\alpha
\end{aligned}$$

$$\beta: \frac{3}{2} \bar{I}_z (\beta^\infty - 2\Omega\alpha)$$

$$\begin{aligned}
& -\frac{3}{4} \frac{\sigma_{xzr}^2}{\bar{I}_{zr}} \left\{ \left[ \frac{(\omega^2 + 2\Omega\omega)^2}{\omega_{zr}^2 - (\omega + \Omega)^2} \right] (\alpha_s + \beta_c) - \left[ \frac{(\omega^2 - 2\Omega\omega)^2}{\omega_{zr}^2 - (\omega - \Omega)^2} \right] (\alpha_s - \beta_c) \right\} \cos \omega t \\
& + \frac{3}{4} \frac{\sigma_{xzr}^2}{\bar{I}_{zr}} \left\{ \left[ \frac{(\omega^2 + 2\Omega\omega)^2}{\omega_{zr}^2 - (\omega + \Omega)^2} \right] (\alpha_c - \beta_s) - \left[ \frac{(\omega^2 - 2\Omega\omega)^2}{\omega_{zr}^2 - (\omega - \Omega)^2} \right] (\alpha_c + \beta_s) \right\} \sin \omega t = M_\beta
\end{aligned}$$

$$x: 3m_y \ddot{x}$$

$$\begin{aligned}
& -\frac{3}{4} \frac{\sigma_{yr}^2}{\bar{I}_{yr}} \left\{ \left[ \frac{\omega^4}{\omega_{yr}^2 - (\omega + \Omega)^2} \right] (x_c - y_s) + \left[ \frac{\omega^4}{\omega_{yr}^2 - (\omega - \Omega)^2} \right] (x_c + y_s) \right\} \cos \omega t \\
& -\frac{3}{4} \frac{\sigma_{yr}^2}{\bar{I}_{yr}} \left\{ \left[ \frac{\omega^4}{\omega_{yr}^2 - (\omega + \Omega)^2} \right] (x_s + y_c) + \left[ \frac{\omega^4}{\omega_{yr}^2 - (\omega - \Omega)^2} \right] (x_s - y_c) \right\} \sin \omega t = F_x
\end{aligned}$$

$$y: 3m_y \ddot{y}$$

$$\begin{aligned}
& -\frac{3}{4} \frac{\sigma_{yr}^2}{\bar{I}_{yr}} \left\{ \left[ \frac{\omega^4}{\omega_{yr}^2 - (\omega + \Omega)^2} \right] (x_s + y_c) - \left[ \frac{\omega^4}{\omega_{yr}^2 - (\omega - \Omega)^2} \right] (x_s - y_c) \right\} \cos \omega t \\
& + \frac{3}{4} \frac{\sigma_{yr}^2}{\bar{I}_{yr}} \left\{ \left[ \frac{\omega^4}{\omega_{yr}^2 - (\omega + \Omega)^2} \right] (x_c - y_s) - \left[ \frac{\omega^4}{\omega_{yr}^2 - (\omega - \Omega)^2} \right] (x_c + y_s) \right\} \sin \omega t = F_y
\end{aligned}$$

$$\gamma: 3\bar{I}_y \ddot{\gamma} - 3 \frac{\sigma_{xyr}^2}{\bar{I}_{yr}} \left[ \frac{\omega^4}{\omega_{yr}^2 - \omega^2} \right] (\gamma_c \cos \omega t + \gamma_s \sin \omega t) = M_\gamma$$

$$F_{z_c} + (a_1)z_c + (0)z_s = 0$$

$$F_{z_s} + (0)z_c + (a_1)z_s = 0$$

$$M\alpha_c + (a_3)\alpha_c + (0)\alpha_s + (0)\beta_c + (a_6)\beta_s = 0$$

$$M\alpha_s + (0)\alpha_c + (a_3)\alpha_s + (-a_6)\beta_c + (0)\beta_s = 0$$

$$M\beta_c + (0)\alpha_c + (-a_6)\alpha_s + (a_3)\beta_c + (0)\beta_s = 0$$

$$M\beta_s + (a_6)\alpha_c + (0)\alpha_s + (0)\beta_c + (a_3)\beta_s = 0$$

$$F_{x_c} + (a_7)x_c + (0)x_s + (0)y_c + (a_{10})y_s = 0$$

$$F_{x_s} + (0)x_c + (a_7)x_s + (-a_{10})y_c + (0)y_s = 0$$

$$F_{y_c} + (0)x_c + (-a_{10})x_s + (a_7)y_c + (0)y_s = 0$$

$$F_{y_s} + (a_{10})x_c + (0)x_s + (0)y_c + (a_7)y_s = 0$$

$$M\gamma_c + (a_{11})\gamma_c + (0)\gamma_s = 0$$

$$M\gamma_s + (0)\gamma_c + (a_{11})\gamma_s = 0$$

Summary of matrix elements without damping:

$$a_1 = 3m_z\omega^2 + \sum_r 3 \frac{\sigma_{zr}^2}{\bar{I}_{zr}} \left[ \frac{\omega^4}{\omega_{zr}^2 - \omega^2} \right]$$

$$a_3 = \frac{3}{2} \bar{I}_z \omega^2 + \sum_r \frac{3}{4} \frac{\sigma_{xzr}^2}{\bar{I}_{zr}} \left[ \frac{\omega^2(\omega + 2\Omega)^2}{\omega_{zr}^2 - (\omega + \Omega)^2} + \frac{\omega^2(\omega - 2\Omega)^2}{\omega_{zr}^2 - (\omega - \Omega)^2} \right]$$

$$a_6 = -3\bar{I}\Omega\omega - \sum_r \frac{3}{4} \frac{\sigma_{xzr}^2}{\bar{I}_{zr}} \left[ \frac{\omega^2(\omega + 2\Omega)^2}{\omega_{zr}^2 - (\omega + \Omega)^2} - \frac{\omega^2(\omega - 2\Omega)^2}{\omega_{zr}^2 - (\omega - \Omega)^2} \right]$$

$$a_7 = 3m_y\omega^2 + \sum_r \frac{3}{4} \frac{\sigma_{yr}^2}{\bar{I}_{yr}} \left[ \frac{\omega^4}{\omega_{yr}^2 - (\omega + \Omega)^2} + \frac{\omega^4}{\omega_{yr}^2 - (\omega - \Omega)^2} \right]$$

$$a_{10} = - \sum_r \frac{3}{4} \frac{\sigma_{yr}^2}{\bar{I}_{yr}} \left[ \frac{\omega^4}{\omega_{yr}^2 - (\omega + \Omega)^2} - \frac{\omega^4}{\omega_{yr}^2 - (\omega - \Omega)^2} \right]$$

$$a_{11} = 3\bar{I}_y\omega^2 + \sum_r 3 \frac{\sigma_{yr}^2}{\bar{I}_{yr}} \left[ \frac{\omega^4}{\omega_{yr}^2 - \omega^2} \right]$$



### Rotor Matrix (Without Damping)

[illegible]

## Rotor System Modes - Damping Included

Damping terms are included in the blade modes, i.e., aerodynamic damping in the flap modes and mechanical damping in the lag modes.

$C_{zi}$  Flap Aerodynamic Damping of Blade Section  $i$ .

$C_{\xi}$  Lag Mechanical Damping at Blade Root

$\xi_b$  Lag Angle at Blade Root

The damping energy of the system is

$$D = \frac{1}{2} \sum_b \sum_i C_{zi} Z_{bi}^2 + \frac{1}{2} \sum_b C_{\xi} \xi^2$$

Using generalized coordinate theory this gives the flap and lag damping terms below,

$$C_{zr} \ddot{Z}_{br} \text{ and } C_{\xi r} \ddot{\xi}_{br}$$

To be included in the flap and lag blade equations of motion

$$C_{zr} = C_{zi} Z_i(r)^2$$

$$C_{\xi r} = C_{\xi} \xi(r)^2$$

Solution of damped flap generalized coordinate  $Z_{br}$

$$\ddot{Z}_{br} + C_{zr} \dot{Z}_{br} + K_{zr} Z_{br} = -\sigma_{zr} \ddot{Z} - \sigma_{xzr} (\ddot{\alpha} + 2\Omega \dot{\beta}) \sin \psi_b + \sigma_{xzr} (\ddot{\beta} - 2\Omega \dot{\alpha}) \cos \psi_b$$

$$\ddot{Z}_{br} + C_{zr} \dot{Z}_{br} + K_{zr} Z_{br} = + \sigma_{zr} (\omega^2 Z_c \cos \omega t + \omega^2 Z_s \sin \omega t)$$

$$+ \sigma_{xzr} \left\{ \begin{array}{l} \omega^2 \alpha_c \cos \omega t \sin \psi_b + \omega^2 \alpha_s \sin \omega t \sin \psi_b \\ + 2\Omega \omega \beta_c \sin \omega t \sin \psi_b - 2\Omega \omega \beta_s \cos \omega t \sin \psi_b \\ - \omega^2 \beta_c \cos \omega t \cos \psi_b - \omega^2 \beta_s \sin \omega t \cos \psi_b \\ + 2\Omega \omega \alpha_c \sin \omega t \cos \psi_b - 2\Omega \omega \alpha_s \cos \omega t \cos \psi_b \end{array} \right\}$$

$$\ddot{Z}_{br} + C_{zr} \dot{Z}_{br} + K_{zr} Z_{br} = + \sigma_{zr} (\omega^2 Z_c \cos \omega t + \omega^2 Z_s \sin \omega t)$$

$$+ \sigma_{xzr} \left\{ \begin{array}{l} \frac{1}{2} \omega (\omega + 2\Omega) (-\alpha_s - \beta_c) \cos(\omega t + \psi_b) + \frac{1}{2} \omega (\omega - 2\Omega) (\alpha_s - \beta_c) \cos(\omega t - \psi_b) \\ \frac{1}{2} \omega (\omega + 2\Omega) (\alpha_c - \beta_s) \sin(\omega t + \psi_b) + \frac{1}{2} \omega (\omega - 2\Omega) (-\alpha_c - \beta_s) \sin(\omega t - \psi_b) \end{array} \right\}$$

Solution of  $Z_{br}$  (Continued):

$$\begin{aligned}
 Z_{br} = & \frac{\sigma_{zr}}{\bar{I}_{zr}} \left[ \frac{\omega^2}{(\omega_{zr}^2 - \omega^2)^2 + (\lambda_{zr}\omega)^2} \right] \left[ (\omega_{zr}^2 - \omega^2)Z_c - (\lambda_{zr}\omega)Z_s \right] \cos \omega t \\
 & + \frac{\sigma_{zr}}{\bar{I}_{zr}} \left[ \frac{\omega^2}{(\omega_{zr}^2 - \omega^2)^2 + (\lambda_{zr}\omega)^2} \right] \left[ (\omega_{zr}^2 - \omega^2)Z_s + (\lambda_{zr}\omega)Z_c \right] \sin \omega t \\
 & + \frac{1}{2} \frac{\sigma_{xzr}}{\bar{I}_{zr}} \left[ \frac{\omega(\omega + 2\Omega)}{\{\omega_{zr}^2 - (\omega + \Omega)^2\}^2 + \{\lambda_{zr}(\omega + \Omega)\}^2} \right] \left[ \{\omega_{zr}^2 - (\omega + \Omega)^2\}(-\alpha_s - \beta_c) \right. \\
 & \quad \left. - \{\lambda_{zr}(\omega + \Omega)\}(\alpha_c - \beta_s) \right] \cos(\omega t + \psi_b) \\
 & + \frac{1}{2} \frac{\sigma_{xzr}}{\bar{I}_{zr}} \left[ \frac{\omega(\omega + 2\Omega)}{\{\omega_{zr}^2 - (\omega + \Omega)^2\}^2 + \{\lambda_{zr}(\omega + \Omega)\}^2} \right] \left[ \{\omega_{zr}^2 - (\omega + \Omega)^2\}(\alpha_c - \beta_s) \right. \\
 & \quad \left. + \{\lambda_{zr}(\omega + \Omega)\}(-\alpha_s - \beta_c) \right] \sin(\omega t + \psi_b) \\
 & + \frac{1}{2} \frac{\sigma_{xzr}}{\bar{I}_{zr}} \left[ \frac{\omega(\omega - 2\Omega)}{\{\omega_{zr}^2 - (\omega - \Omega)^2\}^2 + \{\lambda_{zr}(\omega - \Omega)\}^2} \right] \left[ \{\omega_{zr}^2 - (\omega - \Omega)^2\}(\alpha_s - \beta_c) \right. \\
 & \quad \left. - \{\lambda_{zr}(\omega - \Omega)\}(-\alpha_c - \beta_s) \right] \cos(\omega t - \psi_b) \\
 & + \frac{\sigma_{xzr}}{\bar{I}_{zr}} \left[ \frac{\omega(\omega - 2\Omega)}{\{\omega_{zr}^2 - (\omega - \Omega)^2\}^2 + \{\lambda_{zr}(\omega - \Omega)\}^2} \right] \left[ \{\omega_{zr}^2 - (\omega - \Omega)^2\}(-\alpha_c - \beta_s) \right. \\
 & \quad \left. + \{\lambda_{zr}(\omega - \Omega)\}(\alpha_s - \beta_c) \right] \sin(\omega t - \psi_b)
 \end{aligned}$$

Solution of Damped Lag Generalized Coordinate  $Y_{br}$ :

$$\bar{I}_{yr} \ddot{Y}_{br} + C_{yr} \dot{Y}_{br} + K_{yr} Y_{br} = -\sigma_{xyr} \ddot{\gamma} + \sigma_{yr} \ddot{\gamma} \sin \psi_b - \sigma_{yr} \ddot{\gamma} \cos \psi_b$$

$$\bar{I}_{yr} \ddot{Y}_{br} + C_{yr} \dot{Y}_{br} + K_{yr} Y_{br} = + \sigma_{xyr} (\omega^2 \gamma_c \cos \omega t + \omega^2 \gamma_s \sin \omega t)$$

$$+ \sigma_{yr} \left\{ \begin{aligned} & -\omega^2 x_c \cos \omega t \sin \psi_b - \omega^2 x_s \sin \omega t \sin \psi_b \\ & + \omega^2 y_c \cos \omega t \cos \psi_b + \omega^2 y_s \sin \omega t \cos \psi_b \end{aligned} \right\}$$

$$\bar{I}_{y_r} \ddot{Y}_{b_r} + C_{y_r} \dot{Y}_{b_r} + K_{y_r} Y_{b_r} = + \sigma_{x_{y_r}} (\omega^2 \gamma_c \cos \omega t + \omega^2 \gamma_s \sin \omega t)$$

$$\sigma_{y_r} \left\{ \begin{aligned} & \frac{1}{2} \omega^2 (x_s + y_c) \cos (\omega t + \psi_b) + \frac{1}{2} \omega^2 (-x_s + y_c) \cos (\omega t - \psi_b) \\ & + \frac{1}{2} \omega^2 (-x_c + y_s) \sin (\omega t + \psi_b) + \frac{1}{2} \omega^2 (x_c + y_s) \sin (\omega t - \psi_b) \end{aligned} \right\}$$

$$\begin{aligned} Y_{b_r} = & \frac{\sigma_{x_{y_r}}}{\bar{I}_{y_r}} \left[ \frac{\omega^2}{(\omega_{y_r}^2 - \omega^2)^2 + (\lambda_{y_r} \omega)^2} \right] \left[ (\omega_{y_r}^2 - \omega^2) \gamma_c - (\lambda_{y_r} \omega) \gamma_s \right] \cos \omega t \\ & + \frac{\sigma_{x_{y_r}}}{\bar{I}_{y_r}} \left[ \frac{\omega^2}{(\omega_{y_r}^2 - \omega^2)^2 + (\lambda_{y_r} \omega)^2} \right] \left[ (\omega_{y_r}^2 - \omega^2) \gamma_s + (\lambda_{y_r} \omega) \gamma_c \right] \sin \omega t \\ & + \frac{1}{2} \frac{\sigma_{y_r}}{\bar{I}_{y_r}} \left[ \frac{\omega^2}{\{\omega_{y_r}^2 - (\omega + \Omega)^2\}^2 + \{\lambda_{y_r} (\omega + \Omega)\}^2} \right] \left[ \begin{aligned} & \{\omega_{y_r}^2 - (\omega + \Omega)^2\} (x_s + y_c) \\ & - \{\lambda_{y_r} (\omega + \Omega)\} (-x_c + y_s) \end{aligned} \right] \cos (\omega t + \psi_b) \\ & + \frac{1}{2} \frac{\sigma_{y_r}}{\bar{I}_{y_r}} \left[ \frac{\omega^2}{\{\omega_{y_r}^2 - (\omega + \Omega)^2\}^2 + \{\lambda_{y_r} (\omega + \Omega)\}^2} \right] \left[ \begin{aligned} & \{\omega_{y_r}^2 - (\omega + \Omega)^2\} (-x_c + y_s) \\ & + \{\lambda_{y_r} (\omega + \Omega)\} (x_s + y_c) \end{aligned} \right] \sin (\omega t + \psi_b) \\ & + \frac{1}{2} \frac{\sigma_{y_r}}{\bar{I}_{y_r}} \left[ \frac{\omega^2}{\{\omega_{y_r}^2 - (\omega - \Omega)^2\}^2 + \{\lambda_{y_r} (\omega - \Omega)\}^2} \right] \left[ \begin{aligned} & \{\omega_{y_r}^2 - (\omega - \Omega)^2\} (-x_s + y_c) \\ & - \{\lambda_{y_r} (\omega - \Omega)\} (x_c + y_s) \end{aligned} \right] \cos (\omega t - \psi_b) \\ & + \frac{1}{2} \frac{\sigma_{y_r}}{\bar{I}_{y_r}} \left[ \frac{\omega^2}{\{\omega_{y_r}^2 - (\omega - \Omega)^2\}^2 + \{\lambda_{y_r} (\omega - \Omega)\}^2} \right] \left[ \begin{aligned} & \{\omega_{y_r}^2 - (\omega - \Omega)^2\} (x_c + y_s) \\ & + \{\lambda_{y_r} (\omega - \Omega)\} (-x_s + y_c) \end{aligned} \right] \sin (\omega t - \psi_b) \end{aligned}$$

Final Equations of Motion:

$$Z : 3m_z \ddot{Z} - 3 \frac{\sigma_{zr}^2}{\bar{I}_{zr}} \left[ \frac{\omega^4}{(\omega_{zr}^2 - \omega)^2 + (\lambda_{zr} \omega)^2} \right] \left[ (\omega_{zr}^2 - \omega^2) Z_c - (\lambda_{zr} \omega) Z_s \right] \cos \omega t \\ - 3 \frac{\sigma_{zr}^2}{\bar{I}_{zr}} \left[ \frac{\omega^4}{(\omega_{zr}^2 - \omega)^2 + (\lambda_{zr} \omega)^2} \right] \left[ (\omega_{zr}^2 - \omega^2) Z_s + (\lambda_{zr} \omega) Z_c \right] \sin \omega t = F_z$$

$$\alpha : \frac{3}{2} \bar{I}_z (\alpha^0 + 2\Omega \beta)$$

$$- \frac{3}{4} \frac{\sigma_{xzr}^2}{\bar{I}_{zr}} \left[ \frac{\omega^2 (\omega + 2\Omega)^2}{\{\omega_{zr}^2 - (\omega + \Omega)^2\}^2 + \{\lambda_{zr} (\omega + \Omega)\}^2} \right] \left[ \{\omega_{zr}^2 - (\omega + \Omega)^2\} (\alpha_c - \beta_s) \right. \\ \left. - \{\lambda_{zr} (\omega + \Omega)\} (-\alpha_s - \beta_c) \right] \cos \omega t \\ - \frac{3}{4} \frac{\sigma_{xzr}^2}{\bar{I}_{zr}} \left[ \frac{\omega^2 (\omega - 2\Omega)^2}{\{\omega_{zr}^2 - (\omega - \Omega)^2\}^2 + \{\lambda_{zr} (\omega - \Omega)\}^2} \right] \left[ \{\omega_{zr}^2 - (\omega - \Omega)^2\} (\alpha_c + \beta_s) \right. \\ \left. - \{\lambda_{zr} (\omega - \Omega)\} (-\alpha_s + \beta_c) \right] \cos \omega t \\ - \frac{3}{4} \frac{\sigma_{xzr}^2}{\bar{I}_{zr}} \left[ \frac{\omega^2 (\omega + 2\Omega)^2}{\{\omega_{zr}^2 - (\omega + \Omega)^2\}^2 + \{\lambda_{zr} (\omega + \Omega)\}^2} \right] \left[ \{\omega_{zr}^2 - (\omega + \Omega)^2\} (\alpha_s + \beta_c) \right. \\ \left. + \{\lambda_{zr} (\omega + \Omega)\} (-\alpha_c + \beta_s) \right] \sin \omega t \\ - \frac{3}{4} \frac{\sigma_{xzr}^2}{\bar{I}_{zr}} \left[ \frac{\omega^2 (\omega - 2\Omega)^2}{\{\omega_{zr}^2 - (\omega - \Omega)^2\}^2 + \{\lambda_{zr} (\omega - \Omega)\}^2} \right] \left[ \{\omega_{zr}^2 - (\omega - \Omega)^2\} (\alpha_s - \beta_c) \right. \\ \left. + \{\lambda_{zr} (\omega - \Omega)\} (-\alpha_c - \beta_s) \right] \sin \omega t = M_x$$

$$\beta : \frac{3}{2} \bar{I}_z (\beta^0 - 2\Omega \alpha)$$

$$- \frac{3}{4} \frac{\sigma_{xzr}^2}{\bar{I}_{zr}} \left[ \frac{\omega^2 (\omega + 2\Omega)^2}{\{\omega_{zr}^2 - (\omega + \Omega)^2\}^2 + \{\lambda_{zr} (\omega + \Omega)\}^2} \right] \left[ \{\omega_{zr}^2 - (\omega + \Omega)^2\} (\alpha_s + \beta_c) \right. \\ \left. - \{\lambda_{zr} (\omega + \Omega)\} (-\alpha_c + \beta_s) \right] \cos \omega t \\ - \frac{3}{4} \frac{\sigma_{xzr}^2}{\bar{I}_{zr}} \left[ \frac{\omega^2 (\omega - 2\Omega)^2}{\{\omega_{zr}^2 - (\omega - \Omega)^2\}^2 + \{\lambda_{zr} (\omega - \Omega)\}^2} \right] \left[ \{\omega_{zr}^2 - (\omega - \Omega)^2\} (\alpha_s + \beta_c) \right. \\ \left. - \{\lambda_{zr} (\omega - \Omega)\} (\alpha_c + \beta_s) \right] \cos \omega t$$

$$\begin{aligned}
& - \frac{3}{4} \frac{\sigma_{zr}^2}{\bar{I}_{zr}} \left[ \frac{\omega^2 (\omega + 2\Omega)^2}{\{\omega_{zr}^2 - (\omega + \Omega)^2\}^2 + \{\lambda_{zr}(\omega + \Omega)\}^2} \right] \left[ \begin{aligned} & \left[ \omega_{zr}^2 - (\omega + \Omega)^2 \right] (-\alpha_c + \beta_s) \\ & + \{\lambda_{zr}(\omega + \Omega)\} (\alpha_s + \beta_c) \end{aligned} \right] \sin \omega t \\
& - \frac{3}{4} \frac{\sigma_{zr}^2}{\bar{I}_{zr}} \left[ \frac{\omega^2 (\omega - 2\Omega)^2}{\{\omega_{zr}^2 - (\omega - \Omega)^2\}^2 + \{\lambda_{zr}(\omega - \Omega)\}^2} \right] \left[ \begin{aligned} & \left[ \omega_{zr}^2 - (\omega - \Omega)^2 \right] (\alpha_c + \beta_s) \\ & + \{\lambda_{zr}(\omega - \Omega)\} (-\alpha_s + \beta_c) \end{aligned} \right] \sin \omega t = M_\theta
\end{aligned}$$

$$\begin{aligned}
x : \quad & 3m_y \ddot{X} \\
& - \frac{3}{4} \frac{\sigma_{yr}^2}{\bar{I}_{yr}} \left[ \frac{\omega^4}{\{\omega_{yr}^2 - (\omega + \Omega)^2\}^2 + \{\lambda_{yr}(\omega + \Omega)\}^2} \right] \left[ \begin{aligned} & \left[ \omega_{yr}^2 - (\omega + \Omega)^2 \right] (x_c - y_s) \\ & - \{\lambda_{yr}(\omega + \Omega)\} (-x_s - y_c) \end{aligned} \right] \cos \omega t \\
& - \frac{3}{4} \frac{\sigma_{yr}^2}{\bar{I}_{yr}} \left[ \frac{\omega^4}{\{\omega_{yr}^2 - (\omega - \Omega)^2\}^2 + \{\lambda_{yr}(\omega - \Omega)\}^2} \right] \left[ \begin{aligned} & \left[ \omega_{yr}^2 - (\omega - \Omega)^2 \right] (x_c + y_s) \\ & - \{\lambda_{yr}(\omega - \Omega)\} (-x_s + y_c) \end{aligned} \right] \cos \omega t \\
& - \frac{3}{4} \frac{\sigma_{yr}^2}{\bar{I}_{yr}} \left[ \frac{\omega^4}{\{\omega_{yr}^2 - (\omega + \Omega)^2\}^2 + \{\lambda_{yr}(\omega + \Omega)\}^2} \right] \left[ \begin{aligned} & \left[ \omega_{yr}^2 - (\omega + \Omega)^2 \right] (x_s + y_c) \\ & + \{\lambda_{yr}(\omega + \Omega)\} (-x_c + y_s) \end{aligned} \right] \sin \omega t \\
& - \frac{3}{4} \frac{\sigma_{yr}^2}{\bar{I}_{yr}} \left[ \frac{\omega^4}{\{\omega_{yr}^2 - (\omega - \Omega)^2\}^2 + \{\lambda_{yr}(\omega - \Omega)\}^2} \right] \left[ \begin{aligned} & \left[ \omega_{yr}^2 - (\omega - \Omega)^2 \right] (x_s - y_c) \\ & + \{\lambda_{yr}(\omega - \Omega)\} (-x_c - y_s) \end{aligned} \right] \sin \omega t = F_x
\end{aligned}$$

$$\begin{aligned}
y : \quad & 3m_y \ddot{y} \\
& - \frac{3}{4} \frac{\sigma_{yr}^2}{\bar{I}_{yr}} \left[ \frac{\omega^4}{\{\omega_{yr}^2 - (\omega + \Omega)^2\}^2 + \{\lambda_{yr}(\omega + \Omega)\}^2} \right] \left[ \begin{aligned} & \left[ \omega_{yr}^2 - (\omega + \Omega)^2 \right] (x_s + y_c) \\ & - \{\lambda_{yr}(\omega + \Omega)\} (-x_c + y_s) \end{aligned} \right] \cos \omega t
\end{aligned}$$

$$\begin{aligned}
& - \frac{3}{4} \frac{\sigma_{y_r}^2}{\bar{I}_{y_r}} \left[ \frac{\omega^4}{\{\omega_{y_r}^2 - (\omega - \Omega)^2\}^2 + \{\lambda_{y_r}(\omega - \Omega)\}^2} \right] \left[ \begin{aligned} & \left\{ \omega_{y_r}^2 - (\omega - \Omega)^2 \right\} (-x_s + y_c) \\ & - \left\{ \lambda_{y_r}(\omega - \Omega) \right\} (x_c + y_s) \end{aligned} \right] \cos \omega t \\
& - \frac{3}{4} \frac{\sigma_{y_r}^2}{\bar{I}_{y_r}} \left[ \frac{\omega^4}{\{\omega_{y_r}^2 - (\omega + \Omega)^2\}^2 + \{\lambda_{y_r}(\omega + \Omega)\}^2} \right] \left[ \begin{aligned} & \left\{ \omega_{y_r}^2 - (\omega + \Omega)^2 \right\} (-x_c + y_s) \\ & + \left\{ \lambda_{y_r}(\omega + \Omega) \right\} (x_s + y_c) \end{aligned} \right] \sin \omega t \\
& - \frac{3}{4} \frac{\sigma_{y_r}^2}{\bar{I}_{y_r}} \left[ \frac{\omega^4}{\{\omega_{y_r}^2 - (\omega - \Omega)^2\}^2 + \{\lambda_{y_r}(\omega - \Omega)\}^2} \right] \left[ \begin{aligned} & \left\{ \omega_{y_r}^2 - (\omega - \Omega)^2 \right\} (x_c + y_s) \\ & + \left\{ \lambda_{y_r}(\omega - \Omega) \right\} (-x_s + y_c) \end{aligned} \right] \sin \omega t = F_y
\end{aligned}$$

$$\begin{aligned}
\gamma: \quad & 3\bar{I}_y \gamma \\
& - \frac{3}{4} \frac{\sigma_{x_{y_r}}^2}{\bar{I}_{y_r}} \left[ \frac{\omega^4}{(\omega_{y_r}^2 - \omega^2)^2 + (\lambda_{y_r} \omega)^2} \right] \left[ \begin{aligned} & (\omega_{y_r}^2 - \omega^2) \gamma_c - (\lambda_{y_r} \omega) \gamma_s \end{aligned} \right] \cos \omega t \\
& - \frac{3}{4} \frac{\sigma_{x_{y_r}}^2}{\bar{I}_{y_r}} \left[ \frac{\omega^4}{(\omega_{y_r}^2 - \omega^2)^2 + (\lambda_{y_r} \omega)^2} \right] \left[ \begin{aligned} & (\omega_{y_r}^2 - \omega^2) \gamma_s + (\lambda_{y_r} \omega) \gamma_c \end{aligned} \right] \sin \omega t = M_y
\end{aligned}$$

$$F_{z_c} + (a_1)z_c + (a_2)z_s = 0$$

$$F_{z_s} + (-a_2)z_c + (a_1)z_s = 0$$

$$M_{\alpha_c} + (a_3)\alpha_c + (a_4)\alpha_s + (a_5)\beta_c + (a_6)\beta_s = 0$$

$$M_{\alpha_s} + (-a_4)\alpha_c + (a_3)\alpha_s + (-a_6)\beta_c + (a_5)\beta_s = 0$$

$$M_{\beta_c} + (a_5)\alpha_c + (-a_6)\alpha_s + (a_3)\beta_c + (-a_4)\beta_s = 0$$

$$M_{\beta_s} + (a_6)\alpha_c + (a_5)\alpha_s + (a_4)\beta_c + (a_3)\beta_s = 0$$

$$F_{z_c} + (a_7)x_c + (a_8)x_s + (a_9)y_c + (a_{10})y_s = 0$$

$$F_{x_s} + (-a_8)x_c + (a_7)x_s + (-a_{10})y_c + (a_9)y_s = 0$$

$$F_{y_c} + (a_9)x_c + (-a_{10})x_s + (a_7)y_c + (-a_8)y_s = 0$$

$$F_{y_s} + (a_{10})x_c + (a_9)x_s + (a_8)y_c + (a_7)y_s = 0$$

$$M_{\gamma_c} + (a_{11})\gamma_c + (a_{12})\gamma_s = 0$$

$$M_{\gamma_s} + (-a_{12})\gamma_c + (a_{11})\gamma_s = 0$$

Summary of Matrix Elements:

$$a_1 = 3m_z\omega^2 + \sum_r 3 \frac{\sigma_{zr}^2}{\bar{I}_{zr}} \left\{ \left[ \frac{\omega^4}{(\omega_{zr}^2 - \omega^2)^2 + (\lambda_{zr}\omega)^2} \right] (\omega_{zr}^2 - \omega^2) \right\} + m_{hz}\omega^2$$

$$a_2 = - \sum_r 3 \frac{\sigma_{zr}^2}{\bar{I}_{zr}} \left\{ \left[ \frac{\omega^4}{(\omega_{zr}^2 - \omega^2)^2 + (\lambda_{zr}\omega)^2} \right] (\lambda_{zr}\omega) \right\}$$

$$a_3 = \frac{3}{2} \bar{I}_z \omega^2 + \sum_r \frac{3}{4} \frac{\sigma_{xzr}^2}{\bar{I}_{zr}} \left\{ \left[ \frac{\omega^2(\omega + 2\Omega)^2}{\{\omega_{zr}^2 - (\omega + \Omega)^2\}^2 + \{\lambda_{zr}(\omega + \Omega)\}^2} \right] \{\omega_{zr}^2 - (\omega + \Omega)^2\} \right. \\ \left. + \left[ \frac{\omega^2(\omega - 2\Omega)^2}{\{\omega_{zr}^2 - (\omega - \Omega)^2\}^2 + \{\lambda_{zr}(\omega - \Omega)\}^2} \right] \{\omega_{zr}^2 - (\omega - \Omega)^2\} \right\} \\ + I_{h\alpha}\omega^2$$

$$a_4 = \sum_r \frac{3}{4} \frac{\sigma_{xzr}^2}{\bar{I}_{zr}} \left\{ \left[ \frac{\omega^2(\omega + 2\Omega)^2}{\{\omega_{zr}^2 - (\omega + \Omega)^2\}^2 + \{\lambda_{zr}(\omega + \Omega)\}^2} \right] \{\lambda_{zr}(\omega + \Omega)\} \right. \\ \left. + \left[ \frac{\omega^2(\omega - 2\Omega)^2}{\{\omega_{zr}^2 - (\omega - \Omega)^2\}^2 + \{\lambda_{zr}(\omega - \Omega)\}^2} \right] \{\lambda_{zr}(\omega - \Omega)\} \right\}$$

$$a_5 = \sum_r \frac{3}{4} \frac{\sigma_{xzr}^2}{\bar{I}_{zr}} \left\{ \left[ \frac{\omega^2(\omega + 2\Omega)^2}{\{\omega_{zr}^2 - (\omega + \Omega)^2\}^2 + \{\lambda_{zr}(\omega + \Omega)\}^2} \right] \{\lambda_{zr}(\omega + \Omega)\} \right. \\ \left. - \left[ \frac{\omega^2(\omega - 2\Omega)^2}{\{\omega_{zr}^2 - (\omega - \Omega)^2\}^2 + \{\lambda_{zr}(\omega - \Omega)\}^2} \right] \{\lambda_{zr}(\omega - \Omega)\} \right\}$$

$$a_6 = -3\bar{I}_z\Omega\omega - \sum_r \frac{3}{4} \frac{\sigma_{xzr}^2}{\bar{I}_{zr}} \left\{ \left[ \frac{\omega^2(\omega + 2\Omega)^2}{\{\omega_{zr}^2 - (\omega + \Omega)^2\}^2 + \{\lambda_{zr}(\omega + \Omega)\}^2} \right] \right. \\ \left. \{\omega_{zr}^2 - (\omega + \Omega)^2\} \right. \\ \left. - \left[ \frac{\omega^2(\omega - 2\Omega)^2}{\{\omega_{zr}^2 - (\omega - \Omega)^2\}^2 + \{\lambda_{zr}(\omega - \Omega)\}^2} \right] \right. \\ \left. \{\omega_{zr}^2 - (\omega - \Omega)^2\} \right\} - 2I_{h\alpha}\Omega\omega$$



$$\begin{aligned}
a_7 = 3m_y \omega^2 + \sum_r \frac{3}{4} \frac{\sigma_{yr}^2}{\bar{I}_{yr}} & \left\{ \left[ \frac{\omega^4}{\{\omega_{yr}^2 - (\omega + \Omega)^2\}^2 + \{\lambda_{yr}(\omega + \Omega)\}^2} \right] \{\omega_{yr}^2 - (\omega + \Omega)^2\} \right. \\
& + \left. \left[ \frac{\omega^4}{\{\omega_{yr}^2 - (\omega - \Omega)^2\}^2 + \{\lambda_{yr}(\omega - \Omega)\}^2} \right] \{\omega_{yr}^2 - (\omega - \Omega)^2\} \right\} \\
& + m_{hy} \omega^2
\end{aligned}$$

$$\begin{aligned}
a_8 = \sum_r \frac{3}{4} \frac{\sigma_{yr}^2}{\bar{I}_{yr}} & \left\{ \left[ \frac{\omega^4}{\{\omega_{yr}^2 - (\omega + \Omega)^2\}^2 + \{\lambda_{yr}(\omega + \Omega)\}^2} \right] \{\lambda_{yr}(\omega + \Omega)\} \right. \\
& + \left. \left[ \frac{\omega^4}{\{\omega_{yr}^2 - (\omega - \Omega)^2\}^2 + \{\lambda_{yr}(\omega - \Omega)\}^2} \right] \{\lambda_{yr}(\omega - \Omega)\} \right\}
\end{aligned}$$

$$\begin{aligned}
a_9 = \sum_r \frac{3}{4} \frac{\sigma_{yr}^2}{\bar{I}_{yr}} & \left\{ \left[ \frac{\omega^4}{\{\omega_{yr}^2 - (\omega + \Omega)^2\}^2 + \{\lambda_{yr}(\omega + \Omega)\}^2} \right] \{\lambda_{yr}(\omega + \Omega)\} \right. \\
& - \left. \left[ \frac{\omega^4}{\{\omega_{yr}^2 - (\omega - \Omega)^2\}^2 + \{\lambda_{yr}(\omega - \Omega)\}^2} \right] \{\lambda_{yr}(\omega - \Omega)\} \right\}
\end{aligned}$$

$$\begin{aligned}
a_{10} = \sum_r \frac{3}{4} \frac{\sigma_{yr}^2}{\bar{I}_{yr}} & \left\{ \left[ \frac{\omega^4}{\{\omega_{yr}^2 - (\omega + \Omega)^2\}^2 + \{\lambda_{yr}(\omega + \Omega)\}^2} \right] \{\omega_{yr}^2 - (\omega + \Omega)^2\} \right. \\
& - \left. \left[ \frac{\omega^4}{\{\omega_{yr}^2 - (\omega - \Omega)^2\}^2 + \{\lambda_{yr}(\omega - \Omega)\}^2} \right] \{\omega_{yr}^2 - (\omega - \Omega)^2\} \right\}
\end{aligned}$$

$$a_{11} = 3\bar{I}_y \omega^2 + \sum_r 3 \frac{\sigma_{xyr}^2}{\bar{I}_{yr}} \left\{ \left[ \frac{\omega^4}{(\omega_{yr}^2 - \omega^2)^2 + (\lambda_{yr}\omega)^2} \right] (\omega_{yr}^2 - \omega^2) \right\} + I_{hy} \omega^2$$

$$a_{12} = - \sum_r 3 \frac{\sigma_{xyr}^2}{\bar{I}_{yr}} \left\{ \left[ \frac{\omega^4}{(\omega_{yr}^2 - \omega^2)^2 + (\lambda_{yr}\omega)^2} \right] (\lambda_{yr}\omega) \right\}$$

# Rotor Matrix

$F_{zc}$	$M_{Ac}$	$F_{xc}$	$x_c$	$\beta_c$	$Z_c$	$F_{yc}$	$M_{\delta c}$	$M_{\alpha c}$	$\alpha_c$	$\delta_c$	$y_c$	1	$F_{zs}$	$M_{\beta s}$	$F_{xs}$	$x_s$	$\beta_s$	$Z_s$	$F_{ys}$	$M_{\delta s}$	$M_{\alpha s}$	$\alpha_s$	$\delta_s$	$y_s$	1	$n$	
1	1				$a_1$				$a_5$																		
		1	$a_7$		$a_3$																						
			1		1																						
				1																							
					1																						
			$a_9$																								
						1																					
							1																				
								1																			
									1																		
										1																	
											1																
												1															
													1														
														1													
															1												
																1											
																	1										
																		1									
																			1								
																				1							
																					1						
																						1					
																							1				
																								1			
																									1		
																										1	
																											1

=

$F_{zc}$	$M_{Ac}$	$F_{xc}$	$x_c$	$\beta_c$	$Z_c$	$F_{yc}$	$M_{\delta c}$	$M_{\alpha c}$	$\alpha_c$	$\delta_c$	$y_c$	1	$F_{zs}$	$M_{\beta s}$	$F_{xs}$	$x_s$	$\beta_s$	$Z_s$	$F_{ys}$	$M_{\delta s}$	$M_{\alpha s}$	$\alpha_s$	$\delta_s$	$y_s$	1	$n+1$	
1	1				$a_1$				$a_5$																		
		1	$a_7$		$a_3$																						
			1		1																						
				1																							
					1																						
			$a_9$																								
						1																					
							1																				
								1																			
									1																		
										1																	
											1																
												1															
													1														
														1													
															1												
																1											
																	1										
																		1									
																			1								
																				1							
																					1						
																						1					
																							1				
																								1			
																									1		
																										1	
																											1

The input necessary for the calculation of the rotor matrix, i.e., Elements  $a_1, a_2, a_3, \dots, a_{12}$ , is

$$\begin{array}{ccccccccc} \omega & m_{hz} & m_{hy} & m_z & m_y & & & & & \\ \Omega & I_{hx} & I_{hy} & I_z & I_y & & & & & \\ \omega_{z1} & \sigma_{z1} & I_{z1} & \sigma_{xz1} & c_{z1} & \omega_{y1} & \sigma_{y1} & I_{y1} & \sigma_{xy1} & c_{\xi1} \\ \omega_{z2} & \sigma_{z2} & I_{z2} & \sigma_{xz2} & c_{z2} & \omega_{y2} & \sigma_{y2} & I_{y2} & \sigma_{xy2} & c_{\xi2} \\ \omega_{z3} & \sigma_{z3} & I_{z3} & \sigma_{xz3} & c_{z3} & & & & & \end{array}$$

The input necessary for the calculation of the blade forced response is

$$\begin{array}{cccccc} x_c & \beta_c & z_c & \alpha_c & \gamma_c & y_c \\ x_s & \beta_s & z_s & \alpha_s & \gamma_s & y_s \end{array}$$

and the input used to calculate  $a_1, a_2, \dots, a_{12}$ .  
Calculate all coefficients of  $Z_{br}$  and  $Y_{br}$

$$\begin{aligned} Z_{br} = & (Z_{br})_{c\omega} \cos \omega t + (Z_{br})_{s\omega} \sin \omega t + (Z_{br})_{c(\omega+\Omega)} \cos(\omega t + \psi_b) \\ & + (Z_{br})_s(\omega+\Omega) \sin(\omega t + \psi_b) \\ & + (Z_{br})_{c(\omega-\Omega)} \cos(\omega t - \psi_b) + (Z_{br})_s(\omega-\Omega) \sin(\omega t - \psi_b) \\ Y_{br} = & (Y_{br})_{c\omega} \cos \omega t + (Y_{br})_{s\omega} \sin \omega t + (Y_{br})_{c(\omega+\Omega)} \cos(\omega t + \psi_b) \\ & + (Y_{br})_s(\omega+\Omega) \sin(\omega t + \psi_b) \\ & + (Y_{br})_{c(\omega-\Omega)} \cos(\omega t - \psi_b) + (Y_{br})_s(\omega-\Omega) \sin(\omega t - \psi_b) \end{aligned}$$

Finally, calculate rotor blade tip deflection at frequencies of  $\omega, \omega + \Omega$ , and  $\omega - \Omega$

$$Z_{bi} = \sum_r Z_i^{(r)} Z_{br} \qquad y_{bi} = \sum_r y_i^{(r)} Y_{br}$$

Tip Station is at  $i = 1$  or

$$\begin{aligned} Z_1^{(r)} &= 1.0 & y_1^{(r)} &= 1.0 \\ Z_{b1} &= \sum_r Z_{br} & y_{b1} &= \sum_r Y_{br} \end{aligned}$$

$$(Z_{b1})_{c\omega} = \sum_r (Z_{br})_{c\omega}$$

$$(Z_{b1})_{s\omega} = \sum_r (Z_{br})_{s\omega}$$

$$(Z_{b1})_{c(\omega+\Omega)} = \sum_r (Z_{br})_{c(\omega+\Omega)}$$

$$(Z_{b1})_{s(\omega+\Omega)} = \sum_r (Z_{br})_{s(\omega+\Omega)}$$

$$(Z_{b1})_{c(\omega-\Omega)} = \sum_r (Z_{br})_{c(\omega-\Omega)}$$

$$(Z_{b1})_{s(\omega-\Omega)} = \sum_r (Z_{br})_{s(\omega-\Omega)}$$

$$(y_{b1})_{c\omega} = \sum_r (y_{br})_{c\omega}$$

$$(y_{b1})_{s\omega} = \sum_r (y_{br})_{s\omega}$$

$$(y_{b1})_{c(\omega+\Omega)} = \sum_r (y_{br})_{c(\omega+\Omega)}$$

$$(y_{b1})_{s(\omega+\Omega)} = \sum_r (y_{br})_{s(\omega+\Omega)}$$

$$(y_{b1})_{c(\omega-\Omega)} = \sum_r (y_{br})_{c(\omega-\Omega)}$$

$$(y_{b1})_{s(\omega-\Omega)} = \sum_r (y_{br})_{s(\omega-\Omega)}$$

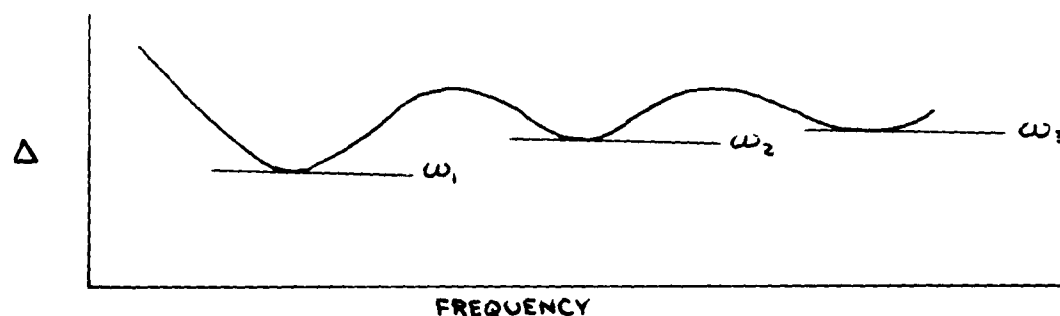


For the free-free boundaries, eliminating the zero column and considering only the force equations the collapsed matrix becomes,

$$\begin{bmatrix} F_{ZR} \\ M_{\phi R} \\ F_{XR} \\ F_{YR} \\ M_{\theta R} \\ M_{\omega R} \\ F_{Zi} \\ M_{\phi i} \\ F_{Xi} \\ M_{Yi} \\ M_{\theta i} \\ M_{\omega i} \end{bmatrix} = \begin{bmatrix} a_{1,4} & a_{1,5} & a_{1,6} & a_{1,10} & a_{1,11} & a_{1,12} & a_{1,17} & a_{1,18} & a_{1,19} & a_{1,23} & a_{1,24} & a_{1,25} \\ a_{2,4} & a_{2,5} & a_{2,6} & a_{2,10} & a_{2,11} & a_{2,12} & a_{2,17} & a_{2,18} & a_{2,19} & a_{2,23} & a_{2,24} & a_{2,25} \\ a_{3,4} & a_{3,5} & & & & & & & & & & \\ a_{7,4} & a_{7,5} & & & & & & & & & & \\ a_{8,4} & a_{8,5} & & & & & & & & & & \\ a_{9,4} & a_{9,5} & & & & & & & & & & \\ a_{14,4} & a_{14,5} & & & & & & & & & & \\ a_{15,4} & a_{15,5} & & & & & & & & & & \\ a_{16,4} & a_{16,5} & & & & & & & & & & \\ a_{20,4} & a_{20,5} & & & & & & & & & & \\ a_{21,4} & a_{21,5} & & & & & & & & & & \\ a_{22,4} & a_{22,5} & & & & & & & & & & \end{bmatrix} \begin{bmatrix} X_R \\ \phi_R \\ Z_R \\ \alpha_R \\ \delta_R \\ Y_R \\ X_i \\ \beta_i \\ Z_i \\ \alpha_i \\ \delta_i \\ Y_i \end{bmatrix}$$

In the undamped solution presented in Appendix C, the condition that the coefficient determinant be equal to zero was necessary to satisfy the boundary conditions. However, in this analysis with damping, the coefficient determinant can only approach zero as repeated trials of the frequency,  $\omega$ , are made, indicating that a steady state harmonic solution does not exist. Minimum values of the coefficient determinant correspond to the damped natural frequencies of the system.

In practice, the residual is plotted against the frequency trials and minimum values determine the damped natural frequencies  $\omega_1, \omega_2, \dots, \omega_n$ .



### Forced Response

In the forced solution, the collapsed matrix can be written as shown in Page 285, but unlike the damped frequency solution the "Q" columns must be included. As shown in the force matrix on Page 255, the "Q" columns are used to introduce the sine and cosine force excitation.

For the forced solution, the collapsed matrix is reduced by eliminating the zero columns and considering only the equations for the force boundaries.

$$\begin{bmatrix} F_{ZR} \\ M_{\theta R} \\ F_{XR} \\ F_{YR} \\ M_{\theta R} \\ M_{\theta R} \\ F_{Zi} \\ M_{\theta i} \\ F_{Xi} \\ F_{Yi} \\ M_{\theta i} \\ M_{\theta i} \end{bmatrix} = \begin{bmatrix} a_{1,4} & a_{1,5} & a_{1,6} & a_{1,10} & a_{1,11} & a_{1,12} & a_{1,13} & a_{1,17} & a_{1,18} & a_{1,19} & a_{1,23} & -a_{1,26} \end{bmatrix} \begin{bmatrix} X_R \\ \theta_R \\ Z_R \\ \alpha_R \\ \delta_R \\ Y_R \\ X_i \\ \theta_i \\ Z_i \\ \alpha_i \\ \delta_i \\ Y_i \\ Q_i \end{bmatrix}$$

Equating the force column to zero and solving for the boundary deflections

$$\begin{bmatrix} X_R \\ \theta_R \\ Z_R \\ \alpha_R \\ \delta_R \\ Y_R \\ X_i \\ \theta_i \\ Z_i \\ \alpha_i \\ \delta_i \\ Y_i \end{bmatrix} = \begin{bmatrix} a_{1,4} & a_{1,5} & a_{1,6} & a_{1,10} & a_{1,11} & a_{1,12} & a_{1,17} & a_{1,18} & a_{1,19} & a_{1,23} & a_{1,24} & a_{1,25} \end{bmatrix} \times$$

$$\begin{bmatrix} a_{1,13} & a_{1,26} \\ a_{2,13} & a_{2,26} \\ a_{3,13} & a_{3,26} \\ a_{7,13} & a_{7,26} \\ a_{8,13} & a_{8,26} \\ a_{9,13} & a_{9,26} \\ a_{14,13} & a_{14,26} \\ a_{15,13} & a_{15,26} \\ a_{16,13} & a_{16,26} \\ a_{20,13} & a_{20,26} \\ a_{21,13} & a_{21,26} \\ a_{22,13} & a_{22,26} \end{bmatrix} \times \begin{bmatrix} Q_R \\ Q_i \end{bmatrix}$$

In the solution, using the above boundary deflections with  $Q_R = Q_i = 1$ , the force mode shape is obtained by progressive multiplication and print-out at each station using the individual matrices and a trial frequency,  $\omega$  corresponding to the frequency of excitation.

Aeronautical Systems Division, Dir/Aero-  
mechanics, Flight Dynamics Laboratory,  
Wright-Patterson Air Force Base, Ohio.  
Rpt No. ASD-TDR-62-284. A STUDY OF TANDEM  
HELICOPTER FUSELAGE VIBRATION. Final report,  
Sep 62, 285p incl illus., 12 refs.

Unclassified Report

A comprehensive research program covering  
many facets of tandem rotor helicopter  
fuselage vibration was conducted. Analytical  
portions consisted of the development of  
methods for the prediction of fuselage natural  
and forced modes; test portions of the pro-  
gram determined fuselage stiffness properties.

( over )

rotor shaft vibratory loads and in-flight  
natural frequencies, modes and vibration  
levels. The results have proven to be of  
considerable value in the design of the  
present generation of helicopters.

1. Vibration
2. Helicopters
- I. AFSC Project 1370  
Task 137004
- II. Contract AF33(616)-  
5240
- III. Vertol Division,  
The Boeing Company,  
Morton, Pa.
- IV. Robert G. Ricks  
V. R-275
- VI. Aval fr OTS
- VII. In ASTIA collection

Aeronautical Systems Division, Dir/Aero-  
mechanics, Flight Dynamics Laboratory,  
Wright-Patterson Air Force Base, Ohio.  
Rpt No. ASD-TDR-62-284. A STUDY OF TANDEM  
HELICOPTER FUSELAGE VIBRATION. Final report,  
Sep 62, 285p incl illus., 12 refs.

Unclassified Report

A comprehensive research program covering  
many facets of tandem rotor helicopter  
fuselage vibration was conducted. Analytical  
portions consisted of the development of  
methods for the prediction of fuselage natural  
and forced modes; test portions of the pro-  
gram determined fuselage stiffness properties.

( over )

rotor shaft vibratory loads and in-flight  
natural frequencies, modes and vibration  
levels. The results have proven to be of  
considerable value in the design of the  
present generation of helicopters.

1. Vibration
2. Helicopters
- I. AFSC Project 1370  
Task 137004
- II. Contract AF33(616)-  
5240
- III. Vertol Division,  
The Boeing Company,  
Morton, Pa.
- IV. Robert G. Ricks  
V. R-275
- VI. Aval fr OTS
- VII. In ASTIA collection



Aeronautical Systems Division, Dir/Aero-  
mechanics, Flight Dynamics Laboratory,  
Wright-Patterson Air Force Base, Ohio.  
Rpt No. ASD-TDR-62-284. A STUDY OF TANDEM  
HELICOPTER FUSELAGE VIBRATION. Final report,  
Sep 62, 285p incl illus., 12 refs.

Unclassified Report

A comprehensive research program covering  
many facets of tandem rotor helicopter  
fuselage vibration was conducted. Analytical  
portions consisted of the development of  
methods for the prediction of fuselage natural  
and forced modes; test portions of the pro-  
gram determined fuselage stiffness properties.

( over )

rotor shaft vibratory loads and in-flight  
natural frequencies, modes and vibration  
levels. The results have proven to be of  
considerable value in the design of the  
present generation of helicopters.

1. Vibration  
2. Helicopters  
I. AFSC Project 1370  
Task 137004  
II. Contract AF33(616)-  
5240  
III. Vertol Division,  
The Boeing Company,  
Morton, Pa.

IV. Robert G. Ricks  
V. R-275  
VI. Aval fr OTS  
VII. In ASTIA collection

Aeronautical Systems Division, Dir/Aero-  
mechanics, Flight Dynamics Laboratory,  
Wright-Patterson Air Force Base, Ohio.  
Rpt No. ASD-TDR-62-284. A STUDY OF TANDEM  
HELICOPTER FUSELAGE VIBRATION. Final report,  
Sep 62, 285p incl illus., 12 refs.

Unclassified Report

A comprehensive research program covering  
many facets of tandem rotor helicopter  
fuselage vibration was conducted. Analytical  
portions consisted of the development of  
methods for the prediction of fuselage natural  
and forced modes; test portions of the pro-  
gram determined fuselage stiffness properties.

( over )

rotor shaft vibratory loads and in-flight  
natural frequencies, modes and vibration  
levels. The results have proven to be of  
considerable value in the design of the  
present generation of helicopters.

1. Vibration  
2. Helicopters  
I. AFSC Project 1370  
Task 137004  
II. Contract AF33(616)-  
5240  
III. Vertol Division,  
The Boeing Company,  
Morton, Pa.  
IV. Robert G. Ricks  
V. R-275  
VI. Aval fr OTS  
VII. In ASTIA collection